QUANTUM LIQUIDS AND QUANTUM CRYSTALS

NMR line broadening in ^{3}He–^{4}He heterophase solid mixtures below 50 mK

N. P. Mikhin*

B. Verkin Institute for Low Temperature Physics and Engineering, National Academy of Sciences of Ukraine, pr. Lenina 47, Kharkov 61103, Ukraine

(Submitted July 10, 2003; revised February 10, 2004)
Fiz. Nizk. Temp. **39**, 575–578 (June 2004)

The possible causes of the previously observed low-temperature decrease in the spin–spin relaxation time in phase-separated ^{3}He–^{4}He solid mixtures are analyzed. It is shown that the jump in magnetic susceptibility at the boundary between the nuclear paramagnet ^{3}He and the diamagnetic ^{4}He matrix gives rise to appreciable local gradients of the external magnetic field at low temperatures in ^{3}He clusters several microns in size, effectively broadening the NMR line. The results of the calculations give a good description of the experimental data. © *2004 American Institute of Physics.* [DOI: 10.1063/1.1768331]

It is of interest to study the magnetic properties of phase-separated ^{3}He–^{4}He solid mixtures not only because of the quantum nature of solid helium but also because of the unique structure of such objects. For example, at low temperatures a phase-separated mixture containing a few percent ^{3}He consists of clusters of the solid nuclear paramagnet ^{3}He with a bcc lattice surrounded by a diamagnetic matrix of practically pure ^{4}He with the hcp structure. Recent experiments[1–3] have shown that the nuclear magnetic relaxation processes for ^{3}He in such systems are substantially different from those in bulk homogeneous samples. It has been shown[4] that in the case of spin–lattice relaxation those differences are due to the influence of the interphase boundaries, the role of which increases especially for a finely disperse daughter phase with characteristic cluster sizes of 2–4 μm.

However, several features of the relaxation processes observed in such systems still remain unexplained. Among these are the monotonic decrease in the spin–lattice (transverse) relaxation time T_2 in the bcc ^{3}He daughter phase on cooling below 40–50 mK.[4] In the present study it is shown that at sufficiently low temperatures the shape of the ^{3}He clusters can have a substantial influence on the measured values of T_2.

According to the model of Blombergen, Purcell, and Pound (the BPP model),[5] subsequently developed by Torrey[6] for the case of ^{3}He–^{4}He mixtures, the rate of transverse relaxation, which is manifested in the dephasing of the precessing magnetic moments of the nuclear spins, is dependent on the coupling between the nuclear spins, which is described in terms of local magnetic fields created by neighboring nuclear spins at the lattice sites. The larger the effective value of the local field, the higher the transverse relaxation rate (or, equivalently, the broader the NMR line, since by definition the latter is the Fourier transform of the transverse relaxation function). The rapid relative motion of the spins in the volume of a sample effectively promotes an averaging of the fluctuations, the averaged value of the local field being much lower than its instantaneous value. Therefore a spin system with a large self-diffusion coefficient is usually characterized by a larger value of T_2.

Nevertheless, direct measurements of the spin diffusion coefficient D_s in the concentrated phase have shown that D_s remains practically unchanged in the entire existence region of that phase, all the way down to 1.5 mK, and its value, $(7\pm2)\times10^{-8}$ cm^2/s (Ref. 4), is close to the value of D_s in bulk solid ^{3}He of the same density. This result is in accord with present-day notions of a temperature-independent D_s, and so the decrease in T_2 observed in Ref. 4 cannot be attributed to a change in the value of D_s.

Measurements of T_2 are usually made by the spin echo method, the amplitude $h(\tau)$ of the echo signal in the general case being attenuated in the presence of a magnetic field gradient G as[7]

$$h = h_0 \exp\left(-\frac{2\tau}{T_2} - \frac{2}{3}\gamma^2 G^2 \tau^3 D_s \right), \tag{1}$$

where τ is the time interval between probe pulses, γ is the gyromagnetic constants, and h_0 is the maximum amplitude of the echo for τ approaching zero. In a homogeneous sample G is the result of nonuniformity of the external field H_0, and therefore, by the use of standard technical measures to improve the geometry of the magnetic field of the solenoid, the second term in the argument of the exponential function (1) can be made negligibly small even for τ larger than T_2.

There is another mechanism of acceleration of the dephasing of the magnetic moments of the ^{3}He nuclear spins that has hardly been discussed in relation to spin–spin relaxation and self-diffusion in a restricted geometry. This involves local gradients of the magnetic field which arise because of the jump in magnetic susceptibility χ at the boundaries of the concentrated and dilute phases. These gradients give rise to a static distribution of Larmor frequencies that can accelerate the dephasing markedly, and that leads to

a decrease in the experimentally observed value of T_2. The NMR line broadening due to such an effect was first observed in the study of powder samples.[8–11]

The results of a computer simulation[12] confirmed by experiments[9–11] showed that inside particles of arbitrary shape with a characteristic size d there arises an effective magnetic-field gradient G^*, proportional to the external magnetic field H_0 and to the difference $\delta\chi$ of the magnetic susceptibilities of the substances of the particles and of the medium surrounding them:

$$G^* \approx 3\,\delta\chi H_0/d. \tag{2}$$

Relation (2) suggests that in the case of solid helium the decrease of T_2 is due to precipitation of the bcc daughter phase in the form of finely disperse formations.

The significant crystallographic misfit between the bcc lattice of ^{3}He and the hcp lattice of the ^{4}He matrix means that the boundary between these phases is an accumulation of structural defects which are associated with local strains and substantial nonuniformity of the magnetic properties. Because the changes in magnetic field occur over those regions, the parameter d in Eq. (2) essentially plays the role of an effective width of the boundary layer. In that sense the formation of the bcc phase in the form of a finely disperse structure is an effective way of accelerating the spin–spin relaxation, since the smaller the size of the particles, the larger the ratio of surface area to volume of the inclusions at a given concentration of the initial mixture. Moreover, if the shape of the inclusions is substantially aspherical, then a particle will have regions with larger curvature of the boundary, and that, in turn, will lead to an increase of the local field gradients.

This model is supported by the results of Refs. 13 and 14 where it was shown by an analysis of the heat capacity data that phase-separated solid mixtures of helium isotopes should contain quasi-one-dimensional fractal structures of ^{3}He. Furthermore, the authors of Refs. 15 and 16 came to the conclusion that at the first-order phase transitions in solids the new-phase clusters should be lenticular or acicular in shape.

The molar magnetic susceptibility χ_4 of the diamagnet ^{4}He is independent of temperature and equal to -2×10^{-6} cgs units per mole.[17] The magnetic susceptibility χ_3 of the nuclear paramagnet ^{3}He, calculated according to the Van Vleck quantum-mechanical theory,[17] is inversely proportional to temperature and is equal to A/T, with $A=1.2\times10^{-7}$ cgs·K/mole. Thus it is obvious that $\delta\chi=|\chi_3-\chi_4|$ varies substantially at $T<100$ mK, when the nuclear susceptibility of ^{3}He begins to exceed the susceptibility of ^{4}He in absolute value.

Estimates according to formula (2) show that at sufficiently low temperatures and for ^{3}He clusters with substantially aspherical parts not more than 10^{-4} cm in size, the gradient G^* of the magnetic field H_0 in them can reach $(0.1–10)H_0$/cm. In such a case the nonuniformity of the real distribution of $G^*(r)$ over the volume of the cluster does not permit making exact calculations. Let $a<1$ be the relative fraction of ^{3}He found in the volume of such aspherical parts where the effective value of G^* is appreciable. Then the attenuation of the spin echo can be described by a sum of two exponentials:

$$h=h_0\left[a\exp\left(-\frac{2\tau}{T_2}-\frac{2}{3}\gamma^2G^{*2}D_S\tau^3\right)+(1-a)\exp\left(-\frac{2\tau}{T_2}\right)\right], \tag{3}$$

where the second term is the contribution of the regions with negligible G^*.

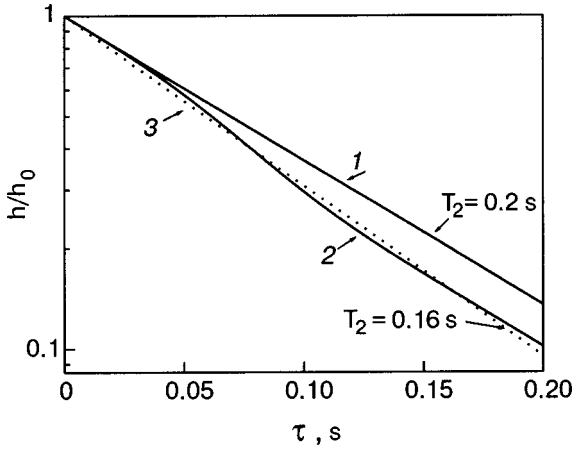

FIG. 1. Calculation of the relative attenuation of the spin echo, $h/h_0(\tau)$: in a uniform magnetic field in accordance with Eq. (1) for $T_2=200$ ms (*1*); in accordance with Eq. (3) for $T_2=200$ ms, $G^*=0.12H_0$/cm, $a=0.25$ (*2*); the result of a least-squares processing of curve *2* according to formula (1) on the assumption that $G=0$, in which case the value $T_2=160$ ms was obtained (*3*).

Figure 1 shows the form of the function (3) with the parameters $T_2=200$ ms, $G^*=0.12H_0$/cm, and $a=0.25$ (curve *2*) in comparison with a dependence of the form (1) for $T_2=200$ ms (curve *1*). The parameter a was chosen so as to achieve the best agreement with the experimental value

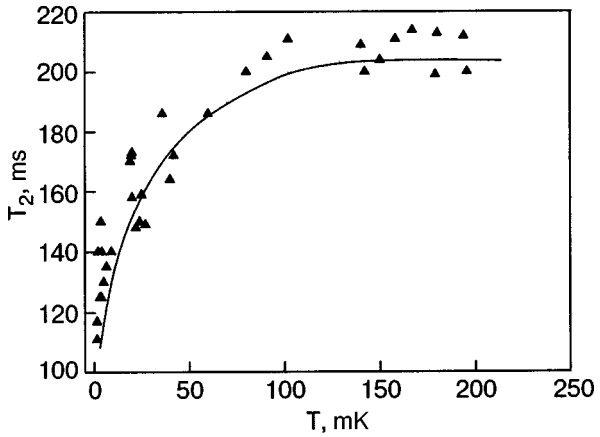

FIG. 2. Temperature dependence of the spin–spin relaxation time below the phase separation temperature in a solid mixture containing 3.18% ^{3}He. The points are the experimental data from Ref. 4. The solid curve is the result of a calculation of the effective T_2 according to formulas (2) and (3) with the true $T_2=0.2$ s.

$T_2 = 160$ ms. Curve *3* in Fig. 1 is the result of a calculation according to formula (1) with the parameters $T_2 = 160$ ms and $G^* = 0$. Taking into account the usual scatter in the echo signal amplitude ($\sim 5\%$), one can consider the agreement of curves *3* and *2* to be satisfactory.

We note that the curve in Fig. 2 is the result of a calculation of an effective T_2 carried out in a manner analogous to that presented in Fig. 1. The good agreement of the result of the calculation with the experimental data[4] is evidence that a substantial fraction of the ^{3}He daughter phase in a phase-separated 1% ^{3}He–^{4}He solid mixture exists in a far from spherical form.

Thus we have shown that to explain the previously observed[4] decrease of T_2 in a phase-separated ^{3}He–^{4}He solid mixtures at temperatures below 50 mK one must admit the existence of aspherical clusters of ^{3}He, which makes for appreciable magnetic-field gradients in those regions. When the influence of these gradients on the relaxation rate of the transverse magnetization is taken into account, one can understand the nature of the previously observed[4] decrease in T_2 at temperatures below 50 mK.

The author is grateful to V. N. Grigor'ev, E. Ya. Rudavskii, S. S. Sokolov, and K. A. Chishko for helpful discussions and also to the co-authors of Ref. 3.

This study was supported by the Ukrainian Foundation for Basic Research 02.07/00391 (Project No. F7/286-2001).

*E-mail: mikhin@ilt.kharkov.ua

[1] N. P. Mikhin, A. V Polev, É. Ya. Rudavskii, and V. A. Shvarts, Fiz. Nizk. Temp. **23**, 607 (1997) [Low Temp. Phys. **23**, 455 (1997)].
[2] S. Kingsley, V. Maidanov, J. Saunders, and B. Cowan, J. Low Temp. Phys. **113**, 1017 (1998).
[3] N. P. Mikhin, A. V. Polev, E. Ya. Rudavskii, E. V. Syrnikov, and V. A. Shvarts, Fiz. Nizk. Temp. **26**, 541 (2000) [Low Temp. Phys. **26**, 395 (2000)].
[4] N. P. Mikhin, V. A. Maidanov, and A. V. Polev, Fiz. Nizk. Temp. **28**, 344 (2002) [Low Temp. Phys. **28**, 239 (2002)].
[5] N. Blombergen, E. M. Purcell, and R. V. Pound, Phys. Rev. **73**, 679 (1948).
[6] H. C. Torrey, Phys. Rev. **92**, 962 (1953); Phys. Rev. **96**, 690 (1954).
[7] A. Abragam, *The Principles of Nuclear Magnetism*, Clarendon Press, Oxford (1961), Izd.-vo Inostr. Lit., Moscow (1963).
[8] F. J. Leech, L. C. Brown, and J. R. Gaines, Phys. Rev. Lett. **11**, 121 (1963).
[9] D. Zamir and R. M. Cotts, Bull. Am. Phys. Soc. **9**, 26 (1964).
[10] D. Zamir, R. C. Wayne, and R. M. Cotts, Phys. Rev. Lett. **12**, 327 (1964).
[11] D. Zamir and R. M. Cotts, Phys. Rev. **134**, A 666 (1964).
[12] L. E. Drain, Proc. Phys. Soc. London **80**, 1380 (1962).
[13] T. N. Antsygina, V. A. Slyusarev, and K. A. Chishko, Fiz. Nizk. Temp. **21**, 583 (1995) [Low Temp. Phys. **21**, 453 (1995)].
[14] T. N. Antsygina, V. A. Slyusarev, and K. A. Chishko, Fiz. Tverd. Tela (St. Petersburg) **40**, 355 (1998) [Phys. Solid State **40**, 325 (1998)].
[15] E. A. Brener, S. V. Iordanskii, and V. I. Marchenko, Phys. Rev. Lett. **82**, 1506 (1999).
[16] E. A. Brener, V. I. Marchenko, H. Muller-Krumbhaar, and R. Spatschek, Phys. Rev. Lett. **84**, 4914 (2000).
[17] S. V. Vonsovskii, *Magnetism*, Vols. 1 and 2, Wiley, New York (1974), Nauka, Moscow (1971)

Translated by Steve Torstveit

Evolution of a pulse of noninteracting quasiparticles with dispersion and initial angular width

I. N. Adamenko

Karazin Kharkov National University, 4 Svobody Sq., Kharkov 61077, Ukraine; Scientific and Technological Center of Electrophysics, National Academy of Sciences of Ukraine, 28 Chernyshevskyi St., P.O. Box 8812, Kharkov 61002, Ukraine

K. E. Nemchenko* and V. A. Slipko

Karazin Kharkov National University, 4 Svobody Sq., Kharkov 61077, Ukraine

A. F. G. Wyatt

School of Physics, University of Exeter, Exeter EX4 4QL, UK
(Submitted December 18, 2003)
Fiz. Nizk. Temp. **30**, 579–589 (June 2004)

The evolution of a pulse of noninteracting quasiparticles, caused by their different velocities and angular distribution of momenta, is studied theoretically. Equations are found that describe the shape of the pulse surface at any time. The times of the beginning and end and the duration of the quasiparticle energy flux density is determined at a general spatial point. The quasiparticle energy density is considered at all times and positions, and it is shown that in the region of high energy density, in the middle of the pulse, it is equal to the initial energy density under certain conditions. These theoretical results are discussed in relation to experimental data on the evolution of a pulse of noninteracting phonons in superfluid helium. © *2004 American Institute of Physics.* [DOI: 10.1063/1.1768332]

1. INTRODUCTION

Quasiparticle pulses are studied theoretically and experimentally in various fields of modern physics. The diverse phenomena that appear are due to a number of factors, the most important of which is the role played by following:

1. The dependence of the quasiparticle energy on momentum (the dispersion or energy—momentum relation). Classical particles can be considered as quasiparticles with a quadratic energy—momentum relation.

2. The angular width of the pulse, which is determined by the angular range of the quasiparticles' momenta.

3. Interactions between quasiparticles.

4. The interaction of quasiparticles with the medium in which the pulse moves.

The above-mentioned factors determine, for example, phenomena observed in photon pulses propagating in an optically transparent medium with variable refractive index, e.g., optical waveguides, or in a medium where the refractive index depends on photon energy. Another interesting property of anisotropic crystals is phonon focusing, which is caused by phonons having different velocities in different directions. Also a wide variety of phenomena are observed in pulses of common particles.

Superfluid helium (He II) is a unique medium for considering quasiparticle propagation. This is due to a number of factors.

1. In superfluid helium there exists quasiparticles with different energy-momentum relations, phonons with an almost linear relation, R^+ rotons with a relation which is close to quadratic but at a finite energy and momentum, and R^- rotons, whose velocity and momentum have opposite directions. The results of experiments on phonon pulses can be found in Refs. 1 and 2, R^+ rotons in Refs. 3 and 4, and R^- rotons in Ref. 5.

2. By changing the temperature of superfluid helium, one can control the interactions of quasiparticles with the ambient medium. So, at relatively high temperatures, a pulse of quasiparticles moving in superfluid helium interacts with the gas of thermal excitations of He II. At relatively low temperatures, when the contribution of the thermal excitation can be neglected, the pulse propagates in a ''superfluid vacuum,'' and its evolution is just determined by the properties of the quasiparticles in the pulse.

3. Interactions between quasiparticles in superfluid helium can be altered by pressure. The use of pressure allows us to reach two limiting cases: the creation of a pulse of strongly interacting phonons and a pulse of almost noninteracting phonons.

At the saturated vapor pressure, low-energy phonons (l phonons) with energy $\varepsilon < 10$ K have anomalous dispersion.[6] In this case, fast three-phonon processes are allowed and cause an almost instantaneous equilibrium in the system of l phonons that form the pulse. This fast relaxation causes a unique phenomenon; a pulse of low energy-phonons creates high-energy phonons (h phonons). Their energy $\varepsilon \geqslant 10$ K, is an order of magnitude greater than the temperature of the l phonons. This phenomenpon was discovered and described in Refs. 7 and 8, and theory of this process was presented in Refs. 9–11. The results of an experimental study of the evolution of strongly interacting phonons was presented in Refs. 12 and 13 and the theory for these pulses was given in Ref. 14.

At a pressure of 19 atm, the dispersion of phonons becomes normal.[15] In this case fast three-phonon processes are prohibited by energy and momentum conservation laws, and four-phonon processes are weak. Thus, it is possible to create a pulse of almost noninteracting phonons, that move in a ''superfluid vacuum,'' formed by He II. Results of experiments on the evolution of such pulses formed by noninteracting phonons are presented in Refs. 16 and 17.

The main aim of this paper is the theoretical study of the evolution in time and space of a pulse of noninteracting quasiparticles propagating in vacuum.

This is the first step in solving the inverse problem, which would enable us to derive the initial characteristics of a phonon pulse, created by a heater, from detected signals at different points in space. The results of this theory are compared to the experimental data of Refs. 16 and 17. It complements the theory of the evolution of a pulse of strongly interacting phonons (see Refs. 14) and can stimulate new experiments. Moreover, the methods presented in this paper can be used to describe the evolution of pulses formed by weakly interacting particles and quasiparticles in other fields of physics.

2. DESCRIPTION OF A PULSE OF NONINTERACTING QUASIPARTICLES

A pulse of quasiparticles can be described by the quasiparticle distribution function $n(\mathbf{p},\mathbf{r},t)$ that determines the number of quasiparticles in a quantum state, which includes the point of phase space $\mathbf{p}$, $\mathbf{r}$.

An important property of a pulse is its energy density

$$E(\mathbf{r},t)=\int_{p_0}^{p_1}\int_{\Omega_p}\varepsilon n\,\frac{p^2dpd\Omega}{(2\pi\hbar)^3}, \tag{1}$$

where $\varepsilon=\varepsilon(p)$ is the energy of the quasiparticle, Ω_p is the solid angle in which the momenta of the quasiparticles lie, and the limits p_0 and p_1 determine the momentum interval for the quasiparticles under consideration. However, the signal amplitude measured by a bolometer is determined by the energy flux density I through the area $d\mathbf{a}$, which is equal to the energy passing per unit time through a unit surface area $d\mathbf{a}$ situated at point $\mathbf{r}$:

$$I(\mathbf{r},t)=\int_{p_0}^{p_1}\int_{\Omega_p}\varepsilon\mathbf{v}_{\rm gr}\mathbf{N}_{\mathbf{a}}n\,\frac{p^2dpd\Omega}{(2\pi\hbar)^3}, \tag{2}$$

where $\mathbf{v}_{\rm gr}=\partial\varepsilon/\partial\mathbf{p}$ is the group velocity of the quasiparticle, and $\mathbf{N}_{\mathbf{a}}$ is the unit vector of the area $d\mathbf{a}$.

The distribution function n appearing in Eqs. (1) and (2) can be found from the solution of the kinetic equation

$$\frac{\partial\mathbf{n}}{\partial t}+\mathbf{v}_{\rm gr}\frac{\partial n}{\partial\mathbf{r}}=J, \tag{3}$$

where J is the collision integral, which determines the change in the number of quasiparticles per unit time in the quantum state under consideration, caused by their interaction.

The kinetic equation (3) should be supplemented by the initial condition

$$n(\mathbf{p},\mathbf{r},t=0)=n_0(\mathbf{p},\mathbf{r}), \tag{4}$$

which determines the pulse in its initial state at $t=0$. In experiments this is the time of the end of the heater pulse. Equation (3) together with the initial condition (4) is the complete formulation of the mathematical problem for deriving the function $n(\mathbf{p},\mathbf{r},t)$. In the general case such a problem has no analytical solution, since the collision integral J in (3) is a nonlinear integral operator, including distribution functions with different momenta. For this reason various model solutions are used to treat definite physical problems. For example, in Ref. 14, a model solution for a phonon system with fast relaxation allowed a complete description of the evolution of a phonon pulse in superfluid helium and gave results which compared with experimental data.[12,13]

Here we consider the opposite limiting case, when the interactions between quasiparticles are so weak that their contribution to the evolution of the pulse can be neglected. In this case, the collision integral J in the kinetic equation (3) is equal to zero, and the solution of the problem can be easily found and looks like

$$n(\mathbf{p},\mathbf{r},t)=n_0(\mathbf{p},\mathbf{r}-\mathbf{v}_{\rm gr}t). \tag{5}$$

Using this solution we can rewrite (1) and (2) as follows:

$$E(\mathbf{r},t)=\int_{p_0}^{p_1}\int_{\Omega_p}\varepsilon n_0\,(\mathbf{p},\mathbf{r}-\mathbf{v}_{\rm gr}t)\,\frac{p^2dpd\Omega}{(2\pi\hbar)^3}, \tag{6}$$

$$I(\mathbf{r},t)=\int_{p_0}^{p_1}\int_{\Omega_p}\varepsilon\mathbf{v}_{\rm gr}\mathbf{N}_{\mathbf{a}}n_0(\mathbf{p},\mathbf{r}-\mathbf{v}_{gr}t)\,\frac{p^2dpd\Omega}{(2\pi\hbar)^3}. \tag{7}$$

According to Eqs. (6) and (7) the temporal deformation of the pulse from its initial state is determined by two factors:

1. The finite angular range of the momenta in the pulse, which is defined by the solid angle

$$\Omega_p=2\pi\zeta_p, \tag{8}$$

where

$$\zeta_p=1-\cos\theta_p \tag{9}$$

is the angular-width parameter. If $\zeta_p\neq 0$, quasiparticles in the pulse have different directions, and this results in a deformation of the initial pulse.

2. The dispersion, when quasiparticles with different momentum have different group velocities, results in a temporal broadening of initial pulse.

If dispersion is neglected, the group velocity can be written in the form $\mathbf{v}_{\rm gr}=c\mathbf{p}/p$, and it follows from Eqs. (6) and (7) when $n_0(p,\mathbf{r})$ that

$$E(\mathbf{r},t)=\int_{\Omega_p}E_0\left(\mathbf{r}-ct\frac{\mathbf{p}}{p}\right)\frac{d\Omega}{\Omega_p}, \tag{10}$$

$$I(\mathbf{r},t)=c\int_{\Omega_p}E_0\left(\mathbf{r}-ct\frac{\mathbf{p}}{p}\right)\frac{\mathbf{p}}{p}\mathbf{N}_{\mathbf{a}}\frac{d\Omega}{\Omega_p}, \tag{11}$$

where

$$E_0(\mathbf{r})=E(\mathbf{r},t=0)=\int_{p_0}^{p_1}\varepsilon\mathbf{n}_0(p,\mathbf{r})\,\frac{p^2dp\Omega_p}{(2\pi\hbar)^3} \tag{12}$$

is the energy density in the initial pulse.

Equations (10) and (11) have a simple physical meaning which allows us to describe the temporal and spatial evolution of the phonon pulse without doing the integration. In

order to find the energy density and the energy flux density at the point $\mathbf{r}$ and at time t according to Eqs. (10) and (11), one should consider a sphere of radius ct and center at $\mathbf{r}$. The energy density at the point $\mathbf{r}$ is equal to the average value of the initial density on the spherical surface of a segment of this sphere with solid angle Ω_p.

By analogy, one can interpret the integrands in the general expressions (6) and (7) as the partial contribution from quasiparticles with momentum $\mathbf{p}$ to the energy $E(\mathbf{r},t)$ and to the flux $I(\mathbf{r},t)$.

3. THE SHAPE OF THE QUASIPARTICLE PULSE AT DIFFERENT TIMES

Let us consider a pulse, moving along the z axis, with the initial distribution function

$$n_0(\mathbf{p},r)=\tilde{n}_0(\rho,\mathbf{r})g(\mathbf{r})\,\eta\left(\frac{p_z}{p}-\cos\theta_p\right), \tag{13}$$

where

$$g(\mathbf{r})=\eta(L_\perp-r)\,\eta(L_\parallel-z)\,\eta(z). \tag{14}$$

Here η is the Heaviside step function, which is equal to unity or zero when the argument is positive or negative, respectively, and $n_0(\mathbf{p},r)$ is nonzero inside the cylinder (14) for all values of momentum specified by the limits of integration in Eqs. (1) and (2). This distribution function describes the pulse considered below. It consists of quasiparticles whose momenta lie inside a cone with solid angle Ω_p, moving along an axis parallel to the z axis of the cylinder (14).

Let us suppose that the moduli of the group velocities of the quasiparticles in this pulse vary between the maximum value

$$v_{\max}=c+v_1 \tag{15}$$

and the minimum value

$$v_{\min}=c-v_2. \tag{16}$$

Let us obtain the equation that describes the shape of this pulse at different times. At time t, the length of the quasiparticle's path changes from its maximum value

$$L_{\max}=v_{\max}t \tag{17}$$

to its minimum value

$$L_{\min}=v_{\min}t. \tag{18}$$

At time t, the cross section of the pulse which includes the z axis (see Fig. 1) is bounded by the front, back, and side surfaces. These are formed by quasiparicles which were in the corresponding surfaces of the initial pulse.

According to (6), the front and the side surfaces of the pulse at time t are formed by the points z and r, which are the centers of segments of spherical surfaces with radius $L_{\max}$ and solid angle Ω_p with axes directed oppositely to the z axis. The spherical surface of a segment should not intersect the front surface of initial pulse but just have a common point with the initial front surface. A plane section through the symmetry axis is shown in Fig. 1. In other words, the points that form the front and side surfaces are at the maximum distance $L_{\max}$ from the initial pulse.

As a result, when r varies between the limits

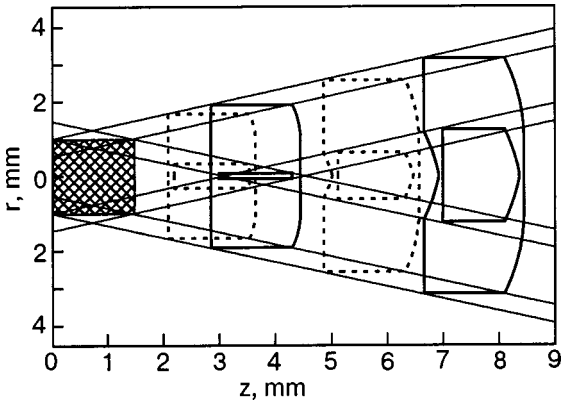

FIG. 1. The shape and form of the structure of the phonon pulse with $t_p=4\,\mu$s and $\theta_p=18°$, and $L_\perp=1$ mm at times $t_1=8.3\,\mu\text{s}<t_\alpha$ and $t_2=19\,\mu\text{s}>t_\alpha$ in the plane of the cross section which includes the axis of the initial pulse. The solid lines represent phonons which move with maximum velocity $v_{\max}=363$ m/s, and the dotted lines correspond to the minimum velocity $v_{\min}=265$ m/s. At time t_1 the rectangular region at the center of the pulse has the initial value of the energy density for phonons with a given velocity. The intersection of all these regions gives the region with the initial value of the energy density. At time t_2 the region at the center of the pulse has a relatively high energy density, but the dispersion has already led to its decrease.

$$0\leqslant r\leqslant L_\perp \tag{19}$$

the front surface is the vertical plane with coordinate

$$z_F=L_\parallel+L_{\max}. \tag{20}$$

As r increases in the range:

$$L_\perp\leqslant r\leqslant r_F(t), \tag{21}$$

where

$$r_F(t)=L_\perp+L_{\max}\sin\theta_p, \tag{22}$$

the front surface becomes an arc, which is described by the equation

$$(z-L_\parallel)^2+(r-L_\perp)^2=L_{\max}^2. \tag{23}$$

This equation determines the r and z coordinates of the front surface of the pulse.

At $r=r_F$ the side surface is a cylinder of radius r_F, with front surface at $z=L_\parallel+L_{\max}\cos\theta_p$ and back surface at $z=L_{\max}\cos\theta_p$.

At points $r>r_F$ the signal is equal to zero. Here it should be noted that the second term in Eq. (22) describes the broadening of the pulse caused by its finite angular width.

According to (6), the back surface of the pulse at time t is defined by the points z and r, which are the centers of segments of spherical surfaces with radius $L_{\min}$ and solid angle Ω_p with axes directed oppositely to the z axis. The spherical surface of this segment should intersect the back surface of the initial pulse and the segment should include the maximum volume of the initial pulse. In this case, the points that form the back surface are at the minimum distance from the back surface of the initial pulse, for a given $L_{\min}$; see Fig. 1.

As a result, at

$$t<t_\alpha=\frac{z_\alpha}{v_{\min}\cos\theta_p}, \tag{24}$$

where

$$z_\alpha = L_\perp / \tan\theta_p \tag{25}$$

(see the pulse at $t=t_1$ in Fig. 1), the back surface is the vertical plane with the coordinates

$$z_B = L_{\min}\cos\theta_p, \tag{26}$$

and the coordinates r are confined by the following inequality:

$$0 \leqslant r \leqslant r_B(t), \tag{27}$$

where

$$r_B(t) = L_\perp + L_{\min}\sin\theta_p. \tag{28}$$

At the time $t>t_\alpha$ (see pulse at $t=t_2$ in Fig. 1) the back surface is the vertical plane with coordinates z_B, if the coordinates r are confined by the following inequality

$$r_a(t) \leqslant r \leqslant r_B(t), \tag{29}$$

where

$$r_a(t) = L_{\min}\sin\theta_p - L_\perp. \tag{30}$$

For smaller values of r, in the range

$$0 \leqslant r \leqslant r_a(t), \tag{31}$$

the back surface becomes an arc and is described by the equation

$$z^2 + (r+L_\perp)^2 = L_{\min}^2. \tag{32}$$

This surface connects the points $r=r_a$, $z=z_B$ with the points

$$r=0; \quad z=\sqrt{L_{\min}^2 - L_\perp^2}. \tag{33}$$

The points of the back vertical surface with coordinates $r=r_B$, $z=z_B$ are connected with the end of the side face, which has the following coordinates: $r=r_M=L_\perp + L_{\max}\sin\theta_p$, $z=z_M=L_{\max}\cos\theta_p$ by a cone-like surface formed by the dispersion.

The length of the pulse $L_z(t,r)$ at various t and r is given by the relation

$$L_z(t,r) = z_{\text{front}}(t,r) - z_{\text{back}}(t,r). \tag{34}$$

At $t<t_\alpha$ when r is changing between the limits (19), using the relations (20), (26), and (34), we get

$$L_z(t<t_\alpha, 0 \leqslant r \leqslant L_\perp) = L_\parallel + (v_1+v_2)t + ct\zeta_p - v_2 t\zeta_p. \tag{35}$$

The second term on the right-hand side of this equation describes the broadening of the pulse caused by dispersion, the third term is caused by the finite angular width of the pulse, and the fourth term is due to the product of dispersion and finite angular width.

At $t>t_\alpha$ and $r=0$, from relations (20), (33) and (34) we obtain

$$L_z(t>t_\alpha, r=0) = L_\parallel + (v_1+v_2)t + L_{\min}\left(1 - \sqrt{\frac{L_\perp^2}{L_{\min}^2}}\right). \tag{36}$$

At $L_\perp^2/L_{\min}^2 \ll 1$ in the third term of the right-hand side of Eq. (36) one can extract the contribution due to the finite angular width:

$$L_z(t>t_\alpha, r=0) = L_\parallel + (v_1+v_2)t + \frac{L_\perp^2}{2ct} + \frac{L_\perp^2}{2ct}\left(\frac{c}{v_{\min}} - 1\right). \tag{37}$$

From a comparison of the results of (35) with (36) and (37) it follows that at any time the broadening of the pulse caused by dispersion is growing. The influence of a finite angular width has the opposite effect (near the axis of the pulse). At $t<t_\alpha$ the length of the pulse grows linearly, and at $t>t_\alpha$ the pulse width, caused by the finite angular width, begins to decrease as $1/t$.

4. THE ENERGY DENSITY OF A PHONON PULSE

The energy density of a phonon pulse at different points in space and time is determined by the initial phonon distribution function (4). Let us consider the case when the initial distribution (5) is given in the following form:

$$n_0(\mathbf{p},\mathbf{r}) = n_0(p)g(\mathbf{r})\eta\left(\frac{p_z}{p} - \cos\theta_p\right). \tag{38}$$

In order to simplify this problem we will not take dispersion into account. Then the energy density at different points in space and time can be calculated by Eq. (6) together with (38) and can be rewritten as follows:

$$E(\mathbf{r},t) = \int_{\Omega_p} E_0 g\left(\mathbf{r} - ct\frac{\mathbf{p}}{p}\right)\frac{d\Omega}{\Omega_p}, \tag{39}$$

where

$$E_0 = \int_{p_0}^{p_1} \varepsilon n_0(p)\frac{p^2 dp\Omega_p}{(2\pi\hbar)^3} \tag{40}$$

is the initial energy density.

According to Eq. (39), in order to find the energy density at the point $\mathbf{r}$ at time t one should build a circular cone with apex at the point $\mathbf{r}$ and radius

$$L_c = ct, \tag{41}$$

solid angle Ω_p and with a spherical end cap of radius L_c. The axis is directed oppositely to the z axis. Below, we refer to this circular cone as simply the cone.

The energy density at the center of the pulse is determined by that part of the spherical surface which lies inside the initial pulse (38). If it lies completely inside the initial pulse, then, according to Eq. (39), the energy density at the point of the apex of this segment is equal to the initial value of the energy density (40). If the spherical surface includes no points of the initial pulse, then the energy density at the apex is zero.

This graphical method of explanation helps us to consider the distribution of the energy. At times $t<t_\alpha$ (see pulse at $t=t_1$ in Fig. 1) the energy density has a maximum value inside the circle with coordinates

$$z_R = L_\parallel + L_c\cos\theta_p, \text{ and } 0 \leqslant r \leqslant r_a(z_R), \tag{42}$$

where

$$r_a(z) = L_\perp\left(1 - \frac{z-L_\parallel}{z_\alpha}\right) \tag{43}$$

for the case

$$L_{\|} > L_c \zeta_p . \tag{44}$$

The spherical surfaces of the cones whose apexes are situated on the circle (42) are found to lie completely inside the initial pulse, and so the energy density on the circle (42) is equal to the initial value.

It should be noted that according to Eq. (35), when the inequality (44) is valid, the length of the initial pulse is greater than its longitudinal broadening caused by the finite angular width. In this case, according to inequality (44), there exists a region inside the pulse in which the energy density is maximal and equal to the value of the energy density in the initial pulse (40) (see the cylindrical region at $t = t_1$ in Fig. 1). This region is closed by two circles at each end, one of which is given by Eq. (42) and the other by the following expressions:

$$z_L = L_c , \text{ and } 0 \leqslant r \leqslant r_a(z_R). \tag{45}$$

The side surface is described by the equation $r = r_a(z_R)$.

The length of this region is

$$z_R - z_L = L_{\|} - L_c \zeta_p , \tag{46}$$

and the length of the pulse at this time is equal to

$$L_z = L_{\|} + L_c \zeta_p . \tag{47}$$

As a result, the region with the maximum value of energy density, E_0, is separated from the front and back surfaces by the distance $L_c \zeta_p$, which is equal to the broadening of the pulse. During the motion of the pulse along the z axis, the size of this region with E_0 shows a monotonic decrease and disappears at the point $z = L_{\|} + z_\alpha$, which is the point of intersection of the lines $r_a(z)$ with the z axis.

Here we should note that according to Ref. 14 a region of the pulse with density E_0 exists in the opposite limiting case, when the pulse is formed by strongly interacting phonons. However, the physical reasons for this region and its decrease are quite different in the two cases. Moreover, a phonon pulse of strongly interacting phonons, with the initial distribution function (38), moves along the z axis with much less transverse broadening than for noninteracting particles, in spite of the angular width and dispersion (see Ref. 14).

At $t > t_\alpha$ the integral (39) always has a region which gives no contribution to the energy density, i.e., where the initial pulse is absent (see pulse at $t = t_2$ in Fig. 1). That is why at times $t > t_\alpha$ the energy density, at all points in the pulse, is less than the initial energy density (40).

However, in this case the pulse has a region where the energy density is greater than at other points in the pulse. This region has coordinates

$$z'_R = L_{\|} + \sqrt{L_c^2 - L_{\perp}^2} \text{ and } r = 0, \tag{48}$$

since the spherical surface of the cone, with apex at the point (48), intersects the edges of the front surface of the initial pulse at the point with coordinates $z = L_{\|}$ and $r = L_{\perp}$. Clearly this region contributes most to the integral (39).

The situation corresponding to inequality (44) in the case considered case takes place at

$$L_{\|} > L_c \left(1 - \sqrt{1 - \frac{L_{\perp}^2}{L_c^2}} \right), \tag{49}$$

when the length of the initial pulse is greater than the broadening caused by the finite angular width, described by the third term on the right-hand side of Eq. (36).

When the inequality (49) is satisfied, the pulse at $t > t_\alpha$ has a relatively high energy density, separated by the surfaces described by Eq. (48) and the point

$$z'_L = L_c \text{ and } r = 0, \tag{50}$$

which is the apex of the cone whose spherical surface intersects the side face of the initial pulse and touches its back face.

5. THE BEGINNING, END, AND DURATION OF THE QUASIPARTICLE PULSE AT DIFFERENT SPATIAL POINTS

Consider the pulse at $t = 0$, described at the beginning of Sec. 3. Taking into account the symmetry of the initial pulse, it is sufficient to consider the solution of the problem in the plane of the cross section which includes the z axis and coincides with the axis of the cylinder (14), which describes the surface boundaries of the initial pulse.

In experiments, the signals are detected with detectors which are oriented so that all the quasiparticles in the pulse have

$$\mathbf{v}_{gr} \cdot \mathbf{N_a} \neq 0. \tag{51}$$

Thus we shall assume below that the condition (51) holds.

The time of the start of the signal $t_{beg}(z,r)$ detected at the point with coordinates z and r can be found from the geometric interpretation of formula (6) in the way we now describe. One should again construct a cone with apex at the point z,r and axis directed oppositely to axis z, with solid angle Ω_p. The surface of the cone's spherical end cap should have just one common point with the front or side surfaces of the initial pulse. Then the radius of this segment is calculated and this value gives us the minimum value $R_{min}(z,r)$, determined by position of point z,r. The time of the start of the signal is given by the following formula:

$$t_{beg}(z,r) = \frac{R_{min}(z,r)}{v_{max}}. \tag{52}$$

Using this interpretation, the dependence on coordinates z at any r is given by

$$t_{beg}(z, 0 \leqslant r \leqslant L_{\perp}) = \frac{z - L_{\|}}{v_{max}}. \tag{53}$$

The signal at time (53) is formed by phonons moving parallel to the z axis with velocity v_{max} from the front surface of the initial pulse. In Fig. 1 at $t = t_1$ and $t = t_2$ these phonons create the front surface.

Figure 2 shows the dependence on time of the signals at points with different values of r with a fixed value of z. In Fig. 2 the time (53) at $z = z_1$ and $z = z_2$ is shown by the vertical lines which are determined by the interval (19).

On further increasing r, when

$$L_{\perp} \leqslant r \leqslant r_F(z), \tag{54}$$

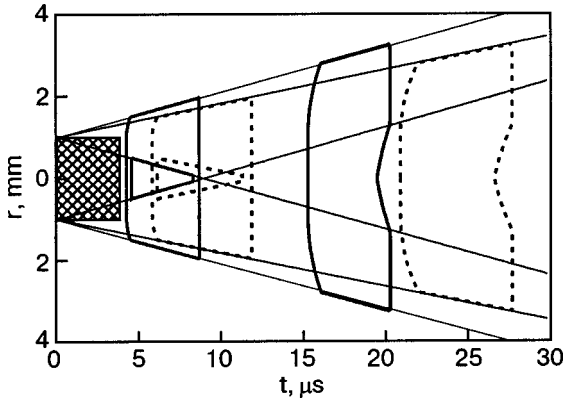

FIG. 2. The beginning, end, and duration of the same phonon signal as in Fig. 1 at points with coordinates z $z_1<z_\alpha$ and $z_2>z_\alpha$ at different values of the radius r. The solid lines represent phonons moving with maximum velocities, and the dotted lines, phonons with minimum velocities. The cone-like region at $z=z_1=3$ mm represents the maximum possible amplitude of the signal. At the point $z=z_2=7$ mm there is no region of constant signal.

where

$$r_F(z)=L_\perp+(z-L_\parallel)\tan\theta_p=L_\perp\frac{z+z_\alpha-L_\parallel}{z_\alpha}, \tag{55}$$

the time of the start of the signal is given by

$$t_{\rm beg}(z,L_\perp\leqslant r\leqslant r_F(z))=\frac{1}{v_{\max}}\sqrt{(r-L_\perp)^2+(z-L_\parallel)^2}. \tag{56}$$

The signal at time (56) is formed by quasiparticles that move at a definite angle $0\leqslant\theta\leqslant\theta_p$ with respect to the z axis, with velocity $v_{\max}$ from the point $z=L_\parallel$ and $r=L_\perp$ of the initial pulse. Figure 1 shows that at $t=t_1$ and $t=t_2$ these quasiparticles create the arc on the front surface of the pulse (23). In Fig. 2 at $z=z_1$ and $z=z_2$, the time (56) is shown by the curve (56).

And, finally, when r lies between the limits

$$r_F(z)\leqslant r\leqslant r_B(z), \tag{57}$$

where

$$r_B(z)=L_\perp+z\tan\theta_p=L_\perp\frac{z+z_\alpha}{z_\alpha}, \tag{58}$$

the time of the start of the signal is given by

$$t_{\rm beg}(z,r_F(z)\leqslant r\leqslant r_B(z))=\frac{r-L_\perp}{v_{\max}\sin\theta_p}. \tag{59}$$

The signals at time (59) are formed by quasiparticles moving at angle θ_p with respect to the z axis with the velocity $v_{\max}$ from the side surface of the initial pulse. In Fig. 1 at $t=t_1$ and $t=t_2$ these quasiparticles form the cylindrical side surface $r=r_F(t)$ [see Eq. (22) and the second sentence after Eq. (23)]. Figure 2 at $z=z_1$ and $z=z_2$ shows the time (59) by the line segment inside the interval (59).

At $r>r_B(z)$ there is no quasiparticle signal because θ_p is the maximum angle of quasiparticle motion in the initial pulse.

Using the geometric interpretation of expression (6), let us find the time $t_{\rm end}(z,r)$ of the end of the signal at a definite point z,r. In order to do this, it is sufficient to create the same cone as before but now this segment must intersect the back face of the initial pulse and include as many points of the initial pulse as possible. Then we find the radius of this segment $R_{\max}(z,r)$ and calculate the desired time:

$$t_{\rm end}(z,r)=\frac{R_{\max}(z,r)}{v_{\min}}. \tag{60}$$

Using this approach, for points with $z<z_\alpha$, when the radius varies inside the interval

$$0\leqslant r\leqslant r_B(z), \tag{61}$$

we find the maximum value for the time of the end of the signal, as will be shown below,

$$t_{\rm end}^{(\max)}=\frac{z}{v_{\min}(1-\zeta_p)}. \tag{62}$$

The signal at time (62) is created by quasiparticles which move at the angle θ_p with respect to the z axis, with velocity $v_{\min}$, from the back surface of the initial pulse. In Fig. 1, at $t=t_1$, these phonons form the back surface of the pulse. Figure 2 at $z=z_1$, shows the time (62) by the segment of the vertical line inside the interval (61).

In Fig. 2 at $z=z_1$ and $z=z_2$ an imaginary horizontal line connects the end of the line describing the beginning of the signal (59) with the end of the vertical line, which describes the time of the end of the signal. These correspond to $v=v_{\max}$ and $v=v_{\min}$. In Fig. 1 at $t=t_1$ and $t=t_2$ the corresponding construction connects the ends of the back vertical surfaces.

At $z>z_\alpha$, when the radius changes inside the interval

$$r_A(z)\leqslant r\leqslant r_B(z), \tag{63}$$

where

$$r_A(z)=L_\perp\frac{z-z_\alpha}{z_\alpha}, \tag{64}$$

the time of the signal end is given by formula (62) and this signal is formed by the same quasiparticles as those at the end of the pulse at $z=z_1$. In Fig. 1 at $t=t_2$ these quasiparticles form the back surface of the pulse. In Fig. 2 at $z=z_2$, the time (62) is shown by the segment of the right vertical line, which is bounded by inequalities (63).

At $z>z_\alpha$, when the radius changes inside the interval

$$0\leqslant r\leqslant r_A(z), \tag{65}$$

the time of the end of the signal is given by

$$t_{\rm end}(z>z_\alpha,0\leqslant r\leqslant r_A(z))=\frac{1}{v_{\min}}\sqrt{z^2+(r+L_\perp)^2}. \tag{66}$$

At this time, signals are created by quasiparticles that move at a definite angle $0\leqslant\theta\leqslant\theta_p$ with respect to the z axis with velocity $v_{\min}$, from the point $z=0$, $r=L_\perp$ of the initial pulse. In Fig. 1 at $t=t_2$ these quasiparticles form the arc of the back surface, and in Fig. 2 at $z=z_2$, the time (66) is described by the right arc of a hyperbola.

The duration of the pulse at the point z,r is determined by the equality

$$\Delta t(z,r)=t_{\rm end}(z,r)-t_{\rm beg}(z,r). \tag{67}$$

According to (53), (56), (59), and (60) at $z<z_\alpha$ the duration of the pulse has a maximum value when r is inside the interval $0\leqslant r\leqslant L_\perp$ and equal to

$$\Delta t_{\max}=t_p+z\frac{v_1+v_2}{v_{\max}v_{\min}}+z\frac{\zeta_p}{v_{\min}(1-\zeta_p)}, \tag{68}$$

where $t_p=L_\parallel/v_{\max}$ is the initial length of the pulse. In the right-hand side of Eq. (68) the second term describes the increase in pulse length due to dispersion, and the third term is caused by the finite angular width.

With the use of relations (56), (62), and (67) at $z<z_\alpha$ when $L_\perp\leqslant r\leqslant r_F$ the pulse duration is given by

$$\Delta t_F=\Delta t_{\max}+\frac{1}{v_{\max}}(z-L_\parallel-\sqrt{(z-L_\parallel)^2+(r-L_\perp)^2}). \tag{69}$$

At $r=L_\perp$ the increase in the pulse length, according to (69), reaches its maximum value at $\Delta t_{\max}$. Increasing r causes the signal length to decrease, so that at $r=r_F$ we have

$$\Delta t_F(r=r_F)=\frac{t_p}{1-\zeta_p}+\frac{z}{1-\zeta_p}\frac{v_1+v_2}{v_{\max}v_{\min}}. \tag{70}$$

According to Eqs. (59), (62), and (67) at $z<z_\alpha$ when $r_F\leqslant r\leqslant r_B$, the pulse length is given by

$$\Delta t_B=\frac{z}{v_{\min}\cos\theta_p}-\frac{r-L_\perp}{v_{\max}\sin\theta_p}. \tag{71}$$

From this equation it follows that the length of the pulse decreases from the maximum value (70) to the minimum value at $r=r_B$ and is given by

$$\Delta t_B(r=r_B)=\frac{z}{1-\zeta_p}\frac{v_1+v_2}{v_{\max}v_{\min}}, \tag{72}$$

where the length of the signal does not depend on t_p and is determined by the dispersion together with an additional contribution from the finite value of the angular width. At $r>r_B$ there is no signal. Expressions (68)–(72) give the length of the pulse at $z<z_\alpha$ for all r.

At $z>z_\alpha$, from Eqs. (53), (66), and (67), for a value of r inside the interval

$$0\leqslant r\leqslant\min(L_\perp,r_A), \tag{73}$$

it follows that

$$\Delta t_\perp=t_p+z\frac{v_1+v_2}{v_{\max}v_{\min}}+\frac{z}{v_{\min}}\left(\sqrt{1+\left(\frac{r+L_\perp}{z}\right)^2}-1\right). \tag{74}$$

At $r_A<L_\perp$ expression (74) has a maximum value (68), when r is changing inside the interval $r_A\leqslant r\leqslant L_\perp$.

At $z>z_\alpha$ and $r_A<L_\perp$, when $L_\perp\leqslant r\leqslant r_F$, the length of the pulse can be found from expression (69), and for greater r ($r_F\leqslant r\leqslant r_B$) by expression (71).

Using the equations (56), (62), and (66) at $z<2z_\alpha$ for r inside the interval $L_\perp\leqslant r\leqslant r_A$ for the pulse length we get

$$\Delta t_A=t_p+z\frac{v_1+v_2}{v_{\max}v_{\min}}+\frac{(r+L_\perp)^2}{2zv_{\min}}-\frac{(r-L_\perp)^2}{2(z-L_\parallel)v_{\max}}. \tag{75}$$

On the right-hand side of this equation, the third and fourth terms describe the contribution of the finite angular width, which decreases with increasing z.

At $z>2z_\alpha$ and $L_\perp<r_A<r<r_F$ the length of the signal is given by Eq. (69), and at $r_F\leqslant r\leqslant r_B$, by the relation (71). At $r>r_B$ there is no signal.

The result (68)–(75) describes the length of the pulse at any value of r and z. From an examination of these results, it follows that the length of the pulse always grows linearly due to dispersion. As to the contribution of the finite angular width, at first (when $z<z_\alpha$ and $0\leqslant r\leqslant L_\perp$) the signal length grows linearly with z. At $z>z_\alpha$ such a dependence takes place only at $z_\alpha<z<2z_\alpha$ and $r_A\leqslant r\leqslant L_\perp$. In all other cases, the contribution of the finite angular width to the increase of the pulse length is either constant [or grows when $\zeta_p=0$—see Eq. (70)], or decreases with increasing z. For large z the contribution of the finite angular width to the increase of the pulse length can be neglected [see Eqs. (74) and (75)].

However, it should be emphasized that according to Eq. (58) it is the finite angular width that always leads to the linear increase of the transverse width of the pulse with increasing z. As energy is conserved, this results in the signal decreasing monotonically along the z axis during the motion of the signal.

6. TEMPORAL DEPENDENCE OF THE SIGNAL AMPLITUDE IN SPACE

Let us consider the case when the initial distribution is given by relation (38) and omit dispersion, which is not so important for the signal amplitude. In this case relation (7) can be written as

$$I(\mathbf{r},t)=c\int_{\Omega_p}E_0 g\left(\mathbf{r}-ct\frac{\mathbf{p}}{p}\right)\frac{\mathbf{p}}{p}\mathbf{N_a}\frac{d\Omega_p}{\Omega_p}. \tag{76}$$

The temporal dependence of the signal amplitude at the point z,r can be obtained from the geometrical interpretation of the formula (76) which we used above. To find the amplitude at the point z,r we create a cone with its apex at this point, with solid angle Ω_p and radius R, and with its axis directed oppositely to the z axis. The signal amplitude at the apex is determined by the averaged value of (76) using the initial energy density (40). The time $t(R,z,r)$ of the signal detected at the point z,r under consideration is determined by

$$t(R,z,r)=R/c. \tag{77}$$

If all of the spherical end surface of the cone lies inside the initial pulse, then, according to (76) at time (77) the signal amplitude is equal to the initial value which would be detected by the bolometer at $t=0$, with the given $\mathbf{N_a}$, situated inside the initial pulse. If the curved surface of the cone has no points within the initial pulse, the signal at time (77) is equal to zero.

Using this approach we can find, without integration, the point z,r at which the amplitude will have maximum value and find the time interval when the maximum value will be observed. During the initial stage of the evolution, there exists, for a definite time, a region (denoted by the subscript ''spot'') where the amplitude is equal to its initial value. It follows from (76) at time t that this region is bound by two planes

$$z_L = ct \leqslant z \leqslant z_R = L_\parallel + ct\cos\theta_p \tag{78}$$

and the cylindrical surface which describes the right-hand side of the inequality

$$0 \leqslant r \leqslant r_a(z_R) = L_\perp - ct\sin\theta_p . \tag{79}$$

From inequalities (78) and (79), we see that the time duration that this region exists is determined as follows:

$$t \leqslant t_{\text{spot}} = \min\left(\frac{L_\perp}{c\sin\theta_p}, \frac{L_\parallel}{c(1-\cos\theta_p)}\right). \tag{80}$$

At $t \leqslant t_{\text{spot}}$ the region lies within the pulse. In the case of a sufficiently long pulse, for which

$$\frac{L_\parallel}{1-\cos\theta_p} > \frac{L_\perp}{\sin\theta_p}, \tag{81}$$

the maximum values of z where one can observe the maximum amplitude according to inequalities (78) and (80) is equal to

$$z_{\max} = z_R(t_{\text{spot}}) = L_\parallel + L_\perp\cos\theta_p = L_\parallel + z_\alpha . \tag{82}$$

In the case of sufficiently short pulses

$$\frac{L_\parallel}{1-\cos\theta_p} < \frac{L_\parallel}{\sin\theta_p} \tag{83}$$

from the inequalities (78) and (80), we get

$$z_{\max} = z_R(t_{\text{spot}}) = \frac{L_\parallel}{1-\cos\theta_p}.$$

The evolution of the maximum-region for the case (81) is presented in Figs. 1 and 2.

In the case (81), at fixed valuez $z = z_1 < z_{\max}$ in the plane r,t (see Fig. 2) the high-energy-density region, with the initial value of the signal amplitude, is determined by the inequalities [see inequalities (78)]

$$\frac{z_1 - L_\parallel}{c\cos\theta_p} \leqslant t \leqslant \frac{z_1}{c} \tag{84}$$

and is bounded by the conical side surface [see inequality (79)]

$$r = L_\perp - ct\sin\theta_p . \tag{85}$$

When $z > z_{\max}$ the high-energy-density region is absent and there is no region where amplitude of the signal is constant (see Fig. 2).

7. DISCUSSION

The results obtained above allow us to discuss the experimental data presented in Ref. 16. In these experiments the amplitude of the phonon signal was measured by a bolometer, situated at the distance $z_B = 8$ mm.

The helium had such a low temperature ($T_{\text{He}} \leqslant 0.1$ K) that the thermal excitations can be neglected. A heater injected a pulse of phonons into this pure and isotropic superfluid helium (''the superfluid vacuum''). The duration of the pulse was 5 μs and it moved in the direction normal to the surface of the heater.

The helium was under 24 atm pressure, at which phonon interactions are determined by the relatively slow four-phonon processes. This fact justified the authors' using a model of noninteracting phonons, moving ballistically. We start from this model, as it allows us to use the results obtained in this paper.

Here we present the numerical values of all parameters that describe the experiments of Ref. 16. The sound velocity in helium at pressure of 24 atm is equal to $c = 363$ m/s. The heater was made from a gold film and had dimensions $L_\perp = 0.5$ mm. The velocity of longitudinal sound in gold is equal to $c_l = 3240$ m/s and that of transverse sound, $c_t = 1200$ m/s.

Using the acoustical theory of transmission,[18,19] we find the maximum value θ_0 for a phonon radiated by a perfectly plane heater into helium:

$$\theta_0 = \arcsin c/c_t = 0.307 \ \text{ rad.} \tag{86}$$

Below, we use this numerical value of the parameter $\theta_p = \theta_0$ even though the evaporated gold film is rough and the conditions for a critical cone are not met. However, the phonon emission from a gold film has been measured and is found to be strongly peaked in the direction of the surface normal.[20] Then for typical distance z_α, according to (25) we have $z_\alpha = 1.58$ mm, and for the length of the initial pulse $L_\parallel = t_p c$ in this case we have $L_\parallel = 1.82$ mm. The size of bolometer was 1×1 mm.

The amplitude of the phonon signal was measured at a distance z_B which was five times greater than z_α. In this case we will use expression (74) for calculating the pulse length.

To calculate the velocities v_1 and v_2 appearing in (74), we use the energy—momentum relation for phonons:

$$\varepsilon = cp(1-\gamma p^2), \tag{87}$$

where, according to Ref. 16, at a pressure of 24 atm the dispersion parameter is equal to $\gamma = 8.96 \times 10^{-4}$ K^{-2}. According to (87) one can consider that $v_1 = 0$ [see Eqs. (15) and (16)], and v_2 can be found from the relation

$$v_2 = \overline{(c - v_{\text{gr}})}, \tag{88}$$

where the overbar denotes averaging with respect to momentum with an equilibrium function for the initial phonons in the pulse. Integration of (88) with the Bose—Einstein distribution function gives

$$\frac{v_2}{c} = 0.028 T_0^2, \tag{89}$$

where T_0 is the temperature that describes the distribution of the initial phonon pulse.

Comparing the numerical values of the second and third terms on the right-hand side of Eq. (74), which describe the broadening of the pulse caused, respectively, by dispersion and the finite angular width of the initial pulse, we conclude that the contribution of the latter is negligibly small. The numerical value of the contribution of the dispersion is equal to

$$\delta t_{\text{disp}} = \frac{z_B}{c}\frac{v_2}{v_{\min}} = \frac{0.62 T_0^2}{1 - 0.028 T_0^2}\,\mu\text{s}. \tag{90}$$

According to the result presented in Sec. 6, when z_B exceeds z_α by a factor of five, even in the region of maximum phonon energy density, the energy density is much less

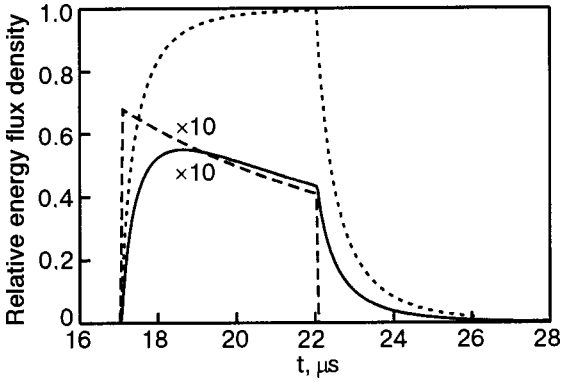

FIG. 3. The temporal dependence of the energy flux density at $z=8$ mm, $t_p=5$ μs, $\theta_p \approx 17.6°$, and $L_\perp = 0.5$ mm, relative to that of the initial pulse. The initial temperature of the pulse is $T_0=1.0$ K. The dotted line represents the signal when there is only dispersion, the dashed line represents the signal without dispersion but with a finite angular width in the initial pulse, and the solid line represents the signal with both dispersion and finite angular width. Note that the dashed and solid lines have had their y values multiplied by 10.

than its initial value. Under the conditions of the experiments considered, the intensity was 0.055 of its initial value.

Figure 3 shows the temporal dependence of signal amplitude for a definite value of temperature $T_0=1.0$ K in the initial Bose—Einstein distribution function. The plots in Fig. 3 are obtained from formula (7) with the numerical values of the parameters given above. Figure 3 shows that the half-width of the pulse broadening due to dispersion is close to (90), and the contribution of the angular width is negligible, in accordance with the result obtained from Eq. (74).

Estimations of the temperatures of the heater in the experiments[16] gave >1 K for heater powers >0.3 mW. However, the theoretical length of a pulse at $T=1$ K exceed the observed ones for heater powers >0.3 mW. The theoretical values of the increase in pulse length, at different initial temperatures (see Ref. 16) agree with those calculated here, for initial temperatures in the interval 0.2–0.8 K. The same results were found in Ref. 16 using a computer calculation. These calculations were made using the expression in Ref. 16, which describes the ballistic motion of phonons moving strictly parallel to the z axis, with group velocities given by the dispersion law (87). This model phonon pulse changes its form just because of dispersion.

The conclusions from both analyses is that the temperature of the initial pulse of phonons is much lower than the temperature of the heater which creates them.

According to the experimental conditions in Ref. 16, angular spreading does not contribute to the increase of the length of the pulse. However, the finite value of the angle θ_p determines the transverse spreading of the pulse. Under the experimental conditions,[16] this spreading results in a considerable decrease of the amplitude of the signal along the axis of the pulse. Thus, the amplitude of the pulse at the detector is a factor of 0.055 smaller than the amplitude of the initial pulse.

Undoubtedly, a series of high-pressure experiments similar to the experiments at the saturated vapor pressure[13] would be of great interest. This would give the temporal and spatial dependence of the phonon energy density for different pulse lengths. Comparison of the results of such experiments at high pressure and saturated vapor pressure would make it possible to compare the observed values with those calculated with the model of strongly interacting phonons (see Ref. 14) and the results obtained here for a system of phonons without interactions. Such a comparison would give us important information about anisotropic systems of phonons in superfluid helium.

We express our gratitude to EPSRC of the UK (Grant GR/S24855 and GR/N20225), and to GFFI of Ukraine (Grant N02.07/000372) for support of this work.

*E-mail: nemchenko@pht.univer.kharkov.ua

[1] A. F. G. Wyatt, N. A. Lockerbie, and R. A. Sherlock, Phys. Rev. Lett. **33**, 1425 (1974).
[2] M. J. Baird, F. R. Hope, and A. F. G. Wyatt, Nature (London) **304**, 325 (1982).
[3] F. R. Hope, M. J. Baird, and A. F. G. Wyatt, Phys. Rev. Lett. **52**, 1528 (1984).
[4] M. Brown and A. F. G. Wyatt, J. Phys.: Condens. Matter **2**, 5025 (1990).
[5] M. A. H. Tucker and A. F. G. Wyatt, Science **283**, 1150 (1999).
[6] H. J. Marris and W. E. Massey, Phys. Rev. Lett. **25**, 220 (1970).
[7] M. A. H. Tucker and A. F. G. Wyatt, J. Phys.: Condens. Matter **6**, 2813 (1994).
[8] M. A. H. Tucker and A. F. G. Wyatt, J. Phys.: Condens. Matter **6**, 2825 (1994).
[9] I. N. Adamenko, K. E. Nemchenko, A. V. Zhukov, M. A. H. Tucker, and A. F. G. Wyatt, Phys. Rev. Lett. **82**, 1482 (1999).
[10] A. F. G. Wyatt, M. A. H. Tucker, I. N. Adamenko, K. E. Nemchenko, and A. V. Zhukov, Phys. Rev. B **62**, 9402 (2000).
[11] I. N. Adamenko, K. E. Nemchenko, and A. F. G. Wyatt, Fiz. Nizk. Temp. **28**, 123 (2002) [Low Temp. Phys. **28**, 85 (2002)].
[12] M. A. H. Tucker and A. F. G. Wyatt, J. Low Temp. Phys. **113**, 621 (1998).
[13] R. V. Vovk, C. D. H. Williams, and A. F. G. Wyatt, Phys. Rev. B **68**, 134508 (2003).
[14] I. N. Adamenko, K. E. Nemchenko, V. A. Slipko, and A. F. G. Wyatt, Phys. Rev. B **68**, 134507 (2003).
[15] R. C. Dynes and V. Narayanamurti, Phys. Rev. Lett. **33**, 1195 (1974).
[16] A. F. G. Wyatt, R. A. Sherlock, and D. R. Allum, J. Phys.: Condens. Matter **15**, 1897 (1982).
[17] A. F. G. Wyatt and D. R. Allum, J. Phys.: Condens. Matter **15**, 1917 (1982).
[18] I. M. Khalatnikov, *An Introduction to the Theory of Superfluidity*, Addison-Wesley, New York (1988).
[19] I. M. Khalatnikov, Zh. Eksp. Teor. Fiz. **22**, 687 (1952).
[20] N. A. Lockerbie, Ph.D. Thesis, Nottingham University (1975).

This article was published in English in the original Russian journal. Reproduced here with stylistic changes by AIP.

Turbulence of second sound waves in superfluid He II

M. Yu. Brazhnikov, V. B. Efimov, G. V. Kolmakov,* A. A. Levchenko, E. V. Lebedeva, and L. P. Mezhov-Deglin

Institute of Solid State Physics of the Russian Academy of Sciences, Chernogolovka, Moscow Region, 142432, Russia

(Submitted January 12, 2004; revised January 23, 2004)
Fiz. Nizk. Temp. **30**, 590–595 (June 2004)

We communicate the results of numerical studies of acoustic turbulence in a system of slightly dissipating, nonlinear second sound waves in superfluid He II. It is shown that at sufficiently high amplitude of the external driving force a power-like energy distribution over frequency is formed in the system of second sound waves. This distribution is attributed to formation of the acoustic turbulence regime in the system. The interval of frequencies in which the distribution has a power-like form is expanded to high frequencies with increasing amplitude of the driving force. The energy distribution inside this interval is close to $E_\omega \sim \omega^2$. It is shown that the distribution of energy E_ω depends on the value of the nonlinearity coefficient of the second sound but does not depend on the sign of the coefficient, i.e., the coherent structures (shock waves) do not contribute to the statistical properties of the turbulent state. © *2004 American Institute of Physics.* [DOI: 10.1063/1.1768333]

1. INTRODUCTION

We report the observation, in a numerical experiment, of a spectrum of turbulence of the Kolmogorov type in a system of one-dimensional weakly dissipating sound waves. Studies of turbulence of sound waves (acoustic turbulence) is of importance due to many applications in physics: nonlinear waves in superfluid He II,[1–3] phonon turbulence in perfect crystals,[4] waves in an interstellar space,[5] etc.

Traditionally the theory of weak, or wave turbulence could be used as an appropriate basis for understanding the turbulent phenomena in a system of interacting waves (see the monograph[6] and references therein). For example, recent studies of the turbulence of capillary waves at the surface of liquid hydrogen[7–9] and of water[10–13] have demonstrated that the experimental observations are in good accordance with the predictions of the theory[6,14] and with the results of numerical computations[15] based on this theory.

In the case of turbulence in a system of sound waves with the dispersion law

$$\omega_k = uk \tag{1}$$

the approach based on the ideas of the weak turbulence theory meets difficulties due to divergence in the perturbation theory series[18] (here ω_k is the frequency of the linear wave with the wave vector k, and u is the sound velocity). This divergence appears owing to degeneration of the resonance manifold for three-wave interaction in k space in case of the linear dispersion law (1): only waves whose k vectors are collinear with each other can interact efficiently. Due to this fact the peculiarities of the nonlinear and turbulent behavior of such a system could differ from that of the system of waves in dispersive media.

Numerical calculations provide a nice opportunity to study from first principles the peculiarities in turbulent behavior of a system of acoustic waves, by integrating numerically the equations of motion of the liquid. The results of similar studies done for dispersive systems—gravity and capillary waves at the free surface of a liquid—have been published recently in Refs. 15–17.

The present paper addresses the numerical studies of acoustic turbulence in a system of sound waves with small damping. Theoretical estimations have shown that strongly anisotropic turbulent patterns could be formed in a system of sound waves.[6] In order to avoid additional difficulties related to the pattern formation we consider here the simplest model case, in which one-dimensional sound waves in He II are considered. We suppose that the medium in which the one-dimensional sound waves propagate is restricted from both sides by reflecting walls (waves in a resonator of finite size). This consideration corresponds in general to the conditions of the experiments[1,2] with one-dimensional nonlinear second sound waves in superfluid He II. The results of our calculations can also be used for qualitative treatment of the experiments[7–9] with capillary waves at the surface of liquid hydrogen in a cell of small dimensions.

Our calculations show that at high amplitudes of the external driving force, a power-law distribution of the amplitudes of the sound waves over the frequency is formed at frequencies higher than the driving frequency.

This distribution can be attributed to formation of the wave turbulence regime in a system of sound waves, and it is similar to the Kolmogorov spectrum of turbulence.[20] The range of frequencies in which the power-law distribution is established expands to high frequencies with increasing amplitude of the driving force. The power-law spectrum is violated at high frequencies due to the transition from the regime where the nonlinear wave transformation plays the essential role in the energy transfer through the scale to the regime where the viscous damping dominates.

2. BASIC EQUATIONS

In this paper we study the turbulence in a system of second sound waves in He II as an example of a nonlinear

wave system. It is known that the second sound waves in He II demonstrate a highly nonlinear behavior, and they are a nice test object for studying the dynamics of nonlinear waves.[1,2]

It is convenient in numerical calculations to use the Hamiltonian formulation of superfluid hydrodynamics. The Hamiltonian formalism in the hydrodynamics of superfluid He II has been developed in Ref. 21. This approach has been generalized for superfluid ^{4}He–^{3}He mixtures in Ref. 22.

For the sake of convenience of the readers and for a statement of the notation used in the subsequent calculations we shall write out the known[22,23] basic equations of motion for nonlinear waves of second sound in He II in the Hamiltonian representation for planar (one-dimensional) second sound waves in a resonator. This representation is a classical limit for superfluid helium hydrodynamics formulated in terms of the first and second sound quanta. Such classical limit can be used, obviously, if the occupation number of the corresponding states is sufficiently large,

$$|b_n|^2 \gg \hbar, \tag{2}$$

where b_n is the canonical amplitude of the second sound; see below. Moreover, the term ''second sound quantum'' itself is correct only if the wavelength of the second sound is much larger than the mean free path l_f of the quantum excitations,[23,24]

$$k l_f \ll 1, \tag{3}$$

where k is the wave vector of the second sound wave; see (6). We suppose in this paper that both conditions (2) and (3) are satisfied.

An arbitrary flow of superfluid He II can be described by three pairs of conjugate variables (φ, ρ), (β, S) and (γ, f).[21] Here φ is the superfluid velocity potential, ρ is the density of the liquid, S is the entropy per unit mass, β is the phase variable conjugate to S, and γ and f are the Clebsch variables. The Hamiltonian function of the system is given by the total energy of the liquid:

$$H = \int d^3\mathbf{r}\left(\frac{1}{2}\rho \mathbf{v}_s^2 + \rho \mathbf{v}_s + E_0(\rho, S, \mathbf{p})\right). \tag{4}$$

Here $E_0(\rho, S, \mathbf{p})$ is the energy of a unit of volume of the liquid in the reference frame moving with the velocity $\mathbf{v}_s$ of the superfluid component, and $\mathbf{p}$ is the momentum of the relative motion of the normal component.

In the subsequent analysis we neglect the oscillations of the density ρ in the second wave due to the fact that the thermal expansion coefficient of the liquid helium is small $(T/\rho)(\partial\rho/\partial T) \ll 1$ if the temperature of the helium bath is not very close to the temperature of the superfluid transition T_λ. In this approximation the oscillations of the two variables β and S are nonzero only in the second sound wave propagating through the unperturbed superfluid. The equations of motion in this representation are

$$\dot{S} = \frac{\delta H}{\delta \beta}, \quad \dot{\beta} = -\frac{\delta H}{\delta S}, \tag{5}$$

with the Hamiltonian (4). The momentum of relative motion of the normal component is

$$\mathbf{p} = S \nabla \beta.$$

If the sound waves are propagating in unrestricted superfluid the Hamiltonian variables β and S could be expressed via the normal coordinates—the amplitudes $b_{\mathbf{k}}$ of the sound waves with the wave vector $\mathbf{k}$ (Ref. 21). In the case under study (waves in a superfluid helium in a resonator) the corresponding normal variables are given by the amplitudes b_n of standing second sound waves. The frequencies of the standing waves are equal to the resonant frequencies $\omega_n = u_{20} k_n$, where u_{20} is the second sound velocity, and the wave number k_n corresponding to the nth resonant frequency is

$$k_n = \pi n / L, \tag{6}$$

and L is the length of the resonator. The number $n = 1$ will correspond to the lowest resonant frequency of the cell.

Oscillations of the variables β and S in the one-dimensional second sound wave are expressed via the normal coordinates as follows

$$\beta(x,t) = \sum_n \overline{\beta_n} \cos(k_n x)(b_n - b_n^*), \tag{7}$$

$$\delta S(x,t) = \sum_n \overline{S_n} \cos(k_n x)(b_n + b_n^*), \tag{8}$$

where the normalization factors are

$$\overline{\beta_n} = -i\left[\omega_n L\left(\frac{\partial S}{\partial T}\right)\right]^{-1/2}, \quad \overline{S_n} = \left[\frac{\omega_n}{L}\left(\frac{\partial S}{\partial T}\right)\right]^{1/2}. \tag{9}$$

The equations of motion to be integrated are provided by the Hamilton's equations for the normal coordinates b_n,

$$i\dot{b}_n = \frac{\partial H}{\partial b_n^*} - i\gamma_n b_n + f_n. \tag{10}$$

The dissipation and the interaction with the external driving force are included phenomenologically in these equations, H is the Hamiltonian function of the system, γ_n is the damping coefficient of the nth standing wave, f_n is the driving force acting on the nth resonance, a dot denotes the derivative with respect to time t, and a star denotes the complex conjugate.

The standard way to describe the dynamics of the system of interacting waves is to use an expansion of the Hamiltonian H in a series in the normal coordinates b_n

$$H = H_2 + H_3. \tag{11}$$

The term H_2 is a quadratic function of the normal coordinates b_n

$$H_2 = \sum_n \omega_n |b_n|^2; \tag{12}$$

it describes the propagation of linear second sound waves. The term H_3 is cubic in the amplitude b_n and corresponds to mutual interaction of three second sound waves—splitting of one wave into two waves and confluence of two waves into one wave. The higher-order terms are omitted in the expansion (11), so the nonlinear processes of fourth and higher order are disregarded. These processes involve the interaction of four or more of waves. They are important for isotropization of the spectrum in the three-dimensional case, and they should be taken into account in a more general theory. The general form of the interaction Hamiltonian is

$$H_3 = \sum_{n_1,n_2,n_3} V_{n_1,n_2,n_3} b^*_{n_1} b_{n_2} b_{n_3} \delta_{n_1-n_2-n_3} + \text{c.c.} \qquad (13)$$

Here V_{n_1,n_2,n_3} is the amplitude of nonlinear interaction of three second-sound waves. It is supposed that the nonresonant terms in (13), for which the resonance condition

$$\omega_1 - \omega_2 - \omega_3 = 0 \qquad (14)$$

is not satisfied, are eliminated from the Hamiltonian function by canonical transformation (see Ref. 6 for details). For the second sound waves with the dispersion relation (1) it follows from Eq. (6) that the resonance condition (14) is equivalent to the condition

$$n_1 - n_2 - n_3 = 0.$$

This corresponds to the presence of the Kronecker delta in the right-hand side of Eq. (13).

The amplitude of interaction of second sound waves in He II with wave vectors k_1, k_2, and k_3 is equal to[22]

$$V(k_1,k_2,k_3) = \frac{\alpha}{\sqrt{2}} \frac{\sigma}{(\partial\sigma/\partial \mathrm{T})} \sqrt{\frac{\rho_s u_{20}}{\rho\rho_n}} \sqrt{k_1 k_2 k_3} = \overline{V}\sqrt{k_1 k_2 k_3}. \qquad (15)$$

Here α is the nonlinearity coefficient of the second sound waves, σ is the entropy per unit mass, ρ_s and ρ_n are the superfluid and normal density, and u_{20} is the second sound velocity. In case of interaction of three standing second sound waves in a resonator the amplitude of interaction acquires the form

$$V_{n_1,n_2,n_3} = V_0 \sqrt{n_1 n_2 n_3}, \qquad (16)$$

where $V_0 = \overline{V}/u_{20}^{3/2}$. The sign of the interaction amplitude V_{n_1,n_2,n_3} coincides with the sign of the nonlinearity coefficient α of second sound and it could be negative or positive, depending on the temperature and pressure in the superfluid liquid. It is known[23] that in superfluid ^{4}He at saturated vapor pressure the nonlinearity coefficient α of the roton second sound is negative at temperatures $T_\alpha < T < T_\lambda$ (where T_λ is the temperature of the superfluid transition) and is positive at $T < T_\alpha$. At $T = T_\alpha = 1.88$ K the nonlinearity coefficient α is equal to zero. Increase of the pressure in a superfluid, as well as introduction of ^{3}He atoms into He II, should lead to lowering of the temperature T_α (Refs. 2 and 22). For example, in superfluid He II containing a 10% impurity of ^{3}He atoms the temperature T_α is lowered to 1.7 K at saturated vapor pressure. So both cases $V_0 > 0$ and $V_0 < 0$ in Eq. (16) have physical meaning.

The damping coefficient of the second sound wave is chosen as $\gamma_n = Cn^2$. In a real experiment the value of the constant C is determined by viscous damping of the sound waves in the bulk of the liquid and, also, by the energy losses at the walls of the resonator. The constant C is estimated roughly as $C \sim 1/Q$, where Q is the quality factor of the resonator. The typical value of the Q factor in experiments[1] with second sound waves was $Q \sim 10^2 - 10^3$. In the calculation reported we put $C = 10^{-2}$ (which corresponds to $Q \sim 10^2$ at $n = 1$), so $\gamma_n = 10^{-2} n^2$.

The basic system of equations (10) to be integrated numerically is obtained by collecting the formulas (10)–(13), (16):

$$i\dot{b}_n = V_0 \sum_{n_1,n_2} (n n_1 n_2)^{1/2} (b_{n_1} b_{n_2} \delta_{n-n_1-n_2} + 2 b_{n_1} b^*_{n_2} \delta_{n_1-n_2-n}) - i\gamma_n b_n + f_n. \qquad (17)$$

The linear term $\omega_n b_n$, which arises in the right-hand side of Eq. (17) from the quadratic part H_2 of the Hamiltonian (11), is eliminated by the change of variables $b_n \to b_n \times \exp(-i\omega_n t)$. The simplest initial conditions for the second sound wave amplitude is used in this paper:

$$b_n(t=0) = 0.$$

We integrate numerically the equations of motion (17) in two cases: a) the second sound in a resonator is excited by a harmonic external driving force with a frequency equal to one of the resonant frequencies, and b) the second sound is driven by a quasiperiodic force, the frequency spectrum of which contains several harmonics.

The distribution of the amplitudes of the second sound waves

$$P(n) = \langle |b_n(t)|^2 \rangle \qquad (18)$$

over the wave number n averaged over time t is calculated from the results of the integration. The energy distribution over frequency can be found from Eq. (11). In the present case of one-dimensional waves as a first approximation it is equal to

$$E_\omega = \omega_n P(n). \qquad (19)$$

We now evaluate the frequency dependence of the energy distribution E_ω of the second sound wave system from the calculated $P(n)$ dependence.

3. RESULTS AND DISCUSSION

Driving at a single resonance frequency

First, we consider the case where a periodic driving force excites a standing second sound wave at the frequency equal to the lowest resonant frequency ω_1 of the resonator,

$$f_1(t) = f_0 \exp(-i\omega_1 t),$$

where f_0 is the amplitude of the driving force. As was pointed above, the dependence on time t of the amplitudes of second sound waves b_n is determined by numerical integration of the equations (10). At long times (when the relaxation processes are finished) the amplitudes b_n tend to some constant values. This means that we may omit the averaging over time in the definition (18) in this case.

We calculate the spectrum $P(n)$ for given amplitude f_0 and study the evolution of the distribution $P(n)$ with increasing driving amplitude f_0. Figure 1 shows the distributions $P(n)$ calculated for three values of the driving force: $f_0 = 0.01$ (circles), 0.1 (triangles), and 1.0 (boxes). The lines connecting the symbols are drawn as a guide to the eye. The straight line corresponds to the dependence $P(n) \sim n^{-3}$.

In the inset in Fig. 1 the dependence of the effective exponent

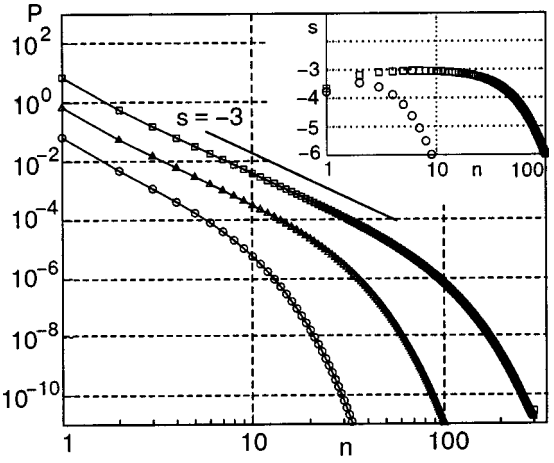

FIG. 1. The spectrum $P(n)$ of second sound oscillations calculated for the amplitudes of the monochromatic driving force $f_0=0.01$ (○), 0.1 (△), and 1 (□). The driving is applied at the lowest resonance frequency. The straight line corresponds to the power distribution $P(n)\sim n^{-3}$. The inset shows the dependence of the effective scaling exponent s on the resonance number n for $f_0=0.01$ and $f_0=1$.

$$s(n)=\frac{d\log P(n)}{d\log n} \tag{20}$$

on the resonance number n is shown for $f=0.01$ and $f_0=1$. It is seen that in the case $f_0=1$ there is an interval of resonance numbers n in which the effective exponent s is close to $s=-3$.

From Fig. 1 it is seen that at sufficiently high amplitudes of the driving force there exists a range of frequencies, higher the driving frequency, in which the distribution $P(n)$ of the amplitudes of weakly dissipating acoustic waves can be described by a power-like function $P(n)\sim n^{-3}$. This dependence corresponds to an energy distribution in the frequency scale [see Eq. (19)]

$$E_\omega=\text{const}\cdot\omega^{-2}. \tag{21}$$

The interval of frequencies in which the power-law spectrum (21) is established is enlarged to high frequencies with increasing amplitude of the driving force.

Driving by a quasiperiodic force

In this Section we present the results of calculations in which the driving force is not monochromatic, but the frequency spectrum of the force has several harmonics (quasiperiodic force).

In the calculations it is assumed that the external driving force excites the three lowest resonant modes directly, and $f_n=0$ for $n>3$. For each resonant mode n $(n=1,2,3)$ the corresponding driving force f_n is the sum of three periodic harmonics, the frequencies of which are incommensurate with each other and with the resonant frequency of the given resonance. The integral power that is pumped by the driving force into the system can be characterized in this case by the effective dispersion

$$D=\sum_n \langle f_n f_n^*\rangle,$$

where the angle brackets denote averaging over time.

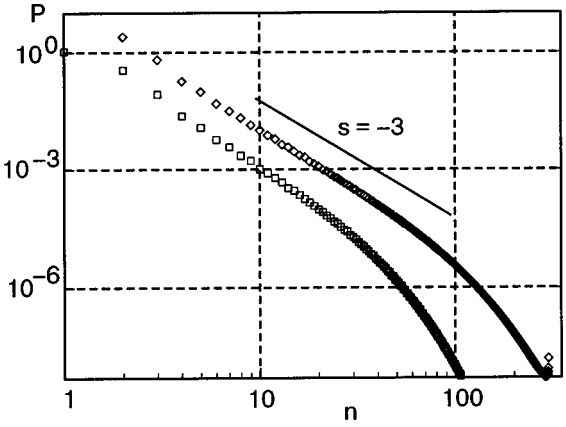

FIG. 2. Evolution of the spectrum with increasing of the effective dispersion of the quasiperiodic driving force from $D=0.63$ to 4.2. The straight line corresponds to the power-like distribution $P(n)\sim n^{-3}$.

In the case of pumping of the system by a quasiperiodic force the amplitudes b_n do not tend to some limiting values at large time but are fluctuating at all t. In calculations the distribution $P(n)$ averaged over time t is determined from the results of numerical integration of the equations (17). Figure 2 demonstrates the evolution of the distribution $P(n)$ with increasing D from 0.63 to 4.2. It is seen from Fig. 2 that at high D the power-like distribution

$$P(n)\sim n^{-3} \tag{22}$$

is formed in some region of wave numbers, similarly to the case of pumping by a monochromatic driving force.

The observed power-like spectrum of oscillations could be attributed to the formation of the acoustic turbulent state in the system of second sound waves. The range of frequencies (or the region of the wave numbers) in which the scale-invariant distribution (22) is established can be called "the inertial range" in analogy with the interval of frequencies where the scaling law is valid in Kolmogorov's picture of turbulence. At low frequencies the inertial range is limited by the characteristic driving frequency, and at high frequencies the inertial range is limited by the transition from the regime of nonlinear transfer of the energy of waves over scales to the regime where the viscous damping dominates.

The calculations are performed for both positive and negative signs of the nonlinearity coefficients α (i.e., for positive and negative V_0 in Eq. (16)). It is observed that the phases of the high-frequency waves generated due to nonlinearity are different in the cases $V_0>0$ and $V_0<0$ (with the same absolute value $|V_0|$), but the averaged distributions $P(n)$ are the same in the two cases. This indicates that formation of the coherent structures (like shock waves) did not affect the turbulent distribution of acoustic waves in a resonator. The physical sense of this fact is that the mutual nonlinear interaction of the second sound waves reflected from the resonator's walls prevents shock-front formation. This fact could be important for future analyses of the acoustic turbulence in superfluid helium, because earlier the sound turbulence has been considered mainly as a statistic of shock waves propagating in an unrestricted medium.

Note that in case of one-dimensional waves with a non-decaying dispersion law, for which the four-wave interaction

plays the main role, the coherent effects (the wave collapse or the soliton formation) are quite important in a turbulent regime.[19]

We should note that the scaling index of the turbulent distribution $s=-3$ observed in these calculations is distinguished from the index $s_0=-2.5$ which could be calculated by using the kinetic equation of the weak acoustic turbulence theory[1] in the case of one-dimensional acoustic waves. This could indicate that the high-order corrections to the standard kinetic equations are important in the case under study. Thus the applicability of the kinetic equations (or some of its improved variants) for description of turbulence in a system of one-dimensional sound waves could be a question for further studies.

4. CONCLUSIONS

Numerical studies of the dynamics of the nonlinearly interacting one-dimensional sound waves shows that a power-like distribution of energy is formed in some range of frequencies if the amplitude of the low-frequency driving force is sufficiently high. In this inertial range of frequencies the distribution of energy over frequency is close to $E_\omega \sim \omega^2$. This spectrum can be attributed to the formation of a turbulent state in the system of acoustic waves. The inertial range is expanded toward high frequencies with increasing amplitude of the driving force. At high frequencies the inertial range is limited by a change of the mechanism of energy transfer from nonlinear wave transformation to viscous damping. The shape of the energy spectrum depends on the absolute value of the nonlinearity coefficient of the sound waves (does not depend on its sign), which manifests the fact that the formation of the coherent structures does not influence the energy distribution in this turbulent system.

These investigations are supported in part by INTAS (Grant 2001-0618), by RFBR (Grants 03-02-16865 and 03-02-16121), and by the Ministry of Industry, Science and Technology of the Russian Federation in framework of contract No. 40.012.1.1.11.64, theme "Quantum phenomena at low and ultralow temperatures," and by Grant NSh-2169.2003.2. G.K. also acknowledges support from the Science Support Foundation (Russia).

*E-mail: german@issp.ac.ru

[1] I. Yu. Borisenko, V. B. Efimov, and L. P. Mezhov-Deglin, Fiz. Nizk. Temp. **14**, 1123 (1988) [Sov. J. Low Temp. Phys. **14**, 619 (1988)].
[2] V. B. Efimov, G. V. Kolmakov, E. V. Lebedeva, L. P. Mezhov-Deglin, and A. B. Trusov, J. Low Temp. Phys. **119**, 309 (2000).
[3] G. V. Kolmakov, Physica D **86**, 470 (1995).
[4] V. S. Tsoi, Centr. Europ. J. Phys. **1**, 72 (2003).
[5] S. Grzedzielski and R. Lallement, Space Sci. Rev. **78**, Nos. 1–2 (1996).
[6] V. Zakharov, V. L'vov, and G. Fal'kovich, *Kolmogorov Spectra of Turbulence*, Springer-Verlag, Berlin (1992), Vol. 1.
[7] M. Yu. Brazhnikov, G. V. Kolmakov, A. A. Levchenko, and L. P. Mezhov-Deglin, JETP Lett. **73**, 398 (2001).
[8] M. Yu. Brazhnikov, G. V. Kolmakov, A. A. Levchenko, and L. P. Mezhov-Deglin, JETP Lett. **74**, 583 (2001).
[9] M. Yu. Brazhnikov, G. V. Kolmakov, and A. A. Levchenko, JETP **95**, 447 (2002).
[10] W. B. Wright, R. Budakian, and S. J. Putterman, Phys. Rev. Lett. **76**, 4528 (1996).
[11] E. Henry, P. Alstrom, and M. T. Levinsen, Europhys. Lett. **52**, 27 (2000).
[12] M. Yu. Brazhnikov, G. V. Kolmakov, A. A. Levchenko, and L. P. Mezhov-Deglin, Europhys. Lett. **58**, 510 (2002).
[13] M. Lommer and M. T. Levinsen, J. Fluoresc. **12**, 45 (2002).
[14] V. E. Zakharov and N. N. Filonenko, J. Appl. Mech. Tech. Phys. **5**, 62 (1967).
[15] A. N. Pushkarev and V. E. Zakharov, Physica D **135**, 98 (2000).
[16] A. I. Dyachenko, A. O. Korotkevich, and V. E. Zakharov, JETP Lett. **77**, 477 (2003).
[17] A. I. Dyachenko, A. O. Korotkevich, and V. E. Zakharov, JETP Lett. **77**, 546 (2003).
[18] V. L'vov, Yu. L'vov, A. C. Newell, and V. E. Zakharov, Phys. Rev. E **56**, 390 (1997).
[19] V. E. Zakharov, P. Guyenne, A. N. Pushkarev, and F. Dias, Physica D **152–153**, 573 (2001).
[20] A. N. Kolmogorov, Dokl. Akad. Nauk SSSR **30**, 299 (1941).
[21] V. L. Pokrovskii and I. M. Khalatnikov, Sov. Phys. JETP **44**, 1036 (1976).
[22] G. V. Kolmakov, Fiz. Nizk. Temp. **29**, 667 (2003) [Low Temp. Phys. **29**, 495 (2003)].
[23] I. M. Khalatnikov, *An Introduction to the Theory of Superfluidity*, Perseus Publishing (1989).
[24] E. M. Lifshitz and L. P. Pitaevskii, *Statistical Physics*, Part 2, Pergamon Press, Oxford (1980), Nauka, Moscow (1978), Russ. p. 121.

This article was published in English in the original Russian journal. Reproduced here with stylistic changes by AIP.

SUPERCONDUCTIVITY, INCLUDING HIGH-TEMPERATURE SUPERCONDUCTIVITY

Hysteresis of the magnetic properties and the irreversibility line in $Bi_2Sr_2CaCu_2O_y$ layered superconductors

Yu. M. Vashakidze, T. S. Shaposhnikova, and Yu. I. Talanov*

Kazan Physico-Technical Institute of the Russian Academy of Sciences, Sibirskiĭ trakt 10/7, Kazan 420029, Russia

(Submitted February 11, 2003; revised January 30, 2004)
Fiz. Nizk. Temp. **30**, 596–603 (June 2004)

Measurements of the irreversibility line in $Bi_2Sr_2CaCu_2O_y$ single crystals are made by three experimental methods: by dc magnetization measurements, microwave absorption measurements, and registration of the harmonics in the high-frequency response of the superconductor. It is found that the position of the irreversibility line on the magnetic phase diagram depends substantially on the method of measurement and the frequency used. Analysis of the results shows that the discrepancy in the irreversibility lines is due to both a difference in the mechanisms of hysteresis of the magnetic properties and to the different scales of the measurement times. It is shown that the position of the irreversibility line is determined at low temperatures by the limiting value of the vortex creep rate for the given method of registration and at high temperatures by the time required for two-dimensional vortices to overcome the surface barrier. It is concluded that the irreversibility line is a dynamic phase transition. The first experimental evidence of the presence of a surface barrier for 2D vortices is obtained. [DOI: 10.1063/1.1768334]

INTRODUCTION

Since the hysteresis and relaxation of the magnetic properties of high-T_c superconductors (HTSCs) are governed by vortex pinning, measurement of magnetic properties is widely used for studying the vortex dynamics (see, e.g., Refs. 1–5). The hysteresis of the magnetic properties observed in a significant region of the $H-T$ magnetic phase diagram of HTSCs vanishes at the transition through the so-called irreversibility line (IL).[6–8] At the present time there are two main models of the IL, which explain its nature differently. In the ''flux creep'' model proposed by Anderson and Kim,[9] it is assumed that the IL is a dynamic transition from the flux-creep regime (below the IL) to the flux-flow regime. In the alternative model, that of a vortex glass and its melting,[10,11] the IL is determined as a line of thermodynamic phase transitions. The authors of that model assume that below the transition temperature the vortex lines, interacting with pinning centers, are ''frozen.'' Therefore the vortices in a superconductor form a vortex glass structure, analogous to the distribution of magnetic moments in a spin glass. However, it has been shown experimentally (see, e.g., Ref. 2) that the vanishing of irreversibility and the melting of the frozen vortex structure are two different transitions in the vortex lattice. In some regions of the phase diagram the line corresponding to the melting of the vortex structure lies above the irreversibility line while in others it lies below that line.[2] Thus the irreversibility line is most likely a dynamic transition of the vortex system.

Each superconductor is characterized by its own irreversibility line. In the low-temperature superconductors the IL is almost coincident with the second critical field $H_{c2}(T)$, while in $YBa_2Cu_3O_7$ it differs from $H_{c2}(T)$ by several degrees, and in the highly layered superconductors the difference between the IL and $H_{c2}(T)$ is rather large, sometimes reaching a value of $T_c/2$. Furthermore, the position of the IL on the phase plane depends on the mechanism of the hysteresis (bulk pinning of vortices or vortex bundles,[6,12] pinning due to a surface[13–15] or geometric[16] barrier, etc.). It has also been noted that the position of the IL in a given material varies for different methods of measurement (see, e.g., Refs. 3 and 5–8). As the frequency used in the experiment increases, the IL shifts to higher magnetic fields and temperatures.[5] Such a shift can also be observed with increasing sweep rate of the static magnetic field in magnetization measurements.[3] The pronounced ambiguity in the determination of the IL requires explanation and additional experimental checking.

In the present study the position of the IL was determined for the same $Bi_2Sr_2CaCu_2O_y$ single crystal by three different experimental setups working at substantially different frequencies. A comparison of the results obtained by the different methods made it possible to acquire a large set of data on the vortex dynamics, hysteresis mechanisms, and frequency dependence of the position of the IL. This approach allowed us to ascertain which of the hysteresis mechanisms determine the position of the IL in different regions of the $H-T$ phase plane and which of the hysteresis mechanisms can be detected by the different methods.

The structure of this paper is as follows. In Sec. 1 we describe the techniques used in this study to measure the hysteresis of the magnetic characteristics of the superconductor. The results of the measurements are presented in Sec.

2. In Sec. 3 we discuss the results and construct a phase diagram of the vortex state. The main conclusions as to the mechanisms of hysteresis in different regions of the phase diagram are presented in the Conclusion.

1. EXPERIMENTAL

In this study we have used three experimental methods: measurement of the hysteresis loop of the dc magnetization $M(H)$ by means of Hall probes, measurement of the microwave absorption (MWA) at frequency $\nu = 10$ GHz, and registration of the harmonics of the high-frequency ($\nu = 10$ MHz) response of the superconductor. The MWA method, which has been used successfully for studying the vortex state of HTSCs,[17–22] has a high sensitivity and permits determination of the type of pinning and the position of the IL.

The studies were done on a $Bi_2Sr_2CaCu_2O_y$ single crystal with $T_c = 87$ K and dimensions of $3.5 \times 1.3 \times 0.1$ m^3. All of the measurements were made in an orientation for which the applied dc magnetic field was perpendicular to the plane of the crystal (parallel to the c axis).

The first method of determining the IL used in this study was to record the hysteresis loop of the magnetization $M(H)$ using Hall probes. The Hall probes had dimensions of the working zone of 0.5×0.5 m^2 and a sensitivity of 9.8 μV/G. One of the probes was placed directly on the surface of the sample and measured the local magnetic induction B. The second probe was located far from the sample and measured the applied magnetic field strength H. The hysteresis loops of the magnetization $M(H)$ were recorded with the external magnetic field swept upward and downward at a rate of 5 Oe/s, permitting registration of the magnetization M, which is proportional to the difference $(B-H)$, as a function of the applied magnetic field strength H. The field at which the hysteresis of the magnetization vanished was identified as the irreversibility field $H_{\rm irr}(T)$.

The next method is based on registration of the harmonics of the high-frequency response of the superconductor. The transition from linear and reversible behavior of the magnetization to nonlinear and irreversible behavior gives rise to magnetic losses and the generation of harmonics in the rf susceptibility.[4,8] It has been shown (in Ref. 8, for example) that the first harmonic of the susceptibility characterizes the penetration depth of the alternating magnetic field into the superconductor. The appearance of higher harmonics as the magnetic field and temperature are lowered is due to the onset of irreversibility of the magnetic properties of the superconductor.[8] In this study the frequency of the fundamental (first) harmonic was $\nu = 10$ MHz. The sample was cooled in a magnetic field of 7 kOe from $T > T_c$ to the measurement temperature, and then the signal at the frequency 3ν was recorded as the external magnetic field was decreased to zero at a rate of 5 Oe/s. The field at which the amplitude of the signal rose sharply was taken as the irreversibility field $H_{\rm irr}$.

The third method of determining the IL was to register the vanishing of the hysteresis of the microwave absorption. The nonresonance MWA was measured using a Bruker BER-418s spectrometer working in the frequency range 9.2–9.7 GHz. The dc magnetic field was modulated at a frequency of 100 kHz with an amplitude from 0.1 to 10 Oe. The sample was placed in the resonator of the spectrometer and was cooled by a flow of gaseous helium. The temperature of the sample was varied from 10 K to the critical temperature. The crystal was oriented so that the applied dc magnetic field H was parallel to the c axis and the microwave field H_1 lay in the basal plane ab of the crystal. The MWA signal was detected and amplified using a lock-in amplifier at the frequency of the fundamental harmonic of the modulation (the details are given in Ref. 21).

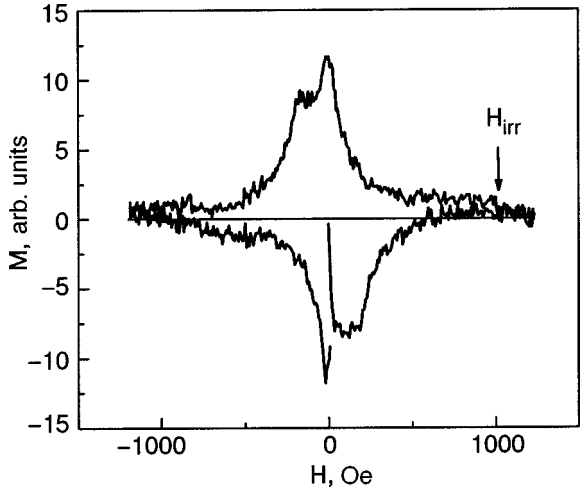

FIG. 1. Hysteresis loop of the magnetization $M(H)$ obtained from measurements by dc Hall probes at a temperature $T = 36$ K. The field $H_{\rm irr}$ at which the hysteresis vanishes is indicated by an arrow.

The procedure used for recording the signal was as follows: at a fixed field H_i the sample was cooled from above the critical temperature to the measurement temperature, after which the field was swept up and down at a rate of 16 Oe/s. The swept range was 150–200 Oe. The magnetic field at which the hysteresis of the MWA signal vanished was taken as the irreversibility field $H_{\rm irr}$. By varying the external conditions, we obtained curves of the amplitude of the hysteresis loop as a function of temperature, magnetic field H, and modulation amplitude H_m. The amplitude of the hysteresis loop was taken as the averaged value of $L = S/\Delta H$, where S is the area of the loop and ΔH is the swept range. The irreversibility field $H_{\rm irr}$ was taken as the point at which the hysteresis loop of the MWA collapsed.

2. EXPERIMENTAL RESULTS

Figure 1 shows the hysteresis loop of the magnetization $M(H)$ measured at a temperature of 36 K by means of Hall probes. The magnetization loop was obtained for a reversal of the direction of sweep of the dc magnetic field H. The irreversibility field $H_{\rm irr} = 1000$ Oe at which the collapse of the hysteresis loop occurred is indicated by an arrow in the figure. The points of the irreversibility line $H_{\rm irr}(T)$ obtained by this method are represented by squares on the phase diagram in Fig. 3.

Figure 2 shows the third-harmonic signal of the susceptibility, χ_3, as a function of magnetic field at temperatures of 55, 63, and 74 K. It is seen in the figure that at a certain value of the decreasing magnetic field there is a sharp increase in the signal. This indicates the onset of nonlinear

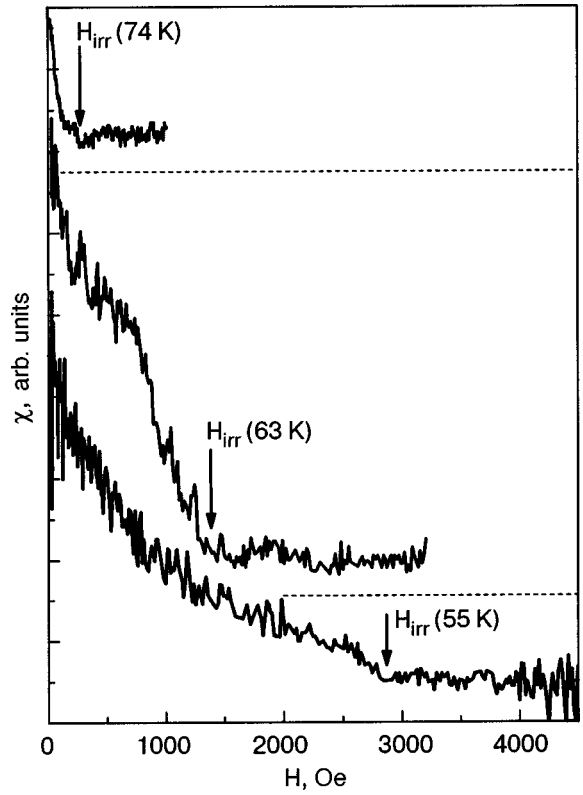

FIG. 2. Field dependence of the third harmonic signals at temperatures of 55, 63, and 74 K. The excitation frequency was ~10 MHz. The fields at which the third harmonic signals appears, which corresponds to the irreversibility field H_{irr}, are indicated by arrows. The dashed lines show the zero levels of the signal during registration at $T=74$ and 63 K.

response and defines the irreversibility field H_{irr}. In Refs. 23–25, where numerical calculations of the frequency and magnetic-field dependence of the amplitude of the harmonics were carried out, it was shown that the inflection on the curve of the field dependence of the susceptibility becomes

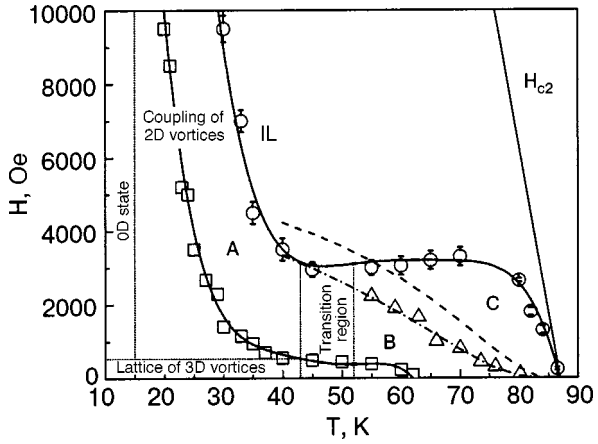

FIG. 3. Irreversibility lines obtained from measurement of the dc magnetization $M(H)$ by means of Hall probes (□), measurement of the hysteretic microwave absorption (○), and registration of the third harmonic in the high-frequency response of the superconductor (△). The solid curves drawn through the experimental points correspond to irreversibility lines obtained by different methods and at different frequencies. The vertical and horizontal dotted lines separate regions with different states of the vortex system. The theoretical curves are calculated with the use of expression (2) for $\tau=10^{-7}$ s (the dot-and-dash curve) and $\tau=10^{-10}$ s (the dashed curve).

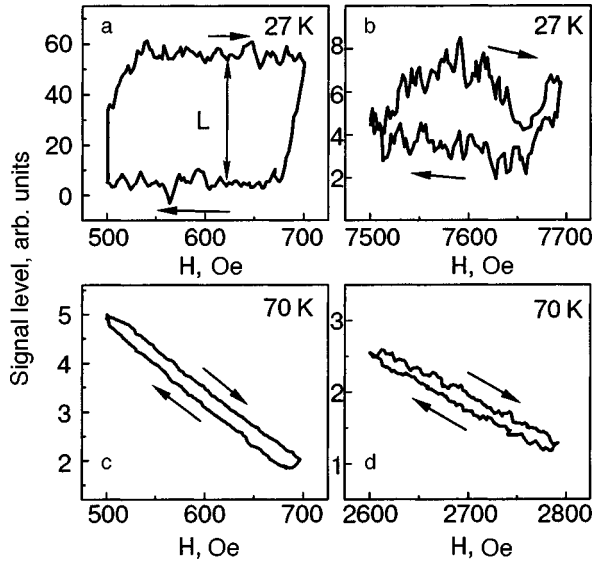

FIG. 4. Shape of the hysteresis loop of the microwave absorption observed in different regions of the phase plane: $T=27$ K, $H=600$ Oe (a); $T=27$ K, $H=7600$ Oe (b); $T=70$ K, $H=600$ Oe (c); $T=70$ K, $H=2600$ Oe (d). The arrows indicate the direction of sweep of the magnetic field. The two-headed arrow in panel (a) indicates the value of the difference of the signal levels for different directions of sweep of the magnetic field, which is adopted as the amplitude L of the hysteresis.

smooth. These features of the behavior of χ_3 are also observed in our experiment. They are responsible for the substantial uncertainty in the location of the irreversibility field at temperature below 55 K. The points of the IL determined by this method are represented by triangles in Fig. 3.

The method of MWA measurement was used not only to find the points of the IL but also to obtain information about the phase state of the vortex matter and the changes of it. Figure 4 shows the hysteresis loops of the MWA observed in different regions of magnetic field and temperature. As the temperature is raised from 40 to 55 K at fields around 500 Oe the shape of the hysteresis loop undergoes fundamental changes, from the type in Fig. 4a to the type in Fig. 4c. At this value of the magnetic field the amplitude of the loop goes to zero at $T_{irr}=85.8$ K. Increasing the magnetic field at a fixed temperature $T=27$ K does not result in significant changes in the shape of the loop. As can be seen in Fig. 4a,b, the loop loses its definite characteristic shape in fields of the order of 8000 Oe. At high fields the amplitude of the hysteresis falls off, while the noise level remains unchanged, and therefore the ''signal-to-noise'' ratio decreases (Fig. 4b). A similar process is also observed at higher temperatures ($T=70$ K): with increasing field the shape of the loop remains practically unchanged, but the amplitude of the signal falls off rather rapidly (Fig. 4d) and the hysteresis loop of the MWA collapses completely at $H_{irr}=3200$ Oe. Thus by varying the external conditions we were able to track the evolution of the signal over a wide range of magnetic fields and temperatures and to determine the position of the irreversibility line. The points of the IL obtained by this method are represented by circles in the phase diagram (Fig. 3).

3. DISCUSSION OF THE RESULTS

The irreversibility lines are plotted in Fig. 3 on the basis of the measurements of the magnetization and hysteretic mi-

crowave absorption and registration of the third harmonic in the high-frequency response of the superconductor. It is seen that the positions of these lines differ remarkably from one another. The IL obtained from measurements of the magnetization $M(H)$ is in good agreement with the data obtained by other dc methods (see Ref. 6, for example). The IL determined from the third harmonic of the susceptibility, χ_3, and the IL obtained from measurements of the MWA hysteresis are shifted significantly to higher magnetic fields and temperatures. The cause of this discrepancy is understandable in view of the nature of the hysteresis in the different regions of the phase diagram.

It is known that the bulk pinning of vortices at point defects is the main pinning mechanism in unirradiated samples of $Bi_2Sr_2CaCu_2O_y$ at low temperatures.[26] In the presence of bulk pinning a change of the applied magnetic field results in a nonuniform distribution of vortices in the volume of the sample. The sample is in a so-called critical state, i.e., a persistent current with a density $j \leqslant j_c$, where $j_c(T,H)$ is the critical current density, can occur in it. In Ref. 21 it was found that in the case of bulk pinning the amplitude of the hysteresis loop of the microwave absorption $L(T,H)$ is proportional to $j_c^2(T,H)$. The value and functional dependence of the critical current $j_c(T,H)$ characterize the dynamics of the vortex matter.[26] In Refs. 21 and 22 we analyzed the applicability of different functional dependences $j_c(T,H)$ corresponding to the dynamics of vortex lines, the dynamics of large and small 2D-vortex bundles, and the dynamics of noninteracting isolated 2D vortices. In Ref. 22 a fitting of the theoretical curves to the experimental data led to the conclusion that in fields $H>500$ Oe and temperatures 15 K$<T<$40 K (region A in Fig. 3) the hysteresis of the magnetic properties is governed by the bulk pinning of 2D vortices, which form small bundles. The presence of bulk pinning of 2D-vortex bundles also governs the hysteresis loops of the magnetization $M(H)$ (Fig. 1, $H_{irr}=1000$ Oe at $T=36$ K).

As is seen in Fig. 3, the shift between the IL measured by the Hall probes and the IL measured by the MWA method, in which an alternating current with frequency $\nu \approx 10^{10}$ Hz is excited, amounts to 10–12 K. This shift can be explained by the frequency dependence of the position of the IL, which has been determined in the theory of vortex creep.[9,27] According to that theory, at long measurement times (or low frequencies) there is sufficient time for relaxation of the vortex position to equilibrium, and therefore reversible behavior can be achieved at lower temperatures or higher magnetic fields. Since the pinning force decreases with increasing applied magnetic field, so does the characteristic lifetime of a 2D vortex in the potential well of a pinning center. Therefore the weakened bulk pinning at high fields can be detected only by a high-frequency method, while dc measurements show reversible behavior because of vortex relaxation.

As was shown in Ref. 22, at fields $H<500$ Oe and temperatures $T<15$ K the $j_c(T,H)$ dependence for 2D-vortex bundles no longer describes the experimental dependence of the MWA hysteresis. Most likely in the field region $H<500$ Oe (15 K$<T<$40 K) the dynamics of the vortex lines matter is governed by the motion of vortex lines (3D region), while for $T<15$ K, $H>500$ Oe the dynamics of

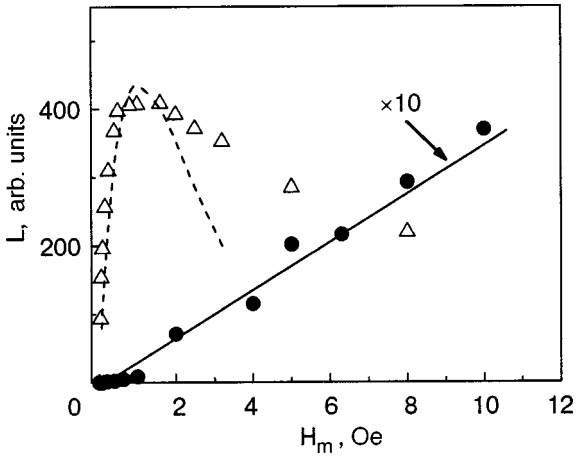

FIG. 5. Amplitude of the hysteresis of the microwave absorption as a function of the amplitude H_m of the field modulation at a temperature of 25 K (triangles) and 65 K (filled circles) at a field of 1000 Oe. The dashed curve was constructed in accordance with the bulk-pinning model for the MWA hysteresis.[22] The solid line corresponds to the hysteresis of the MWA in the case of a surface barrier.[22]

mutually isolated 2D vortices is dominant. These ideas correlate well with published data.[26,28]

The hysteresis of the magnetic properties has a different nature at higher temperatures (50 K$<T<T_c$; region B on the phase diagram in Fig. 3). As previous studies of the magnetic flux profile have shown,[29] in this region of temperatures the bulk pinning is no longer effective, and irreversibility is due to either a surface or edge geometric barrier.

As is seen in Fig. 4c, in this temperature region the MWA hysteresis loop has a completely different shape in comparison with the loops in region A (Fig. 4a), while the amplitude of the hysteresis is an order of magnitude lower. Analysis of the functional dependence of the amplitude of the loop with the use of a theoretical model[22] can explain these changes as being due to a transition to flux trapping by a surface barrier, since it is known that the edge geometric barrier is not effective at such high magnetic fields.

Additional confirmation of the existence of the above-named vortex states comes from the dependence of the amplitude L of the hysteresis loop on the modulation amplitude H_m of the applied magnetic field (Fig. 5). The $L(H_m)$ curve for a superconductor in the critical state (the triangles and dashed line) differs sharply from the $L(H_m)$ curve for a superconductor in which the hysteresis of the MWA is governed by flux trapping by a surface barrier (the black circles and solid line). In the case when the superconductor is in the critical state, the dependence of the amplitude of the MWA hysteresis loop L on the field modulation H_m has a nonmonotonic character, since only some but not all of the vortices contribute to the amplitude of the hysteresis. With increasing modulation amplitude the fraction of vortices that contribute to the amplitude of the hysteresis decreases. This effect is considered in more detail in Ref. 21. In the case of a surface barrier the MWA signal detected on sweeping the magnetic field up and down is proportional to the total number of vortices in the sample, which is determined by the external magnetic field strength.[22] Therefore with the use of magnetic-field modulation the amplitude L of the hysteresis

loop is proportional to the derivative of the absorbed microwave power with respect to the field.[22]

It is seen in Fig. 3 that for $T>50$ K the positions of the ILs measured by the three different methods differ strongly. The IL determined from dc magnetization measurements coincides with a line of first-order phase transitions.[6,13] Measurements made by the μ-SR (muon spin rotation) method[30] have shown that the vortex lines that exist at fields and temperatures below that line decompose into mutually uncoupled 2D vortices above the transition. The ILs determined from the appearance of the third harmonic of the rf susceptibility and from the hysteresis of the microwave absorption lie at substantially higher magnetic fields. We suppose that the irreversibility observed below these lines but above the IL obtained from magnetization measurements is due to the presence of a surface barrier for 2D vortices.[14,15] The mechanism of irreversibility due to the presence of this barrier is apparently the only mechanism that can exist at such high magnetic fields and temperatures, since all the other sources of hysteresis (bulk pinning, a geometric barrier, a surface barrier for vortex lines) are no longer effective. The bulk pinning in these materials acts only at temperatures below 50 K (if they are not irradiated by heavy ions) (see, e.g., Ref. 29). The surface barrier for vortex lines exists only in the presence of large regions of smooth (defect-free) surface, unlike the case of the lateral surface of the thin crystal that we used. An edge geometric barrier for vortex lines can be realized under these conditions, but it is effective only at low magnetic fields of the order of first critical field H_{c1} and below.[16] Therefore the hysteresis observed in fields an order of magnitude higher than the first critical field can be explained only by the presence of a surface barrier for 2D vortices, for which the lateral surface is large and flat enough.

Since the frequencies of the ac magnetic fields used in the two methods (registration of the third harmonic of the rf susceptibility and measurement of the MWA hysteresis) differ by three orders of magnitude, the fact that the ILs obtained by these methods do not coincide is an indication that the frequency of hops of 2D vortices across the surface barrier is dependent on the temperature and magnetic field. In Ref. 14 an expression was obtained for the time τ required for a 2D vortex to overcome a surface barrier with energy G_g:

$$\tau=\gamma_\tau\tau_0\left(\frac{kT}{d}\left(\frac{4\pi\lambda}{\Phi_0}\right)^2\right)^{1/2}\exp\left(\frac{G_g}{kT}\right), \tag{1}$$

where

$$G_g=\left(\frac{\Phi_0}{4\pi\lambda}\right)^2 d\ln\left(\frac{\Phi_0}{2\pi}\frac{1}{\lambda\xi H}\right).$$

Here $\tau_0=\lambda^2/(\rho_n c^2)$ is a characteristic constant that arises in the theory of nonequilibrium superconductivity, ρ_n is the resistivity in the normal state, Φ_0 is the magnetic flux quantum, k is Boltzmann's constant, λ is the magnetic-field penetration depth in the superconductor, $\xi=\xi_{ab}$ is the coherence length, d is the distance between superconducting planes, γ_τ is a constant of the order of unity, T is the temperature in kelvin, and the field H is given in tesla. The following values of the parameters of $Bi_2Sr_2CaCu_2O_y$, taken from Ref. 26, were used in the calculation: $\lambda(0)=1.5\times10^{-7}$ m, $\xi(0)=3.5\times10^{-9}$ m, $d=1.5\times10^{-9}$ m, $\rho_n=10^{-3}\ \Omega\cdot$m. Furthermore, it was assumed that $\lambda(T)$ and $\xi(T)$ vary near the critical temperature T_c as $(1-t^4)^{-0.5}$, where $t=T/T_c$. Then the time τ measured in seconds is given by

$$\tau=10^{-13}\left(\frac{T}{1200(1-t^4)}\right)^{1/2}\times\exp\left(\frac{1200(1-t^4)}{T}\ln\left(\frac{0.6(1-t^4)}{H}\right)\right). \tag{2}$$

Figure 3 shows the ILs calculated with the use of formula (2). The time required for a 2D vortex to overcome the surface barrier is of the order of 10^{-7} s for the lower, dot-and-dash line, and 10^{-10} s for the upper dashed line. It is seen that the theoretical dependence gives a good description of the experimental points obtained in measurements of the rf susceptibility. The agreement of theory and experiment confirms our assumptions as to the presence of a surface barrier for 2D vortices and shows that this barrier can be a source of irreversibility.

Both the theoretical and experimental lines shift in the same direction, to higher fields, when the frequency is increased to 10^{10} Hz. That is, the trends are qualitatively the same. However, the points of the IL measured from the MWA lie noticeably higher than the theoretical curve (the dashed curve on the phase diagram in Fig. 3). The difference of the latter theoretical dependence from the experimental dependence is apparently due to the fact that there exist some additional mechanisms of irreversibility that we have not been able to reveal and which require additional studies.

CONCLUSION

We have made a comprehensive study of the hysteretic magnetic properties of a $Bi_2Sr_2CaCu_2O_y$ single crystal by three experimental methods: from measurements of the magnetization $M(H)$ by Hall probes, from measurements of the hysteresis of the microwave absorption, and by registration of the harmonics in the high-frequency response of the superconductor. A phase diagram of the vortex matter of the crystal under study was constructed. It was found that the IL is strongly shifted to higher fields and temperatures when high-frequency methods of study based on measurements of the rf susceptibility and MWA are used. Analysis of the results obtained showed that in the region $T<40$ K the shift of the IL can be explained with the use of a dynamic model of flux creep. For $T>50$ K and $H>500$ Oe a possible source of hysteresis is the surface barrier for 2D vortices, and the shift of the IL is due to the change of the time required for vortices to overcome this barrier.

The authors thank V. Yu. Petukhov for a helpful discussion of the results. This study was supported by the Ministry of Industry and Science of Russia as part of Project No. 107-1(00)-P and by the Russian Foundation for Basic Research (Project No. 03-02-96230) and the foundation NIOKR RT (Project No. 06-6.2-234).

*E-mail: talanov@kfti.knc.ru

[1] Y. Yamaguchi, N. Aoki, F. Iga, and Y. Nishihava, Physica C **246**, 216 (1995).
[2] D. Majer, E. Zeldov, and M. Konczykowski, Phys. Rev. Lett. **75**, 1166 (1995).
[3] Haui-hu Wen and Zhong-Xian Zhao, Phys. Rev. B **50**, 13853 (1994).
[4] A. Shaulov and D. Dorman, Appl. Phys. Lett. **53**, 2680 (1988).
[5] M. Polichetti, M. G. Adesso, T. Di Matteo, A. Vecchione, and S. Pace, Physica C **332**, 378 (2000).
[6] W. D. Wu, A. Keren, L. P. Le, B. J. Sternlieb, G. N. Luke, Y. J. Uemura, P. Dosanjh, and T. M. Riseman, Phys. Rev. B **47**, 8172 (1993).
[7] J. Deak, M. McElfresh, J. R. Clem, Zhidong Hao, M. Konczykowski, R. Muenchausen, S. Foltin, and R. Dye, Phys. Rev. B **47**, 8377 (1993); **49**, 6270 (1994).
[8] S. Dubois, F. Carmona, and S. Flandrois, Physica C **260**, 19 (1996).
[9] P. W. Anderson, Phys. Rev. Lett. **9**, 309 (1962); P. W. Anderson and Y. B. Kim, Rev. Mod. Phys. **36**, 39 (1964).
[10] M. V. Feigel'man, V. B. Geshkenbein, and A. I. Larkin, Physica C **167**, 177 (1996).
[11] A. Houghton, R. A. Pelcovits, and A. Sudbo, Phys. Rev. B **40**, 6763 (1989).
[12] G. D'Anna, M. O. Andre, M. V. Indenbom, and W. Benoit, Physica C **230**, 115 (1994).
[13] D. T. Fuchs, E. Zeldov, T. Tamegai, S. Ooi, M. Rappaport, and H. Shtrikman, Phys. Rev. Lett. **80**, 4971 (1998).
[14] R. G. Mints and I. B. Snapiro, Phys. Rev. B **47**, 3273 (1993).
[15] L. Burlachkov, A. E. Koshelev, and V. M. Vinokur, Phys. Rev. B **54**, 6750 (1996).
[16] E. Zeldov, A. I. Larkin, V. B. Geshkenbein, M. Konczykowski, D. Majer, B. Khaykovich, V. M. Vinokur, and H. Shtrikman, Phys. Rev. Lett. **73**, 1428 (1994).
[17] M. Požek, A. Dulčic, and B. Rakvin, Physica C **197**, 175 (1992).
[18] A. A. Koshta, A. A. Romanyukha, Yu. N. Shvachko, N. A. Viglin, V. V. Ustinov, and S. V. Naumov, Sverkhprovodimost' (KIAE) **3**, 838 (1990) [Superconductivity **3**, 787 (1990)]; A. A. Romanyukha, Yu. N. Shvachko, D. Z. Khusainov, A. A. Koshta, and V. V. Ustinov, Physica C **235–240**, 2060 (1994).
[19] V. A. Atsarkin, V. V. Demidov, and N. E. Noginova, Sverkhprovodimost' (KIAE) **5**, 305 (1992) [Superconductivity **5**, 301 (1992)].
[20] T. Endo, H. Yan, S. Nagase, and H. Shibata, J. Superconduct. **8**, 259 (1995).
[21] T. Shaposhnikova, Yu. Vashakidze, R. Khasanov, and Yu. Talanov, Physica C **300**, 239 (1998).
[22] T. Shaposhnikova, Yu. Vashakidze, and Yu. Talanov, Physica C **385**, 383 (2003).
[23] M. J. Qin and X. X. Yao, Phys. Rev. B **54**, 7536 (1996).
[24] M. J. Qin and C. K. Ong, Physica C **319**, 41 (1999).
[25] M. J. Qin and C. K. Ong, Phys. Rev. B **61**, 9786 (2000).
[26] G. Blatter, M. V. Feigel'man, V. B. Geshkenbein, A. I. Larkin, and V. M. Vinokur, Rev. Mod. Phys. **66**, 1147 (1994).
[27] A. P. Malozemoff, T. K. Worthington, Y. Yeshurun, F. Holtzberg, and P. H. Kes, Phys. Rev. B **38**, 7203 (1988).
[28] M. F. Goffman, J. A. Herbsommer, F. de la Cruz, T. W. Li, and P. H. Kes, Phys. Rev. B **57**, 3663 (1998).
[29] R. I. Khasanov, Yu. I. Talanov, W. Assmus, and G. B. Teitelbaum, Phys. Rev. B **54**, 13339 (1996).
[30] S. L. Lee, P. Zimmermann, H. Keller, M. Warden, I. M. Savic, R. Schauwecker, D. Zech, R. Cubitt, E. M. Forgan, P. H. Kes, T. W. Li, A. A. Menovsky, and Z. Tarnawski, Phys. Rev. Lett. **71**, 3862 (1993).

Translated by Steve Torstveit

Frozen magnetoresistance in the magnetization reversal of granular Bi(Pb)-HTSCs

A. A. Sukhanov* and V. I. Omelchenko

Institute of Radio Engineering and Electronics of the Russian Academy of Sciences, pl. Vvedenskogo 1, Fryazino, Moscow District, 141190, Russia

(Submitted November 20, 2003)
Fiz. Nizk. Temp. **30**, 604–609 (June 2004)

The frozen magnetoresistance of ceramic Bi(Pb)-HTSC samples is investigated as a function of the fields initiating magnetic flux trapping and the magnetization-reversing fields: $R_t(H_i, H_r)$. It is found that the $R_t(H_r)$ curves are nonmonotonic. The value of the frozen magnetoresistance decreases substantially after application of the first H_r pulse ($H_r < H_i$) but remains practically unchanged upon subsequent magnetization reversals by pulses of the same magnitude but of either polarity. The influence of the magnetization reversal on the anisotropy of the magnetoresistance and the negative magnetoresistance effect are studied. It is shown that the results are in conflict with models of the critical state for the granules and superconducting loops but are well described quantitatively by the proposed model of granular Bi(Pb)-HTSCs, according to which the magnetic flux trapping occurs in ''normal'' granules wrapped in superconducting shells, while the resistance of the samples is determined by chains of weak links. © *2004 American Institute of Physics.*
[DOI: 10.1063/1.1768335]

INTRODUCTION

Despite continuing studies,[1–3] the nature of the magnetic flux trapping in granular HTSCs, especially in the superconducting transition region, remains largely unclear. In particular, it has not yet been established whether the trapping in this case occurs in the individual superconducting (SC) granules[4,5] or in closed loops formed by SC granules.[6]

We assume that this can be clarified by studying the influence of magnetization reversal on the value of the frozen magnetoresistance (MR). The point is that, in contrast to the dependence of the trapped fields (TFs) and frozen MR on the trapping-initiating field, $H_t(H_i)$ and $R_t(H_i)$, the dependence of the frozen MR on the magnetization-reversing field $R_t(H_r)$ according to the superconducting loops model and according to the model of the critical state in the granules should be different.

Indeed, the resistance of granular HTSCs after the trapping of a magnetic flux is determined by the influence of the trapped fields on the weak links of the current channels, and therefore the frozen MR depends only on the absolute values of the local TFs. According to the model of ''thick'' SC loops (rings with a superconducting wall thickness greater than the London length), magnetic flux trapping initiated by pulses of a magnetic field $\mathbf{H}_i$ after cooling in zero field (the ZFC regime) occurs only upon application to the ring of a field higher than a critical value ($H_i \equiv |\mathbf{H}_i| > H_c$), and the value of the TFs is always equal to H_c. Therefore, after magnetization reversal of the samples by pulses of an external field $\mathbf{H}_r \| -\mathbf{H}_i$ for which $H_r \equiv |\mathbf{H}_r| < H_i$ the value of the frozen MR should not change, since magnetization reversal of the ''strong'' loops with higher critical fields ($H_c > H_r$) does not occur, and the TFs of the ''weak'' loops with $H_c < H_r$ remain equal to H_c in magnitude, although their direction varies.

In contrast, if the flux trapping occurs in individual granules, where, as in crystals, the field distribution is usually described by the model of the critical state, after magnetization reversal the distribution of the trapped fields changes throughout the whole volume of the granule, and the direction of the TFs in an outer layer of the granules changes to the opposite. As a result of this, the flux trapped in each of the granules falls and, hence, the field outside the granules should decrease and consequently so should the value of the frozen MR.

Thus by studying the influence of magnetization reversal on the frozen MR of granular HTSC samples, one can decide between the different models of flux trapping in the region of the resistive transition. In this connection we have studied the features of the field dependence of the frozen MR of Bi(Pb)-HTSC ceramics upon their magnetization reversal.

1. SAMPLES, MEASUREMENT TECHNIQUES, AND RESULTS

The measurements were made on samples of Bi(Pb)–Sr–Ca–Cu–O ceramics prepared by the one-step sintering of a mixture of Bi_2O_3, PbO_2, SrO, CaO, and CuO powders with a nominal composition of $Pb_{0.5}Bi_2Sr_3Ca_5Cu_6O_{18}$ in air at 870 °C for 120–144 hours. The samples were in the form of tablets 2–4 mm thick and 8–10 mm in diameter. Measurements of the magnetic susceptibility showed that the samples contained two SC phases with critical temperatures $T_{c1} \approx 110$ K (the 2223 phase) and $T_{c2} \approx 80$ K (the 2212 phase). The volume fractions of these places were equal to 7–10% and 30–40%, respectively.

The resistance of the samples was determined by the four-probe method in alternating current ($J = 0.5$ mA, $f = 7$ Hz). The curves of the temperature dependence of the resistance $R(T)$ of the samples exhibited a region of sharp decrease in R at $T_{c0} > T > T_{cm}$ ($T_{c0} = 107$–110 K, $T_{cm} = 98$–100 K) and a ''tail'' ending at $T_{cf} = 78$–85 K. The

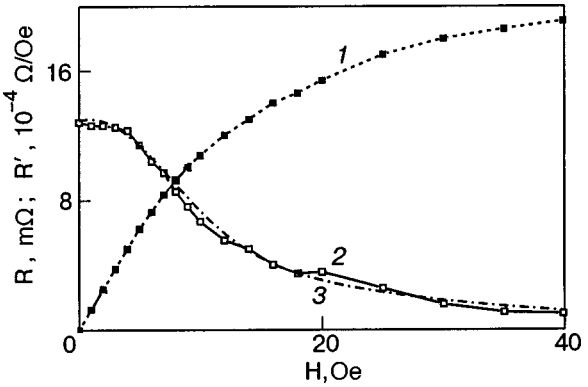

FIG. 1. Field dependence of the magnetoresistance $R(H)$ (curve *1*) and the derivative $R'(H)=dR/dH$ (curve *2*) for a ceramic sample of a Bi(Pb)-HTSC. The dot-and-dash curve *3* is the approximation of the dependence $R'(H)$ by the function in Eq. (8).

MR of the samples had distinctively large values in the region $T_{cm}>T>T_{cf}$.

The strong field dependence of the magnetoresistance $R(H)$ at low fields $H=1-15$ Oe (curve *1* in Fig. 1) is apparently explained by disruption of the network of weak links of the granular HTSC by the magnetic field and is determined by the distribution function of the weak links of the current channels over critical fields. The magnetic flux trapping and magnetization reversal of the samples was done at $T=77.4-85$ K in the ZFC regime by applying a pulse of a trapping-initiating field $\mathbf{H}_i$, and then pulses of the magnetization-reversing fields $-\mathbf{H}_r$ and $+\mathbf{H}_r$ ($H_r \leqslant H_i$). The magnetic fields were applied perpendicular to the direction of the measuring current. The duration of the field pulses was 30 s, and the frozen MR was measured 300 s after the application of each pulse.

Figure 2 shows a typical monotonically increasing curve of the frozen MR as a function of the pulse amplitude of the initiating fields, $R_t(H_i)$; the curve has a tendency toward saturation at $H_i=200-500$ Oe. It is seen in Fig. 1 and 2 that the trapped fields at $H_i=200-300$ Oe lead to the same MR as an external field $H=7-10$ Oe. At the same time, the trapped fields measured by the Hall probes amount to 0.01–0.2 Oe for $H_i=200-300$ Oe. This means that the local TFs are 2–3 orders of magnitude higher than the average TFs

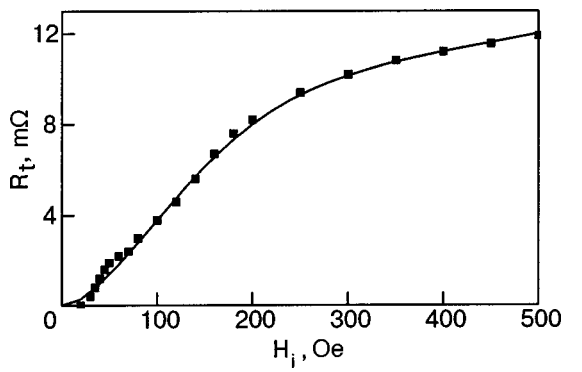

FIG. 2. The dependence of the frozen MR on the magnetic field inducing flux trapping. The points are experimental data. The curve shows the dependence $R_t(H_i)$ calculated with the use of expressions (5), (8), and (9).

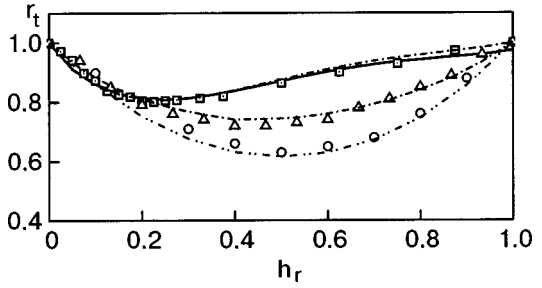

FIG. 3. Normalized curves of the frozen MR of Bi(Pb)-HTSC ceramics versus the magnetization-reversing field ($r_t=R_t(H_r)/R_t(0)$ and $h_r=H_r/H_i$) at $T=80$ K for various inducing fields H_i [Oe]: 400 (□), 150 (△), 50 (○). The solid line is the $r_t(h_r)$ curve calculated according to Eq. (6) for $H_i=400$ Oe. The dot-and-dash lines are the $r_t(h_r)$ curves calculated for the unsaturated regime of magnetic flux trapping.

measured by the Hall probes and, as in the case of Bi-HTSC films,[6] are sign-varying and are closed inside the sample.

We stress that all of the data plotted in this paper were obtained on a single sample. This allows one to find the distribution function of the TFs from the plots of $R_t(H_i)$ and $R(H)$ (Figs. 1 and 2) and then to calculate the dependence of the frozen MR on the magnetization–reversing field $R_t(H_r)$ and compare it to the experimental curves.

Normalized curves of the frozen MR versus magnetization-reversing field $r_t(h_r)$ ($r_t=R_t(H_r)/R_t(0)$ and $h_r=H_r/H_i$) for different values of H_i in the magnetization reversal of a sample by single pulses are shown in Fig. 3. These curves have a nonmonotonic form with a minimum at $h_r=0.2-0.5$. With increasing H_i the position of the minimum of $r_t(h_r)$ is shifted to lower values, and the depth of the dip decreases from 30% to 10%.

Significantly, within the experimental error ($\sim 3-5\%$) the $r_t(h_r)$ curves in the case of two or more magnetization reversals by alternating pulses of different polarity, $-\mathbf{H}_r$ and $+\mathbf{H}_r$ turn out to be the same as for a single magnetization reversal.

Despite this, measurements of the MR have shown that the spatial distributions of TFs in these cases are substantially different. It has been found that after the initial flux trapping and a double magnetization reversal the MR is anisotropic, and in an applied magnetic field $\mathbf{H}\|\mathbf{H}_i$ a negative MR is observed (curves *1* and *3* in Fig. 4) because the external field $\mathbf{H}$ compensates the TFs directed opposite to $\mathbf{H}_i$ near the current channels.[7] In the case of magnetization reversal by a single $-\mathbf{H}_r$ pulse the anisotropy of the MR varies depending on the magnitude H_r of the pulse. For $H_r \ll H_i$ a negative MR is observed for $\mathbf{H}\|\mathbf{H}_i$, at fields H_{rm} corresponding to the minimum of $R_t(H_r)$ the anisotropy of the MR and the negative MR vanish (curve *2* in Fig. 4), and, finally, for $H_r \lesssim H_i$ the negative MR effect is again observed, only now for fields $\mathbf{H}\|-\mathbf{H}_i$. This means that after the first magnetization reversal the trapped fields with different directions arise near the weak links of the current channels, and after a second magnetization reversal the TFs are directed opposite to $\mathbf{H}_i$.

2. DISCUSSION OF THE RESULTS. MODEL OF MAGNETIC FLUX TRAPPING AND FROZEN MAGNETORESISTANCE

In the region of the resistive transition a granular HTSC constitutes a dilute Josephson medium in which isolated SC

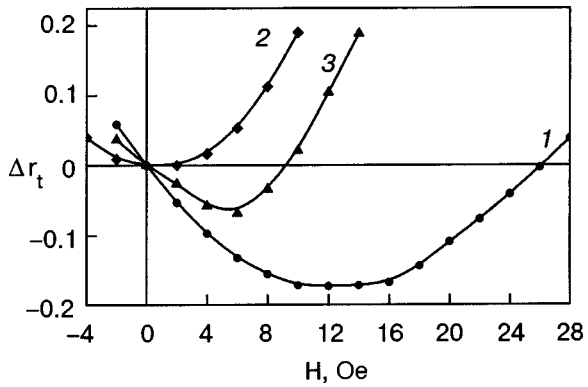

FIG. 4. Field dependence of the normalized MR of a Bi(Pb)-HTSC sample with trapped fields $\Delta r_t(H)=[R_t(H)-R_t(0)]/R_t(0)$: after magnetic flux trapping initiated by a pulse of field $H_i=200$ Oe (*1*), after magnetization reversal of the sample by a pulse of field $-\mathbf{H}_{rm}$, $|H_{rm}|=60$ Oe (*2*); after a subsequent magnetization reversal of the ceramic by two magnetic-field pulses, $-\mathbf{H}_{rm}$ and $+\mathbf{H}_{rm}$ (*3*).

granules or SC grannules connected by weak links are immersed in a normal granular matrix. Here the SC granules and weak links can form chains (current channels) and clusters, including closed loops. The MR and frozen MR of such media are determined by the destruction of the superconductivity of the weak links of the current channels by the external and local trapped magnetic fields, and the magnetic flux trapping can occur both in the SC granules[4,5] and in the SC loops.[6] As we have said, both models can explain the field dependence of the trapped fields and frozen MR and also the appearance of sign-varying TFs.

However, the results of experiments disagree with the predictions of both models. According to the thick-ring model, the frozen MR during magnetization reversal should not change at all (see the Introduction). Furthermore, the notions of magnetic flux trapping in closed SC loops containing weak links disagree with the results of measurements of the temperature dependence of the frozen MR. Those measurements imply that flux trapping can occur at temperatures $T_{cm}<T<T_{c0}$, where individual granules undergo a transition to the SC state but neither current channels nor loops containing weak links are formed yet.[8]

According to the model of the critical state in the granules, in the magnetization reversal of samples by pulses of alternating polarity the frozen MR should be changed after each pulse because of the change in the direction of the fields trapped in the outer layers of the granules with $H_c>H_r$. Calculations show that the changes of the resistance after the second and subsequent magnetization-reversing pulses should have been 30–50% of the decrease in the frozen MR after the first pulse.

At the same time, the results obtained are described well in the framework of a model of magnetic flux trapping in normal granules with SC shells. It is known that shells of the 2223 phase, with $T_c=105$ K, can form on the surface of granules of the 2212 phase, with $T_c=77-82$ K, in the final stage of synthesis of Bi(Pb)-HTSC ceramics.[9–11] As the temperature of such a material is lowered, individual parts of the envelopes of the granules can undergo transition to the SC state and form closed SC loops.

For a comparison with the experimental results, let us consider the flux trapping in a system of ''one-dimensional'' normal granules with thin superconducting shells in which a critical state with current density j_c is realized. We neglect the flux trapped in the shells (the wall of the loop) in comparison with the trapped flux enclosed by it, which is valid for $d/D\ll 1$, where D and d are, respectively, the size of the granule and the thickness of the shells. Then according to the model of the critical state the field trapped in the granule after imposition of a pulse H_i is given by

$$H_t(H_i)=\begin{cases} 0 \ \text{ for } \ H_i\leqslant H_c, \\ H_i-H_c \ \text{ for } \ 2H_c\geqslant H_i\geqslant H_c, \\ H_c \ \text{ for } \ H_i\geqslant 2H_c, \end{cases} \tag{1}$$

where $H_c=j_c d$ is the critical value beginning with which the field penetrates inside granules with a superconducting shell. It is seen from Eq. (1) that for $H_i<H_c$ the field does not penetrate inside the granules, while for $H_i>H_c$ the value of the TF increases linearly with H_i until it reaches a value equal to H_c.

Let us now consider the simple case of magnetization reversal by a pulse $-\mathbf{H}_r$ from the regime of saturation, when the TFs in all the loops after the initial flux trapping reach the limiting value H_c. In this case

$$H_t(H_r)=\begin{cases} H_c-H_r \ \text{ for } \ H_r\leqslant 2H_c, \\ -H_c \ \text{ for } \ H_r\geqslant 2H_c. \end{cases} \tag{2}$$

It is seen from (2) that even weak magnetization-reversing fields H_r penetrate into the granules and decrease the trapped fields H_t in them, leading to a decrease in the frozen MR upon magnetization reversal. It is also seen that after magnetization reversal by a pulse $-\mathbf{H}_r$, trapped fields of different sign will have arisen in granules with different H_c and hence along the current channels. Because of this, the anisotropy of the MR and the negative MR effect can vanish.

In the case of magnetization reversal by two successive pulses $-\mathbf{H}_r$ and $+\mathbf{H}_r$ we obtain

$$H_t(H_r)=\begin{cases} H_c-H_r \ \text{ for } \ H_r\leqslant H_c, \\ H_r-H_c \ \text{ for } \ H_c\leqslant H_r\leqslant 2H_c, \\ H_c \ \text{ for } \ H_r\geqslant 2H_c. \end{cases} \tag{3}$$

Since the frozen MR is determined only by the absolute values of the TFs, it follows from a comparison of (3) and (2), in agreement with experiment, that the value of the frozen MR remains unchanged upon repeated magnetization reversal of granules with thin shells.

In the description of the field dependence of the frozen MR we assume that: 1) the resistance of the sample is determined by the series-connected weak links of the current channel, which are found near granules with SC shells in which the flux trapping occurs; 2) a weak link undergoes transition to the normal state under the condition $k|H_t|>H_{\rm cr}$, where $H_{\rm cr}$ is the critical field of the weak link, H_t is the TF of the nearest granule, and k is a geometric factor that takes into account the attenuation of the TF in the region of the weak links ($k\leqslant 1$). Then the frozen MR induced by the TFs $H_t(H_i,H_r)$ of granules with SC shells is equal to

$$R_t(H_i,H_r)=\int_0^{H_i} f(H_c)\int_0^{k|H_t(H_i,H_r)|}\varphi(H_{\rm cr})\,dH_{\rm cr}\,dH_c, \tag{4}$$

where $f(H_c)$ and $\varphi(H_{cr})$ are the distribution functions of the SC coatings and of the resistances of the weak links of the current channels with respect to the corresponding critical fields.

Using Eq. (4) together with expressions (1) and (2), we obtain the dependence of the frozen MR on the inducing field H_i in the case of flux trapping and on the reversing field H_r in the case of magnetization reversal from the saturation regime:

$$R_t(H_i)=\int_0^{H_i/2} f(H_c)\int_0^{kH_c}\varphi(H_{cr})dH_{cr}\,dH_c + \int_{H_i/2}^{H_i} f(H_c)\int_0^{k(H_i-H_c)}\varphi(H_{cr})dH_{cr}\,dH_c, \quad (5)$$

$$R_t(H_r)=\int_0^{H_r/2} f(H_c)\int_0^{kH_c}\varphi(H_{cr})dH_{cr}\,dH_c + \int_{H_r/2}^{H_i} f(H_c)\int_0^{k|H_r-H_c|}\varphi(H_{cr})dH_{cr}\,dH_c. \quad (6)$$

As we have said, the distribution function $\varphi(H_{cr})$ can be determined from the field dependence of the MR of the samples, $R(H)$. For the current-channel model under consideration, we have

$$R(H)=\int_0^H \varphi(H_{cr})dH_{cr}$$

and

$$\varphi(H_{cr})=R'(H)|_{H_{cr}}=\left.\frac{\partial R(H)}{\partial H}\right|_{H_{cr}}. \quad (7)$$

Using Eq. (7) and the data in Fig. 1, we find the following empirical expression for the distribution of weak links of the current channel with respect to critical fields:

$$\varphi(H_{cr})\simeq\frac{H_{rm}}{H_{cr}^2-H_{r1}^2}+0.04\exp\left[-\left(\frac{H_{cr}-1}{9}\right)^2\right],$$

$$H_{rm}=12\ \text{Oe},\quad H_{r1}=20\ \text{Oe}. \quad (8)$$

Then from Fig. 2 and expression (5) by analytical or fitting methods we find the distribution function of the shells over critical fields, which can be written approximately in the form

$$f(H_c)=\exp\left[-\left(\frac{H_c-H_M}{\sqrt{2}H_1}\right)^2\right]+0.15\exp\left(-\frac{H_c}{30H_1}\right),$$

$$H_m=40\ \text{Oe},\quad H_1=110\ \text{Oe}. \quad (9)$$

Then, using Eqs. (6), (8), and (9), we calculate the dependence $R_t(H_r)$ for magnetization reversal from saturation ($H_i=400$ Oe); this dependence in normalized form is shown by the solid curve in Fig. 3. We note that we used the value $k=0.85$ in all the calculations. The disagreement of the calculated curve with the experimental data at large values of H_r is due to the fact that the saturation regime has not yet been reached at the field $H_i=400$ Oe.

We also carried out an analogous examination for magnetization reversal at arbitrary values of H_i. The expressions obtained for $R_t(H_r,H_i)$ have a rather lengthy form and are therefore not given here. The calculated graphs of $R_t(H_r)$ for magnetization reversal after the imposition of inducing pulses $H_i=50$, 150, and 400 Oe are shown by the dot-and-dash curves in Fig. 3. It is seen from these graphs that the results of the calculations are in good agreement with the experimental data.

When the magnetic flux trapped in the wall of the loop is taken into account, the $R_t(H_r)$ curves for single and double magnetization reversal become different. Calculations show that the increase in the frozen MR in the second magnetization reversal amounts to $\delta R_t\approx\Delta R_t d/D$, where ΔR_t is the decrease of the frozen MR in the case of single magnetization reversal. For $d/D=0.1$ and $\Delta R_t/R_t=0.25$ the increase of $\delta R_t/R_t$ lies within the measurement error ($\approx 3\%$).

Let us estimate the thickness of the SC shells of the granules. For $H_c=40-120$ Oe and the typical value for single crystals $j_c=10^{10}$ A/m^2 we find $d=0.32-1$ μm, which is approximately an order of magnitude smaller than the granule size D in the ceramics studied.

Thus we have investigated the field dependence of the frozen MR in the magnetization reversal of Bi(Pb)-HTSC ceramics. We have shown that the results obtained (nonmonotonic dependence of the frozen MR on the magnetization-reversing field, the absence of changes in the frozen MR after the second and subsequent magnetization-reversing pulses) are not explained by the known models of the critical state in the granules and SC rings. A model of granular Bi(Pb)-HTSCs is proposed, according to which the magnetic flux trapping occurs in normal granules with SC shells and the resistive properties are determined by chains of weak links. On the basis of this model the field dependence of the frozen magnetoresistance is described in a unified way for both magnetic flux trapping and magnetization reversal.

*E-mail: sukh@ms.ire.rssi.ru

[1] K. Tanabe, K. Suzuki, S. Adachi, T. Takagi, and N. Koshizuka, Physica C **372–376**, 706 (2002).
[2] M. Zeisberger, T. Habisreuther, D. Litzkendorf, R. Muller, O. Surzhenko, and W. Gawalek, Physica C **372–376**, 1890 (2002).
[3] Hirofumi Fukai, Masaru Tomita, Motohide Matsui, Masato Murakami, and Takao Nagatomo, Physica C **378–381**, 738 (2002).
[4] A. I. Belyaeva, S. V. Voĭtsenya, and V. P. Yur'ev, Sverkhprovodimost' (KIAE) **4**, 680 (1991) [Superconductivity **4**, 589 (1991)].
[5] P. Mune and J. Lopez, Physica C **257**, 360 (1996).
[6] A. A. Sukhanov and V. I. Omelchenko, Fiz. Nizk. Temp. **27**, 826 (2001) [Low Temp. Phys. **27**, 609 (2001)].
[7] A. A. Sukhanov and V. I. Omelchenko, Fiz. Nizk. Temp. **29**, 396 (2003) [Low Temp. Phys. **29**, 297 (2003)].
[8] A. A. Sukhanov, V. I. Omelchenko, and G. A. Orlova, cond-mat/0208226 (2002).
[9] J. M. Tarascon, Y. Le Page, L. H. Green, B. G. Bagley, P. Barboux, D. M. Hwang, G. W. Hull, W. R. McKinnon, and M. Giroud, Phys. Rev. B **38**, 2504 (1988).
[10] Yu. Ya. Tomashpol'skiĭ, F. L. Kochetov, N. V. Sadovskaya, S. G. Prutchenko, and S. A. Ivanov, Sverkhprovodimost' (KIAE) **3**, 708 (1990) [Superconductivity **3**, 669 (1990)].
[11] S. C. Kwon, H. G. Lee, B. T. Ahn, and S. W. Nam, Supercond. Sci. Technol. **8**, 552 (1995).

Translated by Steve Torstveit

Static vortices in long Josephson junctions of exponentially varying width

E. G. Semerdjieva[a)]

Plovdiv University, Plovdiv, Bulgaria; Joint Institute for Nuclear Research, Dubna 141980, Russia

T. L. Boyadjiev[b)]

Joint Institute for Nuclear Research, Dubna 141980, Russia; Sofia University, Sofia, Bulgaria

Yu. M. Shukrinov[c)]

Joint Institute for Nuclear Research, Dubna 141980, Russia; Physical Technical Institute, Dushanbe, Tajikistan

(Submitted January 16, 2004)
Fiz. Nizk. Temp. **30**, 610–618 (June 2004)

A numerical simulation is carried out for static vortices in a long Josephson junction with an exponentially varying width. At specified values of the parameters the corresponding boundary-value problem admits more than one solution. Each solution (distribution of the magnetic flux in the junction) is associated to a Sturm–Liouville problem, the smallest eigenvalue of which can be used, in a first approximation, to assess the stability of the vortex against relatively small spatiotemporal perturbations. The change in width of the junction leads to a renormalization of the magnetic flux in comparison with the case of a linear one-dimensional model. The influence of the model parameters on the stability of the states of the magnetic flux is investigated in detail, particularly that of the shape parameter. The critical curve of the junction is constructed from pieces of the critical curves for the different magnetic flux distributions having the highest critical currents for the given magnetic field. © *2004 American Institute of Physics.* [DOI: 10.1063/1.1768336]

1. STATEMENT OF THE PROBLEM

A Josephson junction model that takes into account the influence of the shape in the xy plane was considered in Refs. 1–3. For a model junction with generatrices that vary by an exponential law[2,3] (see Fig. 1) the basic equation for the phase $\varphi(t,x)$ in the junction can be written in the form

$$\ddot{\varphi}+\alpha\dot{\varphi}-\varphi''+\sin\varphi+g(t,x)=0, \quad x\in(0,l), \quad t>0. \quad (1)$$

The spatial coordinate x is normalized to the Josephson penetration depth λ_J, and $l=(L_0+L_s+L_L)/\lambda_J$. The time t is normalized to the plasma frequency (see, e.g., the monograph cited as Ref. 4). The parameter α describes dissipative effects in the junction. An overdot denotes differentiation with respect to time t, and a prime denotes differentiation with respect to the spatial coordinate x.

The term $g(t,x)\equiv\sigma[\varphi'(t,x)-h_B]$ in Eq. (1) models the current caused by the exponential variation of the width of the junction. The dimensionless shape parameter $\sigma\geqslant 0$ is determined by the following expression (see Fig. 1 for notation):

$$\sigma=\frac{\lambda_J}{L_s}\ln\left(\frac{W_0}{W_L}\right),$$

where it is assumed that $W_0>W_L$. It is known that after suitable normalization the function $\varphi(t,x)$ can be interpreted as the (dimensionless) magnetic flux along the junction. Then the value of h_B is the (dimensionless) strength of the external (boundary) magnetic field along the y axis. For simplicity it is assumed below that the field h_B is independent of time.

A detailed derivation of Eq. (1) is given in Ref. 2.

In the present paper we restrict consideration to a model junction with an in-line geometry. If the injection current density through the end L_0 of the junction is denoted by γ (which is assumed constant), the boundary conditions at $x=0$ and $x=l$, after the transition to the corresponding limits, take the form

$$\varphi'(t,0)=h_B-l\gamma, \quad \varphi'(t,l)=h_B. \quad (2)$$

Because of the presence of a dissipative term $\alpha\dot{\varphi}$ the

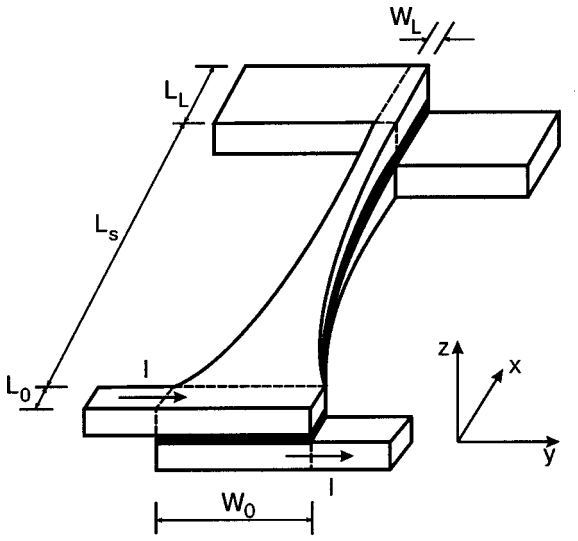

FIG. 1. Diagram of the Josephson junction of exponentially varying width.

solution $\varphi(t,x)$ of equation (1) can lose energy and, consequently, for $t\to\infty$ it will approach the corresponding static distribution $\varphi_s(x)$ (to simplify the notation below we shall use the subscript s when necessary). This makes it necessary to investigate in detail the static distributions in the Josephson junction and their behavior upon variations of the model parameters.

The boundary-value problem for the static distributions follows directly from relations (1) and (2):

$$-\varphi''+\sin\varphi+g(x)=0, \quad x\in(0,l), \tag{3a}$$

$$\varphi'(0)-h_B+l\gamma=0, \tag{3b}$$

$$\varphi'(l)-h_B=0, \tag{3c}$$

where the ''geometric'' current is given by the expression

$$g(x)\equiv\sigma[\varphi'(x)-h_B]. \tag{4}$$

We note that the solutions of the problem (3) depends not only on the spatial coordinate x but also on the set of parameters $p\equiv\{l,\sigma,h_B,\gamma\}$, i.e., $\varphi(x,p)$. When necessary below we shall indicate the dependence of the quantities on the parameters.

Let $\varphi_s(x)$ be some static solution of equation (1), i.e., a solution of the boundary-value problem (3). With the goal of investigating the stability of the solution $\varphi_s(x)$, following Ref. 5, we consider a spatiotemporal fluctuation of the form

$$\varphi(t,x)=\varphi_s(x)+\varepsilon\exp(-\alpha t/2)\sum_n[\exp(i\omega_n t)\psi_n(x) + \exp(-i\omega_n t)\psi_n^*(x)], \tag{5}$$

which depends on the small parameter ε. Substituting the expansion (5) into Eq. (1) and condition (2), to a first approximation in ε we arrive at the Sturm–Liouville (SL) problem

$$-\psi''+\sigma\psi'+q(x)\psi=\lambda\psi, \quad x\in(0,l), \tag{6a}$$

$$\psi'(0)=0, \quad \psi'(l)=0, \tag{6b}$$

the potential of which, $q(x)\equiv\cos\varphi_s(x)$, is determined by the known static solution $\varphi_s(x)$. Here $\lambda=(\omega^2+\alpha^2/4)^{1/2}$ is the spectral parameter.

In view of the boundedness of the function $|q(x,p)|\leqslant 1$ on a finite interval of the variable x there exists[6] a countable sequence, bounded from below, of real eigenvalues $\lambda_{\min}\equiv\lambda_0<\lambda_1<\lambda_2<...<\lambda_n<...$ of problem (6). To each eigenvalue λ_n $(n=0,1,2,\ldots)$ there corresponds a single real eigenfunction $\psi_n(x)$ satisfying the normalization condition

$$\int_0^l\psi_n^2(x)dx=1.$$

Here the number of zeroes of the eigenfunction $\psi_n(x)$ on the interval $(0,l)$ is equal to the index n. In particular, the eigenfunction $\psi_0(x)$ corresponding to the smallest eigenvalue $\lambda_{\min}$ does not have zeroes on $(0,l)$.

Since $\varphi(x,p)$ depends on the set of parameters p, the potential of the SL problem and, hence, the corresponding eigenvalues and eigenfunctions of the SL problem also depend on the parameters, i.e., $\lambda_n=\lambda_n(p)$ and $\psi_n=\psi_n(x,p)$.

We shall say[5] that in a certain range of variation of the parameters $\mathcal{P}\subset\mathbb{R}^4$ the static solution $\varphi_s(x)$ is stable in a first approximation with respect to spatiotemporal perturbations of the form (5) if in that region $\lambda_{\min}(p)>0$. If $\lambda_{\min}(p)<0$, then a component that is rapidly growing in time appears in the expansion (5), and the solution $\varphi_s(x)$ is unstable. The points of the vector of parameters which lie on the hypersurface

$$\lambda_{\min}(p)=0 \tag{7}$$

in the space $\mathcal{P}$ are points of bifurcation (branching) for the solution $\varphi(x,p)$. The values of the parameters for which Eq. (7) holds are called the bifurcation or critical values for the solution $\varphi(x)$. The corresponding bifurcation curves for the remaining two parameters are given by the sections of the surface (7) by hyperplanes corresponding to fixed values of the two parameters. The most important from the standpoint of the possibility of experimental verification are the critical curves of the current versus magnetic field type,

$$\lambda_{\min}(\gamma,h_B)=0, \tag{8}$$

corresponding to fixed geometric parameters l and σ of the junction.

From a theoretical standpoint knowledge of the bifurcation curves enables one to find the number of equilibrium solutions, to understand their structure, and to describe the physics of the phenomenon. Numerical simulation simplifies the study and makes it possible to estimate the range of variation of the parameters in which one can expect stability or instability of the magnetic flux distributions in the Josephson junction.

Especially important for practical purposes is the ability to check experimentally the bifurcation curves of the parameters of the Josephson junction, which in turn is an important source of information for refining the physical model. As a concrete example let us indicate the methods of studying solitonlike vortex structures of the magnetic flux in Josephson junctions on the basis of measurements of the magnetic-field dependence of the critical current (see, e.g., Refs. 3, 5 and 7–10).

We note that a number of papers have been devoted to the laying of a rigorous mathematical groundwork for reducing the problem of stability of the solutions of nonlinear operator equations to an investigation of eigenvalue problems for a linear operator (see, e.g., the review[11] and the collected papers[12] and the literature cited therein).

Josephson junctions with an exponentially varying width in the xy plane have been studied theoretically and experimentally in Refs. 2 and 3. The influence of the shape on the current–voltage characteristics of the junctions was studied in detail. However, the problems involving the determination of the stability regions of the static distributions and the structure of the critical curves have not been adequately studied. The present paper is devoted to a study of those questions, which are important from the applied and theoretical points of view.

2. NUMERICAL RESULTS AND DISCUSSION

The exact analytical solutions of equation (3a) for the case $\sigma=0$ are expressed in terms of elliptic functions.[13] For $\sigma>0$ approximate methods can be used.[2] In both cases a stability analysis of the solutions using the SL problem (6) is

difficult in view of the complexity of the corresponding expressions for the potential $q(x)$. Therefore it is advisable to carry out a detailed analysis of the possible states of the magnetic flux in the junction and analysis of their stability with the help of a numerical simulation.

In this paper we use a continuous analog of Newton's method for solution of the boundary-value problems (3) and (6) (see reviews[14,15]). The linearized boundary-value problems arising at each iteration were solved numerically with the use of a spline collocation scheme[16] of improved accuracy.

To permit comparison of our results with the results of Ref. 3, the majority of the numerical simulations were carried out for Josephson junctions of length $l=10$ and $l=20$.

For an ''infinite'' one-dimensional and uniform Josephson junction $[\sigma=0,\ l\to\infty,\ x\in(-\infty,\infty)]$ the well-known exact analytical expression (see, e.g., Refs. 4 and 5)

$$\varphi(x)=4\arctan(\exp(\pm x)), \tag{9}$$

usually called the fluxon and antifluxon, respectively, is valid. For realistic Josephson junctions of finite length those entities are deformed by the geometry of the junction and also by the influence of the magnetic field h_B and/or the external current γ and are not fluxons in the strict sense of the word (the functions (9) do not satisfy conditions (2)). However, because of a number of features of those soliton-like solutions, in particular, their finite energy and size, it is appropriate and convenient to use these conventional names. For brevity below we denote the fluxon in the Josephson junction as Φ^1.

According to Ref. 5, on the entire axis $(-\infty,\infty)$ the discrete spectrum of the SL problem generated by solution (9) consists of an isolated point $\lambda=0$, i.e., the fluxon/antifluxon in an ''infinite'' Josephson junction is found in a quasi-stable (bifurcation) state.

It follows from general comparison theorems for SL problems that for a finite Josephson junction the condition $\lambda_{\min}<0$ holds, i.e., the stability of Φ^1 becomes worse.

For $\gamma=0$ and small $|h_B|$ the only stable state in a Josephson junction of finite length is the Meissner (vacuum) state, which will be denoted by M. For $h_B=0$, $\gamma=0$ this ''trivial'' solution of problem (3), of the form $\varphi(x)=0$, $\pm2\pi,\pm4\pi,\ldots$ (there is no magnetic field in the junction). For these same parameters the smallest eigenvalue of the SL problem for the M distribution is $\lambda_{\min}(M)=1$. In addition to M there is also an unstable Meissner solution $\varphi(x)=\pm\pi$, $\pm3\pi,\ldots$, for which $\lambda_{\min}=-1$.

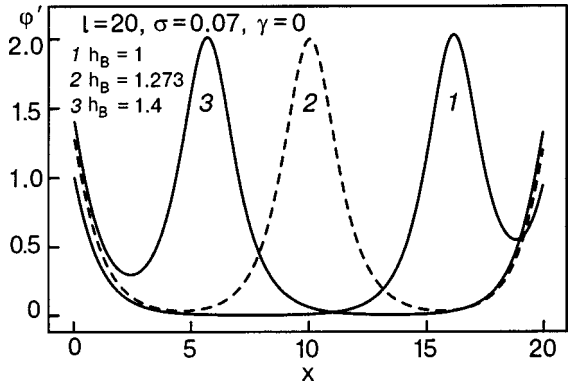

FIG. 3. The $\varphi'(x)$ curves for different h_B.

For sufficiently large values of the boundary magnetic field h_B, stable fluxon vortices are generated in the Josephson junction. For example, for $h_B=1.4$, $\gamma=0$ and $\sigma=0.07$, the Josephson junction contains, in addition to the M distribution, the multifluxon vortices Φ^n, $n=1,2,3,4$, graphs of which are shown in Fig. 2. The number of vortices is determined by the value of the total magnetic flux[5] in the Josephson junction:

$$\Delta\varphi=\varphi(l)-\varphi(0).$$

For an ''infinite'' junction (for $l\to\infty$) the value $\Delta\varphi/2\pi\to k$, where $k=0,1,2,\ldots$ is the number of vortices (fluxons) in the distribution $\varphi(x)$. For the solution in Fig. 2 we have, respectively, $\Delta\varphi(\Phi^1)/2\pi\approx1.49$, $\Delta\varphi(\Phi^2)/2\pi\approx2.48$, $\Delta\varphi(\Phi^3)/2\pi\approx3.45$, and $\Delta\varphi(\Phi^4)/2\pi\approx4.36$, while for the Meissner solution $\Delta\varphi(M)/2\pi\approx0.49$.

The influence of the external magnetic field h_B on the magnetic flux distribution $\varphi'(x)$ in the junction for the main fluxon Φ^1 at $\sigma=0.07$ is demonstrated in Fig. 3. At a certain value $h_B=h_m$ the maximum of the derivative $\varphi'(x)$ is localized in the middle of the junction (curve *2*, $h_B\approx1.273$). For $h_B<h_m$ the fluxon is ''expelled'' to the end $x=l$ by the ''geometric'' current $g(x)$ (curve *1*, $h_B=1$). For $h_B>h_m$ the fluxon is shifted by the external field toward the end $x=0$ (curve *3*, $h_B=1.4$).

If the length of the Josephson junction is sufficiently large, then a change of the current γ, equivalent to a change

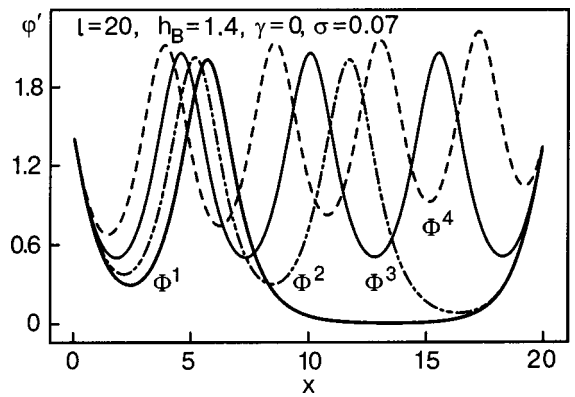

FIG. 2. Fluxon vortices in a Josephson junction.

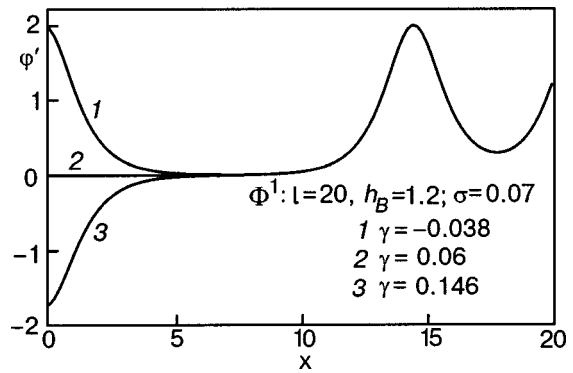

FIG. 4. The $\varphi'(x)$ curve for $\sigma=0.07$.

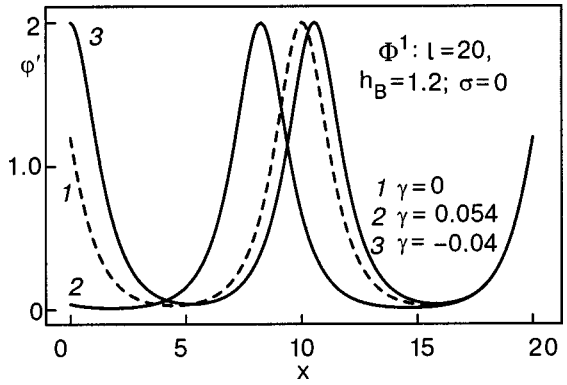

FIG. 5. The $\varphi'(x)$ curve for $\sigma=0$.

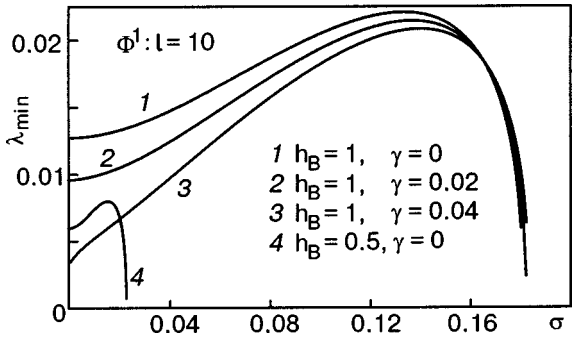

FIG. 7. Bifurcation upon a change in σ.

in magnetic field at the left end $x=0$, turns out to have only a slight influence on the local maximum magnetic field in the junction, as is well demonstrated by Fig. 4. For comparison, the situation in which the shape factor $\sigma=0$ is demonstrated in Fig. 5 for the same values of the remaining parameters. It is seen that variations of the current γ cause the maximum of the magnetic field to shift to the right or left of the center of the Josephson junction, depending on the direction of the current.[17]

For values $h_B>h_m$ the scheme x_m of the maximum of the field $\varphi'(x)$ of the fluxon Φ^1 is shifted to the left from the center $x=l/2$ toward the $x=0$ end (see Fig. 3). The "motion" of the maximum of the function $\varphi'(x)$ upon variations of the parameters of the problem occurs in accordance with the equation

$$\sin\varphi(x_m,p)+\sigma[\varphi'(x_m,p)-h_B]=0,$$

which expresses the balance of the Josephson and "geometric" currents at the point x_m. Here for the Φ^1 distribution the coordinate $x_m=l/2$ for $\sigma=0$, $\gamma=0$, and any attainable h_B. This case corresponds to the dashed line in Fig. 6, which shows graphs of the function $x_m(h_B,\sigma)$ for several values of the shape parameter σ. Each curve for $\sigma>0$ intersects the straight line $x_m(h_B,0)=l/2$ at a certain point $h_m(\sigma)=\varphi'(l/2,\sigma)$ at which the maximum magnetic field inside the Josephson junction is centered. It is important to note that for $\sigma>0$ the $x_m(h_B)$ curves change sharply in the vicinity of h_m: slight deviations of the external field h_B from the value h_m cause a significant displacement of the field maximum from the center of the junction.

Let us consider the influence of two geometric parameters of the model, viz., the shape parameter σ and length l, on the magnetic flux distribution in the Josephson junction.

The dependence of the smallest eigenvalue of the SL problem for the main fluxon Φ^1 on the shape parameter σ is shown in Fig. 7. It is seen that for fixed h_B and γ there exists a certain maximum value of σ above which the distribution of Φ^1 loses stability, i.e., a bifurcation of the vortex occurs upon a change in σ. Large values of the magnetic field h_B correspond to large critical values of σ. The value of the current is important at small values of σ and plays practically no role at values of σ close to the maximum. Figure 7 thereby demonstrates the destructive character of the shape parameter at large values of it and also the stabilizing role of the boundary magnetic field h_B.

The influence of the length l of the Josephson junction on the stability of the main fluxon Φ^1 is shown in Fig. 8. It is seen that $\lambda_{\min}(l)\approx$const at $l>12$, and therefore to a certain accuracy the Josephson junction can be considered "infinite" for Φ^1. At $l<6$ the smallest eigenvalue of the SL problem (6) falls rapidly, going to zero at $l\approx5.23$. Thus there exists a minimum length of the junction for which the fluxon Φ^1 maintains stability.[18] The minimum length clearly depends on all the remaining parameters of the model—the external magnetic field h_B, the external injection current γ, and also the shape parameter σ. An analogous statement is also valid for multifluxon distributions of the magnetic flux in the junction, including unstable ones. The minimum length for mul-

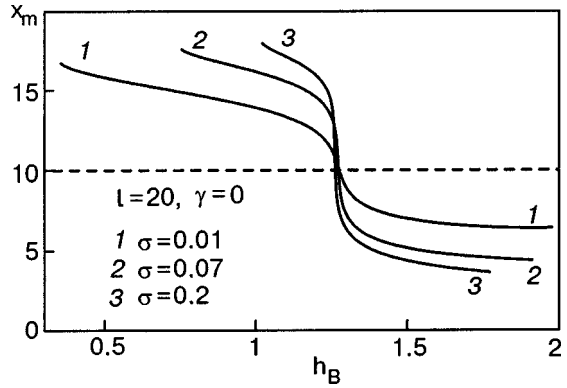

FIG. 6. "Movement" of the maximum of the magnetic field in a Josephson junction upon a change in h_B.

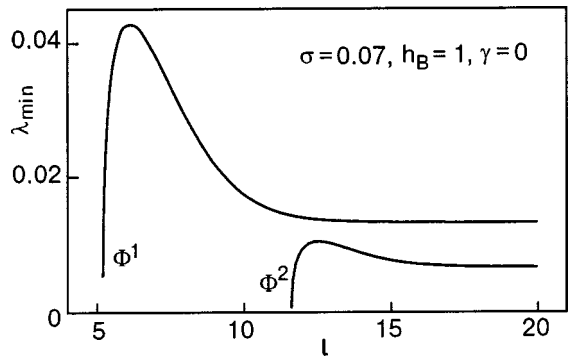

FIG. 8. Influence of the length of the Josephson junction on the stability of Φ^1 and Φ^2.

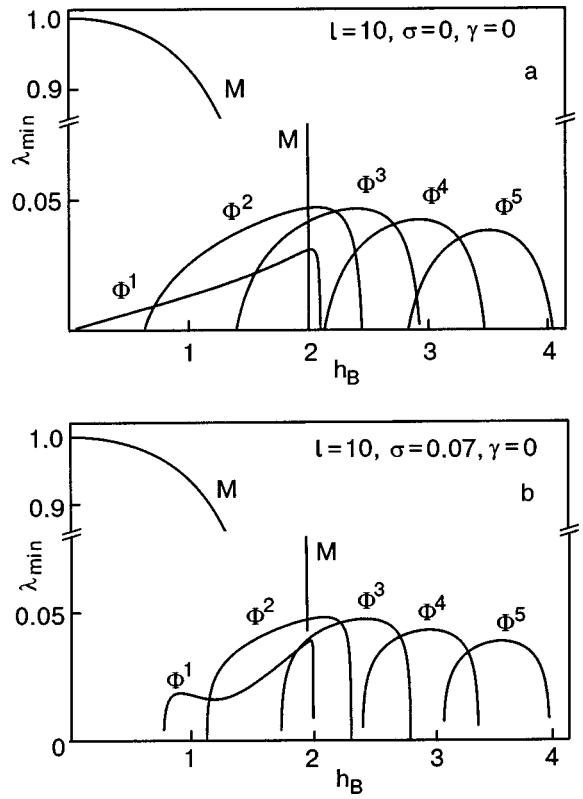

FIG. 9. The $\lambda_{min}(h_B)$ curves for different σ.

tifluxon distributions Φ^n falls off rapidly with increasing index n. For example, at otherwise equal parameters the vortex Φ^2 exists in Josephson junctions with $l>11.64$ (see Fig. 8). Consequently, if $\sigma=0.07$, $h_B=1$, and $\gamma=0$, then at lengths $l<5.23$ the junction is in all respects short, and the only stable distribution in the junction is the Meissner one. For $5.23<l<11.64$ the junction is short for Φ^2, but a nontrivial stable vortex Φ^1 can exist in it.

Let us now consider the question of constructing by numerical means the critical current versus magnetic field relation, which is determined implicitly by Eq. (8) for each magnetic flux distribution in the Josephson junction. The importance of this problem stems from the possibility of measuring this relation experimentally.[3,5,7–10] We note that for different configurations of the magnetic flux in the Josephson junction the values of the critical parameters—in particular, the critical current and magnetic field—can be substantially different. One should therefore identify the critical parameters for specific distributions and for the Josephson junction as a whole.

The curves of $\lambda_{min}(h_B)$ for the M distribution and the first few stable vortices in a Josephson junction at current $\gamma=0$ and $\sigma=0$ are demonstrated in Fig. 9a. For comparison the analogous curves for $\sigma=0.07$ are shown in Fig. 9b. Each curve has two zeroes, the distance between which determines the stability region of the vortex upon variation of the magnetic field h_B. The zeroes themselves are critical values of the field h_B at zero current γ.

It is well seen that the role of the shape parameter σ is most important at small values of h_B. In particular, the Φ^1 vortex at $\sigma=0$ exists already at $h_B\approx0.054$. At $\sigma=0.07$, however, the existence region in respect to field h_B is considerably compressed, and the vortex exists starting at $h_B>0.75$. The amount of compression of the $\lambda_{min}(h_B)$ curves for different vortices decreases rapidly with increasing h_B.

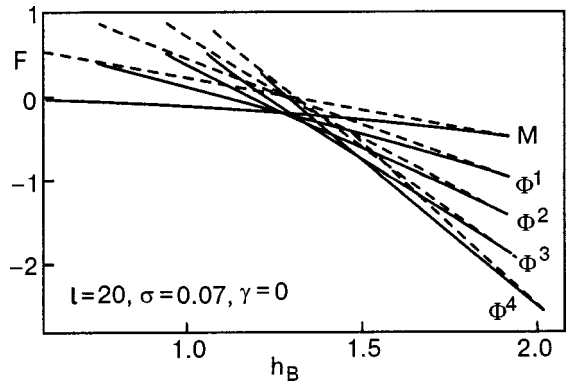

FIG. 10. The $F(h_B)$ curves for $\sigma=0.07$.

To complete the picture, Fig. 10 shows graphs of the total energy of several magnetic flux distributions in the Josephson junction

$$F(p)=\int_0^l\left[\frac{1}{2}\varphi'^2+(1-\cos\varphi)\right]dx-h_B\Delta\varphi-l\gamma\varphi(0) \tag{10}$$

as a function of the external magnetic field h_B for $\sigma=0.07$ and current $\gamma=0$. The energy values are divided by the total energy $F[\Phi^1]=8$ of an isolated fluxon in an infinite Josephson junction.[5] The solid and dashed curves show the energy of the stable and unstable distributions, respectively. The points of tangency of the solid and dashed curves are the points at which the magnetic flux loses stability.

Let us now consider the situation for $\gamma\neq0$. To find the dependence of the critical current γ_c on the external magnetic field h_B it is necessary to determine the stability region with respect to current for the distributions M, Φ^1, Φ^2, etc. The results of such calculations for certain values of h_B are given in Figs. 11–13.

Figure 11 shows the $\lambda_{min}(\gamma)$ curves for stable solutions of the problem (3) in a field $h_B=1.6$. The distances between zeroes of the functions are the stability intervals of the corresponding distributions with respect to the current γ. The right and left zeroes of the function $\lambda_{min}(\gamma)$ are the positive and negative critical currents, respectively, of the distribution

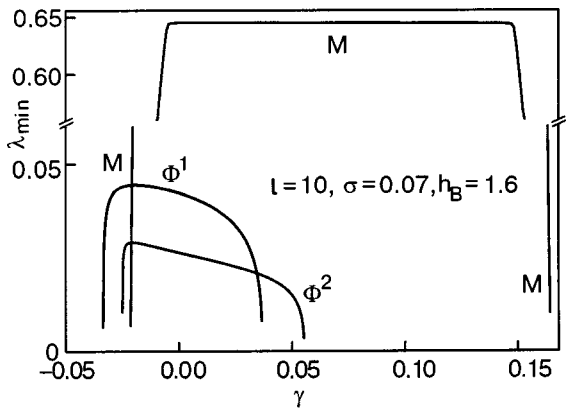

FIG. 11. The $\lambda_{min}(\gamma)$ curves for $h_B=1.6$.

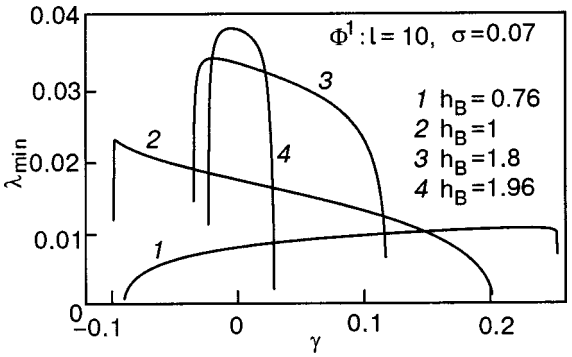

FIG. 12. The $\lambda_{\min}(\gamma)$ curves for Φ^1.

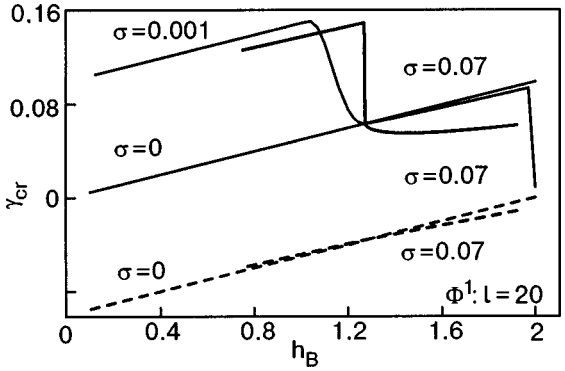

FIG. 14. The critical curve of the fluxon Φ^1.

in the given field h_B. Because of the asymmetry of the boundary conditions (3b) and (3c) for $\gamma>0$ the critical current of the Meissner distribution [which we denote by $\gamma_c(M)$] is the highest, but for $\gamma<0$ the largest in modulus is the critical current $\gamma_c(\Phi^1)$ of the vortex Φ^1. Consequently, in a field $h_B=1.6$ the positive critical current of the junction is $\gamma_c=\gamma_c(M)$, while the negative critical current is $\gamma_c=\gamma_c(\Phi^1)$.

We note that for the junction geometry under consideration the curve for the M distribution has a characteristic plateau—the "breakoff" of the Meissner solution sets in at a rather large modulus of the external current.

Figure 12 demonstrates the $\lambda_{\min}(\gamma)$ curves for the main fluxon Φ^1 at $\sigma=0.07$ and several values of h_B. The analogous curves for the Φ^2 distribution are shown in Fig. 13. We note that with increasing external magnetic field h_B the stability region of the vortices with respect to current is narrowed. Consequently, by varying h_B one can construct the bifurcation curves for individual vortices to acceptable accuracy and from them determine the critical values of the current γ_c for a Josephson junction.

A method of direct calculation of the bifurcation points of the vortices in a Josephson junction was proposed in Refs. 19 and 20.

Figure 14 shows the critical curves (8) for the main stable fluxon Φ^1 for values of the shape parameter $\sigma=0$, $\sigma=0.001$, and $\sigma=0.07$. The solid curves correspond to a current $\gamma>0$ and the dashed curves to $\gamma<0$. We note that at a value $h_B\approx1.273$ the critical curves corresponding to $\gamma>0$ intersect with each other and with the curve corresponding to $\sigma=0$ in some narrow region. This means that in that region of h_B the critical current depends only slightly on the shape of the junction. Geometrically the influence of σ reduces to a rotation of the critical curves clockwise about the curve for $\sigma=0$ by an angle that depends on σ. An analogous effect takes place for the critical curves corresponding to $\gamma<0$.

The critical curve $\gamma_c(h_B)$ for a junction is constructed as the envelope of the critical curves corresponding to different magnetic flux distributions in the junction. In other words, the critical curve consists of pieces of the critical curves for individual states with the largest moduli of the critical current at a given h_B. The part of the critical curve corresponding to the interval $h_B\in[0,2,8)$ is illustrated in Fig. 15. For example, let $h_B=1.4$. At a current $\gamma=0$ there are five different magnetic field distributions in the junction, which are described above (see Fig. 2). With increasing current γ in the direction of positive values the vortices lose stability in the following order:

$$\Phi^4\rightarrow\Phi^3\rightarrow\Phi^2\rightarrow\Phi^1\rightarrow M.$$

The last to break off is the Meissner distribution, the critical current of which, $\gamma_c(M)\approx0.156$, is the critical current of the junction at a fixed value of the external field. Consequently, the resistive regime in the junction at $h_B=1.4$ exists for $\gamma>0.156$.

If the current γ is increased from zero in the negative direction, then the breakoff of the distributions occurs in the opposite order: $M\rightarrow\Phi^1\rightarrow\Phi^2\rightarrow\Phi^3\rightarrow\Phi^4$, and the critical current for the junction will be that of the vortex Φ^4: $\gamma_c(\Phi^4)\approx-0.039$.

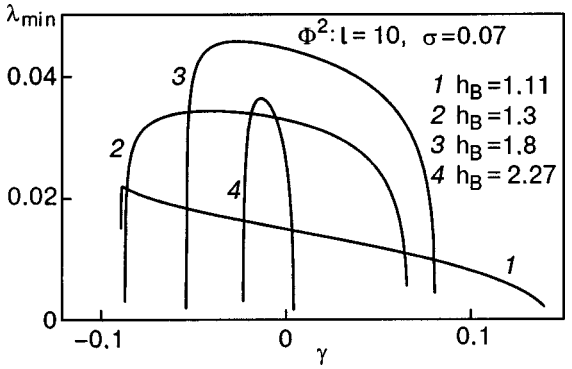

FIG. 13. The $\lambda_{\min}(\gamma)$ curves for Φ^2.

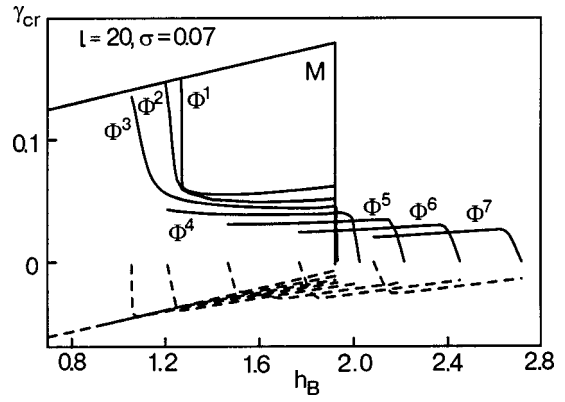

FIG. 15. The critical curve of the junction.

Analogously, for example, at $h_B=2.1$ the positive critical current for the junction is that of the vortex Φ^5, $\gamma_c(\Phi^5)\approx 0.034$, while the negative critical current is that of the vortex Φ^6, $\gamma_c(\Phi^6)\approx 0.024$, etc.

Of course, the ''switching'' of the vortices depends on all the remaining parameters of the problem. For example, for a junction with $l=10$ and $\sigma=0.07$ in an external field $h_B=1.6$ the order of breakoff is as follows: $\Phi^1\to\Phi^2\to M$ if $\gamma>0$, and $M\to\Phi^2\to\Phi^1$ if $\gamma<0$, as is clearly seen in Fig. 11.

We note that our numerically constructed critical curve of the Josephson junction (see Fig. 15) matches well with the theoretical and experimental results presented in Figs. 6a and 7a of Ref. 3.

3. CONCLUSION

We have carried out a numerical simulation of the magnetic flux distributions and their bifurcations upon variation of the model parameters in a long Josephson junction of exponentially varying width. For a stability analysis each distribution is placed in correspondence with a Sturm–Liouville problem with a potential determined by the given distribution. The distributions and, hence, the spectrum of the SL problem depend on the model parameters. It is shown that at certain critical (bifurcation) values of one or several parameters the magnetic flux in the junction can have a change of stability. For vortex configurations in a Josephson junction there are narrow regions of variation of the boundary magnetic field in which the critical current of the vortices depends only slightly on the shape parameter. Corresponding to the magnetic flux vortices are minimum lengths of the junction at which the distributions maintain their stability. The critical current versus magnetic field curves were constructed by a numerical method for the first few stable magnetic field flux distributions in a Josephson junction. The critical curve for the junction as a whole is the envelope of the critical curves of the individual distributions.

The authors thank Yu. A. Kolesnichenko (FTINT, Kharkov) for helpful discussions.

[a)]E-mail: elis@jinr.ru
[b)]E-mail: todorlb@jinr.ru
[c)]E-mail: shukrinv@thsun1.jinr.ru

[1] A. T. Filippov, T. Boyadjiev, Yu. S. Gal'pern, and I. V. Puzynin, Comm. JINR E17-89-106, Dubna (1989).
[2] A. Benabdallah, J. G. Caputo, and A. C. Scott, Phys. Rev. B **54**, 16139 (1996).
[3] G. Carapella, N. Martucciello, and G. Costabile, cond-mat/0203055.
[4] K. K. Licharev, *Dynamics of Josephson Junctions and Circuits*, Gordon and Breach, New York (1986).
[5] Yu. S. Gal'pern and A. T. Filippov, Zh. Éksp. Teor. Fiz. **86**, 1527 (1984) [Sov. Phys. JETP **59**, 894 (1984)].
[6] B. M. Levitan and I. S. Sargsyan, *Sturm–Liouville and Dirac Operators* [in Russian], Nauka, Moscow (1988).
[7] Jhy-Jiun Chang and C. H. Ho, Appl. Phys. Lett. **45**, 192 (1984).
[8] A. N. Vystavkin, Yu. F. Drachevskii, V. P. Koshelets, and I. L. Serpuchenko, Fiz. Nizk. Temp. **14**, 646 (1988) [Sov. J. Low Temp. Phys. **14**, 357 (1988)].
[9] B. H. Larsen, J. Mygind, and A. V. Ustinov, Phys. Lett. A **193**, 359 (1994).
[10] B. H. Larsen, J. Mygind, and A. V. Ustinov, Physica B **194–196**, 1729 (1994).
[11] M. A. Krasnosel'skiĭ, Usp. Matem. Nauk **IX**, vyp. 3(61), 57 (1954).
[12] J. B. Keller and S. Antman (ed.), *Bifurcation Theory and Nonlinear Eigenvalue Problems*, Benjamin, Reading, Mass. (1969), Mir, Moscow (1974).
[13] C. S. Owen and D. J. Scalapino, Phys. Rev. **164(2)**, 538 (1967).
[14] E. P. Zhidkov, G. I. Makarenko, and I. V. Puzynin, Fiz. Élem. Chastits At. Yadra **4**, 127 (1979) [Sov. J. Part. Nucl. **4**, 53 (1979)].
[15] I. V. Puzynin, I. V. Amirkhanov, E. V. Zemlyanaya, V. N. Pervushin, T. P. Puzynina, T. A. Strizh, and V. D. Lakhno, Fiz. Élem. Chastits At. Yadra **30**, 97 (1999) [Phys. Part. Nucl. **30**, 87 (1999)].
[16] T. L. Boyadzhiev, Soobshchenie OIYaI R2-2002-101, Dubna (2002).
[17] T. L. Boyadzhiev, D. V. Pavlov, and I. V. Puzynin, Soobshchenie OIYaI R11-88-409, Dubna (1988).
[18] T. L. Boyadzhiev, D. V. Pavlov, and I. V. Puzynin, in *Numerical Methods and Applications*, Proc. Int. Conf. Num. Math. and Appl., Bl. Sendov, R. Lazarov, and I. Dimov (eds.), Sofia, August 22–27, 1988.
[19] D. W. McLaughlin and A. C. Scott, Phys. Rev. A **18**, 1652 (1978).
[20] T. Boyadjiev and M. Todorov, Supercond. Sci. Technol. **14**, 1 (2002)

Translated by Steve Torstveit

LOW-TEMPERATURE MAGNETISM

Magnetic and transport properties of $La_{0.7}Sr_{0.3}MnO_3/Pr_{0.65}Ca_{0.35}MnO_3$ multilayered films with different microstructure

V. G. Prokhorov,* V. S. Flis, and G. G. Kaminsky

Institute of Metal Physics, National Academy of Sciences of Ukraine 36 Vernadskogo Ave., Kiev, 03142, Ukraine

Y. P. Lee

Quantum Photonic Science Research Center and Department of Physics, Hanyang University, Seoul, 133-791 Korea

(Submitted October 29, 2003; revised December 19, 2003)
Fiz. Nizk. Temp. **30**, 619–625 (June 2004)

The magnetic and transport properties of single-crystal and polycrystalline $La_{0.7}Sr_{0.3}MnO_3/Pr_{0.65}Ca_{0.35}MnO_3$ multilayered films are investigated in the temperature range 4.2–300 K. It is shown that the transformation from an incoherent to a coherent interface between layers leads to an enhancement of the ferromagnetic coupling, which is accompanied by a modification in the temperature dependence of the resistance and by a grown negative magnetoresistance ratio at room temperature. The influence of grain boundaries on the transport of carriers in the multilayered films is discussed on the basis of modern theoretical approaches. © *2004 American Institute of Physics.* [DOI: 10.1063/1.1768337]

The hole-doped perovskite manganites, $R_{1-x}A_xMnO_3$ (R=rare-earth cation, A=alkali or alkaline-earth cation), have attracted considerable attention due to not only their interesting fundamental science, partly connected with the discovery of colossal magnetoresistance (CMR), but their potential for device applications.[1,2] Most of the early theoretical works on manganites focused on the relation between the transport and magnetic properties and explained the coexistence of ferromagnetism and metallic behavior within the framework of a ''double exchange'' (DE) model, which considers the magnetic coupling between Mn^{3+} and Mn^{4+} that results from the motion of an electron between two partially filled d shells with strong on-site Hund's coupling.[3–5] In spite of considerable scientific efforts, however, the complex interplay between the charge, lattice, spin, and orbital degrees of freedom in these systems is not completely understood. The situation is further complicated by the fact that the magnetic and transport properties depend significantly on the cation size, the lattice strain, and the microstructure. Recently it was found that the presence of grain boundaries (GBs) in the polycrystalline manganites leads to a large MR effect over a wide temperature range below the Curie temperature T_C, whereas the CMR in the single-crystal materials is restricted to a narrower temperature range just around T_C.[6–8]

The most widely different manganite compounds were chosen for fabrication of the multilayer structure in this work: $Pr_{0.65}Ca_{0.35}MnO_3$ (PCMO) and $La_{0.7}Sr_{0.3}MnO_3$ (LSMO). The first of them remains insulator in both the paramagnetic and ferromagnetic states[9] (or displays an incomplete metal-insulator (MI) transition in the lattice-strained state[10]), and the second one shows a metal-like behavior of electrical resistance in the whole temperature range.[11] In spite of the fact that the T_C of LSMO exceeds room temperature, this compound manifests insignificant changes in resistance in applied magnetic fields owing to a small value of the intrinsic resistivity in the metallic state. It can be expected that the presence of high-resistance PCMO layers can lead to enhancement of the magnetoresistance effect in the PCMO/LSMO multilayered films. Recently it was reported that the substitution of the small-size Pr ion by La in the compound $Pr_{0.67}Ca_{0.33}MnO_3$ leads to the appearance of a MI transition at low temperature owing to the melting of a charge-ordered insulating state.[12] On the other hand, the substitution of Sr for Ca in $Pr_{0.7}Ca_{0.3-x}Sr_xMnO_3$ induces the formation of a low-temperature metallic state, as well.[13]

In this paper we report experimental results concerning the magnetic and transport properties of $Pr_{0.65}Ca_{0.35}MnO_3/La_{0.7}Sr_{0.3}MnO_3$ (PCMO/LSMO) multilayered (ML) films prepared by laser ablation on single-crystal $LaAlO_3$ (SC) and polycrystalline Al_2O_3 (PC) substrates at two different temperatures, $T_{sub}=560$ and 710 °C. The low substrate temperatures T_{sub} were used for preparation of the ML films to avoid chemical interaction between layers. In the first case, high-textured ML films (which will be denoted by SC) were fabricated with a coherent and an incoherent interface between layers, which was controlled by T_{sub}. In the second case, polycrystalline ML films were obtained. It was shown that the transformation from an incoherent to a coherent interface between layers leads to enhancement of the ferromagnetic coupling in the SCML films. This process is accompanied by a modification of the temperature dependence of the resistance from $R \propto T^3$ to $\propto T^{4.5}$ and has been attributed to transition from one- to two-magnon-electron

scattering. The PCML films demonstrate the $R \propto T^2$ behavior, which is explained by the interference between the elastic electron scattering on GBs and the electron-magnon scattering. The exponential growth of resistance at low temperature, $R(T) \propto \exp\sqrt{E_C/T}$, has its origin in a small Coulomb barrier which formed on the GBs. The MR ratio of the PCML films is dominated by a spin-polarized tunneling between grains. It was shown that the model of two parallel resistances can be used for a simulation of the transport properties in the ML films.

1. EXPERIMENTAL DETAILS

A pulsed-laser-deposition method was employed for the preparation of the films. We used two Nd-YAG lasers with a wavelength of 1064 nm, a pulse duration of 7.8–10.5 ns, and an energy of 0.3 J/pulse. The film deposition was carried out at a pulse repetition rate of 20 Hz. The power density of a laser beam focused on the target was $9.5\times10^8-2\times10^{10}$W/cm^2. The targets were fabricated from $Pr_{0.65}Ca_{0.35}MnO_3$ and $La_{0.7}Sr_{0.3}MnO_3$ powders of the stoichiometric composition by hot-pressing and heating at 1200 °C for 4 days in air. The oxygen pressure in chamber was 200 Torr during deposition and 600 Torr during cooling. Under these conditions we grew the ML films on $LaAlO_3$(100) single-crystal and Al_2O_3 polycrystalline substrates at different temperatures, $T_{sub}=560$ °C and 710 °C. The ML films contain six LSMO and five PCMO layers with LSMO at the top and the bottom. The thickness of each layer was $\simeq$20 nm.

The θ–2θ x-ray diffraction (XRD) patterns were obtained using a Rigaku diffractometer with Cu$K_{\alpha1}$ radiation. The lattice parameters evaluated directly from the XRD data were plotted against $\cos^2\theta/\sin\theta$. With an extrapolated straight line to $\cos^2\theta/\sin\theta=0$, a more precise determination of the lattice parameter was obtained. The resistance measurements were performed by using the standart four-probe method. The temperature dependence of the field-cooled (FC) and the zero-field-cooled (ZFC) in-plane magnetization at a magnetic field of 100 Oe was taken with a Quantum Design SQUID magnetometer.

2. RESULTS AND DISCUSSION

Structure

Figure 1a presents the θ–2θ XRD scans for two ML films deposited on $LaAlO_3$ at $T_{sub}=560$ °C (SCML1) and 710 °C (SCML2). SCML1 and SCML2 are multilayered films deposited on the single-crystal $LaAlO_3$ substrate at 560 °C and 710 °C, respectively. The high intensities of the (00l) peaks attest that the deposition results in highly c-oriented films. Figure 1b is the (002) Bragg peaks for the SCML1 (curve *1*) and SCML2 (curve *2*) films, respectively. It is seen that the decrease in T_{sub} leads to a shift of the Bragg peak towards a larger angle. In addition to the decrease in the out-of-plane lattice parameter, the SCML1 film displays a kink-like peculiarity in the (002) peak, which can be interpreted as the presence of different crystalline phases with the following out-of-plane lattice parameters: $c\simeq0.3877$ and 0.3848 nm. To show this more clearly, Fig. 1b includes a fitting to the split (002) peak by using two Lorentzian functions (dashed lines). The first lattice parameter is almost coincident with that for the bulk LSMO single crystal, $a_c=0.3876$ nm,[11] while the second one is similar to the average lattice parameter of the bulk PCMO compound, $\langle a_c\rangle\simeq0.3843$ nm,[14] for the cubic symmetry. The SCML2 film displays only the unsplit Bragg peak which corresponds to $c\simeq0.3903$ nm. Therefore, one can conclude that at a low T_{sub} the PCMO and the LSMO layers form an incoherent interface and have different lattice parameters close to those of the respective bulk materials. An increase in T_{sub} provides an enhancement of the epitaxial growth process and induces the formation of a coherent interface between layers in the SCML2 film. The ML films deposited on polycrystalline Al_2O_3 (PCML) exhibit the multipeak XRD patterns of very weak intensity, which are beyond an analysis.

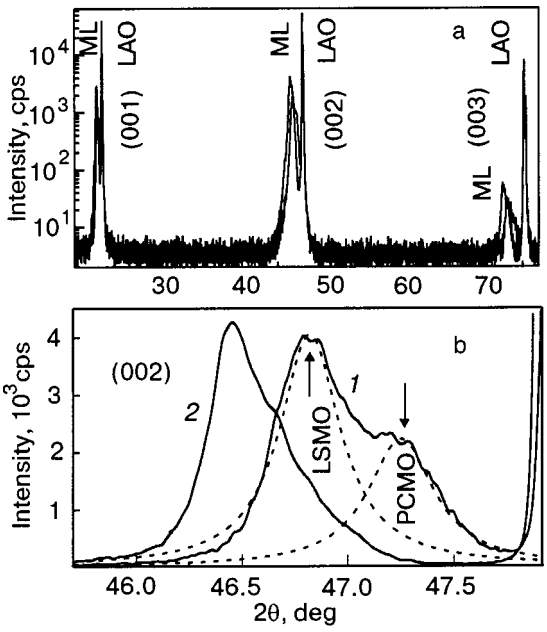

FIG. 1. (a) XRD patterns of the SCML films. LAO and ML denote the diffraction peaks from the substrate and the film itself, respectively. (b) The (002) diffraction peaks for the SCML1 (*1*) and the SCML2 (*2*) films.

Magnetic properties

Figures 2a and 2b present the temperature dependence of the FC and ZFC magnetization, $M(T)$, for SCML1 (curve *1*) and SCML2 (curve *2*), and PCML1 (curve *1*) and PCML2 (curve *2*), respectively. PCML1 and PCML2 are the multilayered films deposited on the polycrystalline Al_2O_3 substrate at $T_{sub}=560$ °C and 710 °C, respectively. The SCML1 film (curve *1* in Fig. 2a) demonstrates an $M(T)$ dependence, which is typical for two-phase magnetic systems, and represents a superposition of two magnetic transitions for the PCMO layers at $T_{C2}\approx130$ K[10] and for the LSMO layers at $T_{C1}>300$ K.[15] Moreover, the absolute value of the magnetization at low temperatures is almost twice greater than that at $T>T_{C2}$. This is evidence for independent magnetic transitions in the six LSMO and five PCMO layers and for a lack of ferromagnetic coupling between them. We are claiming that the main reason for a suppression of the magnetic coupling between layers in this film is the aforementioned incoherence of their interfaces. The increase of T_{sub} leads to con-

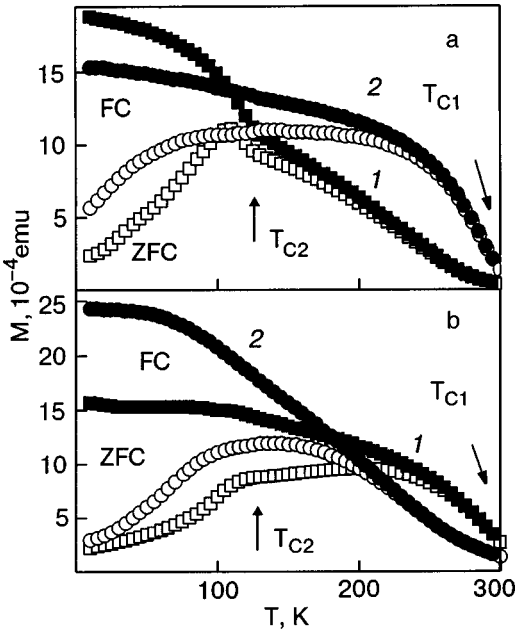

FIG. 2. (a) Temperature dependence of FC (solid) and ZFC (open) magnetization for the SCML1 (*1*) and the SCML2 (*2*) films. (b) The same for the PCLM1 (*1*) and the PCML2 (*2*) films.

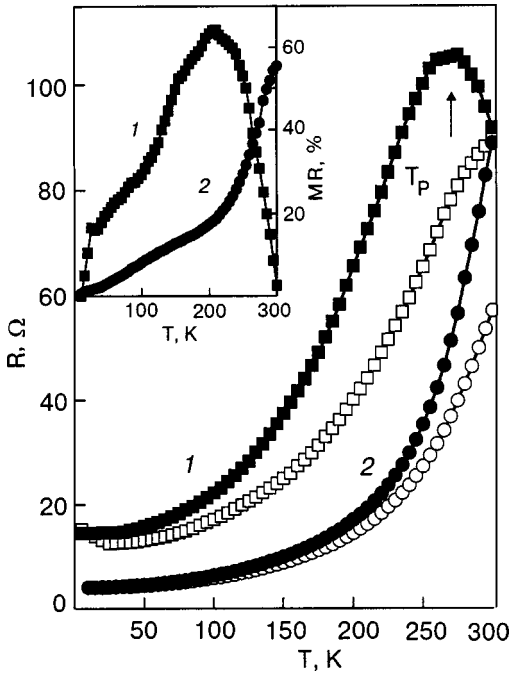

FIG. 3. Temperature-dependent resistance of the SCML1 (*1*) and SCML2 (*2*) films, measured in a magnetic field of zero (solid) and 5 T (open). The inset displays the MR ratio in a perpendicular magnetic field of 5 T. The solid lines are drawn to guide the eye.

version to a coherent interface and thus to the appearance of a ferromagnetic coupling between the two kinds of layers. The SCML2 film displays a monotonic $M(T)$ dependence (curve *2* in Fig. 2a) without any peculiarity at T_{C2} which is relevant to the magnetic transition for the PCMO layers. Figure 2b shows that a similar transformation in the magnetic state governed by the substrate temperature is also typical for the PCML films. The PCML1 film manifests a kink-like peculiarity at T_{C2} on both FC and ZFC $M(T)$ curves (curve *1* in Fig. 2b), although the magnitude is much smaller than that observed for the SCML1 film. The increase of T_{sub} leads to a degradation of the peculiarity (curve *2* in Fig. 2b). A similar ferromagnetic coupling was observed recently in $La_{0.55}Sr_{0.45}MnO_3/La_{0.9}Sr_{0.1}MnO_3(La_{0.67}Ca_{0.33}MnO_3)$ multilayered films prepared at a high substrate temperature.[16]

Therefore, one can conclude that the ferromagnetic coupling between layers in multilayered films is controlled by the coherence ratio of their interfaces.

Transport properties

Figure 3 shows the temperature dependence of the resistance $R(T)$ for the SCML1 (curve *1*) and the SCML2 (curve *2*) films in the absence (solid symbols) and in the presence (open symbols) of an applied magnetic field of 5 T. The magnetic field was parallel to the film surface and normal to the transport current. The change in the magnetic field direction does not transform the $R(T)$ behavior. The experimental curves testify that the resistance peak T_P in the investigated temperature range is observed only for the SCML1 film (curve *1*). A similar temperature behavior of resistance was observed recently for $La_{2/3}Ca_{1/3}MnO_3/Pr_{2/3}Ca_{1/3}MnO_3$ multilayered films with a sublayer thickness of 10 nm, but at a lower temperature.[17] The SCML2 film (curve *2*) demonstrates a metallic-like behavior of $R(T)$ in the whole investigated temperature range. The inset in Fig. 3 shows the temperature dependence of the magnetoresistance ratio. The MR value is defined by $100\% \times [R(0)-R(H)]/R(0)$, where $R(0)$ and $R(H)$ are the resistance with and without a magnetic field of 5 T, respectively. It is seen that for SCML1 (curve *1*) MR(T) displays nonmonotonic dependence with a peak at $T \simeq 200$ K, while MR(T) for SCML2 increases monotonically with temperature and reaches almost 60% at room temperature, which is much greater than that ever observed for the bare LSMO film.[18]

Figure 4 displays the temperature dependence of the resistance for the PCML1 (curve *1*) and the PCML2 (curve *2*) films without (solid symbols) and with (open symbols) an applied magnetic field of 5 T. It is seen that the $R(T)$ behavior of the PCML films differs significantly from that of the SCML films. The inset in Fig. 4 shows that in contrast to the single-crystal ML films, the MR value for the PCML films is minimum at room temperature and increases with decreasing temperature.

Single-crystal multilayered films. First of all, let us consider the $R(T)$ behavior of SCML films. Figure 3 (curve *1*) shows that the MI transition in the SCML1 film ($T_P \simeq 260$ K) occurs at a temperature below the Curie point ($T_C \gtrsim 300$ K). As a rule, the temperature difference between the magnetic and electronic transitions in CMR compounds is explained by an intrinsic inhomogeneity of these materials and by a percolative nature of the conductivity.[19] On the other hand, a more simplified explanation can be employed in our case. Recently the two parallel resistor model was used for description of the transport properties of bi- and trilayer $La_{0.55}Sr_{0.45}MnO_3/La_{0.67}Sr_{0.33}MnO_3$ films.[20] The equivalent resistance for the SCML film can be described by $R^{-1}(T)=R^{-1}_{\text{PCMO}}(T)+R^{-1}_{\text{LSMO}}(T)$, where $R_{\text{PCMO}}(T)$ and $R_{\text{LSMO}}(T)$ are the total resistances of the PCMO and the LSMO layers, respectively. Therefore, the resistance of the

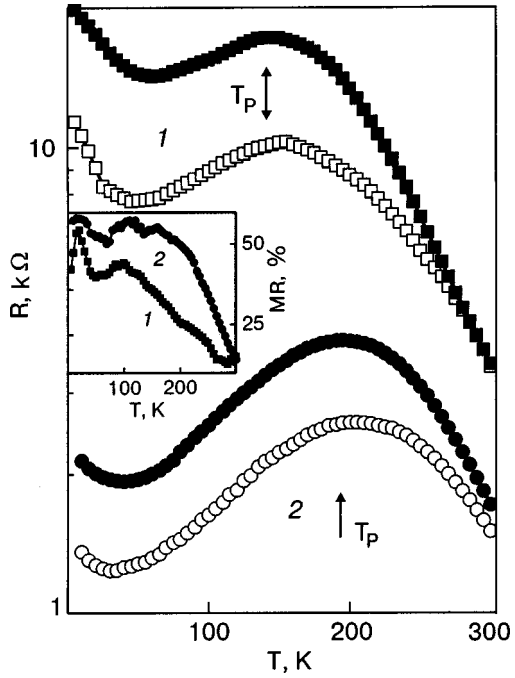

FIG. 4. Temperature-dependent resistance of the PCML1 (*1*) and the PCML2 (*2*) films, measured in a magnetic field of zero (solid) and 5 T (open). The inset displays the MR ratio in a perpendicular magnetic field of 5 T. The solid lines are drawn to guide the eye.

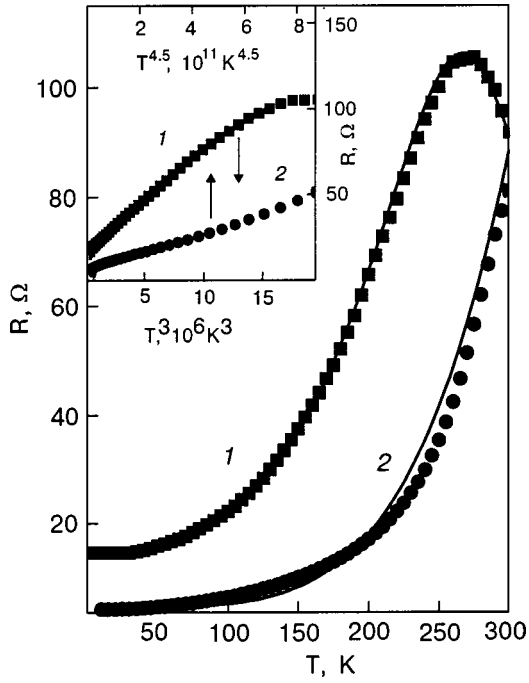

FIG. 5. The comparison of the experimental $R(T)$ data (solid symbols) with the theoretical simulation (solid lines) in the framework of the two-parallel resistance model for the SCML1 (*1*) and the SCML2 (*2*) films. The inset displays plots: R versus T^3 and R versus $T^{4.5}$ for the same films.

multilayered film is determined by the electron transport in PCMO at high temperature ($R_{\mathrm{PCMO}} \ll R_{\mathrm{LSMO}}$) or in LSMO at low temperature ($R_{\mathrm{LSMO}} \ll R_{\mathrm{PCMO}}$). The $R_{\mathrm{PCMO}}(T)$ behavior can be approximated by the usual Arrhenius form, which is typical for the bare PCMO films[10] and is provided by a polaron motion:[2,21] $R_{\mathrm{PCMO}}(T) = R_0 T \exp(T_A/T)$, where T_A is the activation energy in units of temperature. The $R_{\mathrm{LSMO}}(T)$ behavior can be obtained directly from the low-temperature part of the experimental $R(T)$ dependence. The inset in Fig. 5 shows that for the LSMO layers, $R_{\mathrm{LSMO}}(T) = R_1 + \alpha T^3$ for SCML1 and $R_{\mathrm{LSMO}}(T) = R_2 + \beta T^{4.5}$ for SCML2 with the following fitting parameters: $R_1 = 15\ \Omega$, $\alpha = 6.5 \times 10^{-6}\ \Omega \cdot \mathrm{K}^{-3}$, $R_2 = 4.5\ \Omega$, and $\beta = 6 \times 10^{-10}\ \Omega \cdot \mathrm{K}^{-4.5}$. According to theoretical models, the T^3 term in the resistance corresponds to the one-magnon-electron scattering,[22] while the $T^{4.5}$ term reflects the two-magnon-electron scattering processes.[23] Therefore, the electron-magnon scattering is dominant for the LSMO layers in the SCML films and transforms from one- to two-magnon scattering upon enhancement of the ferromagnetic coupling between layers. The solid lines in Fig. 5 display the theoretical $R(T)$ curves, which were calculated in the framework of the two parallel resistor model with the use of the previous fitting parameters for the LSMO layers, and $R_0 \simeq 10^{-3}\ \Omega \cdot \mathrm{K}^{-1}$ and $T_A = 2600$ K for the PCMO layers. It is seen that the theoretical curves agree excellently with the experimental data.

Polycrystalline multilayered films. Figure 4 shows that the $R(T)$ behavior for the PCML films is very different from that for the SCML ones, exhibiting a wide maximum at temperature well below T_C and a minimum at $T_{\min} \simeq 30-40$ K. The temperature dependence of the MR ratio is very close to that for ferromagnetic tunnel junctions.[24] The similar peculiarities in the transport properties are typical for the polycrystalline doped manganites and are explained by the presence of the grain boundaries.[2,8,25,26]

The GBs can play two roles in the mechanism of the transport of carriers—first as a network of magnetic tunnel junctions and second as additional centers for the elastic electron scattering in a metal-like channel of conductivity. First of all, let us consider the $R(T)$ behavior of the PCML films in the metal-like state ($T_{\min} \leqslant T < T_P$) and discuss the influence of GBs on the transport properties. Figure 6a shows that in this temperature range $R(T) \propto T^2$ for both of the polycrystalline multilayered films instead of T^3 and $T^{4.5}$, which were observed for the single-crystal films (see the inset in Fig. 5). Moreover, the applied magnetic field does not change the $R(T)$ behavior fundamentally but only decreases the slope of the curves slightly. In numerous publications the square term in the temperature-dependent resistance is explained by a dominant role of the electron-electron scattering. However, in our case this explanation is unusable. The insertion of GBs into the polycrystalline films leads to enhancement of only the impurity (elastic) contribution to the resistance, and all inelastic scattering processes must become weakly expressed in the temperature dependence of the resistance. We assume that the T^2 contribution to the resistance can be attributed to the interference between the elastic electron scattering on GBs and the electron-magnon scattering, similar to what has been observed in disordered metal films with dominance of the electron-phonon scattering.[27]

Figure 6b displays the $\ln(R)$ versus $T^{-1/2}$ plot for both PCML films. This plot exhibits a linear dependence up to $T_{\min}$ and manifests exponential growth of the resistance at low temperature, which is described by the expression $R(T) \propto \exp\sqrt{\Delta/T}$. It is noteworthy that a similar expression with $\Delta \propto E_C$, where E_C is the charging energy, has been pre-

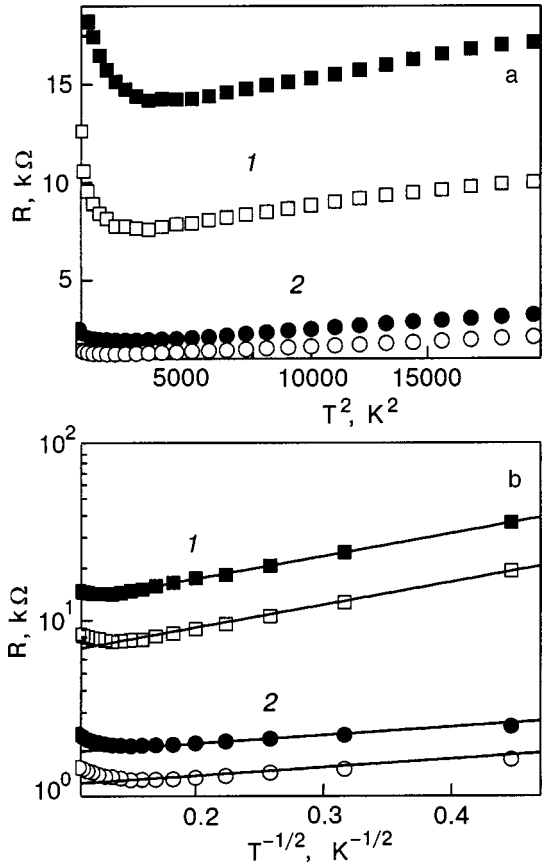

FIG. 6. The R versus T^2 (a) and $\ln(R)$ versus $T^{-1/2}$ (b) plots for the PCML1 (*1*) and the PCML2 (*2*) films, respectively.

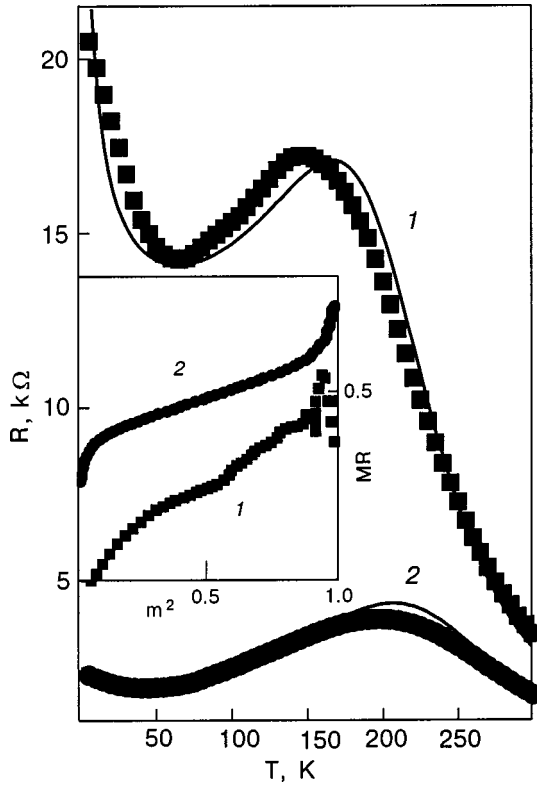

FIG. 7. The comparison of the experimental $R(T)$ data (solid symbols) with the theoretical simulation (solid lines) in the framework of the two parallel resistance model for the PCML1 (*1*) and the PCML2 (*2*) films, respectively. The inset displays the dependence of the MR ratio on the square of the normalized magnetization for these films.

dicted for conductivity in granular metals[28] and used for the explanation of the low-temperature $R(T)$ behavior in ceramic $La_{2/3}Sr_{1/3}MnO_3$ manganite with different grain size.[25] The value of the charging energy estimated from the slope of the $\ln(R)$ versus $T^{-1/2}$ plot was $E_C \simeq 20$ K and $\simeq 2.46$ K for the PCML1 and PCML2 films, respectively. Our results are very close to those obtained for ceramic samples,[25] and the observed difference in E_C value for different PCML films can be explained by the variation of the grain size. Indeed, the deposition of the manganite films at a low substrate temperature leads, as a rule, to the formation of a fine-grain structure, and an increase of T_{sub} stimulates grain growth. On the other hand, $E_C \propto e^2/d$, where e is the electronic charge and d is the grain size.[28] Therefore, the observed larger E_C value for the low-T_{sub} PCML film with respect to the high-T_{sub} one is an absolutely expected result.

Taking into account the peculiarities in $R(T)$ behavior which are governed by the existence of GBs, we will be again try to describe the temperature-dependent resistance of the PCML films on the basis of the parallel circuit model, only in this case the total resistance of the LSMO layers must involve the sum of $R_{LSMO}+R_{GBs}$. Figure 7 shows that in the framework of this approach the nonmonotonic $R(T)$ behavior can be described with satisfactory accuracy (solid lines in Fig. 7). We don't present here the fitting parameters used because of their multiplicity and the difficulty in interpretation of the physical meaning. However, the analysis carried out allows us to conclude that the observed peaks in $R(T)$ are not due to the GBs[8] but arise from the parallel-resistance circuit of the LSMO and PCMO layers.

The negative MR of the polycrystalline manganites is dominated by spin-polarized tunneling between grains owing to a nearly complete polarization of the electrons.[6] The simplified equation for the MR in the framework of the spin-polarized tunneling model[29,30] can be written as

$$\mathrm{MR} \simeq -\frac{JP}{4k_BT}[m^2(H,T)-m^2(0,T)],$$

where J is an intergrain exchange constant, P is the electron polarization, and m is the magnetization normalized to the saturation value. The inset in Fig. 7 shows the dependence of the MR versus m^2 plot, where $m=M(T)/M(0)$ and $M(T)$ is the FC magnetization of the PCML films presented in Fig. 4b. It is seen that the MR ratio is approximately $\propto m^2$ for both polycrystalline films. On the other hand, the temperature dependence of the MR ratio (see the inset in Fig. 3) is very far from that predicted by this model, $\mathrm{MR} \propto 1/T$. This disagreement can be eliminated by considering the temperature dependence of the spin polarization calculated within the framework of the DE approach (see Fig. 1 in Ref. 24).

3. CONCLUSIONS

Summarizing, we have studied the magnetic and transport properties of single-crystal and polycrystalline PCMO/LSMO multilayered films. It was shown that the single-crystal ML film with an incoherent interface between layers manifests the magnetic properties typical for a two-phase

magnetic system. The temperature-dependent resistance of this film in the ferromagnetic metallic state is proportional to T^3 and has been attributed to the one-magnon-electron scattering. The formation of a coherent interface between layers, owing to the enhancement of the epitaxial growth mode, gives rise to a ferromagnetic coupling between layers and to the dominance of a $T^{4.5}$ term in $R(T)$, which is typical for the two-magnon-electron scattering. The negative MR of the single-crystal ML films, which reaches almost 60% at room temperature in an applied magnetic field of 5 T, derives from the MI transition in the LSMO layer near the Curie temperature. The polycrystalline ML films demonstrate $R \propto T^2$ behavior, which is explained by the interference between the elastic electron scattering on GBs and the inelastic electron-magnon scattering. The enhancement of the resistance at low temperature, $R(T) \propto \exp\sqrt{E_C/T}$, has its origin in a small Coulomb barrier which forms on the GBs. The negative MR of the polycrystalline ML films is dominated by a spin-polarized tunneling between grains and can be described within the framework of the DE model. The model of two parallel resistances can be used for simulation of the transport properties in the ML films.

This work was supported by the KOSEF through the Quantum Photonic Science Research Center.

*E-mail: pvg@imp.kiev.ua

[1] Y. Tokura and Y. Tomioka, J. Magn. Magn. Mater. **200**, 1 (1999).
[2] A. P. Raminez, J. Phys. C **9**, 8171 (1997).
[3] C. Zener, Phys. Rev. **82**, 403 (1951).
[4] P. W. Anderson and H. Hasegawa, Phys. Rev. **100**, 675 (1955).
[5] P.-G. de Gennes, Phys. Rev. **118**, 141 (1960).
[6] H. Y. Hwang, S-W. Cheong, N. P. Ong, and B. Batlogg, Phys. Rev. Lett. **77**, 2041 (1996).
[7] A. Gupta, G. Q. Gong, G. Xiao, P. R. Duncombe, P. Lecoeur, P. Trouilloud, Y. Y. Wang, V. P. Dravid, and J. Z. Sun, Phys. Rev. B **54**, R15629 (1996).
[8] R. Gross, L. Alff, B. Büchner, B. H. Freitag, C. Höfener, J. Klein, Y. Lu, W. Mader, J. B. Philipp, M. S. R. Rao, P. Reutler, S. Ritter, S. Thienhaus, S. Uhlenbruck, and B. Wiedenhorst, J. Magn. Magn. Mater. **211**, 150 (2000).
[9] Y. Tomioka, A. Asamitsu, H. Kuwahara, Y. Morimoto, and Y. Tokura, Phys. Rev. B **53**, R1689 (1996).
[10] V. G. Prokhorov, G. G. Kaminsky, V. S. Flis, Y. P. Lee, K. W. Kim, and I. I. Kravchenko, Physica B **307**, 239 (2001).
[11] M. C. Martin, G. Shirane, Y. Endoh, K. Hirota, Y. Morimoto, and Y. Tokura, Phys. Rev. B **53**, 14285 (1996).
[12] T. Wu, S. B. Ogale, S. R. Shinde, Amian Biswas, T. Polletto, R. L. Greene, T. Venkatesan, and A. J. Millis, J. Appl. Phys. **93**, 5507 (2003).
[13] I. Medvedeva, A. Maignan, K. Bärner, Yu. Bersenev, A. Roev, and B. Reveau, Physica B **325**, 57 (2003).
[14] Z. Jirák, S. Krupička, Z. Šimša M. Dlouhá, and S. Vratislav, J. Magn. Magn. Mater. **53**, 153 (1985).
[15] F. Tsui, M. C. Smoak, T. K. Nath, and C. B. Eom, Appl. Phys. Lett. **76**, 2421 (2000).
[16] M. Sirena, N. Haberkom, M. Granada, L. B. Steren, and J. Guimpel, J. Appl. Phys. **93**, 7244 (2003).
[17] H. Li, J. R. Sun, and H. K. Wong, Appl. Phys. Lett. **80**, 628 (2002).
[18] Y. Sun, W. Tong, X. Xu, and Y. Zhang, Appl. Phys. Lett. **78**, 643 (2001).
[19] E. Dagotto, T. Hotta, and A. Moreo, Phys. Rep. **344**, 1 (2001).
[20] M. Sirena, N. Haberkom, L. B. Steren, and J. Guimpel, J. Appl. Phys. **93**, 6177 (2003).
[21] M. Imada, A. Fujimori, and Y. Tokura, Rev. Mod. Phys. **70**, 1039 (1998).
[22] N. Furukawa, Y. Shimomura, T. Akimoto, and Y. Moritomo, J. Magn. Magn. Mater. **226–230**, 782 (2001).
[23] K. Kubo and N. Ohata, J. Phys. Soc. Jpn. **33**, 21 (1972).
[24] H. Itoh, T. Ohsawa, and J. Inoue, Phys. Rev. Lett. **84**, 2501 (2000).
[25] Ll. Balcells, J. Fontcuberta, B. Martínez, and X. Obradors, Phys. Rev. B **58**, R14697 (1998).
[26] J. M. D. Coey, M. Viret, and S. von Molnar, Adv. Phys. **48**, 167 (1999).
[27] N. G. Ptisina, G. M. Chulkova, K. S. Il'in, A. V. Sergeev, F. S. Pochinkov, E. M. Gershenzon, and M. E. Gershenzon, Phys. Rev. B **56**, 10089 (1997).
[28] P. Sheng, B. Abeles, and Y. Arie, Phys. Rev. Lett. **31**, 44 (1973).
[29] J. I. Gittleman, Y. Goldstein, and S. Bozowski, Phys. Rev. B **5**, 3609 (1972).
[30] J. S. Helman and B. Abeles, Phys. Rev. Lett. **37**, 1429 (1976).

This article was published in English in the original Russian journal. Reproduced here with stylistic changes by AIP.

Composition dependence of the low-temperature magnetic ordering and the hyperfine interactions in Fe–N austenite

A. N. Timoshevskii* and B. Z. Yanchitsky

Institute of Mathematics, bul'v. Vernadskogo 36b, Kiev 03142, Ukraine

A. S. Bakai

National Science Center "Kharkov Institute of Physics and Technology," Akademicheskaya 1, Kharkov 61108, Ukraine

(Submitted December 1, 2003)
Fiz. Nizk. Temp. **30**, 626–638 (June 2004)

The electronic structure of two model structures of stoichiometry Fe_8N with different types of ordering of the nitrogen atoms are calculated using the *ab initio* FLAPW method. To first approximation these structures can be treated as a prototype of Fe–N austenite. The influence of the nitrogen atoms on the electronic structure and magnetic properties of γ iron and on the components of the Mössbauer spectrum is investigated, permitting a detailed interpretation of the experimental data. The dependence of the exchange integral on the concentration of nitrogen atoms is obtained, clarifying the influence of nitrogen on the magnetic properties of fcc iron. The effective interatomic interaction potentials of nitrogen atoms in fcc iron in six coordination spheres is calculated using the *ab initio* FLAPW method and the cluster expansion technique. The potentials thus obtained are used in a Monte Carlo investigation of the temperature dependence of the short-range order in the Fe–N system. The temperature dependence of the heat capacity and short-range order parameters is calculated. It is established that a transition from the disordered state to the nitride Fe_4N is observed at 830 K. © *2004 American Institute of Physics.* [DOI: 10.1063/1.1768351]

1. INTRODUCTION

The study of the influence of nitrogen on the atomic structure and physical properties of alloys based on iron with the face-centered cubic (fcc) lattice is a complex and topical problem. This is because nitrogenated austenitic steels are a promising class of construction materials, having good mechanical properties and high strength at low temperatures. Serious difficulties arise in solving this problem because the magnetic structure is not yet completely understood even for pure γ iron at low temperatures. As we know, the magnetic moment in $3d$ fcc metals and alloys need not be a continuously variable quantity of atomic size but can change in a jumplike manner at a certain critical volume, manifesting instability in the volume dependence.[1,2] Calculations of the total energy predict the existence of such instability in the Invar systems Fe–Ni and Fe–Pt and also in pure metals, e.g., fcc Mn and Fe and bcc Cr.[3–6] The states characterizing phases with volumes larger and smaller than the critical value are called the ''high-spin, high-volume state'' (HS) and ''high-spin, low-volume state'' (LS), respectively. As a rule, such states are separated in energy by several mRy. Experimentally the existence of such phases has been inferred from low-temperature Mössbauer measurements made under pressure for the Invar alloys Fe–Ni and Fe–Pt.[7] Remarkably, as was shown by calculations done for $T=0$, unlike the case of Invar Fe–Ni, where the ground state is a high-volume ferromagnetic (FM) state, in γ-Fe the ground state is a low-volume antiferromagnetic (AF) state, and the high-spin ferromagnetic state is energetically unfavorable.[8] The existence of an AF ground state and a high-spin FM state is confirmed by low-temperature Mössbauer experiments on inclusions of the γ-Fe phase in Cu and Cu–Al matrices[9] and on γ-Fe films grown on Cu_3Au.[10] Moreover, Mössbauer studies[11] and neutron-diffraction experiments[12] on inclusions of the γ-Fe phase in a Cu matrix have confirmed the presence of antiferromagnetic order with a Néel temperature $T_N=70$ K.

The introduction of interstitial impurity atoms in the γ-Fe leads to an increase in the unit cell volume, and, consequently, in this system one expects that transitions of the LS–HS type will be manifested. However, the situation is complicated by the fact that the electronic structure of the Fe–N system differs from that of pure iron with the same lattice parameter. Therefore it is of interest to study the microscopic nature of the influence of nitrogen on the electronic subsystem and its macroscopic manifestations in the form a change in structure of the Mössbauer spectra and a modification of the low-temperature magnetic states. Quantum calculations from first principles present unique opportunities for solving this problem. In this paper we report the results of such calculations.

2. CHOICE OF MODEL AND METHOD OF CALCULATION

The influence of the distribution of nitrogen atoms on the electronic structure and hyperfine interaction in austenitic Fe–N alloys was investigated by performing a series of calculations of the electronic structures and total energies of two types of crystal structures with different types of ordering of the nitrogen atoms (Fig. 1).

The first structure, $Fe_8N(A)$ (structure A in Fig. 1) contains two types of iron atoms: $Fe_{0,4}$ (with no nitrogen atoms

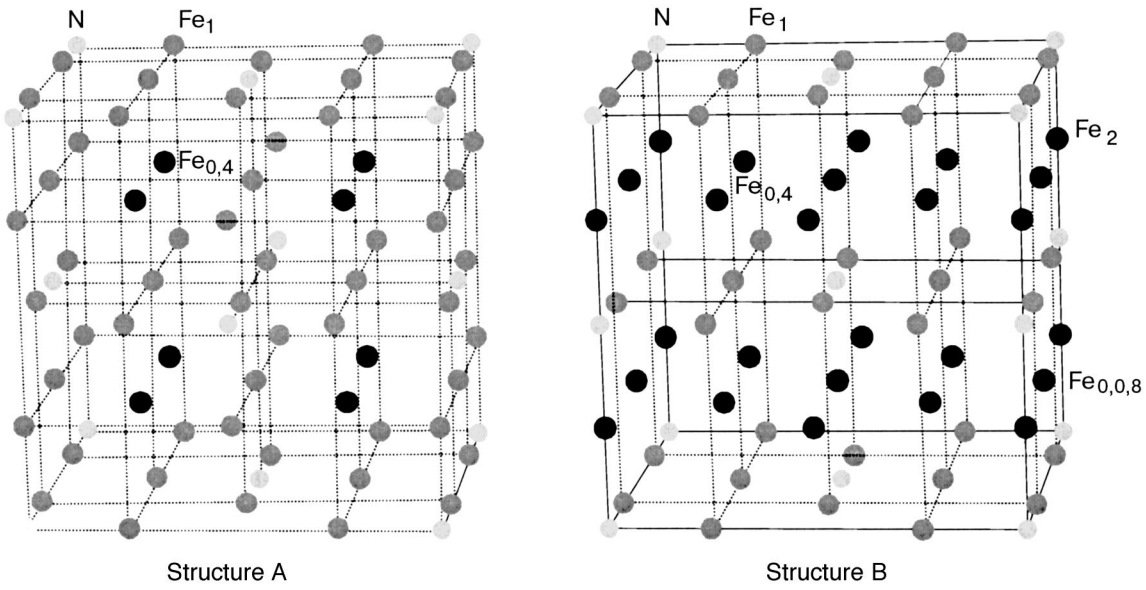

FIG. 1. Ordered structures with the stoichiometry Fe_8N with different distributions of the impurity atoms, modeling the alloy γ-Fe–N.

in the first coordination sphere and 4 of them in the second) and Fe_1 (with one nitrogen atom in the first coordination sphere); the second structure, $Fe_8N(B)$ (structure B in Fig. 1) has, in addition, an atom Fe_2, having two nearest-neighbor nitrogen atoms, and an atom $Fe_{0,0,8}$. Thus the second structure contains a chain of atoms $N–Fe_2–N$, a so-called ''dumbbell'' configuration of an iron atom and two nitrogen atoms. In the structure of type B the iron atoms $Fe_{0,4}$ and $Fe_{0,0,8}$ also have an asymmetric environment with respect to iron atoms. In the case when a real Fe–N alloy is well modeled by an Fe_8N structure the Mössbauer spectrum of the alloy should contain a contribution from the doublet lines of the nuclei of those atoms.

For calculation of the electronic structure we used the full-potential method FLAPW,[13] implemented in the WIEN97 software package.[14] The exchange-correction potential was calculated in the gradient approximation in accordance with the Perdew–Burke–Ernzerhof model.[15] The radii of the atomic spheres were chosen from the condition of tangency and equalled 1.9 and 1.6 a.u. for iron and nitrogen atoms, respectively ($R_{\min}=1.6$ a.u.). In the FLAPW method the accuracy of the results depends on the following main parameters: the number of K points in the Brillouin zone, the number of LM terms and Fourier coefficients in the expansion of the electron density and potential, and also the number of plane waves in the intersphere region. All these parameters were chosen from the condition of convergence of the results of the calculation. By checking for convergence, one can establish the value of the parameter $R_{\min}K_{\max}=8.4$, which corresponds to 190 plane waves per atom in the basis set ($K_{\max}$ is the largest modulus of the basis vector). Inside an atomic sphere the expansion of the wave function was done to $L_{\max}=12$, and the electron density and potential, in a basis of crystal harmonics up to $L_{\max}=6$. In the intersphere region those quantities were expanded in a Fourier series with a parameter $G_{\max}=12$ $Ry^{1/2}$. The calculation was done for 3000 K points in the Brillouin zone. The chosen parameters ensured an accuracy of 0.1 mRy in the calculation of the total energy. States of the iron atom of the $3s$ and $3p$ types were calculated as peninsular by introducing ''local orbitals'' for them.[16] An analogous procedure was used for the $2s$ states of nitrogen. The introduction of local orbitals increases the flexibility of the basis set and improves the accuracy and convergence of the results of calculations. All of the calculations were done in the spin-polarized approximation.

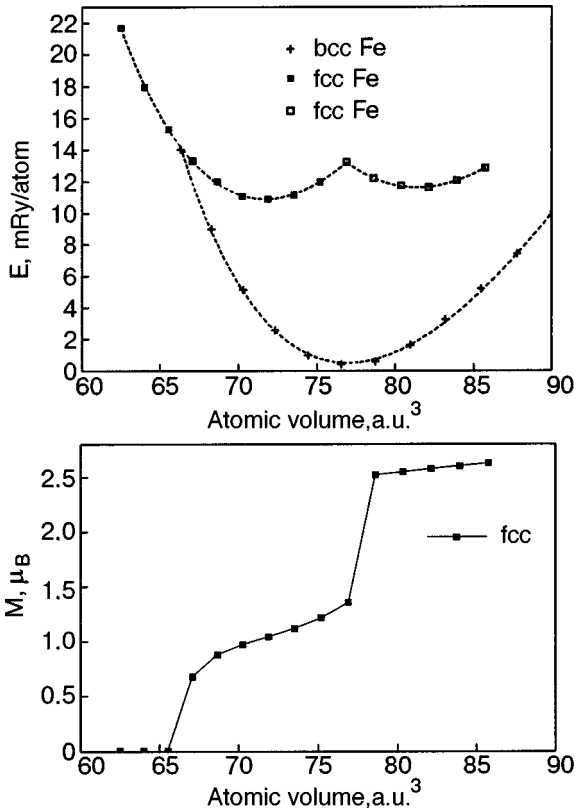

FIG. 2. Total energy E and magnetic moment M of an atom versus the unit cell volume for fcc and bcc iron in the ferromagnetic approximation.

TABLE I. Structural characteristics and magnetic moments of the Fe atoms in the structures $Fe_8N(A)$ and $Fe_8N(B)$.

Structure	Type of Fe atom	Magnetic moment, μ_B	Fe–N distance, a.u.	Lattice parameters, a.u.	Unit cell volume a.u.^{3}/Fe atom
Fe (fcc) LS	Fe	1.04 (0.75 [17,18])	–	a = 6.595 (6.731 [17,18])	71.72 (76.24 [17,18])
Fe (fcc) HS	Fe	2.56	–	a = 6.880 (6.980 [17,18])	81.40 (81.78 [17])
$Fe_8N(A)$ LS	$Fe_{0,4}$	2.38	5.89	a = 13.598	78.57
$Fm\bar{3}m$	Fe_1	0.18	3.45	$a=b=c$	
$Fe_8N(A)$ HS	$Fe_{0,4}$	2.75	6.03	a = 13.914	84.17
	Fe_1	2.08	3.53		
Fe_8N (B) LS	$Fe_{0,4}$	2.31	5.93	a = 13.279	
$P4/mmm$	$Fe_{0,0,8}$	−2.10	7.57	c = 14.518	80.00
	Fe_1	0.69	3.49	$a=b$	
	Fe_2	2.04	3.63		
Fe_8N (B) HS	$Fe_{0,4}$	2.80	6.07	a = 13.579	
	$Fe_{0,0,8}$	2.72	7.74	c = 14.847	85.55
	Fe_1	2.22	3.56		
	Fe_2	2.19	3.71		

3. ATOMIC STRUCTURE OF THE TWO PHASES IN THE SYSTEM γ-Fe–N

In the final step we calculated the dependence of the total energy and magnetic moments of the atoms on the unit cell volume in γ- and α-Fe in the ferromagnetic approximation. Figure 2 shows the results of those calculations. With increasing volume in fcc iron a distinct (first-order) transition from the state with low magnetic moment to the state with high magnetic moment. The results of the calculations are in good agreement with the data of Ref. 8, in which analogous calculations were done. In the ferromagnetic approximation the ground state of γ-Fe is the LS state. The results of the calculations of the lattice parameters and of the magnetic moments of the iron atoms in the two phases are presented in Table I. The theoretically calculated volume of the HS phase is in good agreement with the experimental value. The agreement of the theoretical and experimental volumes of the LS phase is not as good, since the experiment was done for the ground state, which is of low volume and antiferromagnetic—while the calculation was done in the ferromagnetic approximation.

The good agreement of the theoretical and experimental results for γ-Fe permit the hope that accurate and reliable results can be obtained in a study of the Fe–N system. It must be mentioned that at present there are no experimental data on the existence of the low- and high-volume LS and HS phases in nitrogenated austenite.

For optimization of the geometry of the crystal structure we have calculated the optimum positions of the atoms in the unit cell and the lattice parameters in the $Fe_8N(A)$ and $Fe_8N(B)$ structures. The optimization was done for the high-spin, high-volume phase. The results of these calculations are presented in Table I. Upon ordering of the nitrogen atoms into $N–Fe_2–N$ chains and the formation of the $Fe_8N(B)$ structure there occurs a certain increase in the cell volume per atom in comparison with that for the $Fe_8N(A)$ structure (Table I). In this case a substantial tetragonal distortion appears. The calculations showed that the high-spin phase of the $Fe_8N(B)$ structure at 0.01 eV is energetically favorable to the $Fe_8N(A)$ structure. This attests to the advantage of ordering of the nitrogen atoms into $N–Fe_2–N$ chains.

The dependence of the total energy on the unit cell volume for the $Fe_8N(A)$ and $Fe_8N(B)$ structures is calculated in the interval of values from 72 to 90 a.u.^{3}/Fe atom under hydrostatic compression of the cell. It was found that the usual quadratic character of the total energy function is altered. In the $Fe_8N(A)$ structure a discrete change of the magnetic moments at the $Fe_{0,4}$ and Fe_1 sites occurs at the transition from the low-spin to the high-spin state, as is seen in Fig. 3. At a volume of 79.5 a.u.^{3}/Fe atom the magnetic moment at the Fe_1 site jumps from $0.18\mu_B$ to $1.9\mu_B$, while that at the $Fe_{0,4}$ site undergoes a smaller jump, from $2.38\mu_B$ to $2.75\mu_B$ at the theoretically equilibrium volume in the high-spin phase (Table I). As the volume is increased further, the magnetic moment increases slowly. The energy difference between the HS and LS phases in the $Fe_8N(A)$ structure is 0.024 eV/Fe atom.

Thus the nitrogen atoms in this structure stabilize the HS phase, with magnetic moments of the $Fe_{0.4}$ and Fe_1 atoms equal to $2.75\mu_B$ and $2.08\mu_B$, respectively (Table I). As follows from Fig. 3, the transition from the LS to the HS phase is accompanied by an abrupt change in the magnetic moment

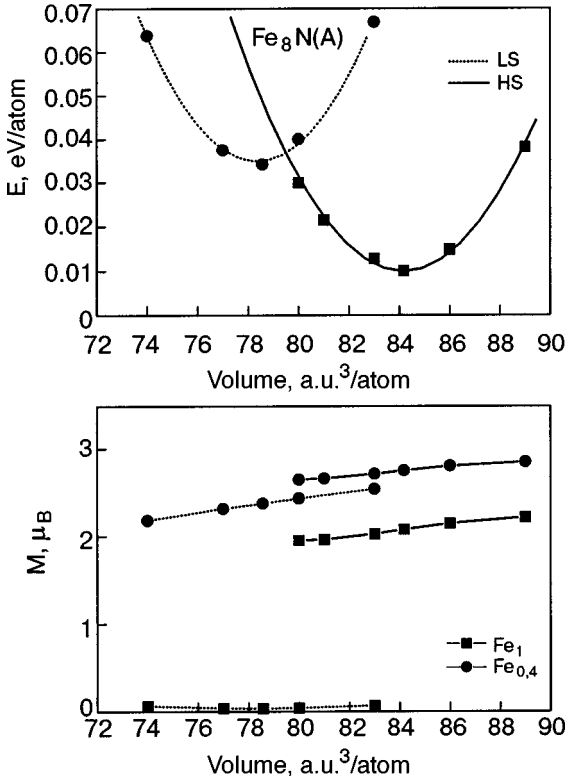

FIG. 3. Total energy E and value of the magnetic moment M for iron atoms in the $Fe_8N(A)$ structure as functions of the unit cell volume.

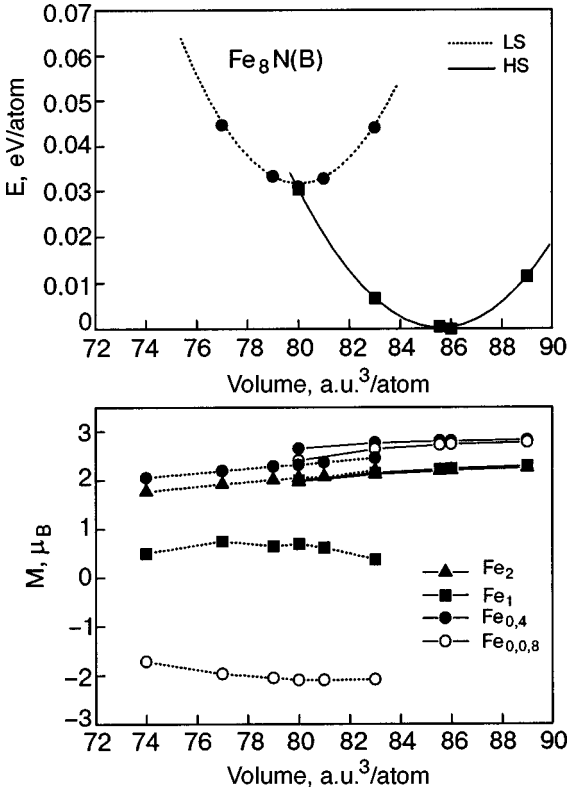

FIG. 4. Total energy E and value of the magnetic moment M of the iron atoms in the $Fe_8N(B)$ structure as functoins of the volume of the unit cell volume.

per $Fe_{0,4}$ atom ($\Delta M = 0.37\mu_B$) at the point of equality of the volumes of the two phases. Investigation of the volume dependence of the total energy and magnetic moments of all types of iron atoms showed that in the $Fe_8N(B)$ structure the high-spin phase is even more favorable in comparison with the $Fe_8N(A)$ structure. It follows from Fig. 4 that the difference between the HS and LS phases is 0.03 eV. It can be assumed that the ordering of the nitrogen atoms into $N–Fe_2–N$ chains leads to stabilization of the high-volume HS phase in the $Fe_8N(B)$ structure. It should be noted that, in contrast to the A structure, antiferromagnetism arises at some lattice sites in the B structure. At the transition to the high-volume phase this occurs at the $Fe_{0,0,8}$ sites. The magnetic moment of the $Fe_{0,0,8}$ atom is $-2.1\mu_B$ in the LS phase and $2.72\mu_B$ in the HS phase. As in the $Fe_8N(A)$ structure, at the transition from the LS to the HS phase the largest jump in magnetic moment is for that at the Fe_1 site (Fig. 4). The magnetic moment of the Fe_1 atom is $0.69\mu_B$ in the LS phase and $2.22\mu_B$ in the HS phase. An interesting factor is the weak dependence of the magnetic moment at the Fe_2 site on the unit cell volume. At the point where the volumes of the two phases are equal, the magnetic moment at the Fe_2 site does not undergo a jump. Thus the appearance of the structural element $N–Fe_2–N$ in the fcc lattice leads to stabilization of the magnetic moments on the Fe_2 sites with respect to a change of the unit cell volume. At the same time, the volume dependence of the magnetic moment at the $Fe_{0,4}$ site is practically no different from the analogous dependence for the $Fe_8N(A)$ structure. Thus the insertion of interstitial nitrogen atoms promotes stabilization of the magnetic moment at those sites for which the first coordination sphere does not contain an impurity atom. The values of the structural parameters and magnetic moments for all types of iron atoms in the $Fe_8N(A)$ and (B) structures, calculated at the equilibrium volume found theoretically, are given in Table I.

Ordering of the nitrogen atoms into $N–Fe_2–N$ chains and the formation of the $Fe_8N(B)$ structure lead to the appearance of a tetragonal distortion of the fcc lattice and to stabilization of the high-volume HS phase with the lattice parameters $a = 13.579$ a.u. and $c = 14.847$ a.u. As we have said, the HS phase in $Fe_8N(B)$ is energetically favored over the HS phase in $Fe_8N(A)$ by 0.01 eV, and it can be concluded that the formation of the structural element of the $N–Fe_2–N$ chains in the Fe_8N structure is energetically favorable. Thus, nitrogenated austenite Fe–N can apparently be represented to a first approximation by the $Fe_8N(B)$ structure. In the real alloy the $N–Fe_2–N$ chains are disoriented, and that may explain the absence of tetragonal distortion of the fcc lattice in the experimental studies. Experimental confirmation of the possibility of existence of long-range order in austenitic Fe–N is provided by the electron-microscopy experiment of Ref. 19 and the results of Mössbauer studies, which are discussed below.

4. ELECTRONIC STRUCTURE AND QUADRUPOLE SPLITTING IN THE Fe_8N STRUCTURE

It is indubitably of interest to study the electronic structure of two crystal structures having different types of ordering of the nitrogen atoms, to interpret the large collection of data obtained by the method of Mössbauer spectroscopy, and to compare the theoretical and experimental results. On the basis of structural optimization calculations we have com-

TABLE II. Contributions of the various $3d$ orbitals to the formation of the local magnetic moments.

Structure	Atom	d_{z^2}	$d_{x^2-y^2}$	d_{xy}	d_{xz}	d_{yz}
$Fe_8N(A)$	Fe_0	0.66	0.66	0.49	0.49	0.49
	Fe_1	0.32	0.53	0.44	0.40	0.40

puted the optimal values of the lattice parameters and coordinates of the atoms in the unit cell for both types of Fe_8N structures. With these structural data we calculated the electronic structure of the two modifications of the Fe_8N structure. The three lowest energy bands are localized in a narrow energy interval and are due to the $2p$ states of the nitrogen atom. As the type of ordering of the nitrogen atoms changes and N–Fe_2–N chains are formed (the $Fe_8N(B)$ structure) the $2p$ bands of the nitrogen atom broaden, overlapping with the d bands of the iron atoms. As we have said, the appearance of the N–Fe_2–N structural elements in the form of chains gives rise to a large number of inequivalent iron atoms: $Fe_{0,4}$, $Fe_{0,0,8}$, Fe_1, and Fe_2, and to tetragonal lattice distortion. This leads to complication of the band structure of $Fe_8N(B)$ owing to the lowering of the symmetry and splitting of the bands.

The calculated band structure of the two types of Fe_8N enabled us to construct the total and partial electron densities of states in these structures. Ordering of the nitrogen atoms into chains (and the formation of the $Fe_8N(B)$ structure) primarily affects the degree of occupation of the states with spin ''up'' and ''down,'' and that is reflected in a change in the local magnetic moments of the iron atoms, viz., to a rather strong change of the magnetic moment at atoms of the same type. For example, in the $Fe_8N(A)$ and $Fe_8N(B)$ structures the magnetic moment at an Fe_1 atom is equal to $2.08\mu_B$ and $2.22\mu_B$, respectively (Table I). To investigate how the value of the local magnetic moment of the iron atoms in the $Fe_8N(A)$ structure is influenced by the degree of hybridization of the $3d$ electronic states of the iron atoms with the $2p$ states of the nitrogen atoms, we calculated the contributions to the magnetic moment from the d orbitals of different symmetry. This enabled us to determine that it is the hybridization of the d_{z^2} states of the iron atoms with the p_z states of the nitrogen atom that sharply reduces the contribution of the d_{z^2} orbital to the total magnetic moment of the Fe_1 atom, which has one nitrogen atom in its nearest neighborhood (Table II). It should be noted that iron atoms that do not have impurity atoms in their nearest neighborhood have a large local magnetic moment. Thus the type of distribution of the nitrogen atoms in the fcc iron lattice and the value of the hybridization of the d states of the iron atoms and p states of the impurity atoms are important factors influencing the value and ordering of the local magnetic moments of the atoms in the alloy. In order to investigate in detail the spatial distribution of the electron density in the Fe–N system, in the present study we have calculated the distributions of electron density in the most interesting planes and directions. Figure 5 shows the distribution of the $2s$ and $2p$ electron densities of the nitrogen atom and the $3d$ electron density of the iron atom for the $2s$, $2p$, and $3d$ energy intervals in the

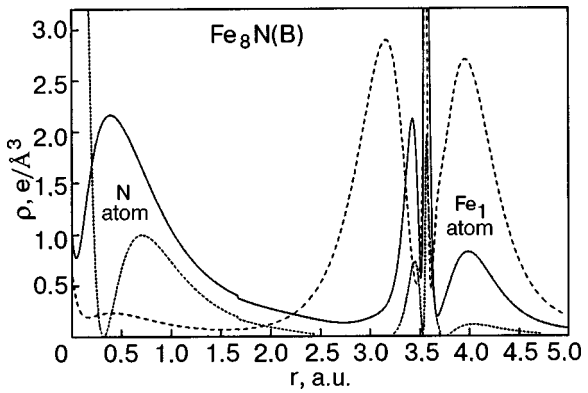

FIG. 5. Distribution of the electron density ρ in the direction r between the N and Fe_1 atoms for the energy intervals corresponding to the $2s$ (· · · ·) and $2p$ (——) states of the nitrogen atom and the $3d$ states of the iron atom (— — —). The values for the $3d$ states were reduced by a factor of 3 for clarity.

N–Fe_1 direction in the $Fe_8N(B)$ structure (in the [110] plane; Fig. 1). It follows from the results that the $2s$ and $2p$ electrons of the nitrogen atom create a certain electron density at the site of the iron atom. In the case of an Fe_1 atom this distribution is substantially anisotropic in the N–Fe_1 direction (Fig. 5), and that should give rise to an electric field gradient (EFG) at the nucleus of the iron atom. Hybridization effects are manifested in a change in shape of the distribution of $2p$ electron density at the site of an Fe_2 atom. The maximum of the distribution of the $3d$ density and the ''lump'' in the distribution of the $2p$ electron density coincide (Fig. 6), attesting to the presence of p–d hybridization.

Since a vast amount of experimental material has by now been accumulated in Mössbauer studies of nitrogenated austenite, it is of definite interest to calculate the hyperfine interactions at the nuclei of the iron atoms in the $Fe_8N(A)$ and (B) structures and to compare the theoretical and experimental results. We have calculated the electric field gradients at the nuclei of the different types of iron atoms; these gradients are manifested in the Mössbauer spectrum in the form of quadrupole splittings. It is believed by many authors[20–22] that the Mössbauer spectrum in Fe–N austenite is formed by contributions from the atoms Fe_0, Fe_1, and $Fe_{2-180°}$ (dumbbell configuration). The value of the quadrupole splitting cor-

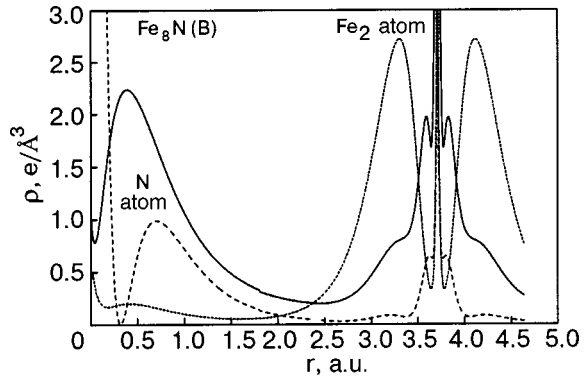

FIG. 6. Distribution of the electron density in the direction between the N and Fe_2 atoms for the energy intervals of the $2s$ (— — —) and $2p$ (——) states of the nitrogen atom and the $3d$ states of the iron atom (· · · ·). The values for the $3d$ states were reduced by a factor of 3 for clarity.

TABLE III. Calculated and experimental values of the quadrupole splitting at the nuclei of the iron atoms in the Fe–N system.

	Structure [Ref.]	Quadrupole splitting, mm/s			
		Fe_1	Fe_2	$Fe_{0,4}$	$Fe_{0,0,8}$
Theory	$Fe_8N(A)$	0.18	–	–	–
	$Fe_8N(B)$	0.28	0.17	0.27	0.48
	Fe_4N (model) [24]	0.03	0.32	–	–
	Fe_4N (nitride) [24]	–	0.50	–	–
Experiment	Fe_4N [23]	–	0.50	–	–
	$Fe_{10.2}N$ [21]	0.25	0.40	–	–
	$Fe_{10.2}N$ [22]	0.39	0.72	–	–
	$Fe_{11}N$ [20]	0.39	0.75	–	–

responds to the distance between maxima in the doublet line. Table III gives the results of calculations of the quadrupole splittings and also experimental data obtained for nitrogenated austenites by different groups of investigators.

In the calculations of the quadrupole splitting Δ for the ^{57}Fe nucleus we used the same value of the quadrupole moment of the nucleus, $Q(^{57}\text{Fe}) = 0.16$ barn, which we used previously for Fe_4N nitride (the γ' phase).[24] The EFG was calculated *ab initio* directly from the electron density distribution by the method developed by Blaha *et al.*[25] The calculations imply that the contribution to V_{zz}, the principal component of the EFG tensor, from regions outside the atomic spheres (the lattice EFG) amounts to 5% for the $Fe_8N(A)$ and (B) structures. Thus in order to understand the origin of the EFG, the main attention should be paid to its principal component—the valence EFG, which is due to the region inside the atomic spheres. A detailed analysis of the formation of the EFG at the nucleus of an Fe_1 atom in the structures $Fe_8N(A)$ and $Fe_8C(A)$ is given in Ref. 26.

The formation of the EFG at the nuclei of iron atoms of different types in the fcc lattice occurs in a substantially different way in the presence of nitrogen impurity atoms. This is reflected in the values of the quadrupole splitting registered in the Mössbauer spectra. Calculations show that the value of the quadrupole splitting at an Fe_1 iron atom in the $Fe_8N(A)$ structure is 0.18 mm/s. This is substantially smaller than the values obtained by several authors for nitrogenated austenite (Table III). In the $Fe_8N(A)$ structure there are no Fe_2 atoms, which many authors believe exist in nitrogenated austenite. From all of these circumstances one can conclude that Fe–N austenite apparently cannot be modeled by the $Fe_8N(A)$ structure. Let us consider the results obtained for the $Fe_8N(B)$ structure. We note that upon the formation of $N–Fe_2–N$ chains in this structure, other types of iron atoms besides Fe_2 appear, having an asymmetric environment in the first coordination sphere. These are the atoms $Fe_{0,4}$ (which in the $Fe_8N(A)$ structure had a cubic environment of 12 Fe_1 atoms) and $Fe_{0,0,8}$. The environment of the $Fe_{0,4}$ atoms consists of eight Fe_1 atoms, two Fe_2 atoms, and two $Fe_{0,0,8}$ atoms. The environment of the $Fe_{0,0,8}$ atoms consists of eight Fe_1 atoms and four $Fe_{0,4}$ atoms. Calculations show that an EFG appears at the nuclei of these atoms which leads to values of the quadrupole splitting comparable to the quadrupole splittings at the nuclei of the Fe_1 and Fe_2 atoms (Table III). The value of the quadrupole splitting at the nucleus of the $Fe_{0,0,8}$ atom is 0.48 mm/s, which is larger than the quadrupole splittings at the nuclei of the atoms Fe_1 (0.28 mm/s) and Fe_2 (0.17 mm/s). Thus these atoms should give a substantial contribution to the Mössbauer spectrum of nitrogenated austenite, since at a nitrogen concentration $C_N \approx 0.1$ the number of these atoms should be quite large. For the $Fe_8N(B)$ structure the concentration of $Fe_{0,4}$ atoms is 0.5 and that of the $Fe_{0,0,8}$ atoms is 0.25. The contribution from atoms of this type were not taken into account in the interpretation of the Mössbauer spectra in previous studies. In real $Fe_{10}N$ alloys the concentration of impurity atoms is lower than in the Fe_8N structures studied here. With decreasing concentration of nitrogen atoms the number of Fe_1 and Fe_2 atoms decreases, leading to a more symmetric environment of the $Fe_{0,4}$ atoms and to the appearance of a singlet in the Mössbauer spectrum (as in the case of the $Fe_8N(A)$ structure).

Thus, on the basis of the calculations done, it can be assumed that the $Fe_8N(B)$ structure apparently can be used as a model for nitrogenated austenite. Here a contribution to the Mössbauer spectrum is given not only by the Fe_1 and Fe_2 atoms but also by atoms of the $Fe_{0,0,8}$ type. By comparing the experimental values of the quadrupole splittings obtained in Ref. 21 for iron atoms in an $Fe_{10.2}N$ alloy with our results, we can conclude that the calculated value of the quadrupole splitting at the Fe_1 atom (0.28 mm/s) is in good agreement with the experimental value 0.25 mm/s (Table III). The theoretical value of the quadrupole splitting at the nucleus of the Fe_2 atom is 0.17 mm/s and is in poor agreement with the experimental value 0.4 mm/s.[21] The agreement with the experimental values obtained in Refs. 20 and 22 is even poorer. It should be noted, however, that the theoretical value of the quadrupole splitting at the nucleus of the $Fe_{0,0,8}$ atom (0.48 mm/s) correlates rather well with the experimental value 0.4 mm/s from Ref. 21. Thus the results of the calculations lead to the conclusion that the interpretation of the Mössbauer spectra (their decomposition into components) must be done using four spectrum-forming components: the singlet contribution from the nucleus of the Fe_0 atom and the doublet components due to the Fe_1, Fe_2, and $Fe_{0,0,8}$ atoms. It should be noted that the experimental values of the quadrupole splitting at the nucleus of the Fe_2 atom (0.72 and 0.75 mm/s) reported in Refs. 20 and 22, respectively, seem somewhat too high. The good agreement of the experimental and theoretical values of the quadrupole splitting at the nucleus of the Fe_2 atom (0.25 mm/s for $T < T_C$ and 0.50 mm/s for $T > T_c$) which we obtained previously[24] for iron nitride Fe_4N attests to the reliability of the theoretical results for the $Fe_8N(B)$ structure. Calculations in a model structure for Fe_4N with structural elements consisting of two intersecting $N–Fe_2–N$ chains (as opposed to three in the nitride) give a value of the quadrupole splitting at the nucleus of the Fe_2 atom equal to 0.32 mm/s,[24] which is much smaller than the quadrupole splitting in the nitride, 0.50 mm/s (in view of the absence of magnetism in Fe–N austenite we compare the quadrupole splittings for the nitride and the model Fe_4N structure for $T > T_C$). In the $Fe_8N(B)$ structure there are completely nonin-

tersecting N–Fe_2–N chains, and that leads to a decrease in the quadrupole splitting at the Fe_2 atom to a value of 0.17 mm/s. Thus one observes a clear tendency toward a decrease in the quadrupole splitting at the Fe_2 atom with misorientation of the N–Fe_2–N chains. Since in real Fe–N austenite the ordering of the chains cannot be higher than in iron nitride Fe_4N, the discussions given above confirm our assumption that the experimental results for the Fe_2 atom are clearly too high, apparently because of the nonuniqueness of the decomposition of the experimental spectrum into components.

5. MAGNETIC ORDERING IN THE Fe–N SYSTEM

A study of the electronic structure of the model structures $Fe_8N(A)$ and (B) makes it possible to understand quantitatively the influence of the nitrogen atoms on the magnetic properties of fcc iron. It follows from an analysis of the total energies of these structures as functions of the unit cell volume (Figs. 3 and 4) at a concentration of nitrogen atoms such that the ferromagnetic HS phase is energetically favorable to the LS phase. Thus the introduction of interstitial nitrogen leads to enhancement of the Invar properties of fcc iron. For a more detailed understanding of the magnetic properties of iron containing impurity nitrogen it is necessary to make an estimate of the exchange integral. For this we have used the dependence of the total energy of the two phases for the $Fe_8N(B)$ structure, which, in our view, gives a more realistic description of austenite than does the $Fe_8N(A)$ structure. It should be noted that in the $Fe_8N(B)$ structure a change in the orientation of the magnetic moment at the $Fe_{0,0,8}$ atoms occurs at the transition from the HS to the LS phase, and that is a better model of austenite than the LS phase of the A structure (the ground state of fcc iron in the approximation of collinear magnetic moments can be assumed antiferromagnetic). Taking into account the magnetic interaction only for nearest neighbors, we have calculated the dependence of the exchange integral $J=(E_{\mathrm{LS}}-E_{\mathrm{HS}})/3$, where the total energies of the two phases E_{HS} and E_{LS} are given per iron atom. Using the known experimental dependence of the lattice parameter on the nitrogen concentration,[27] we have obtained the dependence of the exchange integral on the concentration of nitrogen atoms (Fig. 7a). It follows from the results of the calculations that the ground state of austenite should be antiferromagnetic at concentrations less than 0.057 and ferromagnetic at higher concentrations. To calculate the temperatures of the phase transitions we used the following numerical results, given in Refs. 28 and 29, for the Ising model with a nearest-neighbor interaction: $T_N \approx 1.7\ \mathrm{J}/k_B$, $T_C \approx 9.6\ \mathrm{J}/k_B$. The phase transition temperatures are shown in Fig. 7b. The value $T_N = 170$ K for pure iron is almost a factor of 2.5 times larger than the known experimental value. The Curie temperature $T_C = 952$ K at $C_{\mathrm{N}} = 0.1$ is too high even in comparison with the known[30] temperature $T_C \approx 770$ K for the nitride Fe_4N. These disagreements are apparently due to the following causes:

1) a nitrogen concentration $C_{\mathrm{N}} = 1/8$ is too large for a correct description of the low-spin phase;

2) the average magnetic moment per iron atom in the LS phase for the $Fe_8N(B)$ structure is $1.44\mu_B$, whereas in fcc iron it is substantially smaller ($0.7\mu_B$);[18]

3) the energy integrals of the iron atoms with different coordinations of the nitrogen atoms have been replaced by a single average value;

4) the nearest-neighbor interaction approximation.

We also note that, to the authors' knowledge, all attempts at an *ab initio* description of the low-spin state of fcc iron with the use of collinear configurations for the magnetic subsystem have failed to give good agreement between theory and experiment. The relations obtained in the present study give a qualitatively correct idea of the influence of nitrogen on the magnetic properties of iron, since the nitride Fe_4N is ferromagnetic, while the austenite should be antiferromagnetic at low concentrations. Thus there must exist a nitrogen concentration (our estimates give a value of 0.057) at which the exchange integral becomes equal to zero.

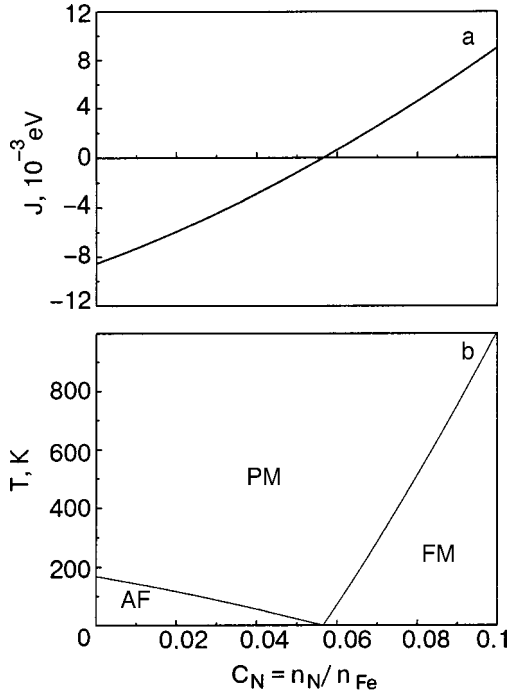

FIG. 7. Dependence of the exchange integral of the iron atoms on the concentration of nitrogen atoms (a) and the types of magnetic ordering for austenite (b) (PM denotes a paramagnet).

6. COMPOSITION ORDERING AT ROOM TEMPERATURES

In the $Fe_8N(A)$ phase there exist three inequivalent sublattices that can be occupied by nitrogen atoms. In equilibrium only one of them is occupied by nitrogen atoms. In the $Fe_8N(B)$ phase the nitrogen atoms are ordered into chains of the N–Fe_2–N type, and there exist four inequivalent sublattices for nitrogen. In the B phase the binding energy per iron atom is calculated to be 0.01 eV higher than in the A phase. Therefore, at low temperatures ($T \to 0$) the equilibrium stable state is the B phase with one completely occupied nitrogen sublattice. With increasing temperature it is natural to expect the formation of the polydomain phase B^*, in which there is an alternation of domains of the chain phase in

which different nitrogen sublattices are occupied. At higher temperatures the $Fe_8N(B)$ fluctuations will appear more and more often.

Other types of short-range ordering of the nitrogen atoms are also possible. Noticing that the difference of the energies belonging to the 8 Fe atoms in configurations A and B is $\Delta E \approx 0.08$ eV, one can assume that at a temperature $T_C \approx \Delta E/k_B$ (k_B is Boltzmann's constant) the ordering should be destroyed because of strong structural fluctuations. It can also be assumed that the nitrogen subsystem at $T > T_C$ is well described in the approximation of an ideal lattice gas. However, correlation effects should appear near T_C, owing to the substantial N–N interactions via the electronic subsystem. The overall picture of the nitrogen subsystem near T_C can be represented in the form of alternating cells with different types of short-range ordering of the N atoms.

Other configurations besides the short-range order of the A and B types can exist. To find the temperature T_C and determine the character of the short-range order near that temperature one can use the Monte Carlo method if the effective many-particle interaction potential of the nitrogen atoms in the iron lattice is known. It should be noted that at the present time there is no reliable information about the quantitative values of the interaction potential of nitrogen atoms in austenite. It can be said with certainty that the interaction cannot be limited to nearest and next-nearest neighbors, since in interstitial solutions the deformation potential has a long-range character. To calculate the interaction potentials in multicomponent systems we have used the cluster expansion technique.[31,32] Since we are studying an interstitial and not a substitutional system, we modified the cluster expansion somewhat. The change consists in going over from the lattice variables s_i, which are convenient for studying systems of substitution ($s_i = 1$ for a site occupied by an atom A, and $s_i = -1$ for a site occupied by an atom B) to the variables $c_i = (1 + s_i)/2$ ($c_i = 0$ for a vacant octahedral interstitial site and $c_i = 1$ for an interstitial site occupied by a nitrogen atom). In this case the cluster expansion has the form

$$E(c) = \sum W_\alpha Q_\alpha, \tag{1}$$

where W_α are the effective impurity–impurity interaction potentials, and $Q_\alpha = c_{i_1} \ldots c_{i_l}$ are the products of the occupation functions specified on a cluster with sites $\alpha = \{i_1, \ldots, i_l\}$. For working with c_i only the impurity–impurity interaction potentials are important, and the potentials between an impurity and a vacant interstitial site or between two vacant interstitial sites are not taken into account, since $Q_\alpha = 0$ for all configurations with an unoccupied interstitial site.

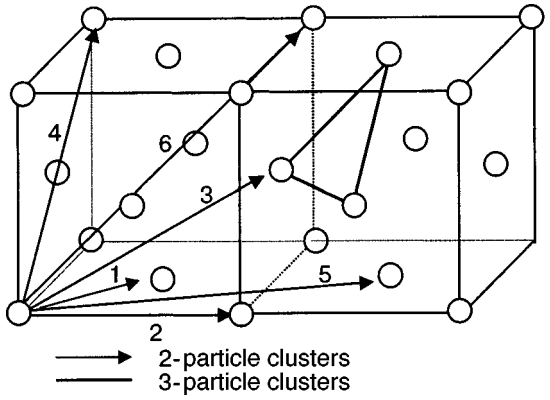

FIG. 8. Many-particle clusters used for the cluster expansion. The cluster consisting of a single site is not shown.

The accuracy of determination of the effective impurity–impurity interaction potential depends on how many coordination spheres are taken into account in the calculations. We chose 10 model structures necessary for finding the interaction potentials. For each of these structures a calculation was carried out by the FLAPW method to minimize the total energy with respect to the positions of the atoms and the unit cell parameters in a given crystallographic system. All of the technical details of the calculation are the same as those given above for the calculation of the model structures $Fe_8N(A)$ and (B). Using the cluster expansion (1) and the total energies of all the structures, we obtained the 9 interaction parameters corresponding to the clusters shown in Fig. 8. The values of the interaction potentials are given in Table IV. The meaning of the notation used is as follows: ω_0 is the energy of an iron atom, ω_1^1 is the energy of a nitrogen atom plus the energy necessary for inserting this atom into austenite at an infinitesimal concentration of nitrogen atoms; ω_1^2, ω_2^2, ω_3^2, ω_4^2, ω_5^2, and ω_6^2 are the energies of the pair interaction for the six coordination spheres, ω_1^3 is the three-particle potential. In a least-squares fit the maximum residual discrepancy in the total energy is 0.0036 eV/Fe atom.

Using the calculated interatomic interaction potentials, we obtained the temperature dependence of the number of iron atoms with different types of nitrogen-atom environments by the Monte Carlo method. The temperature dependence found in this way for the atoms Fe_0, Fe_1, and Fe_2 at a nitrogen concentration of 0.1 is presented in Fig. 9a. The dotted lines show the number of atoms of each type in the absence of interaction between nitrogen atoms, corresponding to the approximation of an ideal solid solution. From the temperature dependence of the fraction of Fe_0, Fe_1, and Fe_2 atoms one can determine that the transition temperature lies

TABLE IV. Effective cluster interactions W_α obtained by the least-squares method for 10 structures with the use of 5 or 6 pair potentials.

Number of parameters	Effective cluster interactions W_α, eV								
	w_0	w_1^1	w_1^2	w_2^2	w_3^2	w_4^2	w_5^2	w_6^2	w_1^3
5	−34634.7004	−1490.8849	0.127	−0.041	0.027	0.018	0.032	–	−0.014
6	−34634.6996	−1490.9087	0.129	−0.034	0.028	0.022	0.031	−0.007	−0.014

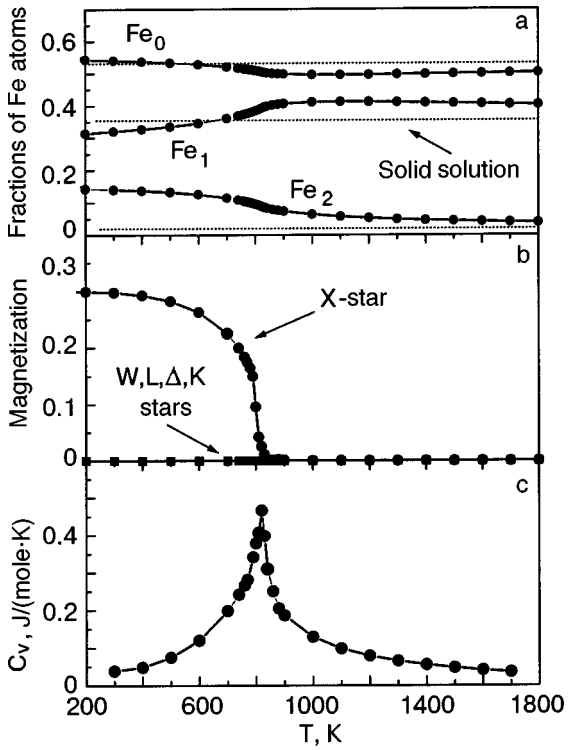

FIG. 9. Temperature dependence of the number of iron atoms with different coordinations of nitrogen (a), long-range order parameters (b), and heat capacity (c) at a nitrogen concentration of $n_N/n_{Fe}=0.1$.

around $T\sim 800$ K, as expected. It is seen that the mutual attraction of nitrogen atoms in the second coordination sphere leads to an increase in the number of Fe_2 atoms, which attests to substantial short-range ordering of the nitrogen atoms even above the transition temperature. The presence of this short-range order can be judged from the shape of the Mössbauer spectra.[22]

The curves of the temperature dependence of the heat capacity (Fig. 9c) and the short-range order parameters (Fig. 9b) clearly exhibit a phase transition in the vicinity of 830 K, from the disordered state to the nitride Fe_4N, which contains the maximum number of $N-Fe_2-N$ chains for the given stoichiometry. The superstructure corresponding to the nitride Fe_4N was deciphered with the aid of a calculation of the absolute values of the Fourier components $|c(\mathbf{k})|$ of the distribution function $c(\mathbf{r})$ for different high-symmetry points of the Brillouin zone. The values of $|c(\mathbf{k})|$ are directly related to the long-range order parameters and the structural constants of the superstructure.[33] As a result of the calculation it was found that the only nonzero Fourier components are those corresponding to the X star, and the absolute values for the three vectors of the X star $(X=(1,0,0),(0,1,0),(0,0,1))$ are equal to each other, and that attests to the formation of the nitride Fe_4N.

Thus, as a result of the calculations done we have not only found the temperature T_C but have also established the character of the behavior of the short-range ordering of nitrogen atoms near that temperature.

7. DISCUSSION AND CONCLUSIONS

The results of a numerical simulation of the Fe–N system by the *ab initio* FLAPW method have been used to investigate the influence of nitrogen on the formation of the low-spin and high-spin phases, which differ in the character of the low-temperature magnetic ordering and in the hyperfine interactions. The calculations of the total energy per iron atom show that in the $Fe_8N(A)$ structure, where the nitrogen atoms form a cubic sublattice and each N atom occupies an octahedral cavity, this energy is 0.01 eV lower than in the $Fe_8N(B)$ structure, where the nitrogen atoms order into chains of the $N-Fe_2-N$ type. According to our calculations, tetragonal distortion arises in the $Fe_8N(B)$ structure. As we have said, the fact that tetragonality is not observed experimentally[27] in this system can be explained by the disordered nature of the chains. Indeed, in view of the existence of four inequivalent sublattices in the B phase, one can conclude that a polydomain structure B^*, with mutually disordered chains, exists at finite temperatures, and the state B, with mutually ordered chains, becomes the ground state at $T\to 0$.

Study of the behavior of the short-range compositional and long-range magnetic ordering has shown that the ordering of the nitrogen atoms according to types B and A is preserved even upon the transition to the paramagnetic state, and that should be reflected in the character of the hyperfine structure.

As to the hyperfine structure, we have calculated the electric field gradients at the nuclei of the iron atoms for the B phase. We found that at the nuclei of iron atoms whose nearest-neighbor environment does not contain impurity atoms, an electric field gradient can arise which is comparable in magnitude and even greater than the field gradients at the nuclei of the Fe_1 and Fe_2 atoms, which have one and two nitrogen atoms in the nearest-neighbor environment. Thus these atoms can give a substantial contribution to the Mössbauer spectrum of nitrogenated austenite.

It follows from the results on the dependence of the exchange integral on the nitrogen concentration that by lowering the energy of the HS phase, nitrogen enhances the ferromagnetic properties of fcc iron. The magnetic ordering diagram constructed enables one to judge the dependence of the magnetic order on the nitrogen concentration.

The authors thank Prof. V. G. Gavrilyuk for helpful discussions. This study was done with the financial support of the Science and Technology Center of Ukraine, Project No. 120.

*E-mail: tim@imag.kiev.ua

[1] E. F. Wassermann, Phys. Scr. **25**, 209 (1989).
[2] E. F. Wassermann, J. Magn. Magn. Mater. **100**, 346 (1991).
[3] V. L. Moruzzi, P. M. Marcus, and J. Kubler, Phys. Rev. B **39**, 6957 (1989).
[4] V. L. Moruzzi and P. M. Marcus, J. Appl. Phys. **64**, 5598 (1988).
[5] M. Podgorny, Phys. Rev. B **43**, 11300 (1991).
[6] P. Entel, E. Hoffmann, P. Mohn, K. Schwarz, and V. L. Moruzzi, Phys. Rev. B **47**, 8706 (1993).
[7] R. D. Ellerbrock, A. Fuest, A. Schatz, W. Keune, and R. A. Brand, Phys. Rev. Lett. **74**, 3053 (1995).
[8] H. C. Herper, E. Hoffmann, and P. Entel, Phys. Rev. B **60**, 3339 (1999).
[9] W. Keune, T. Ezawa, W. A. A. Macedo, U. Glos, K. P. Schletz, and U. Kirschbaum, Physica B **161**, 269 (1989).
[10] C. Carbone, G. S. Sohal, E. Kisker, and E. F. Wassermann, J. Appl. Phys. **63**, 3499 (1988).

[11] P. Ehrhart, B. Schonfeld, H. H. Ettwig, and W. Pepperhoff, J. Magn. Magn. Mater. **22**, 79 (1980).
[12] Y. Tsunoda, Y. Nishioka, and R. M. Nicklow, J. Magn. Magn. Mater. **128**, 133 (1993).
[13] D. J. Singh, *Planewaves, Pseudopotentials, and the LAPW Method*, Kluwer, Boston–Dordrecht–London (1994).
[14] P. Blaha, K. Schwarz, and J. Luitz, *WIEN97, A Full Potential Linearized Augmented Plane Wave Package for Calculating Crystal Properties*, Karlheinz Schwarz, Techn. Universitat Wien, Austria (1999); ISBN 3-9501031-0-4.
[15] J. P. Perdew, K. Burke, and M. Ernzerhof, Phys. Rev. Lett. **77**, 3865 (1996).
[16] D. Singh, Phys. Rev. B **43**, 6388 (1991).
[17] M. Acet, H. Zähres, E. F. Wassermann, and W. Pepperhoff, Phys. Rev. **49**, 6012 (1994).
[18] S. C. Abrahams, L. Guttman, and J. S. Kasper, Phys. Rev. **127**, 2052 (1962).
[19] A. V. Suyazov, M. P. Usikov, and B. M. Mogutnov, Fiz. Met. Metalloved. **42**, 755 (1976).
[20] V. G. Gavriljuk, V. M. Nadutov, and O. Gladun, Phys. Met. Metallogr. **3**, 128 (1990).
[21] J. Foct, P. Rochegude, and A. Hendry, Acta Mater. **36**, 501 (1988).
[22] K. Oda, K. Umezu, and H. Ino, J. Phys.: Condens. Matter **2**, 10147 (1990).
[23] P. Rochegude and J. Foct, Phys. Status Solidi **98**, 51 (1986).
[24] A. N. Timoshevskii, V. A. Timoshevskii, B. Z. Yanchitsky, and V. A. Yavna, Comput. Mater. Sci. **22**, 99 (2001).
[25] P. Blaha, K. Schwarz, and P. Herzig, Phys. Rev. Lett. **54**, 1192 (1985).
[26] A. N. Timoshevskii, V. A. Timoshevskii, and B. Z. Yanchitsky, J. Phys.: Condens. Matter **13**, 1051 (2001).
[27] Liu Cheng, A. Bottger, Th. H. de Keijser, and E. J. Mittemeijer, Scr. Metall. Mater. **24**, 509 (1990).
[28] K. Binder, J. L. Lebowitz, M. K. Phani, and M. H. Kalos, Acta Metall. **29**, 1655 (1981).
[29] J. M. Sanchez and D. de Fontaine, Phys. Rev. B **17**, 2926 (1978).
[30] A. Burdese, Ann. Chim. (Roma) **49**, 1873 (1959).
[31] J. M. Sanchez, F. Ducastelle, and D. Gratias, Physica A **128**, 334 (1984).
[32] J. W. D. Connoly and A. R. Williams, Phys. Rev. B **27**, 5169 (1983).
[33] A. G. Khachaturyan, *Theory of Structural Transformations in Solids*, Wiley, New York (1983).

Translated by Steve Torstveit

Low-temperature behavior of disordered magnetic impurities: Distribution of effective Kondo temperatures

A. A. Zvyagin*

B. Verkin Institute for Low Temperature Physics and Engineering of the National Academy of Science of Ukraine, 47 Lenin Ave., Kharkov 61103, Ukraine; Max-Planck-Institut für Physik Komplexer Systeme, Dresden, Germany

A. V. Makarova

Kharkov State Economic University, Kharkov, Ukraine; B. Verkin Institute for Low Temperature Physics and Engineering of the National Academy of Science of Ukraine, 47 Lenin Ave., Kharkov 61103, Ukraine

(Submitted January 12, 2004)
Fiz. Nizk. Temp. **30**, 639–643 (June 2004)

Several rare-earth compounds, low-dimensional organic conductors, and spin chains exhibit low-temperature divergences of their magnetic susceptibility and specific heat (non-Fermi-liquid behavior). Such divergences are often related to disordered ensembles of magnetic impurities in those systems. In this work the distribution function of the effective characteristic of a single magnetic impurity, the Kondo temperature, is derived. We calculate how the distributions of Kondo temperatures depend on the effective dimensionality of the problem and on the concentration of impurities. © *2004 American Institute of Physics.* [DOI: 10.1063/1.1768352]

The Kondo effect[1] is the well-known example in which modern theoretical methods like renormalization group theory, the Bethe ansatz, bosonization, conformal field theory, etc. have demonstrated their strength.[2,3] It describes the effects of the exchange interaction between the spin of a magnetic impurity and spins of itinerant electrons. The crossover from the strong coupling to the weak coupling regime for a Kondo impurity manifests nonperturbative effects present in condensed matter theory.

During the last decade the interest in non-Fermi-liquid behavior of magnetic systems and metallic alloys has grown considerably. A large class of conducting nonmagnetic materials does not behave as usual Fermi liquids (i.e., with the finite magnetic susceptibility, finite value of the Sommerfeld low-temperature coefficient of the specific heat, and quadratic temperature behavior of the resistivity) at low temperatures. There are several possible reasons for such behavior. One of the best-known examples of the non-Fermi-liquid properties is the Kondo effect for multichannel (n is the number of channels) electron systems: For an impurity spin less than $n/2$ a non-Fermi-liquid critical behavior results.[4] Another possible cause of non-Fermi-liquid behavior is the presence of a quantum critical point[5] (i.e., a phase transition governed not by the temperature but by some other parameter, like pressure, chemical substitution, etc.). In that case fluctuations of the order parameter interact with itinerant electrons and can cause low-temperature divergences of thermodynamic characteristics.

However, for most of the nonstoichiometric conductors in which the non-Fermi-liquid behavior has been observed (see, e.g., the recent reviews[5–8]) the magnetic susceptibility and low-temperature specific heat usually manifest logarithmic or weak power-law behavior with temperature, while their resistivity decreases linearly (or with some power-law exponent less than 2) with temperature, showing a large residual resistivity.[9–19] This is different from the predictions of the theory of the overscreened Kondo effect.[3,4] For example, Ref. 14 reported the results of measurements of the magnetic susceptibility, NMR Knight shift, and low-temperature specific heat. To explain the observed features it was necessary to assume some disorder, with a distribution of Kondo temperatures of magnetic impurities. The inhomogeneous distribution of localized magnetic moments was later confirmed[18] by muon spin rotation experiments. The above-mentioned properties and the alloy nature of the compounds studied suggest that the disorder (a random distribution of localized electrons or a random coupling to the conducting electron host) can play the main role in the low-temperature non-Fermi-liquid character of such systems. The idea of (unscreened) magnetic moments existing in disordered metallic systems was formulated in Refs. 20–24. It was proposed that near the metal–insulator transitions (or for the sufficiently alloyed systems far from the quantum critical point) disordered correlated conductors contain localized magnetic moments. The change in the interactions between the impurity sites and the host spins can be considered as a modification of the characteristic energy scale, the Kondo temperature T_K. At that scale the behavior of the magnetic impurity manifests the crossover from the strong coupling regime (for $T,H \ll T_K$, H being the magnetic field) to the weak coupling regime $T_K \ll H,T$. The impurity spin behaves asymptotically free in the weak coupling case, and it is screened by the spins of itinerant electrons in the strong coupling case. The random distribution of magnetic characteristics of impurities (i.e., their Kondo temperatures) may be connected either with the randomness of exchange couplings of itinerant electrons with the local moments[21] or with the randomness of the densities of conduction electron states.[20] Both types of randomness renormalize the single universal parameter, the Kondo temperature, which characterizes the state of a magnetic impurity. A thorough comparison of experimental results for non-Fermi-liquid behavior of disordered heavy fermion Kondo

alloys has been performed with very good agreement with theoretical predictions of the model for distributed Kondo temperatures.[17] Later it was pointed out that the problem of the behavior of magnetic impurities with random distributions of their Kondo temperatures in metals can be solved exactly, with the help of the Bethe ansatz.[24–26] The role of the long-range (Ruderman–Kittel–Kasuya–Yosida) coupling between local moments was taken into account[25–28] (Griffiths phase[29] theory), exhibiting properties qualitatively similar to those of models with noninteracting local moments. Also, the presence of a spin–orbit interaction in some disordered heavy fermion alloys demands a study of magnetic anisotropy, which can play an essential role in the physics of disordered spin interactions.[26–28,30] Finally, it was exactly proved that for correlated electron systems containing magnetic impurities with random distributions of their couplings to the host it is also possible to introduce a distribution of effective Kondo temperatures[31] which governs the low-temperature non-Fermi-liquid behavior of the system.

It was pointed out[25,26,28,31] that distributions of effective Kondo temperatures for each magnetic impurity can cause divergences of the magnetic susceptibility and the Sommerfeld coefficient of the specific heat for quasi-one-dimensional organic conductors and quantum spin chains, where such behavior was observed.[32–35] To explain power-law divergences of the magnetic susceptibilities and Sommerfeld coefficients of rare-earth and actinide compounds, as well as quasi-one-dimensional organic conductors and quantum spin chains, it was necessary to use a distribution of Kondo temperatures (the strong-disorder distribution, for which the tails are rather large) which starts with the term $P(T_K) \propto G^{-\lambda}(T_K)^{\lambda-1}$ ($\lambda < 1$) valid till some energy scale G for the lowest values of T_K.[25–27,30,31] The goal of this work is to obtain the distribution of Kondo temperatures for a system with magnetic impurities and to show how such a distribution will depend on the effective spatial dimensionality of the system (it turns out that the exponent λ is different for three-dimensional non-Fermi-liquid heavy fermion systems and for quasi-one-dimensional organic conductors and quantum spin systems[16,32,33,35]).

Let us consider the model of electrons (itinerant and localized, where localization centers, i.e., $3d$, $4f$, or $5f$ orbitals, are distributed randomly on a hypercubic lattice with a random nearest-neighbor hopping) with the Hamiltonian[20]

$$\mathcal{H} = \sum_{j,j',\sigma} t(j,j') c^{\dagger}_{j,\sigma} c_{j',\sigma} + \mathcal{H}_{\rm int}, \tag{1}$$

where $c^{\dagger}_{j,\sigma}$ ($c_{j,\sigma}$) creates (annihilates) an electron with spin σ at site j, and $t(j,j')$ are hopping elements. The interaction part of the Hamiltonian, $\mathcal{H}_{\rm int} = (U/2)\Sigma_j n_{j,\sigma} n_{j,-\sigma}$, is determined by the Coulomb interaction of localized electrons (the sum is over random positions of localized electrons, and $n_{j,\sigma} = c^{\dagger}_{j,\sigma} c_{j,\sigma}$). Generally speaking, one can add to the Hamiltonian (1) disordered local potentials $\Sigma_{j,\sigma} \varepsilon_j n_{j\sigma}$. The hopping integrals can be approximated[36] as overlap integrals

$$t(j,j') = E_0 \exp\left(\frac{-r_{j,j'}}{a}\right)\left(1 + \frac{r_{j,j'}}{a} + \ldots\right), \tag{2}$$

where a is the Bohr radius and $E_0 \sim U$ is the effective binding energy of the dopant (localized electron). We suppose that the hopping integrals are random because of the disorder of the distribution of localized electrons.

Let us consider the situation for which localized electrons are in the magnetic state, i.e., their valence is close to 1, which is satisfied if $t^2(j,j')\rho(E_F) \ll -\varepsilon_j, U + \varepsilon_j$ (with negative ε_j, where $\rho(E_F)$ is the density of states at the Fermi level).[2] It is natural to assume that the density of the localized magnetic moments n_l depends on the density of dopants n as

$$n_l = n \exp(-n/n_{\max}), \tag{3}$$

where $n_{\max}$ is related to the critical distance between localization centers R_c via $n_{\max} = 1/V_c$. Here V_c depends on the effective dimensionality of the distribution of localized magnetic moments. It is equal to $V_c = 4\pi R_c^2/3$ for the three-dimensional case, $V_c = \pi R_c^2$ for the effectively two-dimensional situation, and for an effectively one-dimensional distribution of localized magnetic moments one has $V_c = R_c$. Such a distribution is well known in the theory of disordered systems (it follows from simple combinatorics), e.g., in the theory of dislocations with defects it is known as the Koehler formula (Ref. 36; see also Refs. 37 and 38). For large n, n_l is a decreasing function of n, as it must be. Using such an assumption, we can find the probability $P(r)$ of finding the nearest-neighbor localized moment of a given site at a distance r; see below. (Alternatively, $P(r)$ can be derived independently,[39] and we can obtain Eq. (3).) Obviously, the density of the localized magnetic moments can be written as

$$n_l = \int_{R_c}^{\infty} P(r)\,dr. \tag{4}$$

Using the definition of R_c we obtain

$$P(r) = n \begin{cases} \pi r^2 \exp(-4\pi n r^3/3), & d=3 \\ 2\pi r \exp(-\pi n r^2), & d=2 \\ \exp(-nr), & d=1 \end{cases} \tag{5}$$

where d is the effective dimensionality of the distribution of localized electrons; cf. Refs. 36 and 39). One can check that n_l has a maximum at $n_{\max}$, which, actually, justifies Eq. (3).

The next step is to obtain the distribution of hopping integrals $t(j,j')$ between localized moments (in what follows we shall denote them simply as t). Equation (2) implies $r(t) \approx a \ln(2E_0/t)$. Then, using $\tilde{P}(t) = P(r)(dr/dt)$ and Eq. (5), we get

$$\tilde{P}(t) = -\frac{an}{t} \begin{cases} \pi a^2 \ln^2(E_0/t) \exp[-(4\pi n a^3/3)\ln^3(E_0/t)], & d=3 \\ 2\pi a \ln(E_0/t) \exp[-\pi n a^2 \ln^2(E_0/t)], & d=2 \\ \exp[-na \ln(E_0/t)], & d=1 \end{cases} \tag{6}$$

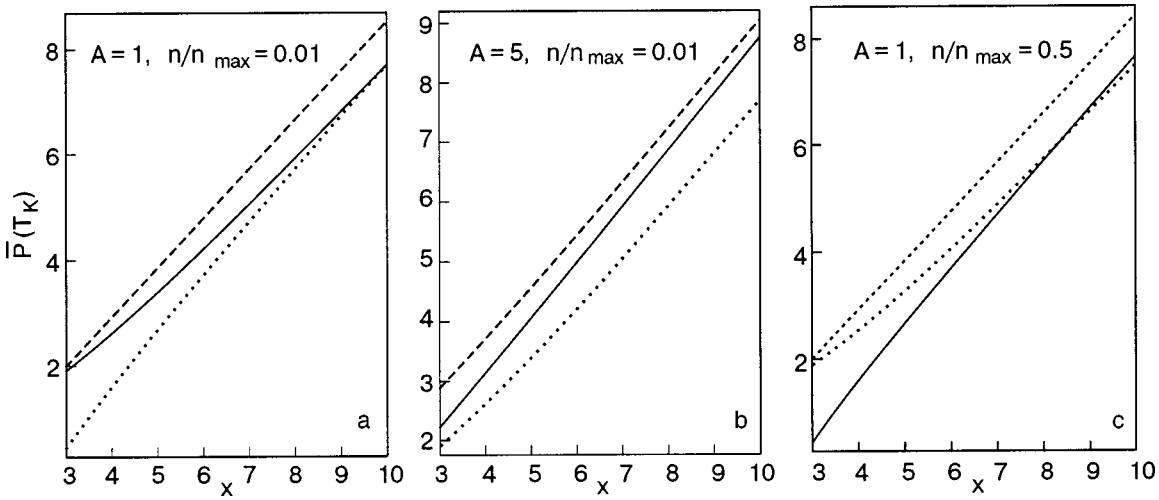

FIG. 1. Logarithms of the distributions of the Kondo temperatures for the three-dimensional (solid line), two-dimensional (dotted line), and one-dimensional (dashed line) cases.

for the three-, two-, and one-dimensional cases, respectively.

The Kondo temperature of the localized magnetic moment can be written as[2]

$$T_K = \sqrt{\frac{2U\rho(E_F)}{\pi}}\, t \exp\left(-\frac{|\varepsilon|(\varepsilon+U)}{2U\rho(E_F)t^2}\right) \approx D \exp \times\left(-\frac{|\varepsilon|(\varepsilon+U)}{2U\rho(E_F)t^2}\right). \tag{7}$$

where we have assumed homogeneous distributions of the local potentials $\varepsilon_j=\varepsilon$ and introduced the low-energy cutoff D, as usual for the Kondo problem.[2] Notice that for $\varepsilon=0$ one can define the Kondo temperature as $T_K=D\exp(-2U/\rho(E_F)t^2)$. Then Eq. (7) implies

$$\frac{dT_K}{dt} \approx -\frac{t}{2T_K \ln(T_K/D)}. \tag{8}$$

Defining $x=\ln(D/T_K)$ and $A=8U\rho(E_F)E_0^2/|\varepsilon|(\varepsilon+U)$, we obtain the distributions of Kondo temperatures

$$\overline{P}(T_K) = \frac{Z_d n}{2n_{\max} T_K x} \begin{cases} (3/16)\ln^2(Ax)\exp[-(n/8n_{\max})\ln^3(Ax)], & d=3 \\ \ln(Ax)\exp[-(n/4n_{\max})\ln^2(Ax)], & d=2 \\ \exp[-(n/2n_{\max})\ln(Ax)], & d=1 \end{cases} \tag{9}$$

for the three-, two-, and one-dimensional cases, respectively, where Z_d are normalization constants. Observe that the divergence of $\overline{P}(T_K)$ as $T_K\to 0$ (due to the factor T_K^{-1}) is weakened by logarithmic factors like $\ln(T_K/D)$. That is why $\overline{P}(T_K)$ can be normalized to unity over some interval $0 \leqslant T_K \leqslant T_{\max}$, where $T_{\max}$ is given by $T_{\max}=D\exp(-|\varepsilon| \times(\varepsilon+U)/8U\rho(E_F)E_0^2)$. $T_{\max}$ can be related to the parameter G; see above. Obviously the distributions of Kondo temperatures depend on the impurity parameters ε, the constant of Coulomb repulsion U, the density of states of itinerant electrons at the Fermi level, the Bohr radius, and the density of localized orbitals. However, Eqs. (9) imply that such a set of parameters is realized in two main governing parameters: $n/n_{\max}$ and A.

It turns out that for large enough intervals of values of T_K the distribution $\overline{P}(T_K)$ is proportional to $T_K^{\lambda-1}$, i.e., it is of the form used in Refs. 25–27, 30, and 31 without derivation, based on experimental results. The exponent $\lambda<1$ is determined by A and $n/n_{\max}$. The plots of the logarithms of $\overline{P}(T_K)$ as functions of x are presented in Fig. 1a for one-, two-, and three-dimensional situations (we did not take into account the terms in Eqs. (9) which do not depend on x here; those terms yield only constant shifts). Here we used the parameters D, ε, U, and E_0 appropriate for real disordered rare-earth and actinide systems, which produces $A\approx 1$. Also, according to experiments, one can expect $n/n_{\max}\approx 0.01$. Notice that the maximal values of intervals of $T_K, T_{\max}$ depend on A via $T_{\max}=D\exp(-1/A)$, and, hence, $x_{\min}=1/A$. That is why we present here the results for large enough values of x (i.e., small enough T_K) that the distributions in the intervals considered are reminiscent of power laws $\propto T_K^{1-\lambda}$. One can see that the exponents of the distributions depend on the effective dimensionality of the distribution of the localized electrons.

To illustrate how the effective exponents depend on A and on the concentration of localized electrons n, we present results for the logarithms of the distributions of Kondo temperatures for $A=5$, $n/n_{\max}=0.01$ in Fig. 1b and for $A=1$, $n/n_{\max}=0.5$ in Fig. 1c. The results show that the effective exponents λ are large ($\lambda\propto 0.8$ for the realistic case $A\sim 1$,

$n/n_{\max}\sim 0.01$ for three space dimensions). It is too large compared to the experiments on three-dimensional heavy fermion systems,[14,16–18] for which values of $\lambda = 0.6-0.85$ were observed. Also, for some values of the parameters a value $\lambda > 1$ was obtained, which implies the absence of low-temperature divergences in such cases. The reason for such an overestimation can lie in disorder in the distribution of the local potentials ε_j of localized electrons, which was not taken into account in our description. However, smaller values of λ (0.26–0.42) have been observed for low-dimensional organic conductors and spin chains.[32,33] It turns out that large values of $\lambda \sim 0.2$ were observed for disordered ensembles of impurities close to a metal–insulator transition.

Such a distribution of Kondo temperatures produces non-Fermi-liquid behavior of many characteristics of the system.[25–27,31] For example, the ground-state magnetization of the system behaves as $M \propto (H/G)^{\lambda}$ (H is an external magnetic field), i.e., essentially in a nonlinear way. The static magnetic susceptibility at low temperatures is divergent as $T^{\lambda-1}/G^{\lambda}$. Also, the nonlinear behavior of the electron specific heat $c \sim (T/G)^{\lambda}$ implies divergent behavior of the Sommerfeld coefficient. The low-temperature behavior of the correlation length is proportional to $(G/T)^{\lambda}$, which implies non-Fermi-liquid behavior of the low-temperature resistivity. Finally, the imaginary part of the dynamic magnetic susceptibility is also divergent as $G^{\lambda-2}T^{1-\lambda}g(\omega/T)$, where $g(x) = x\int_1^{\infty} dy/y^{\lambda-1}(x^2+y^2)$ is a universal scaling function.[25]

Summarizing, in this work we have calculated the distribution of effective Kondo temperatures for a system of correlated electrons in which itinerant electrons are hybridized with randomly distributed localized electrons ($3d$, $4f$, or $5f$ orbitals). Those distributions depend on many parameters: concentration of localized orbitals, their Bohr radii, Coulomb interaction of localized electrons on orbitals, effective energies of localized electrons, bandwidths of itinerant electrons, etc. However, we have shown that only two parameters effectively govern the behavior of the distribution functions of Kondo temperatures. One of those parameters is the ratio of the density of localized electrons to the maximal density (in a hypercubic lattice). The other parameter is related to the maximal Kondo temperatures for which such an approach can be applied. We have shown that distributions of Kondo temperatures depend on the effective dimensionality of the disordered localized electrons. Due to such a disordered behavior of magnetic impurities many thermodynamic and kinetic characteristics of the systems considered manifest non-Fermi-liquid features in their low-energy characteristics.

*E-mail: zvyagin@mpipks-dresden.mpg.de

[1] J. Kondo, in *Solid State Physics: Advances in Research and Applications*, Vol. 23, edited by F. Seitz, D. Turnbull, and H. Ehrenreich, Academic, New York (1969), p. 184.
[2] A. M. Tsvelick and P. B. Wiegmann, Adv. Phys. **32**, 453 (1983).
[3] I. Affleck, Acta Phys. Pol. **26**, 1869 (1995).
[4] P. Schlottmann and P. D. Sacramento, Adv. Phys. **42**, 641 (1993).
[5] F. Steglich, J. Magn. Magn. Mater. **226**, 1 (2001).
[6] H. v. Löhneysen, F. Huster, S. Mock, A. Neubert, T. Pietrus, M. Sieck, O. Stockert, and M. M. Waffenschmidt, Physica B **230–232**, 550 (1997).
[7] M. B. Maple, M. C. de Andrade, J. Herrmann, Y. Dalichaouch, D. A. Gajewski, C. L. Seaman, R. Chau, R. Movshovich, M. C. Aronson, and R. Osborn, J. Low Temp. Phys. **99**, 223 (1995).
[8] G. R. Stewart, Rev. Mod. Phys. **73**, 797 (2001).
[9] C. Seaman, M. B. Maple, B. W. Lee, S. Ghamaty, M. S. Torikachvili, J.-S. Kang, L. Z. Liu, J. W. Allen, and D. L. Cox, Phys. Rev. Lett. **67**, 2882 (1991).
[10] G. R. Stewart, Phys. Rev. B **47**, 3208 (1993).
[11] B. Andraka, Phys. Rev. B **49**, 348 (1994).
[12] B. Andraka, Phys. Rev. B **49**, 3589 (1994).
[13] M. C. Aronson, R. Osborn, R. A. Robinson, J. W. Lynn, R. Chau, S. L. Seaman, and M. B. Maple, Phys. Rev. Lett. **75**, 725 (1995).
[14] O. O. Bernal, D. E. MacLaughlin, H. G. Lukefahr, and B. Andraka, Phys. Rev. Lett. **75**, 2023 (1995).
[15] K. Matsuhira, T. Sakakibara, and H. Amitsuka, Physica B **206–207**, 326 (1995).
[16] M. C. de Andrade, R. Chau, R. P. Dickey, N. R. Dilley, E. J. Freeman, D. A. Gajewski, M. B. Maple, R. Movshovich, A. H. Castro Neto, G. E. Castilla, and B. A. Jones, Phys. Rev. Lett. **81**, 5620 (1998).
[17] C. H. Booth, D. E. MacLaughlin, R. H. Heffner, R. Chau, M. B. Maple, and G. H. Kwei, Phys. Rev. Lett. **81**, 3960 (1998).
[18] D. E. MacLaughlin, R. H. Heffener, G. J. Nieuwenhuys, G. M. Luke, Y. Fudamoto, Y. J. Uemura, R. Chau, M. B. Maple, and B. Andraka, Phys. Rev. B **58**, R11849 (1998).
[19] L. Shlyk, J. C. Waerenborgh, P. Estrela, L. E. De Long, A. de Visser, and M. Almeida, J. Phys.: Condens. Matter **11**, 3525 (1999).
[20] R. N. Bhatt and D. S. Fisher, Phys. Rev. Lett. **68**, 3072 (1992).
[21] V. Dobrosavljević, T. R. Kirkpatrick, and G. Kotliar, Phys. Rev. Lett. **69**, 1113 (1992).
[22] E. Miranda, V. Dobrosavljević, and G. Kotliar, Phys. Rev. Lett. **78**, 290 (1997).
[23] E. Miranda, V. Dobrosavljević, and G. Kotliar, J. Phys.: Condens. Matter **8**, 9871 (1996).
[24] A. Klümper and A. A. Zvyagin, Phys. Rev. Lett. **81**, 4975 (1998).
[25] A. A. Zvyagin, Phys. Rev. B **62**, R6069 (2000).
[26] A. A. Zvyagin, Fiz. Nizk. Temp. **28**, 1274 (2002) [Low Temp. Phys. **28**, 907 (2002)].
[27] A. H. Castro Neto, G. Castilla, and B. A. Jones, Phys. Rev. Lett. **81**, 3531 (1998).
[28] A. Klümper and A. A. Zvyagin, J. Phys.: Condens. Matter **12**, 8705 (2000).
[29] R. B. Griffiths, Phys. Rev. Lett. **23**, 17 (1969).
[30] A. H. Castro Neto and B. A. Jones, Phys. Rev. B **62**, 14975 (2000).
[31] A. A. Zvyagin, Phys. Rev. B **63**, 033101 (2001).
[32] L. N. Bulaevsky, A. V. Zvarykina, Yu. S. Karimov, R. B. Lyubosky, and I. F. Shchegolev, Zh. Éksp. Teor. Fiz. **62**, 725 (1972) [Sov. Phys. JETP **35**, 384 (1972)].
[33] K. Ikegami, S. Kuroda, M. Saito, K. Saito, M. Sugi, T. Nakamura, M. Matsumoto, and Y. Kawabata, Phys. Rev. B **35**, 3667 (1987).
[34] K. Mukai, K. Suzuki, K. Ohara, J. B. Jamali, and N. Achiwa, J. Phys. Soc. Jpn. **68**, 3078 (1999).
[35] S. V. Demishev, R. V. Bunting, L. I. Leonyuk, E. D. Obraztsova, A. A. Pronin, N. E. Sluchanko, N. A. Samarin, and S. V. Terekhov, JETP Lett. **73**, 31 (2001).
[36] J. S. Koehler, in *Imperfections in Nearly Perfect Crystals*, Wiley, New York (1952), p. 197.
[37] C. L. Bauer, Philos. Mag. **11**, 827 (1965).
[38] A. Granato and K. Lücke, J. Appl. Phys. **27**, 583 (1956).
[39] M. Lakner, H. v. Löshneysen, A. Langenfeld, and P. Wölfle, Phys. Rev. B **50**, 17064 (1994).

This article was published in the original Russian journal. Reproduced here with stylistic change by AIP.

ELECTRONIC PROPERTIES OF METALS AND ALLOYS

Low-temperature anomalies heat capacity, Ohmic loss in the 0–100 MHz range, and linear dimensions of samples of uranium and some of its compounds

V. M. Dmitriev*

B. Verkin Institute for Low Temperature Physics and Engineering, National Academy of Sciences of Ukraine, Lenin Ave. 47, Kharkov 61103, Ukraine; International Laboratory of High Magnetic Fields and Low Temperatures, Gajowicka St. 95, Wroclaw 53–421, Poland

N. N. Prentslau, A. M. Gurevich, L. A. Ischenko, and A. V. Terekhov

B. Verkin Institute for Low Temperature Physics and Engineering, National Academy of Sciences of Ukraine, Lenin Ave. 47, Kharkov 61103, Ukraine

W. Suski

International Laboratory of High Magnetic Fields and Low Temperatures, Gajowicka St. 95, Wroclaw 53-421, Poland; W. Trzebiatowski Institute for Low Temperature and Structure Research, Polish Academy of Sciences, P.O. Box 1410, 50–950, Wroclaw, Poland

R. Troć

W. Trzebiatowski Institute for Low Temperature and Structure Research, Polish Academy of Sciences, P.O. Box 1410, 50–950, Wroclaw, Poland

(Submitted February 11, 2004)
Fiz. Nizk. Temp. **30**, 644–657 (June 2004)

From measurements of the heat capacity and resistivity of α uranium and the compounds UCu_5Al, UCu_4Al_8, UFe_4Al_8, and $U_3Ni_3Sn_4$ it is established experimentally for the first time that those properties have anomalies at temperatures near 60 K and in the vicinity of the transitions α_1(43 K), α_2(37 K), and α_3(23 K). It is assumed that these anomalies in compounds containing uranium as a constituent are due specifically to the uranium. It is found that in UCu_5Al the temperature dependence of the Ohmic loss changes from being of a semiconductor character at $T>T_N$ ($T_N=20$ K) to a metallic character at $T<T_N$. It is discovered that the linear dimensions of α uranium and of the compound UCu_5Al suffer a change upon repeated thermocycling from room to low temperatures. © *2004 American Institute of Physics.*
[DOI: 10.1063/1.1768353]

1. INTRODUCTION

According to Refs. 1 and 2, above the superconducting transition temperature ($T_c=1.5$ K) the resistivity ρ of α uranium increases in a practically linear and monotonic manner with increasing temperature, and the temperature curves of the resistivity and heat capacity do not have any anomalous deviations there. More recently[3] it has been shown, however, that the $\rho(T)$ and $C(T)$ curves of single-crystal α uranium both exhibit features at temperatures around 42, 37, and 23 K.

The authors of several papers (e.g., Refs. 4–12) have also observed anomalies on the temperature curves of other physical properties at those temperatures. Since anomalies at those temperatures were first observed in the magnetic susceptibility on top of the regular trend of $\chi(T)$ they have come to be called ''magnetic transitions'' and are denoted as α_1(43 K), α_2(37 K), and α_3(23 K).[4]

Another feature of the temperature curves of the physical properties of uranium in addition to the aforementioned is that, according to Refs. 1 and 13, an increase of the linear dimensions of an α uranium sample with decreasing temperature is observed at $T<60$ K. Although a change in the lattice parameter occurs at $T\sim 60$ K, there is practically no information in the literature concerning the fact that the physical properties should have anomalies at that temperature. It has been found[14–24] that some uranium compounds have anomalies in their physical properties at temperatures near the characteristic anomalies of pure α uranium. Interestingly, changes in the magnetic structure of UP and UAs occur[16] at the characteristic temperatures for pure uranium. At the same time, no anomalies have been observed on the temperature curves of the physical properties of the compound ThAs.[4] This naturally raises the question of whether the characteristic features of uranium are conferred upon its compounds.

After analyzing the above, far from complete, compendium of papers devoted to the low-temperature anomalies of the physical properties of uranium and its compounds, we arrive at some conclusions and pose some questions.

1. The studies of the anomalies of the physical properties of uranium have been done using single crystals. It is therefore unclear whether there are any features on the temperature curves of the Ohmic losses, for example, in the case of a polycrystalline metal and whether they would be manifested at high frequencies (both for uranium and its compounds).

2. Most of the papers cited above have reported one or

two anomalies, as a rule, on the temperature curves of the physical properties of both uranium and its compounds. However, in Refs. 3, 4, and 21 three anomalies were observed, at characteristic temperatures of 43, 37, and 23 K. We know of no studies in which all four anomalies of some physical parameter, at characteristic temperatures of 60, 43, 37, and 23 K, have been observed on the same sample.

3. If, as stated in Ref. 13, there is an anomalous increase in the lattice parameter a of uranium with decreasing temperature at $T \leqslant 60$ K, then, first, why has no reaction of the resistivity to the change in the lattice parameter a at that temperature been observed? Second, it is known[1] that repeated thermocycling of uranium to high temperatures followed by cooling to room temperature leads to a change in the linear dimensions of the samples. The nature of this phenomenon has not been been conclusively determined. It is unclear in this regard whether there will be a change in the size of uranium samples upon repeated thermocycling to cryogenic rather than high temperatures, and how the change in sample size occurs when a uranium sample is thermocycled to $T < 60$ K. Third, will analogous changes in size on thermocycling be observed for samples of uranium-containing compounds?

The goal of this study is to answer to those questions, mainly to decide on the basis of an analysis of the experimental results whether uranium confers the features of its electronic, magnetic, and phonon systems on compounds containing it. For that purpose we investigated the temperature dependence of the Ohmic loss and the heat capacity of α uranium and some uranium compounds at temperatures around 60, 43, 37, and 23 K and also measured the linear dimensions of polycrystalline α uranium and a single crystal of the compound UCu_5Al upon repeated thermocycling of the samples to cryogenic temperatures.

2. SAMPLES AND MEASUREMENT TECHNIQUES

The polycrystalline uranium samples were in the form of cylinders 8 mm in diameter and 10 mm long. The UCu_5Al single crystals were grown by the Bridgman method in the form cylinders 5.6 mm in diameter and 21.5 mm long (No. 1) and 3.7 mm in diameter and 10 mm long (No. 2).

The UFe_4Al_8 single crystal was in the form of a cylinder 2.6 mm in diameter and 7.6 mm long. The polycrystalline samples of the compounds UCu_4Al_8 and $U_3Ni_3Sn_4$ were obtained in the form objects of complex cross section by the technique proposed in Ref. 24.

These compounds were chosen for the study of the temperature dependence of R_s in materials of different crystal structure (uranium has an orthorhombic structure, UCu_5Al tetragonal, UFe_4Al_8 and UCu_4Al_8 tetragonal with the $ThMn_{12}$ lattice, and $U_3Ni_3Sn_4$ a structure of the $ThMn_{17}$ type).

The temperature dependence of the surface resistance R_s at frequencies up to 100 MHz was measured by a resonator method using the equipment described in Ref. 25. Measurements of ρ and of the impedance Z of the samples up to 10 MHz were made by the four-contact method. Since it was assumed that the anomalies of the surface resistance on the $R_s(T)$ curves might be of low amplitude, we made 10–15 measurements of the parameters of the oscillatory measuring circuit with the samples in place and then the results were subjected to mathematical processing. The heat capacity of the samples was measured by the method of adiabatic calorimetry to an accuracy of 0.5%. The change in the linear dimensions of the samples upon thermocycling to room temperature was determined to an accuracy of ± 2 μm by means of a capacitive dilatometer.

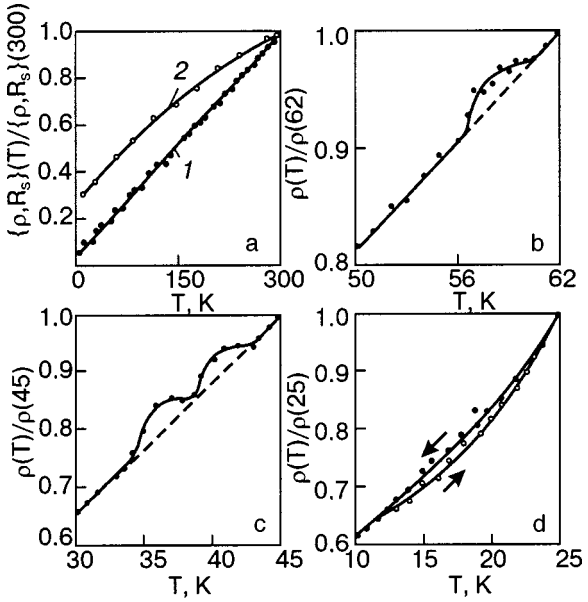

FIG. 1. Temperature dependence of the resistivity ρ (*1*) and surface resistance R_s (*2*) divided by the values $\rho(300)$ and $R_s(300)$, respectively, for polycrystalline α uranium (a), and the $\rho(T)/\rho(62)$ (b), $\rho(T)/\rho(45)$ (c), and $\rho(T)/\rho(25)$ (d) curves for the same sample of α uranium.

3. EXPERIMENTAL RESULTS

Ohmic losses of polycrystalline α uranium

It was found experimentally that the resistivity ρ of the sample of α uranium studied is a linear function of temperature (Fig. 1a, curve *1*), as in Ref. 1. Here $\rho(300) = 33 \times 10^{-8}$ $\Omega \cdot$m, while $\rho(20) = 4.4 \times 10^{-8}$ $\Omega \cdot$m, i.e., $\rho(300)/\rho(20) = 7.5$. Thus the resistivity of the investigated sample of α uranium is typical for a polycrystalline metal.[1]

For polycrystalline α uranium at $T = 300$ K the active and reactive components of the impedance at a measurement frequency of 10 MHz are $R_s = 8 \times 10^{-3}$ Ω and $X_s = 7.9 \times 10^{-3}$ Ω, respectively. Here both R_s and X_s go as $\sim(\rho f)^{0.5}$ (the $R_s(T)$ dependence is shown by curve *2* in Fig. 1a). At the same time, the calculated values of R_s and X_s according to the equations presented in Ref. 26 are equal to 3.6×10^{-3} Ω, which is a factor of 2.2 larger than the experimental values.

We note that the skin depth in α uranium as calculated from the frequency at which the sharp increase of the modulus of the impedance Z begins on the frequency curves measured by the four-contact method is also a factor of 2 larger than that determined from the measured values of ρ and R_s: $\delta = \rho/R_s$ (Ref. 26).

The temperature dependence of the resistivity and of the active and reactive parts of the impedance of α uranium have a number of anomalies in the vicinity of the characteristic temperatures.

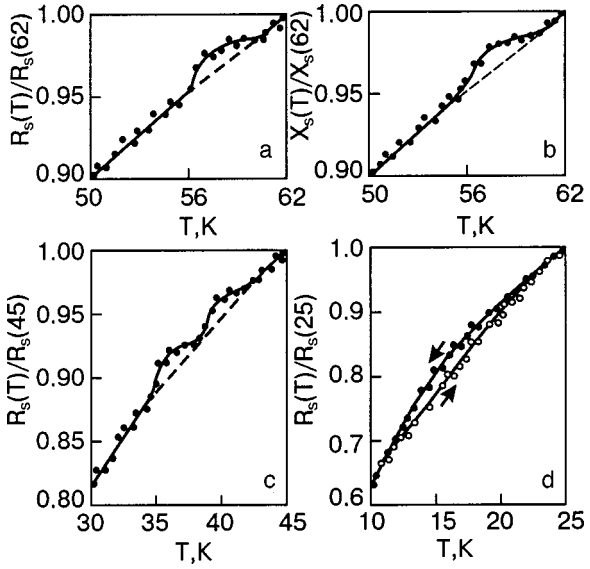

FIG. 2. Temperature dependence of $R_s/R_s(62)$ (a), $X_s/X_s(62)$ (b), $R_s/R_s(45)$ (c), and $R_s/R_s(25)$ (d) for α uranium at a frequency of 9 MHz.

The temperature curves of the resistivity $\rho(T)$ and of the surface resistance R_s and surface reactance X_s of a polycrystalline sample of α uranium at a frequency of 9 MHz in the temperature interval 62–50 K are shown in Figs. 1b, 2a, and 2b, respectively; the curves are normalized to $\rho(62\ \mathrm{K})$, $R_s(62\ \mathrm{K})$, and $X_s(62\ \mathrm{K})$ $[R_s(62\ \mathrm{K})=4.2\times10^{-3}\ \Omega$, and $X_s(62\ \mathrm{K})=4.15\times10^{-3}\ \Omega]$.

It is seen in Figs. 1b, 2a, and 2b that in the interval interval 60–56 K the curves of ρ, R_s, and X_s exhibit anomalies in the form of "steps," i.e., the slope $\partial(\rho,R_sX_s)/\partial T$ decreases in the temperature range 60–58 K. Thus the resistivity and impedance of this substance exhibit features in the vicinity of $\sim$60 K, i.e., at the temperature where the linear expansion coefficient of α uranium was found to have anomalies in Refs. 1 and 13.

Figure 1c,d and 2c,d show the temperature curves analogous to those shown in Fig. 1b and 2a,b but measured in the temperature intervals 45–30 K and 25–10 K. It follows from the data in Fig. 1c and 2c that at the temperatures 43 and 38 K, i.e., the temperatures of the α_1 and α_2 transitions, anomalies of ρ and R_s are observed, similar in shape to the anomalies of these quantities observed at $T\sim60$ K. We note that no temperature hysteresis of ρ and R_s was observed in the vicinity of the temperatures where the transitions α_1 and α_2 occur.

At the same time, at temperatures where the transition $\alpha_3(23\ \mathrm{K})$ ordinarily occurs the anomalies of ρ and R_s have the same character as in single-crystal uranium,[3] and thermal hysteresis is observed in the temperature interval 12–23 K (Figs. 1d and 2d).

Temperature dependence of the optical loss and the heat capacity of the compound UCu_5Al

For comparison, Fig. 3a shows the temperature dependence of the resistivity $\rho(T)$ of a polycrystalline sample of UCu_5Al, taken from Ref. 20. Figure 3b shows the $\rho(T)$ curves for our UCu_5Al single-crystal sample No. 1, measured along the growth axis ($\rho_\parallel$, dots) and in the direction

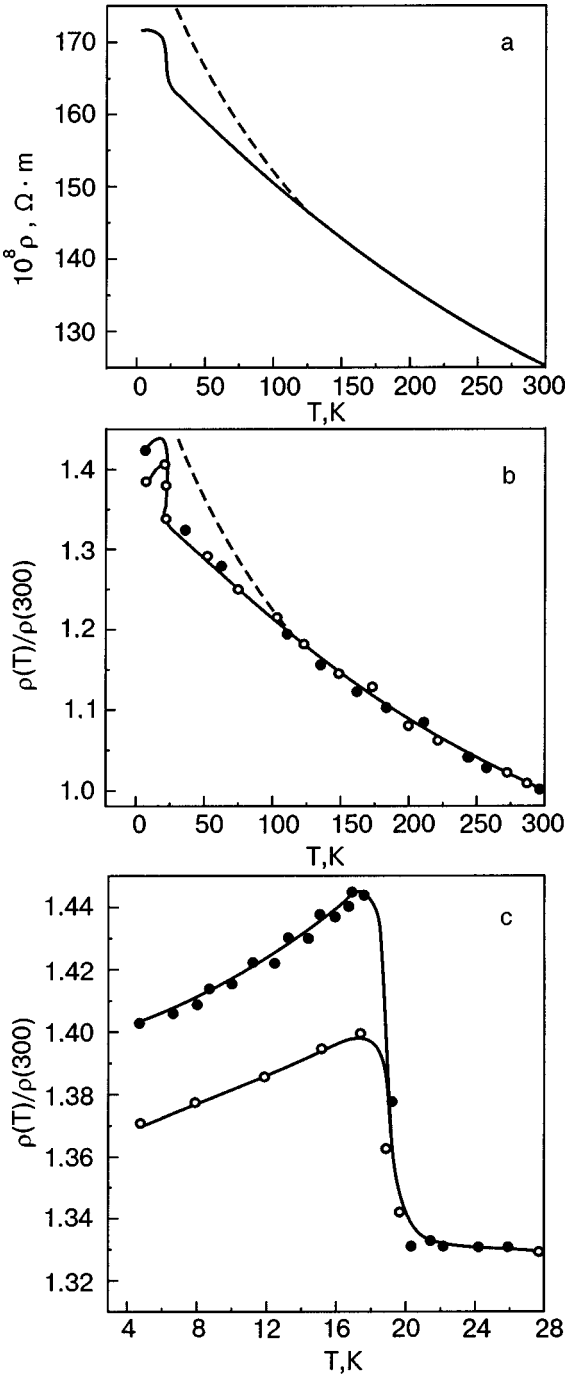

FIG. 3. Temperature dependence of the resistivity $\rho(T)$ of a polycrystalline sample of UCu_5Al according to Ref. 20 (a). The $\rho(T)/\rho(300)$ curves in the temperature intervals 4.2–300 K (b) and 4.2–28 K (c) for a UCu_5Al single crystal, measured along its growth axis (dots) and perpendicular to the growth axis (circlets).

perpendicular to the growth axis ($\rho_\perp$, circlets) (the a axis is slightly inclined to the growth axis of the single crystal).

The $\rho(T)$ curves for both the polycrystalline and single-crystal UCu_5Al can be described in the interval 300–100 K by a single expression:

$$\rho(T)=\rho_0-A\ln T, \tag{1}$$

but with different coefficients. For example, for the polycrystal $\rho_0=257\times10^{-8}\ \Omega\cdot\mathrm{m}$, $A=23.1\times10^{-8}\ \Omega\cdot\mathrm{m}$, $\rho(300)=125\times10^{-8}\ \Omega\cdot\mathrm{m}$, while for the single crystal $\rho_0=176.7\times10^{-8}\ \Omega\cdot\mathrm{m}$, $A=16.3\times10^{-8}\ \Omega\cdot\mathrm{m}$, and $\rho_0(300)=83.7$

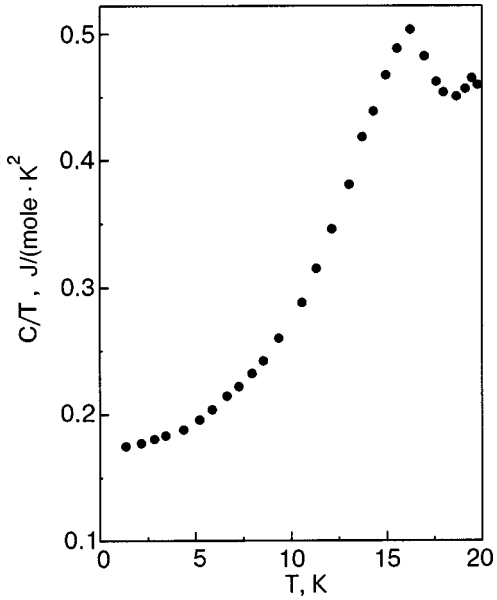

FIG. 4. Temperature dependence of C/T for a UCu_5Al single crystal in the temperature interval 1.5–20 K.

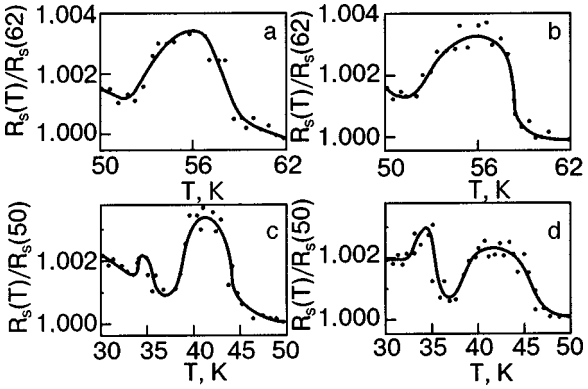

FIG. 5. Temperature dependence of $R_s/R_s(62)$ for a UCu_5Al single crystal, measured at a frequency of 9 MHz with the current flowing along the growth axis of the single crystal (a) and perpendicular to the growth axis (b). The $R_s(T)/R_s(50)$ curves measured at a frequency of 9 MHz with the current flowing along the growth axis of the single crystal (c) and perpendicular to the growth axis (d).

$\times 10^{-8}\ \Omega\cdot$m. Thus the resistivity of the UCu_5Al single crystal is lower than that of the polycrystalline sample by a factor of 1.5.

In both the polycrystalline[20] and single-crystal samples of UCu_5Al an antiferromagnetic transition, accompanied by a jump in ρ, occurs at $T\approx 18$ K. However, in the polycrystalline sample ρ is practically independent of temperature at $T<T_N$, while in the single crystal it decreases with decreasing temperature. Fragments of the curves of Fig. 3b in the temperature interval 28–4.2 K are shown on an expanded scale in Fig. 3c. Here $\rho(T)$ along the growth axis of the single crystal (dots) at $T<18$ K is described by

$$\rho(T)=\rho_1+BT^2, \tag{2}$$

where

$$\rho_1=117.7\times 10^{-8}\ \Omega\cdot\text{m} \quad \text{and} \quad B=1.3\times 10^{-10}\ \Omega\cdot\text{m}\cdot\text{K}^{-2}.$$

From the data in Fig. 3b,c it also follows that a small but quite noticeable anisotropy of $\rho(T)$ is present at $T<T_N$. Here, as in the direction along the growth axis of the single crystal, the $\rho(T)$ dependence in the direction perpendicular to the growth axis also takes on a metallic character and can be described by an equation of the type (2), but $\rho_\perp<\rho_\parallel$. It can be noted that other similar compounds of uranium, e.g., UCu_5In (Ref. 27), also have $\rho(T)$ curves that can be described by Eq. (2) for $T<T_N$.

Studies of the active R_s and reactive X_s components of the impedance of the compound UCu_5Al in the temperature interval 300–5 K and frequency range 100 kHz–11 MHz have shown that the frequency and temperature dependence of $R_s(f,T)$ and $X_s(f,T)$ can be described by the equations

$$R_s=Df^{0.5}\rho^n,\quad X_s=Sf^{0.5}\rho^k, \tag{3}$$

where D and S are some constants and n and k are equal to 0.135 and 0.007, respectively, for the samples measured.

Figure 4 shows a plot of the temperature dependence of the heat capacity for UCu_5Al sample No. 2 in the coordinates C/T versus T. The maximum of the heat capacity, which is due to antiferromagnetic ordering, is observed at $T=16.37$ K, and the start of the transition occurs at $T=18.7$ K.

The $\rho(T)$, $R_s(T)$, and $X_s(T)$ curves of the UCu_5Al single crystal have a series of anomalies near the same temperatures as for pure polycrystalline α uranium.

Figure 5a,b shows the temperature dependence of $R_s(T)/R_s(62)$ of a UCu_5Al single-crystal sample, measured for current directions along the growth axis of the crystal (a) and perpendicular to the growth axis (b). Figure 5a,b show the same relations as in Fig. 5c,d only for the temperature range 50–30 K. The measurements were made at a frequency of 9 MHz.

Thus at temperatures near 60 K and also for temperatures where the α_1 and α_2 transitions occur in α uranium the surface resistance R_s exhibits anomalies in the form of an increase in the Ohmic loss above its regular trend. At temperatures in the region where the α_3 transition is observed in pure polycrystalline α uranium the compound UCu_5Al, according to Ref. 20 and the present study (Fig. 3b), exhibits antiferromagnetic ordering, which is accompanied by a significant (up to 6%) increase in the Ohmic loss.

$R_s(T)$ and $C(T)$ for uranium compounds with a structure of the $ThMn_{12}$ type

The anomalies of the Ohmic loss $R_s(T)$ for polycrystalline samples of the compound UCu_4Al_8 and single crystals of UFe_4Al_8 were investigated at a frequency of 9 MHz.

The temperature dependence of the Ohmic loss and heat capacity of a polycrystalline sample of UCu_4Al_8 is given over a wide temperature interval in Ref. 21. It follows from that study that $R_s(T)$ and $C(T)$ have anomalies in the temperature regions near 60 and 35 K and also near 20 K. Since the scale of the figures in Ref. 21 does not permit a detailed analysis of the anomalies of $R_s(T)$ and $C(T)$, our data from Ref. 21 and some additional measurements are plotted on an expanded scale in Fig. 6 to show the features of these curves.

The anomaly of R_s in the temperature interval 70–50 K is manifested as excess growth of the resistance, with two maxima at temperatures of 60 and 55 K (Fig. 6a). Anomalies

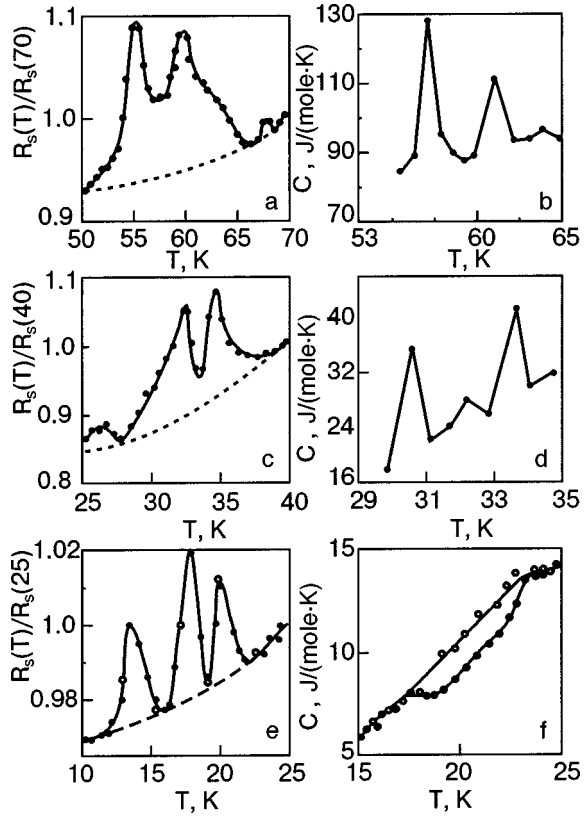

FIG. 6. $R_s(T)/R_s(70)$ (a), $C(T)$ in the temperature interval 53–65 K (b), $R_s(T)/R_s(40)$ (c), $C(T)$ in the temperature interval 29–35 K (d), $R_s(T)/R_s(25)$ (e), and $C(T)$ in the temperature interval 15–25 K (f) for a polycrystalline sample of UCu_4Al_8 (R_s was measured at a frequency of 9 MHz).

of the same shape appear on the temperature dependence of the heat capacity (Fig. 6b) at temperatures of 62 and 57 K.

It is seen in Fig. 6c,d that the anomalies of R_s and C in the temperature regions α_1 and α_2 occur not at 43 and 38 K as in uranium but at somewhat lower temperatures. For example, the maxima of R_s are observed at 34.5 and 32 K, and the maxima of the heat capacity, at 33.5 and 30.6 K.

In the temperature interval 25–10 K the features of R_s are manifested in the form of a series of spikes (Fig. 6e). Here the R_s values measured on cooling (dots) and heating (circlets) did not display any hysteresis. At the same time, the curves of the heat capacity $C(T)$ show multivaluedness in different series of measurements, as can be seen in Fig. 6f, where the dots and circlets are the results of different series of measurements of $C(T)$.

As in the case of UCu_4Al_8, the R_s curves measured at a frequency 70 MHz for UFe_4Al_8 reveal the presence of features in the Ohmic loss (Fig. 7). Unlike the case of pure polycrystalline α uranium, the Ohmic loss does not increase in the interval 70–55 K but decreases, with a minimum at 61 K. The R_s anomalies characteristic for the temperatures of the α_1 and α_2 transitions are observed at 46 and 37 K (Fig. 7b).

The compound UFe_4Al_8 also has a low-temperature feature of R_s, but, unlike α uranium, it does not take the form of hysteresis but rather there is anomalously high Ohmic loss with a maximum at $T=22.5$ K (Fig. 7c).

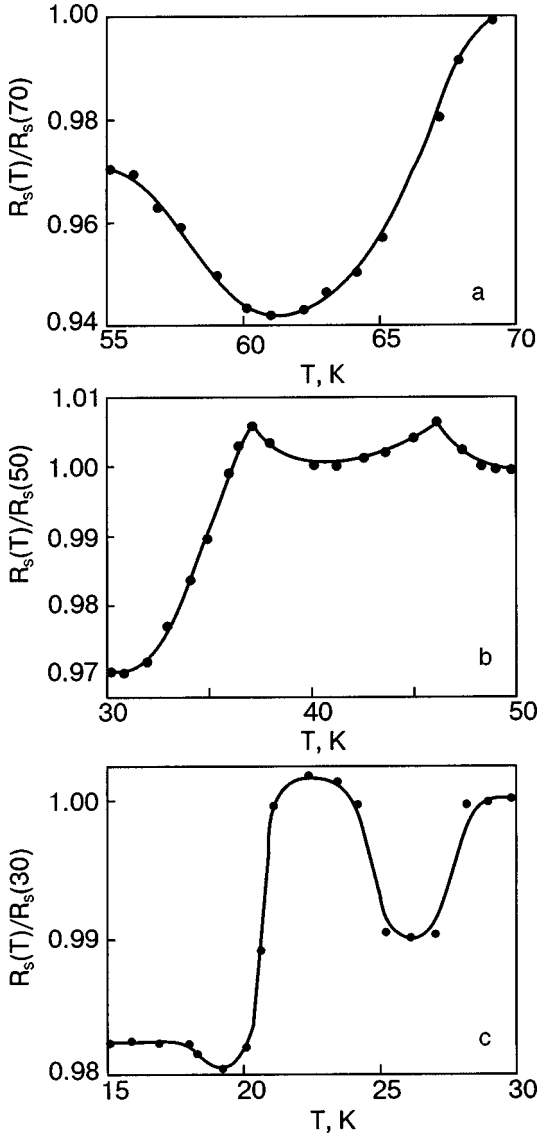

FIG. 7. $R_s(T)/R_s(70)$ (a), $R_s(T)/R_s(50)$ (b), and $R_s(T)/R_s(30)$ (c) for a UFe_4Al_8 single crystal, measured at a frequency of 70 MHz.

Anomalies of the Ohmic loss of the compound $U_3Ni_3Sn_4$

Curve *1* in Fig. 8a shows the temperature dependence $\rho(T)$ measured in the present study for $U_3Ni_3Sn_4$, while curve *2* shows $R_s(T)$ at a frequency of 9 MHz in the temperature interval 300–4.5 K. As is seen from Fig. 8a, $R_s \sim \rho^{1/2}$ in the entire temperature range of the measurements.

In studying the $\rho(T)$ and $R_s(T)$ curves for the compound $U_3Ni_3Sn_4$ we made the first observation of their hysteresis at $T>60$ K (Fig. 8b). The values of $\rho(T)/\rho(300)$ on cooling and heating are shown by curves *1* (dots) and *2* (circlets), respectively. Here $\rho(T)$ is independent of temperature on heating above 190 K. Thus $T=190$ K is some characteristic temperature. At a given temperature the resistivity of the sample during cooling is less than that during heating (Fig. 8b). If the sample is cooled not to $T<60$ K but to intermediate temperatures (e.g., to $T=130$ K; Fig. 8b) and then heated (curve *3*), $\rho(T)$ again becomes independent of temperature at $T>190$ K, but its dependence is different in the temperature interval 190–130 K. If the sample is cooled after being heating only to 190 K (curve *4*), then the hysteresis ρ

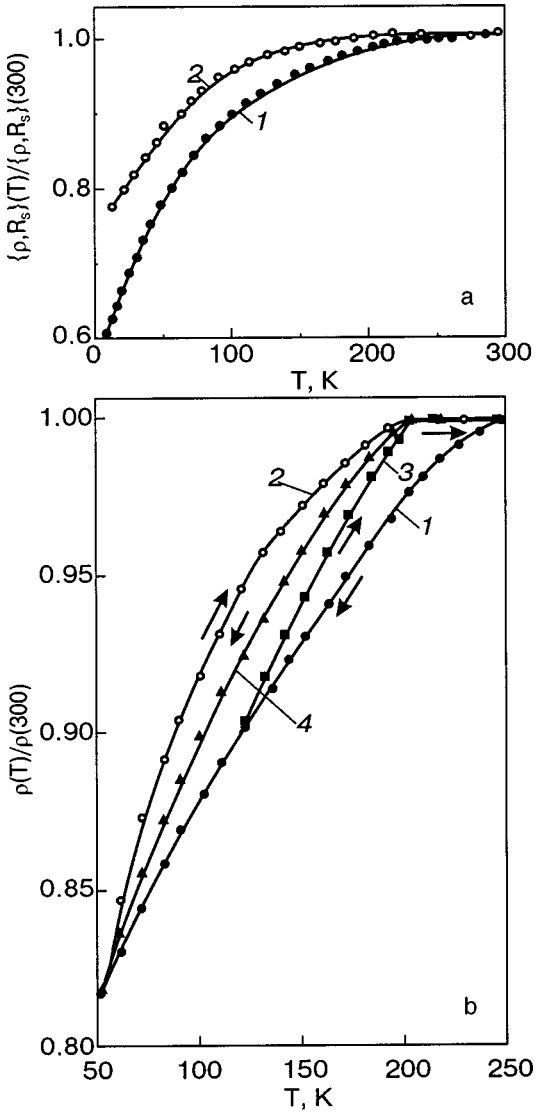

FIG. 8. $\rho(T)/\rho(300)$ (*1*) and $R_s(T)/R_s(300)$ at a frequency of 9 MHz (*2*) for a $U_3Ni_3Sn_4$ sample (a). Curves of $\rho(T)/\rho(300)$ for $U_3Ni_3Sn_4$ in the interval interval 50–250 K (hysteresis effects): cooling of the sample from 250 to 50 K (*1*), heating of the sample from 50 to 250 K (*2*), heating of the samples from 130 to 250 K (*3*), and cooling of the sample from 190 to 50 K (*4*) (b).

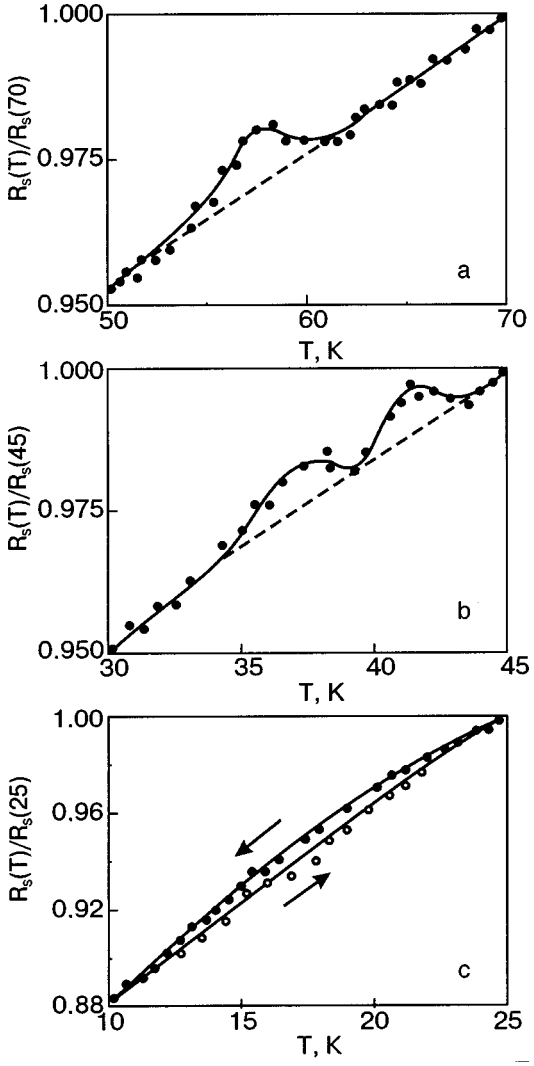

FIG. 9. $R_s(T)/R_s(70)$, $R_s(T)/R_s(45)$, and $R_s(T)/R_s(25)$ for $U_3Ni_3Sn_4$, measured at a frequency of 9 MHz.

is again observed at $T>60$ K and is repeated on heating (curve *2*) (cooling and heating are indicated by arrows in Fig. 8b). As in the case of α uranium, the compound $U_3Ni_3Sn_4$ has anomalies of the Ohmic losses near the temperatures characteristic for α uranium (Fig. 9). It follows from the data in Fig. 9a,b that at $T=60$, 43.5, and 38 K there are features of R_s in the form an increase relative to the regular trend of $R_s(T)$ (dashed curve). At temperatures in the region 25–10 K one observes the same kind of hysteresis of R_s (Fig. 9c) as for polycrystalline α uranium (see Fig. 2d). For $U_3Ni_3Sn_4$ the resistance measured on heating in the temperature region 25–10 K is lower than that measured on cooling (Fig. 2d and 9c), unlike the hysteresis at temperatures above 60 K (Fig. 8b).

Change in the linear dimensions of α uranium and of the compound UCu_5Al upon thermocycling

Figure 10 shows the values of the diameter d (a), length l (b), and volume V (c) of an α uranium sample as functions of the number N of thermocycles, and Fig. 11 shows the same quantities as functions of the number of thermocycles for the compound UCu_5Al.

The thermocycling of the samples and the measurements of their linear dimensions during the thermocycling process were carried out in the following order.

Samples with diameters d_1, lengths l_1, and volumes V_1 were subjected to 150 thermocycles in the temperature interval 300–77 K. The dimensions were checked after every 25 thermocycles. After 50 cooling–heating cycles the diameters, lengths and volumes of the samples had changed to the values d_2, l_2, and V_2 (curves *1* in Figs. 10 and 11). Then the samples with dimensions of d_2, l_2, and V_2 were thermocycled in the temperature interval 300–4.2 K (150 cycles), as a result of which their dimensions changed to the values d_3, l_3, and V_3 (curves *2* in Figs. 10a,b,c and 11a,b,c).

After thermocycling to helium temperatures the samples with dimensions of d_3, l_3, and V_3 were again thermocycled in the temperature interval 300–77 K (100 cycles), as a result of which their dimensions changed to the values d_4, l_4, and V_4 (curves *3* in Figs. 10 and 11).

This order of performance of the series of thermocycles makes it possible to determine the sign of the derivative

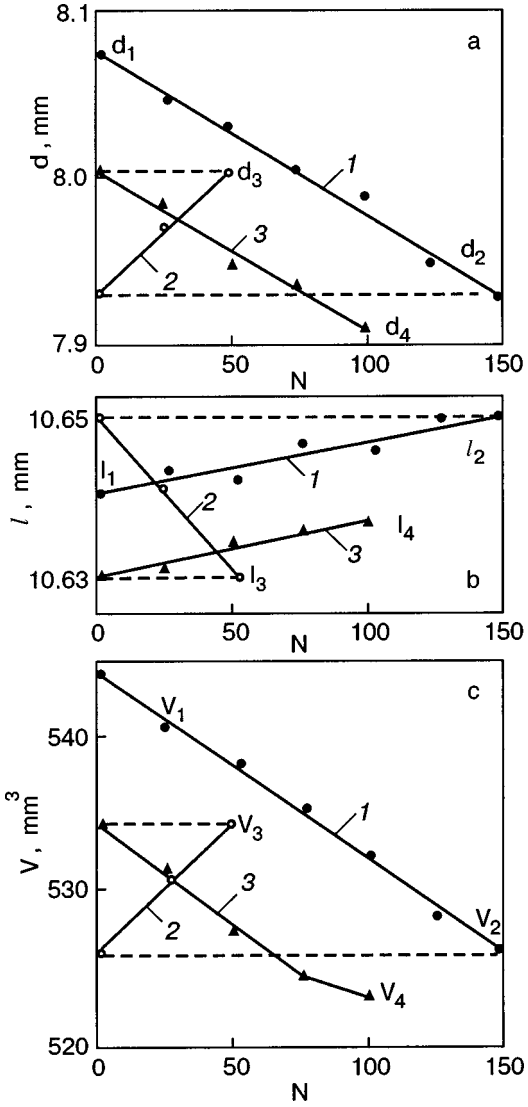

FIG. 10. Values of the diameter d (a), length l (b), and volume V (c) of a polycrystalline sample of α uranium as a function of the number N of thermocycles; thermocycling in the intervals of temperature T [K]: 300–77 (*1*), 300–4.2 (*2*), repeated thermocycling in the temperature interval 300–77 (*3*).

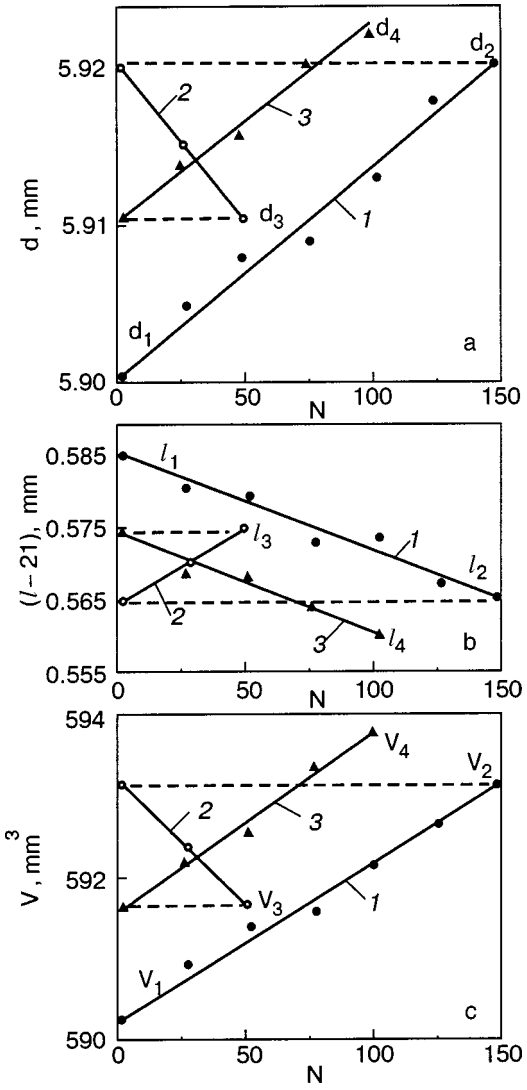

FIG. 11. Values of the diameter d (a), the changes in length $(l-21)$ relative to the original length (b), and volume V (c) for a UCu_5Al single crystal as a function of the number N of thermocycles; thermocycling in the interval of temperatures T [K]: 300–77 (*1*), 300–4.2 (*2*), and repeated thermocycling in the temperature interval 300–77 K (*3*).

$\partial(d,l,V)/\partial N$ on the same samples during their thermocycling in the temperature intervals 300–77 K and 300–4.2 K.

It is seen in Fig. 10 that during thermocycling of a sample of α uranium to nitrogen temperatures its diameter and volume decrease, while its length increases slightly. At the same time, on thermocycling to helium temperatures the diameter and volume increase and the length decreases.

The dimensions of the UCu_5Al single crystal, like the polycrystalline sample of α uranium, also changed during thermocycling. However, unlike the α uranium samples, the diameter and volume increased and its length decreased with increasing number of thermocycles with cooling to nitrogen temperatures. For thermocycling to helium temperatures the diameter and volume of the sample decreased and its length increased.

4. DISCUSSION OF THE RESULTS

Our results show that the functional relation between ρ, R_s, X_s, and f for our α uranium samples obeys the law of classical electrodynamics.[26] We note that throughout the investigated temperature range only the classical skin effect is present. According to Ref. 26, the fact that the reactive part of the impedance is 10% less than the resistive part is typical for cylindrical conductors of all metals at frequencies corresponding to the classical skin effect. The fact that the experimental values of R_s and X_s for α uranium are twice the calculated values may attest to nonuniformity of ρ along the radius of the α uranium sample; ρ may increase from the center toward the periphery of the sample and be maximum near the surface. Because dc measurements give the integrated value of ρ, that value may be smaller than the value of ρ near the surface of the sample, which makes for an increase in R_s and X_s, i.e., quantities whose values are determined by the surface region and the state of the physical quantities near the surface.

It was shown in Refs. 20 and 28 that in the compound UCu_5Al the temperature dependence of $\rho(T)$ in the interval 300–100 K, where $\partial\rho/\partial T<0$, is due to a Kondo interaction. Here, according to Ref. 28, the temperature dependence

$\rho(T)$ in the range 100–20 K is due to the presence of a narrow electron band in the electron spectrum. It follows from the data shown in Fig. 3 that at $T<T_N$ the value of ρ for polycrystalline UCu_5Al is practically independent of temperature, while for the single crystal it decreases by a quadratic law as the temperature is lowered; this may be an indication of Fermi-liquid behavior of UCu_5Al for $T<T_N$. Thus the phase transition at $T=T_N$ in principle reorganizes the system of quasiparticle transport, changing it from a ''semiconductor'' to a metallic type.

The facts adduced above are evidence that the electrical resistance of UCu_5Al is due not only to the causes inherent to pure metals and compounds (electron–phonon interaction, scattering on impurities and dislocations, etc.), but also magnetic factors that materially alter the usual character of $\rho(T)$.

It is possible that the very complex dependence of ρ on many physical factors in the single crystal UCu_5Al is also the reason why anisotropy of the values of ρ and $\partial\rho/\partial T$ measured in different directions with respect to the crystalline axes in different single-crystal samples of UCu_5Al is sometimes observed and sometimes not (for example, compare the results of the present study and Ref. 29).

An interesting feature of the single-crystal samples of UCu_5Al studied here is that for $T\leqslant T_N$ the value of $\rho_\perp$ is smaller than the value of $\rho_\parallel$ (Fig. 3b,c) at the same value of the temperature. Here the difference between $\rho_\parallel$ and $\rho_\perp$ begins at the middle of the transition ($T=18.8$ K), and their maxima in temperature coincide, at $T=17.5$ K. The start of the transition can be taken as $T=20$ K. Thus the width of the phase transition has a value $\Delta T_N=2.5$ K.

Comparing the results of our measurements of the heat capacity on single-crystal UCu_5Al with the results of Ref. 20, obtained on a polycrystalline sample, one can show that the values of γ and T_N in the two cases are close: $\gamma=0.175$ and 0.18, and $T_N=16.4$ and 15.8 K.[20]

It follows from the data in Fig. 3 that a jumplike increase in the resistance of UCu_5Al begins at 20 K, in agreement with the measurements of other authors.[20,28] Here $T_N=17.5$ K, also in agreement with the results of Ref. 30 (18 ± 1) K and close to the data of Refs. 20 and 31 (18 K). The most important result of the comparison of the magnetic ordering effects studied by the different methods is the difference in the values of T_N. Heat-capacity data give a lower temperature for the heat absorption maximum than are obtained from measurements of the magnetic and resistive characteristics. For example, the maximum of the heat capacity in Fig. 4 occurs at $T=16.4$ K, while in Ref. 20 it was observed at 15.8 K. Thus the value of T_N determined by measurements of the electrical resistance and heat capacity on the same sample of UCu_5Al are different, as was previously mentioned in Ref. 20. It is hard to explain this fact at present. One can say, however, that the change of the electronic spectrum in compounds has a stronger influence on the resistive properties of UCu_5Al than on the heat capacity. Therefore, it is possible that the temperature of the start of the transition to the antiferromagnetic state corresponds to the temperature at which the resistances measured in the directions of the different axes are different, and there is also a minimum of the heat capacity.

It was mentioned in Ref. 4 that there is much about low-temperature phase of uranium that remains unclear. In particular, the order of phase transitions taking place at the different characteristic temperatures is not yet clear. The same can be said about the change in the dimensions of uranium samples upon thermocycling.[1] Therefore these questions merit a separate discussion.

The data pertaining to the low-temperature anomalies of α uranium and some of its compounds are presented in Table I. The order of the phase transition is denoted by the Roman numerals I and II, and the physical parameters that were reported in the given source to have a feature at the respective temperatures, with no statement as to the order of the phase transition, are also indicated. The empty cells mean that no features of the physical parameters were observed at that temperature in the given source.

In analyzing the data of Table I we note the following. In the early sources pertaining to the transmission of α uranium (with the exception of Ref. 12 and 32) only the presence of phase transitions was reported without an indication of the order of those transitions. In Ref. 12 it was noted that the α_2 transition is first-order, and in Ref. 32 it was reported that the α_1 transition is second-order. In Ref. 3 it was shown on the basis of an analysis of the temperature dependence of the heat capacity and Ohmic loss that α_1, α_2, and α_3 are all first-order phase transitions.

We note that all of the sources cited have indicated the presence of one or two transitions, both for uranium and for its compounds. Only in Refs. 3, 4, and 21 is the presence of three transitions shown. At a temperature $\sim$60 K in pure α uranium there is only an anomalous change in the dimensions of the crystal lattice, which can attest to a first-order phase transition. At the same time, phase transitions near this temperature are observed in uranium compounds, and for UAs it has been shown that it is a first-order transition that occurs there.

In the compound UNiGe there is a phase transition in the vicinity of α_1 which is reported as second-order in Ref. 23 and first-order in Ref. 33.

In the majority of the sources cited there is practically no information about the crystal structure of the materials studied at temperatures before and after the transitions. References 1, 4, 6, 11, and 14 are exceptions. It was indicated in Ref. 1 that for $T<60$ K the dimension along the a axis of α uranium increases. The same was indicated in Refs. 4 and 6, only the increase in the a axis began at 47 K. According to Ref. 11, the a axis increases below 43 K.

It was noted in Ref. 14 that in the compound UP the coefficient of linear thermal expansion becomes negative at 22 K. It should be noted in this regard that a change in size is a specific characteristic of first-order phase transitions, and a change in size can be caused by magnetostriction effects, which, as we know, are large in the actinides. However, the additional experimental data are needed.

As a result of our experimental studies of the temperature dependence of R_s we have established for the first time that anomalies of the surface resistance take place both in α uranium and in the uranium compounds UCu_5Al, UFe_4Al_8, UCu_4Al_8, and $U_3Ni_3Sn_4$ at temperatures both in the vicinity of 60 K and near the α_1, α_2, and α_3 transitions of uranium. It should be emphasized that we observed the anomalies of

TABLE I. Characteristics of the low-temperature anomalies of the physical properties of α uranium and some uranium compounds.

Compound	~ 60 K	α_1(43 K)	α_2(37 K)	α_3(23 K)	Ref.	Year
α-U	*a*				[13]	1952
		α, ρ, *a*			[6]	1961
	a	*a*			[1]	1962
		ρ, α			[9]	1966
		χ	χ		[5]	1968
			I		[12]	1979
		CDW			[11]	1980
		CDW			[10]	1981
		χ, *a*	χ	χ	[4]	1990
		II, CDW			[32]	2000
		I, ρ, *C*	I, ρ, *C*	I, ρ, *C*	[3]	2001
	R_s, X_s, ρ	R_s, X_s, ρ	R_s, X_s, ρ	I	Present study	2004
UP				*a*	[14]	1980
				I	[15]	1987
UAs	*C*				[16]	1982
	I			I	[17]	1980
UNi_2				ρ	[18]	1980
$U_{(1-x)}Pr_xP$				χ	[19]	1980
UNiGe		I, χ			[33]	1988
		II, *c*			[23]	1991
UCu_5Al				ρ	[20]	1998
	R_s, X_s, ρ	R_s, X_s, ρ	R_s, X_s, ρ	R_s, X_s, ρ	Present study	2004
UCu_4Al_8	R_s, ρ	R_s, ρ	R_s, ρ		[21]	2001
	I, R_s, *C*	I, R_s, *C*	I, R_s, *C*	I, R_s, *C*	Present study	2004
UFe_4Al_8	R_s	R_s	R_s	R_s	Present study	2004
$U_3Ni_3Sn_4$	I, R_s	R_s	R_s	I, R_s	Present study	2004

R_s in samples of polycrystalline α uranium with typical parameters of ρ for uranium and also in polycrystalline and single-crystal compounds with different types of crystal lattices.

In Fig. 6b,d,f we show the experimental data on the heat capacity obtained in different series of measurements. Additional measurements of the heat capacity have established that the character of the $C(T)$ curves in the given temperature intervals is conditioned by the thermal prehistory of the sample and the kinetic parameters of the experiment (the heating rate and temperature "step"). This is typical for a first-order phase transition. The same can be said about the α_3 transition in α uranium and in the compound $U_3Ni_3Sn_4$, since there hysteresis is observed on the $R_s(T)$ curve. We note that for $T=60$ K apparently a first-order transition also occurs in that compound, as is confirmed by the presence of hysteresis on the $R_s(T)$ curve (Fig. 8b).

Thus in the present study and in some of the papers cited it has been shown that the phase transitions at the characteristic temperatures of uranium and its compounds are first-order transitions. An exception is the compound UNiGe, for which the data on the α_1 transition at 43 K are contradictory.[23,33]

We make special note of the following. The authors of Ref. 16 observed an anomaly of the heat capacity $C(T)$ of UAs at 62 K, while in Ref. 17 it was shown that there is a first-order phase transition at that temperature. As was pointed out above, in the compound ThAs there are no anomalies of the physical properties at temperatures near 60 K. Moreover, it was found in Ref. 27 that the $\chi(T)$, $\rho(T)$, and $C(T)$ curves of UCu_5In have anomalies at $T=25$ K. It is seen in that paper that when uranium is replaced by thorium ($ThCu_5In$) the $\rho(T)$ and $C(T)$ curves no longer exhibit any anomalies.

The authors of Ref. 21 investigated a number of pseudobinary compounds with the $ThMn_{12}$ crystal structure. It follows from that paper that only in the compound UCu_4Al_8 in the vicinity of 60 K and also at temperatures corresponding to the transitions α_1, α_2, and α_3 (see also Fig. 6) are anomalies observed in ρ and C. By comparing Fig. 6 with the material from Ref. 21 one can arrive at the conclusion that the substitution R→U in the compounds RFe_4Al_8 (R is

a rare-earth metal) leads to anomalies of R_s at the characteristic temperatures (see Fig. 7), while for R≡Lu, Y, Sc, and Ce no anomalies of $R_s(T)$ were observed.

The evidence adduced above attests to fact that in all the compounds the anomalies of the Ohmic loss and heat capacity in the vicinity of the temperatures 60, 43, 37, and 23 K are due specifically to uranium and to no other element, since the features are not observed when the uranium is replaced by another element that does not alter the crystal structure.

It is known[34] that the cause of the change in the size of a uranium sample upon thermocycling from room temperature to high temperatures is either phase transitions (if the the temperature cycle includes temperatures at which they occur)[35] or anisotropy of the coefficient of linear expansion.[36]

On deep cooling relative to room temperature the role of anisotropy of the linear expansion with respect to the axes of the crystal lattice apparently plays an appreciable role in the change in size of the sample. This is confirmed by the fact that on thermocycling in the range 77–300 K an α uranium sample suffered a decrease in diameter and an increase in length, while for thermocycling in the range 4.2–300 K its length decreased and its diameter increased (Fig. 9). As was pointed out in Refs. 1, 4, 6, 11, 13, and 14, it is precisely between nitrogen and helium temperatures ($\sim$60 K) that the change in sign of the slope of the linear expansion of uranium along the *a* axis occurs (the *a* axis begins to increase).

Comparing our results with the existing ones, we notice many common properties in the change in the size of α uranium sample during thermocycling in the ranges from room to high temperatures and from room to cryogenic temperatures. In particular, the slope $\partial(l,d,V)/\partial N$ changes sign in thermocycling to 4.2 K, attesting to the fact that the change in size occurs, as in the case of thermocycling from room to high temperatures, during cooling of the sample and not during heating; this also follows from the results of Ref. 37.

During thermocycling both from room to high temperatures[37] and from room to cryogenic temperatures the dimensions of the sample change linearly with increasing number of thermocycles.

It has been established experimentally that the change in the size of α uranium occurs specifically during rapid cooling of the sample and during heating at any rate. For example, the change in the size of the samples occurs during their cooling only if they are abruptly plunged into liquid nitrogen or helium, whereas the warming time can be from a few seconds to tens of minutes. If the sample is cooled slowly (the sample is slowly lowered to the level of cryogenic liquid), then, regardless of the rate of its heating (in the case of rapid heating a sample cooled to 77 K was abruptly plunged into liquid at room temperature) there was no noticeable change in the size of the sample. These results agree with the data of Refs. 1 and 37 in the case of thermocycling of uranium from room to high temperatures.

In thermocycling from room to cryogenic temperatures not only the linear dimensions of the sample but also its volume change, as during thermocycling from room to high temperatures.[1]

All of what we have said for polycrystalline α uranium also applies to single-crystal UCu_5Al (Fig. 11). However, according to Ref. 1, single crystals of α uranium during their thermocycling do not change in size, since a change in size during thermocycling requires the presence of grain boundaries with a large mutual misorientation. The fact that we have observed a change in size of a single crystal indicates that some conditions for growth of the latter might be different or that a single crystal with defects was used in the thermocycling.

5. CONCLUSION

We have established for the first time that the temperature curves of the resistivity ρ and surface resistance R_s of samples of α uranium and the uranium compounds UCu_5Al, UCu_4Al_8, UFe_4Al_8, and $U_3Ni_3Sn_4$ exhibit anomalies at temperatures near 60 K and also in the vicinity of the transitions α_1(43 K), α_2(37 K), and α_3(23 K). Similar anomalies of other physical properties have been observed previously at two or three characteristic temperatures in various samples, but those results were insufficient grounds for drawing conclusions as to the commonality of such anomalies in uranium and its compounds. On the basis of our experimental results and analysis of the existing published data we consider that the anomalies of the various physical properties in compounds containing uranium as a constituent are due to the uranium. It follows from published sources and our measurements that, as a rule, these anomalies are due to first-order phase transitions at the corresponding characteristic temperatures. It has been clarified that the phase transition at $T=T_N$ in the compound UCu_5Al fundamentally reorganizes the quasiparticle scattering system, altering the character of the temperature dependence of the Ohmic loss from semiconductor at $T>T_N$ to metallic at $T<T_N$. For $T<T_N$ the $\rho(T)$ curve of the compound falls off by a quadratic law, which may be a sign of Fermi-liquid behavior. At $T<T_N$, axial anisotropy of the resistivity and surface resistance is observed: the resistances measured in the direction perpendicular to the growth axis of the single crystal are lower than those measured along the growth axis.

It has been found that repeated thermocycling from room to low temperatures leads to a change in the linear dimensions of samples of uranium and single-crystal UCu_5Al. These changes are similar in their form and properties to those observed on thermocycling from room to high temperatures. It is shown that the change in size of the samples occurs only during their cooling at a high rate.

The authors thank A. I. Prokhvatilov for reading the manuscript and for valuable comments and helpful discussions.

*E-mail: dmitriev@ilt.kharkov.ua

[1] A. N. Holden, *Physical Metallurgy of Uranium*, Addison-Wesley, Reading, PA (1958), Gosnauchtekhizdat po Chernoĭ i Tsvetnoĭ Metallurgii, Moscow (1962).
[2] P. Ch. Sahu, M. Yosuf, and K. Govinda Rajan, Physica B **183**, 145 (1993).
[3] J. C. Lashley, B. E. Lang, J. Boerio-Goates, B. F. Woodfield, G. M. Schmiedeshoff, E. C. Gay, C. C. McPheeters, D. J. Thoma, W. L. Hults, J. C. Cooley, R. J. Hanrahan, and J. L. Smith, Phys. Rev. B **63**, 224510-1 (2001).
[4] L. G. Chachkhiani and Z. B. Chachkhiani, *Intermetallic Compounds of*

Uranium [in Russian], Izd-vo Metsniereba, Tbilisi (1990).
[5] J. W. Ross and D. J. Lam, Phys. Rev. **165**, 617 (1968).
[6] E. S. Fisher and H. J. McSkimin, Phys. Rev. **124**, 67 (1961).
[7] E. S. Fisher and D. Dever, Solid State Commun. **8**, 649 (1970).
[8] E. S. Fisher and D. Dever, Phys. Rev. **170**, 607 (1968).
[9] J. C. Jousset, Acta Metall. **14**, 193 (1966).
[10] C. A. Cornelius and T. F. Smith, Solid State Commun. **38**, 599 (1981).
[11] H. G. Smith, N. Wakabayashi, W. N. Crummett, R. M. Nichlow, G. H. Lander, and E. S. Fisher, Phys. Rev. Lett. **44**, 1612 (1980).
[12] J. M. Fournier, A. Delapalme, C. Leyen, and G. H. Lander, J. Phys. (Paris) **40**, 4 (1979).
[13] A. F. Schuch and H. L. Laquer, Phys. Rev. **86**, 803 (1952).
[14] F. Hulliger and O. Vogt, Physica B **102**, 316 (1980).
[15] P. G. Thérond, J. M. Fournier, J. Schoenes, and O. Vogt, J. Magn. Magn. Mater. **64**, 45 (1987).
[16] O. Vogt and H. Barthalim, J. Magn. Magn. Mater. **29**, 291 (1982).
[17] J. Rossat-Mignod, D. Burlet, S. Quezell, and O. Vogt, Physica B **102**, 237 (1980).
[18] L. Havela, J. Hžebik, J. Sternberk, A. Meńovsky, and A. Zentko, Phys. Status Solidi A **59**, K165 (1980).
[19] R. Troć, Physica **102**, 233 (1980).
[20] R. Troć, R. Andruszkiewicz, R. Pietri, and B. Andraka, J. Magn. Magn. Mater. **183**, 132 (1998).
[21] A. M. Gurevich, V. M. Dmitriev, V. N. Eropkin, B. Yu. Kotur, N. N. Prentslau, V. Suski, A. V. Terekhov, and L. V. Shlyk, Fiz. Nizk. Temp. **27**, 1308 (2001) [Low Temp. Phys. **27**, 967 (2001)].
[22] B. Ptasiewicz-Bak, A. Baran, W. Suski, and J. Leciewicz, J. Magn. Magn. Mater. **76–77**, 939 (1988).
[23] V. M. Dmitriev, V. N. Eropkin, A. M. Gurevich, A. P. Isakina, V. M. Kobelev, A. J. Prokhvatilov, L. V. Shlyk, R. Troć, and V. H. Tran, Fiz. Nizk. Temp. **17**, 1051 (1991) [Low Temp. Phys. **17**, 547 (1991)].
[24] M. Drulis, A. Baran, B. Stalinski, W. Suski, R. Felten, F. Stedlich, and L. Pawlak, Thermochim. Acta **139**, 219 (1989).
[25] A. M. Gurevich, V. M. Dmitriev, V. N. Eropkin, L. A. Ishchenko, N. N. Prentslau, and L. V. Shlyk, Fiz. Nizk. Temp. **25**, 15 (1999) [Low Temp. Phys. **25**, 10 (1999)].
[26] S. Ramo, J. R. Whinnery, *Fields and Waves in Modern Radio*, Wiley, New York (1947), OGIZ, Moscow–Leningrad (1948).
[27] D. Kaczorowski, R. Troć, A. Czopnik, A. Jezowski, Z. Henkie, and W. Zaremba, Phys. Rev. **63**, 144401 (2001).
[28] E. M. Levin, in *Report of the Scientific Reserach Work of the International Laboratory of High Magnetic Fields and Low Temperatures* [in Russian], Wroclaw, Poland (1998), p. 21.
[29] V. H. Tran, R. Troć, J. Stepien-Damm, T. Komatsubara, F. Steglich, R. Hauser, and E. Bauer, Phys. Rev. B **66**, 054421 (2002).
[30] R. Troć, V. H. Tran, M. Wolcyrz, G. André, and F. Bouré, J. Magn. Magn. Mater. **190**, 251 (1998).
[31] B. Nowak and R. Troć, Solid State Nucl. Magn. Reson. **14**, 157 (1999).
[32] J.-C. Marmeggi, R. Currat, A. Boutet, and G. H. Lander, J. Phys. Soc. Jpn. **70**, 22 (2001).
[33] R. Troć and V. H. Tran, J. Magn. Magn. Mater. **73**, 389 (1988).
[34] S. F. Kovtun and V. S. Kogan, Fiz. Met. Metalloved. **13**, 316 (1962).
[35] A. M. Kosevich and L. V. Tanatarov, Fiz. Met. Metalloved. **8**, 255 (1959).
[36] R. I. Garber, S. Ya. Zalivadnyĭ, and V. M. Mikhaĭlovskiĭ, Fiz. Tverd. Tela (Leningrad) **2**, 1052 (1960) [Sov. Phys. Solid State **2**, 950 (1960)].
[37] B. G. Lazarev, A. I. Sudovtsev, and L. G. Smirnov, Fiz. Met. Metalloved. **7**, 122 (1959).

Translated by Steve Torstveit

LOW-DIMENSIONAL AND DISORDERED SYSTEMS

Size effect in the fluorescence spectra of polysilanes embedded in mesoporous materials

N. Ostapenko* and N. Kotova

Institute of Physics of the National Academy of Sciences of Ukraine, pr. Nauki 46, Kiev 03028, Ukraine

G. Telbiz

Institute of Physical Chemistry of the National Academy of Sciences of Ukraine, pr. Nauki 31, Kiev 03039, Ukraine

S. Suto

Department of Physics, Graduate School of Science, Tohoku University, Sendai, 980-8578, Japan

A. Watanable

Institute of Multidisciplinary Research for Advanced Materials, Sendai, 980-8577, Japan
(Submitted December 9, 2003; revised January 19, 2004)
Fiz. Nizk. Temp. **30**, 658–665 (June 2004)

The low-temperature fluorescence and excitation spectra ($T=5-150$ K) are investigated for the silicon–organic photoconductors poly(di-*n*-hexylsilane) (PDHS) and poly(methylphenylsilane) (PMPS) embedded in pores of the mesoporous materials MSM-41 and SBA-15, with pore diameters of 2.8 and 5.8 nm, respectively. It is found that the fluorescence spectra of the polymer nanostructures depend on the pore size and are substantially different from the spectra of films. New bands in the visible region, with maxima at 410 nm for PDHS and at 460 nm for PMPS, are observed for the first time in the fluorescence spectra of the 2.8 nm nantostructures. It is assumed that the new bands in the fluorescence spectrum are due to the formation of defect states as a result of a substantial change in the conformation of the polymer chains near the surface of the pores. The change in symmetry of the polymer chains near such defects gives rise to a new band with maximum at 300 nm in the excitation spectrum of PDHS. The defect nature of the new fluorescence bands is confirmed by temperature studies and also by the vanishing of these bands when the pore size is increased to 5.8 nm. [DOI: 10.1063/1.1768354]

INTRODUCTION

Interest in the study of the structure and morphology of ultrathin polymer films and composite systems based on them derives primarily from the possibility of modifying the optical and electronic properties of the polymers in restricted volumes as the thickness decreases. Under those conditions the processes of interaction of the polymers with the surface make a substantial contribution in comparison to the intermolecular interaction processes between the polymer chains. The study of those systems also has practical value in connection with the use of ultrathin polymer films in microelectronics and in electroluminescent devices.[1,2] The experimentally obtained characteristics of such films make it possible to create and model composites and lubricating films with pre-specified properties.

Composite systems based on polymers embedded in mesoporous materials with nanosize pores are a new class of structures[3–7] that permit investigating and monitoring the properties of polymers in the transition from films to nanostructures. These studies are also stimulated by the use of ultrathin polysilane films as transport layers in multilayer electroluminescent devices[8] and active electroluminescent materials in the UV region.[1,9] The unique properties of polysilanes, such as the strong absorption in the ultraviolet, the high quantum yield of fluorescence, and the strong dependence of the energy of the electronic transitions on the conformation of the polymer chains,[10] make it possible to register the optical spectra of ultrathin films containing a small amount of material and also to study the change in their photophysical properties in the transition from films to nanostructures.

Typical representatives of this class of polymers with the best-studied properties are poly(di-*n*-hexylsilane) (PDHS) and poly(methylphenylsilane) (PMPS), which differ in their side groups. The side groups of PDHS consist only of alkyl substituents (see the inset in Fig. 1), while the side groups of PMPS contain both alkyl and aryl substituents (see the inset in Fig. 4). The choice of these polymers is also motivated by the possibility of explaining the nature of the visible fluorescence of polysilanes, which is still being debated in the literature.[11–18] The existing models presuppose that the nature of this fluorescence is due to the presence of both aryl

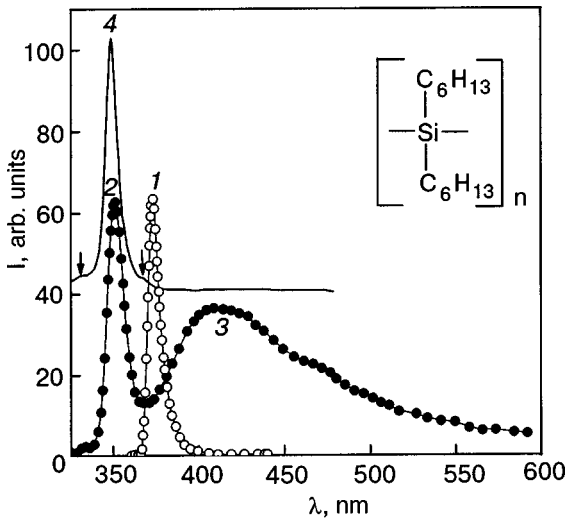

FIG. 1. Fluorescence spectra ($\lambda_{exc}=313$ nm) of a PDHS film (○), a PDHS/MSM-41 composite with a pore diameter of 2.8 nm (●) and a PDHS/SBA-15 composite with a pore diameter of 5.8 nm (solid curve) at 5 K. The curves formed by the unfilled circlets are normalized to the maxima of the bands. The numbers label the main maxima. The structural formula of PDHS is given in the inset.

and alkyl side groups in polysilanes,[11,12,14] and that it also depends on the length of the alkyl substituents.[15,18] As will be shown below, the visible fluorescence of the polysilanes under study does not depend on the type of side groups or the length of the chain of alkyl substituents but derives from the fact that the polymer chains contain defects arising as a result of the conformation of a polymer chain.

In this paper we report the first study of the fluorescence and excitation spectra ($T=5-150$ K) of PDHS and PMPS embedded in the mesoporous materials MSM-41 and SBA-15, with pore diameters of 2.8 and 5.8 nm, respectively. The results are compared with the data for films of these polymers. The substantial changes observed in the fluorescence spectra of polysilanes in the transition from the films to nanostructures are analyzed on the basis of the processes of competition of the interaction of the polymer chains with the surface of the pore and the intermolecular interaction between polymer chains. A simple way of controlling the values of these interactions by changing the pore size is proposed.

EXPERIMENTAL TECHNIQUE

Siliceous MSM-41 was synthesized by the technique described in Ref. 19. The materials obtained were filtered, washed, and dried in air at 323 K. For removal of the template the MSM-41 was baked in dry air for 23 hours at 813 K. Synthesis of the SBA-15 was carried out according to Ref. 20. The solid product was filtered, washed, and dried at 413 K and then baked for 4 hours in air at 823 K. The removal of the template was monitored by IR spectroscopy methods (Specord IR 75). The preservation of the structure of the matrix after processing was confirmed by x-ray diffraction (DRON-3M). The nitrogen adsorption and desorption isotherms were measured on an ASAP-2000. For removal of the residual moisture the samples were dried for 12 hours at room temperature and then stored in an exicator.

Composites (polymer/mesoporous material) with different pore diameters were created by an identical method. This was done by pouring a 1 wt.% solution of the polymer, PDHS ($M=53600$) or PMPS ($M=11160$), in toluene over the corresponding mesoporous material. The solution was placed in a dark vessel and slowly agitated for several hours at 293 K and then held until the solvent evaporated. The resulting composite was washed twice in fresh toluene to remove the polymer from the outer surface. For removal of moisture the samples were dried for 12 hours at room temperature. The polymer films were deposited on a quartz substrate by centrifuging. The fluorescence, phosphorescence, and excitation spectra in the temperature interval 5–150 K were obtained with the use of a Hitachi MPF-4 placed in a helium cryostat. For excitation of the fluorescence the wavelengths 260 and 313 nm were selected by using a xenon lamp and a monochromator.

RESULTS OF THE EXPERIMENTS

Fluorescence and excitation spectra of PDHS embedded in mesoporous materials with pore diameters of 2.8 and 5.8 nm

The absorption and fluorescence spectra of the PDHS films deposited on a quartz substrate were measured at $T=5$ K, and the results agreed with the spectra known from the literature.[21] The fluorescence spectrum of the film ($\lambda_{exc}=313$ nm) is shown in Fig. 1 (the curve formed by the unfilled data points). It consists of a narrow band peaking at 371 nm, caused by the $\sigma^*-\sigma^*$ transition in the polymer chain (band *1*). The absorption spectrum of the PDHS film at 5 K has a strong band peaking at 365 nm, due to $\sigma^*-\sigma^*$ transitions in the polymer chain. In addition, a very weak band with $\lambda_{max}=313$ nm is also observed. In the excitation spectrum of these films with registration of the 371 nm fluorescence band the same bands as in the absorption spectrum are observed.

The fluorescence spectrum ($T=5$ K, $\lambda_{exc}=313$ nm) of PDHS embedded in the mesoporous material MSM-41 with a pore diameter of 2.8 nm is shown in Fig. 1 (the curve formed by the filled data points). It is seen that the fluorescence spectrum of the composite PDHS/MSM-41, unlike the fluorescence spectrum of the film on quartz, consists of two bands: a narrow, short-wavelength band with maximum at 350 nm (band *2*), shifted relative to the corresponding band *1* in the fluorescence spectrum of the film by 20 nm to the short-wavelength side, and a new broad, intense band in the visible region, with maximum at 410 nm (band *3*). The excitation spectra of PDHS embedded in MSM-41 are shown in Fig. 2; they were measured by registration of the fluorescence bands at 350 and 410 nm. (In all the figures except Fig. 3 the zero level is different for the different curves.) We see that when the 350 nm fluorescence band is registered (solid curve) one observes a strong, narrow band with $\lambda_{max}=346$ nm (band *1*) and a weak band with maximum at 336 nm (band *4*). It should be emphasized that in the excitation spectrum recorded at $\lambda=410$ nm (the dotted curve), besides the 344 nm band (band *1*), which in this case is of lower intensity, a new, strong band with $\lambda_{max}=300$ nm appears (band *5*). The fluorescence spectrum of this sample is shown for comparison (the dotted curve; bands *2* and *3*).

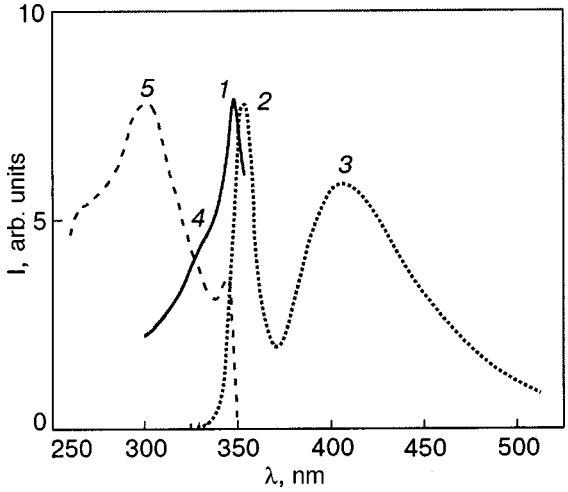

FIG. 2. Fluorescence spectrum (dotted curve) and excitation spectrum with registration of the 350 and 410 fluorescence bands (solid and dashed curves, respectively) for a PDHS/MSM-41 composite with a pore diameter of 2.8 nm ($T=5$ K, $\lambda_{exc}=313$ nm). The numbers label the main maxima.

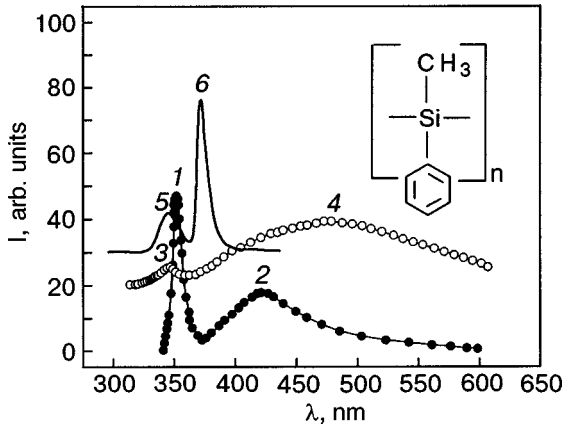

FIG. 4. Fluorescence spectra of a PMPS film (●), a PMPS/MSM-41 composite with a pore diameter of 2.8 nm (○), a PMPS/SBA-15 composite with a pore diameter of 5.8 nm (solid curve) ($\lambda_{exc}=313$ nm, $T=5$ K). The numbers label the main maxima. The structural formula of PMPS is shown in the inset.

In order to understand the nature of the additional fluorescence band with maximum at 410 nm we investigated the temperature dependence of the fluorescence spectrum of PDHS embedded in MSM-41 in the temperature interval 5–150 K. The result is presented in Fig. 3. It is seen that the narrow band shifts slightly to longer wavelengths with increasing temperature, and its intensity decreases somewhat. Meanwhile, the intensity of the broad band decreases substantially with increasing temperature, and at 150 K only the narrow band is observed in the spectrum. The temperature dependence of the bands in the fluorescence spectra of the composite PDHS/MSM-41 and of the film on quartz are substantially different. It is known that the narrow band in the fluorescence spectra of the PDHS film is shifted to longer wavelengths with increasing temperature, its intensity falls, and the half-width increases substantially.[22]

Figure 1 shows the fluorescence spectrum ($T=5$ K, $\lambda_{exc}=313$ nm) of PDHS embedded in SBA-15 with a pore diameter of 5.8 nm (solid curve). In this spectrum one observes a narrow, strong band peaking at 349 nm (band *4*), which coincides with the maximum of the band in the fluorescence spectrum of the PDHS/MSM-41 composite with a pore diameter of 2.8 nm (band *2*), and two new, weak bands with maxima at 333 and 367 nm (indicated by arrows). It should be emphasized that in this case the broad band in the visible region of the spectrum is not observed in the fluorescence spectrum. The intensity of the narrow band *4* remains practically unchanged when the temperature is increased from 5 to 77 K.

The excitation spectrum of PDHS embedded in SBA-15 with registration of the 350 nm fluorescence band coincides with the excitation spectrum of PDHS embedded in MSM-41, i.e., the broad bands with maxima at 336 and 347 nm are observed in the spectrum, while in the case of registration at 367 nm a new band with maximum at 364 nm appears in addition to those.

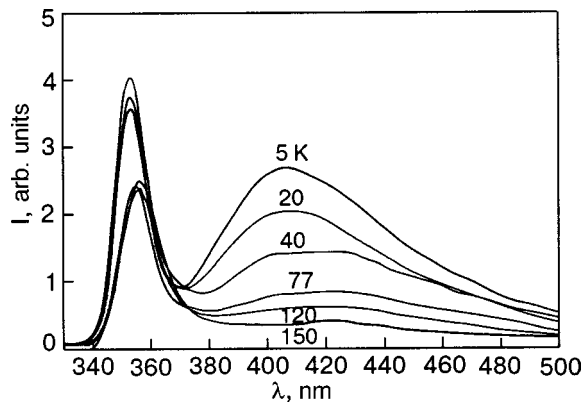

FIG. 3. Temperature dependence of the fluorescence spectrum of the composite PDHS/MSM-41.

Fluorescence and excitation spectra of PMPS embedded in mesoporous materials with pore diameters of 2.8 and 5.8 nm

The absorption, excitation, and fluorescence spectra measured at 5 K for PMPS films placed on quartz agree with the spectra known from the literature.[11]

The fluorescence spectrum of a PMPS film on a quartz substrate ($\lambda_{exc}=313$ nm) is shown in Fig. 4 (the curve formed by the filled data points). It consists of two bands: a narrow, intense band with maximum at 352 nm, due to $\sigma^*-\sigma$ transitions in the polymer chain (band *1*), and a broad band with maximum at 410 nm (band *2*), with a long-wavelength wing extending to 600 nm.

The absorption spectrum of a PMPS film on quartz at $T=5$ K consists of two bands with maxima at 338 and 270 nm, due to $\sigma-\sigma^*$ transitions in the main polymer chain and to transitions to the phenyl ring, respectively.

The excitation spectrum ($T=5$ K) of the film on quartz with registration of the fluorescence band peaking at $\lambda_r=352$ has bands with maxima at 340 and 270 nm, due to transitions in the main polymer chain and to transitions to the phenyl ring, respectively. This spectrum is practically the same as the absorption spectrum. At $\lambda_r=410$ nm, besides those bands, which are substantially weaker in intensity, an additional broad band with $\lambda_{max}=305$ nm is observed.[12]

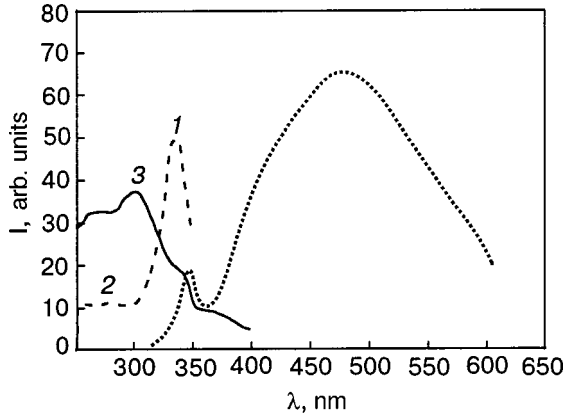

FIG. 5. Fluorescence spectrum (dotted curve) and excitation spectrum with registration of the 345 and 470 nm fluorescence bands (the dashed and solid curves, respectively) of a PMPS/MSM-41 composite with a pore diameter of 2.8 nm ($\lambda_{exc}=313$ nm, $T=5$ K). The numbers label the main maxima in the excitation spectra.

The fluorescence spectrum of PMPS embedded in the mesoporous material MSM-41 with a pore size of 2.8 nm ($T=5$ K, $\lambda_{exc}=313$ nm) is given in Fig. 4 (the curve formed by unfilled data points). It is seen that the spectrum consists of three bands: a weak, narrow band with maximum at 345 nm (band *3*) and two bands in the visible region—a broad band with maximum at ~410 nm, which was observed in the fluorescence spectrum of the film, and a new, very intense and broad band with $\lambda_{max}=470$ nm (band *4*). The maximum of the narrow band is shifted by 7 nm to shorter wavelengths relative to the corresponding band in the fluorescence spectrum of the film (band *1*). When the temperature is raised from 5 to 77 K a decrease in the intensity of the broad band *4* is observed, and its maximum is shifted to longer wavelengths. The intensity of the $\sigma^*-\sigma$ band *3* changes little.

The excitation spectrum of PMPS embedded in the mesoporous material MSM-41 with a pore size of 2.8 nm is presented in Fig. 5. The excitation spectrum of this sample at 5 K (the dashed curve) with registration of the 345 nm fluorescence band exhibited the following bands: 334 nm (band *1*), a very weak band in the 270 nm region (band *2*), and besides those bands, at $\lambda_r=470$ nm (solid curve) an intense, broad band with maximum at 301 nm (band *3*) is observed. For comparison the fluorescence spectrum of this sample is shown by the dotted curve.

The fluorescence spectrum of PMPS embedded in the pores of the mesoscopic material SBA-15 with a pore diameter of 5.8 nm is presented in Fig. 4 (solid curve). In the spectrum one observes a weak band with maximum at 344 nm (band *5*), which coincides with the maximum of the band *3* in the fluorescence spectrum of the polymer in a 2.8 nm pore. Band *5* has a long-wavelength shoulder with a maximum at 352 nm. An important result is that two different bands have vanished: the broad fluorescence band in the visible region of the spectrum with maximum at 470 nm (band *4*), which is observed in the fluorescence spectrum of the polymer embedded in a mesoporous material with a pore diameter of 2.8 nm, and the band with maximum at 410 nm (band *2*), which is observed in the fluorescence spectrum of the film. Meanwhile, in the fluorescence spectrum of the composite PMPS/SBA-15 a new, narrow and intense band appears, with a maximum at 372 nm (band *6*). When the temperature is raised to 77 K the intensities of the fluorescence bands remain practically unchanged. In the excitation spectrum of this sample ($T=5$ K, $\lambda_r=345$ nm) one observes a single broad band with maximum at 326 nm. At $\lambda_r=352$ nm the maximum of the band is shifted to 338 nm, and at $\lambda_r=372$ nm the maximum of the band is shifted to 343 nm. In addition, in the latter case a band peaking at 302 nm appears and also a new narrow band with $\lambda_{max}=366$ nm.

It should be emphasized that the mesoporous materials MSM-41 and SBA-15 do not fluoresce at 5 K; only phosphorescence in the 400–500 nm region is observed, and we can therefore assume that a transfer of excitation energy from the polymer to the mesoporous material does not occur. The absorption spectrum of these materials consists of a broad band peaking at around 250 nm.

DISCUSSION OF THE RESULTS

We investigated the changes in the low-temperature fluorescence and excitation spectra of the silicon–organic polymers PDHS and PMPS in the transition from bulk films to nanostructures when the polymers are embedded in mesoporous materials with pore diameters of 2.8 and 5.8 nm. We have shown that the excitation and fluorescence spectra of such composites exhibit the following important differences from the corresponding spectra of the films:

1. The $\sigma^*-\sigma$ fluorescence bands (bands *1* and *2* in Fig. 1 and bands *1* and *3* in Fig. 4) and the corresponding excitation bands (band *1* in Fig. 2 and band *1* in Fig. 5) are shifted to shorter wavelengths by 20 nm for PDHS and by 7 nm for PMPS.

2. The fluorescence spectra of the polymers embedded in a pore of diameter 2.8 nm have new, broad bands in the visible region, with maxima at 410 and 470 nm for PDHS and PMPS, respectively (bands *3* in Fig. 1 and band *4* in Fig. 4), which were not present in the fluorescence spectra of the film and composites with a pore diameter of 5.8 nm.

3. In the excitation spectrum of PDHS embedded in a pore of diameter 2.8 nm with excitation of the 410 nm fluorescence band, a new band with maximum at 300 nm appears (band *5* in Fig. 2) which is absent from the excitation spectra of the film and of the polymer embedded in pores of diameter 5.8 nm.

The shift of the bands in the fluorescence and excitation spectra of composites to the a short-wavelength side relative to the corresponding bands in the spectra of the films attests to the fact that the polymer is embedded in the pores of a mesoporous material. We attribute this shift to a decrease in the intermolecular interaction between polymer chains found in a pore in comparison with the corresponding interaction in a film. Indeed, the pores in the mesoporous materials are isolated from one another, and so there is no intermolecular coupling between the polymer chains embedded in the neighboring pores. Furthermore, in a pore 2.8 nm in diameter there is a single polymer chain in PDHS and 2–3 polymer chains in PMPS, since the size of a monomeric unit of the macromolecule is equal to 1.6 and 0.97 nm, respectively. This suggests that there is no interaction or a substantially

reduced interaction between the polymer chains found in a pore in the case of composites based on PDHS or PMPS. Then the position of the electronic transition in the fluorescence and absorption spectra of the composites should approach the position of the electronic transition of the corresponding macromolecule in solution, as is in fact observed experimentally. It is known that the maximum of the fluorescence band of PDHS in solution ($T=1.5$ K) lies at 352 nm,[23] and for PMPS, at 348 nm,[11] which are close to the maxima of the fluorescence bands in the spectra of the composites studied. The shift of the absorption and fluorescence spectra of PMPS solutions relative to the spectra of the film amounts to 4 nm, which is substantially less than for PDHS, and accordingly the shift of the $\sigma-\sigma^*$ excitation and fluorescence bands of PMPS embedded in a pore 2.8 nm in diameter is significantly smaller than in the case of PDHS; it is equal to 7 nm.

It should be emphasized that the fluorescence spectrum of a polymer embedded in a pore of diameter 2.8 nm differs substantially from the corresponding spectra of solutions. Indeed, in the fluorescence spectrum of the composite PDHS/MSM-41 a new broad band is observed in the visible region of the spectrum, with a maximum at 410 nm (band *3* in Fig. 1), while for the composite PMPS/MSM-41 there is an additional band that peaks at 470 nm (band *4* in Fig. 4). These bands are not observed in the fluorescence spectra of the films.

The nature of the origin of the visible fluorescence in silicon–organic polymers is still under discussion. For an explanation of this effect a model of charge transfer from the polymer chain to the aryl ring of the side group and a defect model have been proposed. The existing experimental results can be explained only by the model in which the visible fluorescence is due to the presence of defects of the cross-link type in the polymer chains.[12–14] In such a case a branching of the structure of the polymer chain arises, and there are not two but three neighboring atoms near a silicon atom. It has been hypothesized[15,18] that the formation of such structural defects can occur only in polymers for which the alkyl side groups are shorter than the pentyl group. In polymers where the alkyl side groups are pentyl and longer substituents, such defects should not form in view of the steric hindrances and, accordingly, the visible fluorescence should not be observed.

PDHS does not have aryl side groups, and its axial side groups contain hexyl. Therefore, in accordance with the existing models in the literature no visible fluorescence should be observed for this polymer. The observation of visible fluorescence for PDHS embedded in a pore 2.8 nm in diameter attests to the appearance of defects in its polymer chain. In the polymer chain of the PMPS films, defects of the cross-link type already exist. Transitions to these defects are responsible for the broadband fluorescence of the films with maximum at 410 nm.[12,14] The appearance in the fluorescence spectrum of PMPS of an additional broad, longer-wavelength band also attests to the onset of additional defects in the polymer chains.

Consequently, the results which we obtained confirm the defect nature of the visible fluorescence of polysilanes. We assume that when the polymer is embedded in pores of diameter 2.8 nm, because of its interaction with the surface of the pore of the mesoporous material there occurs an orientation of the polymer chain along the surface of the pore. The existence of orientation of the polymer chain near the surface is attested to by the data of Refs. 3, 5, 6, and 24. The interaction of the polymer with the surface of the pore can lead to substantial changes in the conformation of the polymer chain owing to the change in the angle between Si–Si bonds. A change of structure of the polymer found in a restricted volume is confirmed by the data of Ref. 25. The results of a calculation[16] also attest to a change in the angle between Si–Si bond near defects of the cross-link type in the case of specially synthesized polysilanes with branched structures. It is known that the position of the electronic transitions of polysilanes depends strongly on the conformation of the polymer chain. A change of this conformation can give rise to defects in the polymer chain, i.e., the appearance of new bands in the fluorescence spectrum. In that case a part of the polymer chain far from the surface will give a narrow $\sigma^*-\sigma$ fluorescence band, while the defect part of the polymer near the surface of the mesoporous material gives a broad band that is observed experimentally. Thus the appearance of new, broad fluorescence bands in the spectra of PDHS and PMPS composites can be attributed to transitions from defect states arising in the polymer films upon a change in their conformation in the restricted volume. This is a new type of defect, which differs from the known defects of the cross-link type discussed in the literature.

The appearance of such defects can alter the symmetry of the $^1Ag-{}^1Ag$ transition, the maximum of which, according to the calculation, corresponds to 4.2 eV.[26] It is in this region that a new band arises in the excitation spectrum of PDHS embedded in a 2.8 nm pore, and it appears only in the case of registration of the broad fluorescence band, which confirms our hypothesis of a defect nature of the visible fluorescence in the spectrum of PDHS/MSM-41 composites.

The presence of defects of the cross-link type in the polymer chain of PMPS leads to a change in symmetry near those defects, and therefore the transition $^1Ag-{}^1Ag$ is now allowed in the absorption spectrum of the film. Evidence of this is the appearance of a band peaking at 305 nm in the excitation spectrum of the PMPS film in the case of registration of the 410 nm fluorescence band,[12] although the nature of the origin of that band was not determined by the authors. For this reason the excitation spectrum of PMPS/MSM-41 composites with registration of the 410 fluorescence band should not contain any new bands in comparison with the excitation spectrum of the film, and that is in agreement with the experimental result.

The defect origin of the new bands in the fluorescence spectrum of the composites is confirmed by the substantial decrease in the intensity of these bands when the temperature of the samples is raised from 5 to 150 K. As a result of the attraction of the polymer chains toward the surface of the pore there occurs an orientation of the chains with respect to the surface. As the temperature is raised, the role of this attraction in the orientation of the molecular chains decreases, and differently oriented configurations of the polymer chain appear, leading to a change in the relation between the different conformations of the polymer chain.

The hypothesis about the nature of the visible fluorescence is also confirmed in a study of the fluorescence and excitation spectra of PDHS when the pore diameter is increased to 5.8 nm. In that case the number of macromolecules in the pore increases. These macromolecules will be oriented not only along the surface of the pores of the mesoporous material but also with respect to each other. Then the interaction of the polymer and the surface of the mesoporous materials will be weakened, and the intermolecular interaction between the macromolecules will be enhanced, leading to the vanishing of the bands in the visible region of the fluorescence spectrum of the composites and to the appearance of new short- and long-wavelength bands. Since the symmetry of the polymer chain of PDHS in a 5.8 nm pore is the same as in the case of a film, the excitation band peaking at 300 nm in the excitation spectrum of the composite PMPS/MSM-41 with broadband registration should not be manifested, and that is what is observed experimentally. An extremely interesting and surprising fact is that we have not observed the broad fluorescence band in the visible region with maximum at 410 nm, which was observed in the fluorescence spectrum of the film and of the PMPS/MSM-41 composite. Instead, a new, narrow, intense band with $\lambda_{max} = 372$ nm appears. The substantial narrowing of the band of visible fluorescence (by about a factor of 7) is obtained for this class of polymers for the first time. In the polymer chain the macromolecules have a set of defects of the cross-link type with different configurations. It is possible that, as a result of the orientation of the polymer films with respect to each other a part of the configuration is no longer manifested. Additional studies will be needed for a detailed explanation of this phenomenon. The efficiency of migration of excitation energy in systems oriented in that way should be substantially increased, as is attested to by the temperature independence of the intensity of the fluorescence bands in the fluorescence spectrum of the composites having a pore diameter of 5.8 nm.

CONCLUSION

We have investigated the changes in the fluorescence and excitation spectra of the silicon–organic polymers PDHS and PMPS in the transition from films to nanostructures when the polymers are embedded into mesoporous materials with pore diameters of 2.8 and 5.8 nm. We have shown that the substantial dependence of the spectra on the pore diameter is due to a competition between the interaction of the polymers with the surface of the pores and between polymer chains.

It is hypothesized that when the pore diameter decreases to 2.8 nm the interaction of the polymers with the surface increases. This leads to a change in the conformation of the polymer chain near the surface of the pore and gives rise to defects; this is manifested in the appearance of new fluorescence bands in the visible region and also to a new band in the excitation spectrum in the case of PDHS. The vanishing of the visible fluorescence in the spectra of the composites with a pore diameter of 5.8 nm when the interaction between polymer chains exceeds the interaction of the polymer with the surface confirms that it is of a defect nature. The substantial narrowing of the band of visible fluorescence with a maximum at 410 nm for the composites PMPS/SBA-15, i.e., the appearance of a new intense band with maximum at 372 nm, is worthy of note. This effect was observed for the first time in polysilanes, and further studies are required in order to explain it.

The authors are grateful to V. P. Vorob'ev and V. M. Mel'nik for assistance in the investigation of the fluorescence spectra.

*E-mail: ostap@iop.kiev.ua

[1] K. Ebihara, S. Matsushita, S. Koshihara, F. Minami, T. Miyazawa, H. Obata, and M. Kira, J. Lumin. **72–74**, 43 (1997).
[2] S. Hoshino, K. Furukawa, K. Ebata, J. Brey, and H. Suzuki, J. Appl. Phys. **88**, 3408 (2000).
[3] C.-G. Wu and T. Bein, Stud. Surf. Sci. Catal. **84**, 2269 (1994).
[4] F. Marlow, K. Hoffmann, W. Hill, J. Kornatovski, and J. Caro, Stud. Surf. Sci. Catal. **84**, 2277 (1994).
[5] G. Telbiz, O. Shvets, G. Korzhak, M. Brodyn, S. Shevel, and V. Vozny, Functional Materials **5**, 367 (1998).
[6] J. Wu, A. F. Gross, and S. H. Tolbert, J. Phys. Chem. **103**, 2374 (1999).
[7] N. Ostapenko, G. Telbiz, V. Ilyin, S. Suto, and H. Watanabe, Chem. Phys. Lett. **383**, 456 (2004).
[8] A. H. Suzuki, H. Meyer, S. Hohino, and D. Haarer, J. Appl. Phys. **78**, 2684 (1995).
[9] A. Fuyii, K. Yoshimoto, M. Yoshida, Y. Ohwori, and H. Yochino, Jpn. J. Appl. Phys. **34**, 1365 (1995).
[10] R. D. Miller and J. Michl, Chem. Rev. (Washington, D.C.) **89**, 1359 (1989).
[11] O. Ito, M. Terajima, T. Azumi, N. Matsumoto, K. Takeda, and M. Fujino, Macromolecules **22**, 1718 (1989).
[12] M. Fujiki, Chem. Phys. Lett. **198**, 177 (1992).
[13] W. I. Wilson and T. W. Weidman, J. Phys. Chem. **95**, 4568 (1991).
[14] Y. Kanemitsu and K. Suzuki, Phys. Rev. **51**, 13103 (1995).
[15] S. Toyoda and M. Fujiki, Chem. Phys. Lett. **293**, 38 (1998).
[16] A. Watanabe, M. Nanyo, T. Sunaga, and A. Sekiguchi, J. Phys. Chem. A **105**, 6436 (2001).
[17] A. Watanabe, T. Sato, and M. Matsuda, Jpn. J. Appl. Phys. **40**, 6457 (2001).
[18] S. Toyoda and M. Fujiki, Macromolecules **34**, 2630 (2001).
[19] C. T. Kresge, M. E. Leonowicz, W. J. Roth, J. C. Vartuli, and J. S. Beck, Nature (London) **359**, 710 (1992).
[20] D. Y. Zhao, J. L. Feng, Q. S. Huo, N. Melosh, G. H. Fredrickson, B. F. Chmelka, and G. D. Stucky, Science **279**, 548 (1998).
[21] S. Suto, M. Shimizu, T. Goto, A. Watanabe, and M. Matsuda, J. Lumin. **76–77**, 486 (1998).
[22] M. Shimizu, S. Suto, T. Goto, A. Watanabe, and M. Matsuda, Phys. Rev. **63**, 073403 (2001).
[23] A. Tilgner, H. P. Trommsdorft, J. M. Zeigler, and R. M. Hochstrasser, J. Inorganic Organometallic Polymers **1**, 3, 343 (1991).
[24] J. N. Israelashvili and S. J. Kott, J. Chem. Phys. **88**, 7162 (1988).
[25] S. K. Kumar, V. Vacatello, and D. V. Yoon, J. Chem. Phys. **89**, 5206 (1988).
[26] R. G. Kepler and Z. G. Soos, Phys. Rev. **43**, 11908 (1991).

Translated by Steve Torstveit

Interaction of acoustic waves with an interface in highly anisotropic layered crystals

A. M. Kosevich, P. A. Minaev, and E. S. Syrkin*

B. Verkin Institute for Low Temperature Physics and Engineering, National Academy of Sciences of Ukraine, pr. Lenina 47, Kharkov 61103, Ukraine

M. L. Polyakov

1153 Baker Ave., Schenectady, NY 12309, USA
(Submitted December 16, 2003)
Fiz. Nizk. Temp. **30**, 666–671 (June 2004)

The scattering of acoustic waves on a planar defect in the interior of a crystal is studied by the methods of lattice dynamics. The model chosen consists of two semi-infinite, highly anisotropic crystals, the forces of interaction between which are distinct from the interactions within the crystals themselves. The model is used to study the resonant transmission of waves through an impurity monolayer. This resonant transmission effect is due to the weak coupling of the defect to the host lattice and cannot be described in the framework of the standard theory of elasticity, since the displacements of the defect layer and of the closest-lying layers of the host matrix are substantially different. For nongrazing angles of incidence the resonant transmission effect can be illustrated qualitatively by the example of an infinite linear chain containing a point impurity. © *2004 American Institute of Physics.*
[DOI: 10.1063/1.1768355]

INTRODUCTION

Acoustic waves localized near an atomic monolayer adsorbed on the free surface of a crystal have been studied for some years now (see the bibliography in the reviews[1,2]). It has been found that waves of the that kind in highly anisotropic layered crystals have some interesting behavior. We have previously[3] studied the basic characteristics of surface and quasi-surface waves on the microscopic level. In particular, in the long-wavelength approximation we have obtained the singular solutions of the equations of lattice dynamics, some having frequencies lying outside the continuum band (surface states) and some with frequencies inside it (quasi-surface states). For arbitrary values of the two-dimensional wave vector we studied the conditions for the appearance of surface waves of a special type, having one or two end points and a nonmonotonic dependence of the damping parameter on the modulus of that wave vector.

A natural continuation is to study systems in which the planar defect (transition layer) lies not on the surface but in the interior, i.e., is an interface between two media in contact. The physical characteristics of a transition layer between two media, as a rule, is different from the properties of the two adjacent media, and that leads to a number of curious features in the lattice dynamics.[4–6] Systems of this kind are extremely common and are unquestionably of interest both in basic research and in technological applications (see, e.g., the reviews[1,7]). Systems of this type can be relatively easily obtained in a controlled manner (for example, by depositing coatings or by intercalation). They also arise as a result of uncontrolled processes, e.g., in the course of defect formation during crystal growth (twin boundaries and grain boundaries) or during mechanical treatment. The presence of a planar defect has a substantial influence on the various dynamic, thermodynamic, and kinetic characteristics of crystals. To study this influence it is necessary to elucidate the features of the interaction of phonons with a planar defect. The study of resonance effects in the scattering of acoustic vibrations on a defect and problems of formation of bound states related to them are of considerable interest, as are questions of the formation of coupled vibrational states, since such effects can give rise to features in the kinetic characteristics of intercrystalline interfaces, as have been observed in experiments.[8] The description of resonance phenomena in highly anisotropic crystals in the framework of the macroscopic theory encounters significant difficulties, since the domain of applicability of such a theory for highly anisotropic systems is substantially limited.[9] This raises the problem of studying such effects in highly anisotropic compounds with the use of lattice models.

In this study we have used the methods of lattice dynamics to consider the scattering of acoustic waves on an impurity monolayer lying in the interior of a crystal. It is shown that the presence of such a layer can lead to the appearance of a resonant transmission effect. This effect is due to the presence of weak coupling of the defect to the main lattice and cannot be described in the framework of the standard theory of elasticity, since the displacements of the defect layer are substantially different from that of the adjacent layers. For nongrazing angles of incidence this effect can be illustrated qualitatively for the example of an infinite linear chain containing a point impurity.

SCATTERING OF VIBRATIONS ON A POINT DEFECT IN A ONE-DIMENSIONAL LINEAR CHAIN

It is known that one-dimensional models, despite their simplicity, can give a qualitative description of many phenomena inherent to real three-dimensional systems. The various features of the vibrational characteristics of linear chains

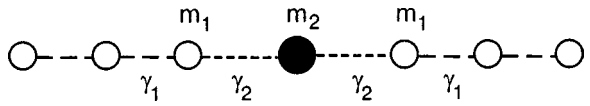

FIG. 1. Linear chain with an impurity atom.

containing defects have been investigated in Refs. 10 and 11. In this Section we shall investigate a point defect in a one-dimensional model as an analog of an interfacial boundary.

Thus we consider the interaction of vibrations with a point defect in an infinite linear chain (see Fig. 1). The following notation has been introduced in the figure: m_1 and γ_1 are the mass of an atom and the force coupling constant between atoms in the linear chain, and m_2 and γ_2 are the mass of an impurity and the constant characterizing its coupling with the atoms of the chain. The analytical results and estimates obtained for such a one-dimensional chain agree up to numerical coefficients with the results of calculations for models of real three-dimensional crystals in the case of nongrazing angles of incidence.

Let a wave incident on a defect be described by the expression $u(n)=\exp(ikn)$ (n enumerates the atoms in the chain, and $n=0$ corresponds to the defect atom); then the reflected wave can be written in the form $u_r(n)=r\exp(i\varphi)\exp(-ikn)$. Here r is the ratio of the moduli of the amplitudes of the reflected and incident waves, and φ is the phase of the reflected wave. Using the equation of motion for a linear chain with a defect, one can easily show that the expression for $r\exp(i\varphi)$ has the following form:

$$r\exp(i\varphi)=\frac{[(\gamma_2-\gamma_1)\varepsilon m_1-\gamma_2^2][\varepsilon m_2-2\gamma_2]+\gamma_2^2[\varepsilon m_1-2\gamma_2]}{[\gamma_1(q(\varepsilon)-1)(\varepsilon m_2-2\gamma_2)-\gamma_2 q(\varepsilon)\varepsilon m_2][\gamma_1(q(\varepsilon)-1)-\gamma_2 q(\varepsilon)]}, \tag{1}$$

where $\varepsilon\equiv\omega^2$ is the square of the vibrational frequency of atoms in the chain; and $q(\varepsilon)$ is a function defined by the expression

$$q(\varepsilon)=1-\frac{\varepsilon m_1}{2\gamma_1}+i\left(\frac{\varepsilon m_1}{\gamma_1}\right)^{1/2}\left(1-\frac{\varepsilon m_1}{4\gamma_1}\right)^{1/2}. \tag{2}$$

It is easy to see that $q(\varepsilon)=\exp(ik(\varepsilon))$, where the dependence $k=k(\varepsilon)$ comes from the dispersion relation of the ideal chain: $\varepsilon=4\gamma_1/m_1\sin^2(k/2)$. The zeroes of the denominator in expression (1) determine the frequencies of local vibrations of the one-dimensional chain with a two-parameter impurity and correspond to the expressions obtained in Ref. 11.

However, we are interested in the features of the numerator in Eq. (1). We note that the vanishing of the numerator corresponds to the resonant transmission of the wave through the impurity. The square of the frequency satisfying this condition has the form

$$\varepsilon_{\rm res}=\frac{2\gamma_1\gamma_2 m_1-\gamma_2^2(m_1+m_2)}{(\gamma_1-\gamma_2)m_1 m_2}. \tag{3}$$

The region of values of the parameters of the chain for which resonant transmission occurs is illustrated in Fig. 2. This region is bounded by the curves $y=(2-x)/x$ and $y=x/(2-x)$, where $x\equiv\gamma_2/\gamma_1$ and $y\equiv m_2/m_1$.

For many systems, microcontacts in particular, the coupling constant of the impurity to the chain is typically much smaller than the coupling constant between atoms in the chain itself ($\gamma_2/\gamma_1\ll 1$). In this case we have the following expression for $\varepsilon_{\rm res}$:

$$\varepsilon_{\rm res}=2\frac{\gamma_2}{m_2}+\frac{\gamma_2}{\gamma_1}\gamma_2\left(\frac{1}{m_2}-\frac{1}{m_1}\right)\approx 2\frac{\gamma_2}{m_2}.$$

Resonant transmission arises owing to the interaction of the incident wave with an eigermode of the chain due to the presence of the impurity. Up to small terms of order γ_2/γ_1 the frequency of this vibrational mode is determined solely by the interaction of the impurity atom with the host matrix and the mass of the impurity.

It should be pointed out that the mechanism of the transmission of the wave through the defect in a linear chain was described in a simple model back in the monograph by Brillouin and Parodi,[12] where a model consisting of two different semi-infinite linear chains connected by a single impurity atom with mass $M=(M_1+M_2)/2$ (M_1 and M_2 are the mass of the atoms of the semichains). It is not hard to show that the square of the resonance frequency in such a problem has the form

$$\varepsilon_{\rm res}=4\frac{\beta_2 M_2-\beta_1 M_1}{M_2^2-M_1^2} \tag{4}$$

(β_1 and β_2 are interatomic coupling constants in each of the semichains). The result has an especially simple form when the coupling constants in the two chains are the same (β_1

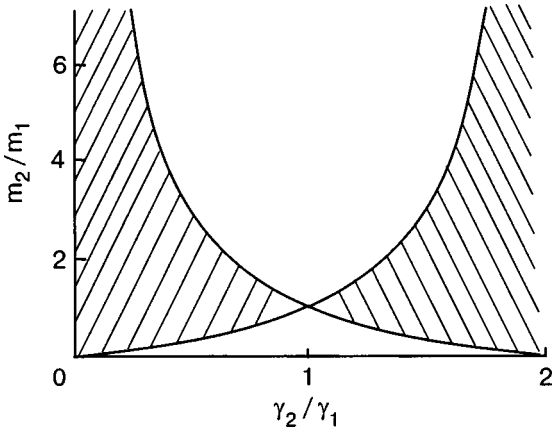

FIG. 2. Region of values of the chain parameters for which resonant transmission of a wave through an impurity atom exists. This region is bounded by the curves $y=(2-x)/x$ and $y=x/(2-x)$, where $x\equiv\gamma_2/\gamma_1$ and $y\equiv m_2/m_1$.

$=\beta_2=\beta$). In that case the square of the frequency of the natural vibrational mode of the impurity atom with respect to the chain, ω_s^2, is equal to $2\beta/M$, and that is the frequency at which the resonant transmission occurs.

Thus, if a point defect of a chain has eigermodes with a definite frequency ω_s, then in the transmission of the wave through the defect an ordinary resonance appears when the frequency of the wave coincides with the frequency ω_s. In the next Section we shall consider the resonant transmission of an acoustic wave through a planar defect separating two highly anisotropic three-dimensional crystals.

RESONANT INTERACTION OF ACOUSTIC WAVE WITH AN IMPURITY MONOLAYER SEPARATING TWO CRYSTALS

For studying the properties of highly anisotropic crystals it is convenient to choose the model of a body-centered tetragonal lattice in which the interlayer interaction is considerably smaller than the intralayer interaction. We consider two such crystals separated by an impurity monolayer. For a description of this model it is convenient to choose the following rectangular coordinate system: the OX and OY axes lie in the plane of a monoatomic defect layer, and the OZ axis is perpendicular to the defect and is directed into the interior of the crystal. Let a be the distance between the nearest-neighbor atoms in the XOY plane, while $b/2$ is the distance between adjacent atomic layers perpendicular to the OZ axis. The interlayer interaction in each of the crystals is taken into account in the nearest-neighbor approximation and is characterized by the parameters γ_1 and γ_3, respectively. The interaction between nearest neighbors within the layers is described by the parameters α_1 and α_3. The condition of high anisotropy means that $\gamma_1 \ll \alpha_1$ and $\gamma_3 \ll \alpha_3$. The interaction constants of the impurity monolayer with the first and second crystals are denoted by $\gamma_2^{(1)}$ and $\gamma_2^{(3)}$, and the interaction constant of the nearest neighbors within the layer itself is denoted by α_2. The masses of the atoms of the two crystals and the impurity monolayer are denoted by m_1, m_3, and m_2, respectively. The coordinates of the atoms in the lattice are described by the vector $\mathbf{n}=(n_1,n_2,n_3)$.

The equations describing the harmonic vibrations of the atoms of the main lattice have the form

$$\begin{aligned}-m(n_3)\ddot{u}(n_1,n_2,n_3)=\alpha(n_3)[&4u(n_1,n_2,n_3)\\&-u(n_1+1,n_2,n_3)-u(n_1,n_2+1,n_3)\\&-u(n_1-1,n_2,n_3)-u(n_1,n_2\\&-1,n_3)]+\gamma(n_3)[8u(n_1,n_2,n_3)\\&-u(n_1+1/2,n_2+1/2,n_3+1/2)\\&-u(n_1-1/2,n_2+1/2,n_3+1/2)\\&-u(n_1-1/2,n_2-1/2,n_3+1/2)\\&-u(n_1+1/2,n_2-1/2,n_3+1/2)\\&-u(n_1+1/2,n_2+1/2,n_3-1/2)\\&-u(n_1-1/2,n_2+1/2,n_3-1/2)\\&-u(n_1-1/2,n_2-1/2,n_3-1/2)\\&-u(n_1+1/2,n_2-1/2,n_3-1/2)],\end{aligned}\tag{5}$$

where $n_3>1/2$, $n_3<-1/2$.

These equations must be supplemented by the equation for the vibrations of the layers with $n_3=0$, $n_3=1/2$, $n_3=-1/2$, which are boundary conditions on (5):

$$\begin{aligned}-m_2\ddot{u}(n_1,n_2,0)=\alpha_2[&4u(n_1,n_2,0)-u(n_1+1,n_2,0)\\&-u(n_1,n_2+1,0)-u(n_1-1,n_2,0)\\&-u(n_1,n_2-1,0)]+\gamma_2^{(1)}[4u(n_1,n_2,0)\\&-u(n_1+1/2,n_2+1/2,1/2)\\&-u(n_1-1/2,n_2+1/2,1/2)-u(n_1-1/2,n_2\\&-1/2,1/2)-u(n_1+1/2,n_2-1/2,1/2)]\\&+\gamma_2^{(3)}[4u(n_1,n_2,0)-u(n_1+1/2,n_2+1/2,\\&-1/2)-u(n_1-1/2,n_2+1/2,-1/2)\\&-u(n_1-1,n_2-1,-1/2)\\&-u(n_1+1,n_2-1,-1/2)];\end{aligned}\tag{6}$$

$$\begin{aligned}-m_1\ddot{u}(n_1,n_2,1/2)=\alpha_1[&4u(n_1,n_2,1/2)\\&-u(n_1+1,n_2,1/2)-u(n_1,n_2+1,1/2)\\&-u(n_1-1,n_2,1/2)-u(n_1,n_2-1,1/2)]\\&+\gamma_1[4u(n_1,n_2,1/2)-u(n_1+1/2,n_2\\&+1/2,1)-u(n_1-1/2,n_2+1/2,1)\\&-u(n_1-1/2,n_2-1/2,1)\\&-u(n_1+1/2,n_2-1/2,1)]\\&+\gamma_2^{(1)}[4u(n_1,n_2,1/2)\\&-u(n_1+1,n_2+1,0)\\&-u(n_1-1,n_2+1,0)-u(n_1-1,n_2-1,0)\\&-u(n_1+1,n_2-1,0)];\end{aligned}\tag{7}$$

$$\begin{aligned}-m_3\ddot{u}(n_1,n_2,-1/2)=\alpha_3[&4u(n_1,n_2,-1/2)\\&-u(n_1+1,n_2,-1/2)\\&-u(n_1,n_2+1,-1/2)\\&-u(n_1-1,n_2,-1/2)\\&-u(n_1,n_2-1,-1/2)]\\&+\gamma_2^{(3)}[4u(n_1,n_2,-1/2)\\&-u(n_1+1/2,n_2+1/2,0)\\&-u(n_1-1/2,n_2+1/2,0)\\&-u(n_1-1/2,n_2-1/2,0)\\&-u(n_1+1/2,n_2-1/2,0)]\\&+\gamma_3[4u(n_1,n_2,-1/2)\\&-u(n_1+1/2,n_2+1/2,-1)\\&-u(n_1-1/2,n_2+1/2,-1)\\&-u(n_1-1/2,n_2-1/2,-1)\\&-u(n_1+1/2,n_2-1/2,-1)].\end{aligned}\tag{8}$$

The solutions of the system of equations (5) with boundary conditions (6)–(8) have the form

$$u(\mathbf{n})=[\exp(-ik_{1z}n_3)+r\exp(i\varphi_1+ik_{1z}n_3)]\times\exp(ik_xn_1+ik_yn_2),\quad n_3>0;$$

$$u(0)=u_0\exp(ik_xn_1+ik_yn_2),\qquad n_3=0;$$

$$u(\mathbf{n})=t\exp(i\varphi_3+ik_{3z}n_3)\exp(ik_xn_1+ik_yn_2),\quad n_3<0.$$

Here r and t are the reflection and transmission coefficients, defined as the ratio of the amplitudes of the reflected and transmitted waves to the amplitude of the incident wave, φ_1 and φ_3 are the phases of the reflected and transmitted waves, and u_0 is the amplitude of the vibrations of the defect layer. After some transformations we obtain the following system of equations for the quantities r, t, φ_1, and φ_3:

$$\begin{aligned}&r\exp(i\varphi_1)\gamma_2^{(3)}[(\gamma_1-\gamma_2^{(1)})\exp(ik_{1z})\\&\quad-\gamma_1\cos(k_x/2)\cos(k_y/2)]+t\exp(i\varphi_3)\gamma_2^{(1)}\\&\quad\times[(\gamma_2^{(3)}-\gamma_3)\exp(ik_{3z})+\gamma_3\cos(k_x/2)\cos(k_y/2)]\\&\quad+\gamma_2^{(3)}(\gamma_1-\gamma_2^{(1)})\exp(-ik_{1z})-\gamma_2^{(3)}\gamma_1\\&\quad\times\cos(k_x/2)\cos(k_y/2)=0;\end{aligned}\tag{9}$$

$$\begin{aligned}&t\exp(i\varphi_3)\{[(\gamma_3-\gamma_2^{(3)})\exp(ik_{3z})\\&\quad-\gamma_3\cos(k_x/2)\cos(k_y/2)][4(\gamma_2^{(1)}+\gamma_2^{(3)})\\&\quad-2\alpha_2(\cos k_x+\cos k_y-2)-\varepsilon m_2]\\&\quad+4(\gamma_2^{(3)})^2\exp(ik_{3z})\cos^2(k_x/2)\cos^2(k_y/2)\}\\&\quad+r\exp(i\varphi_1)\exp(ik_{1z})4\gamma_2^{(1)}\gamma_2^{(3)}\cos^2(k_x/2)\\&\quad\times\cos^2(k_y/2)+4\gamma_2^{(1)}\gamma_2^{(3)}\\&\quad\times\exp(-ik_{1z})\cos^2(k_x/2)\cos^2(k_y/2)=0;\end{aligned}\tag{10}$$

$$\varepsilon=\frac{2\alpha_1}{m_1}(2-\cos k_x-\cos k_y)+\frac{8\gamma_1}{m_1}\times(1-\cos(k_x/2)\cos(k_y/2)\cos k_{1z});\tag{11}$$

$$\varepsilon=\frac{2\alpha_3}{m_3}(2-\cos k_x-\cos k_y)+\frac{8\gamma_3}{m_3}\times(1-\cos(k_x/2)\cos(k_y/2)\cos k_{3z}).\tag{12}$$

Figure 3 shows the result of a numerical solution of the given system of equations in the form of the dependences of the coefficients r and t on the squared frequency ε. The case considered is that in which the crystals separated by the impurity monolayer are identical. The following parameters of the crystals and defect were used in the calculation: $\alpha_1=\alpha_3=1$, $\gamma_1=\gamma_3=0.1$, $m_1=m_2=1$, $\alpha_2=0.5$, $\gamma_2^{(1)}=\gamma_2^{(3)}=0.07$. It is seen in the figure that outside the resonance region ($\varepsilon\neq\varepsilon_{\text{res}}$) the wave incident on the defect is almost completely reflected (the coefficient r is close to unity, and the transmission coefficient t is very small). At a value $\varepsilon=\varepsilon_{\text{res}}$ the reflection coefficient r goes to zero and the transmission coefficient t goes to unity. The resonance frequency $\omega_{\text{res}}=\sqrt{\varepsilon_{\text{res}}}$ characterizes a low-frequency, weak-dispersion mode of the optical type. The amplitude of the displacements of the atoms of the impurity layer in the given mode is significantly greater than the amplitude of the vibrations of the atoms of the host lattice. In the long-wavelength limit for weak coupling of the defect with the main lattice we have the following estimate for the resonant transmission frequency:

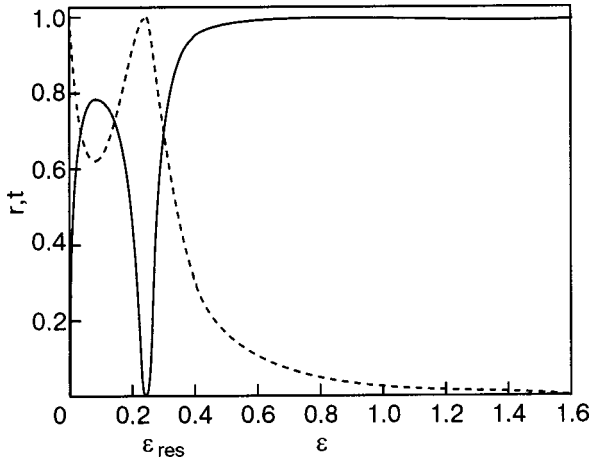

FIG. 3. Coefficients of reflection r (solid curve) and transmission t (dashed curve) versus the squared frequency ε for crystals with identical physical properties.

$$\omega_{\text{res}}\simeq\sqrt{\frac{4(\gamma_2^{(1)}+\gamma_2^{(3)})}{m_2}}.\tag{13}$$

If the crystals separated by the monolayer are different in their physical properties, then the form of the dependence of the reflection coefficient on the square of the frequency is similar to that illustrated in Fig. 3. However, at a frequency ω_{res} the reflection coefficient no longer goes exactly to zero but only has a pronounced minimum.

The results obtained in the long-wavelength limit agree with the results of Ref. 13. In that paper, in the framework of the theory of elasticity with capillary effects taken into account (the theory was set forth in detail in Refs. 14 and 15) the expression $\omega_{\text{res}}\simeq\sqrt{[2(b_2-c_2)]/\rho_s}$ was obtained for the resonance frequency ω_{res}, where ρ_s is the surface mass density of the layer and b_2 and c_2 are the capillary parameters characterizing the elastic properties of the planar defect. Using formula (13), one can obtain a relation between the phenomenological capillary parameters describing the physical properties of the defect in the theory of elasticity and the parameters of the discrete model under consideration: $b_2-c_2\simeq 2(\gamma_2^{(1)}+\gamma_2^{(3)})/a^2$ (a is the lattice constant in the plane of the impurity layer).

We note that in the theory of elasticity there also exists another mechanism of resonant transmission of phonons (under conditions of the so-called geometric resonance—the analog of the antireflective condition in optics[16]), which comes about under certain relations between the thickness of the interface and the wavelength. We plan to take up this problem in the case of an interlayer consisting of several defect atomic layers in the very near future.

The authors thank A. G. Shkorbatov for his interest in this study and for a helpful discussion of the results.

*E-mail: syrkin@ilt.kharkov.ua

[1] Yu. A. Kosevich, E. S. Syrkin, and A. M. Kossevich, Prog. Surf. Sci. **55**, 59 (1997).
[2] Yu. A. Kosevich, Prog. Surf. Sci. **55**, 1 (1997).
[3] A. M. Kosevich, P. A. Minaev, E. S. Syrkin, and M. L. Polyakov, Fiz. Nizk. Temp. **29**, 556 (2003) [Low Temp. Phys. **29**, 414 (2003)].
[4] A. M. Kosevich, S. E. Savotchenko, and D. V. Matsokin, Fiz. Nizk. Temp. **25**, 63 (1999) [Low Temp. Phys. **25**, 48 (1999)].
[5] M. A. Ivanov, Yu. V. Skripnik, and N. N. Gumenchuk, Fiz. Nizk. Temp. **23**, 208 (1997) [Low Temp. Phys. **23**, 153 (1997)].
[6] A. M. Kosevich, S. E. Savotchenko, and D. V. Matsokin, Fiz. Nizk. Temp. **24**, 992 (1998) [Low Temp. Phys. **24**, 748 (1998)].
[7] P. Masri, Surf. Sci. Rep. **9**, 293 (1988).
[8] A. G. Shkorbatov, A. Feher, and P. Stefanyi, Physica B **218**, 242 (1996).
[9] I. M. Gel'fgat and E. S. Syrkin, Fiz. Nizk. Temp. **4**, 521 (1978) [Sov. J. Low Temp. Phys. **4**, 324 (1978)].
[10] M. A. Mamaluĭ, E. S. Syrkin, and S. B. Feodos'ev, Fiz. Tverd. Tela (St. Petersburg) **38**, 3683 (1996) [Phys. Solid State **38**, 2006 (1996)].
[11] M. A. Mamalui, E. S. Syrkin, and S. B. Feodosyev, Fiz. Nizk. Temp. **25**, 976 (1999) [Low Temp. Phys. **25**, 732 (1999)].
[12] L. Brillouin and M. Parodi, *Propagation des Ondes dans les Milieux Périodiques*, Masson, Paris (1956), Izd-vo Inostr. Lit., Moscow (1959) [expanded version of L. Brillouin, *Wave Propation in Periodic Structures*, McGraw-Hill, New York (1946), repr. Dover, New York (1953)].
[13] Yu. A. Kosevich and E. S. Syrkin, Fiz. Tverd. Tela (Leningrad) **33**, 2053 (1991) [Phys. Solid State **33**, 1156 (1991)].
[14] A. F. Andreev and Yu. A. Kosevich, Zh. Éksp. Teor. Fiz. **81**, 1435 (1981) [Sov. Phys. JETP **54**, 761 (1981)].
[15] Yu. A. Kosevich and E. S. Syrkin, Kristallografiya **33**, 1339 (1988) [Sov. Phys. Crystallogr. **33**, 797, 801 (1988)].
[16] L. M. Brekhovskikh, *Waves in Layered Media* [in Russian], Nauka, Moscow (1973).

Translated by Steve Torstveit

QUANTUM EFFECTS IN SEMICONDUCTORS AND DIELECTRICS

Integral and differential developments of the carrier density of states in intercalated layered crystals

N. K. Tovstyuk*

Lviv Ivan Franko National University, Department of Electronics, 50 Dragomanov St., Lviv 290005, Ukraine

Submitted December 17, 2003; revised February 6, 2004)
Fiz. Nizk. Temp. **30**, 672–678 (June 2004)

The effect of the layered crystal intercalation on the functional dependence of the carrier density of states is analyzed. The conditions of thermodynamic stability of the intercalation process in relation to the Fermi energy and microscopic parameters are studied. © *2004 American Institute of Physics.* [DOI: 10.1063/1.1768356]

INTRODUCTION

The density of states of elementary excitations, $\rho(\omega)$, is widely used in calculating the physical quantities observed in experiments. Two approximations can be distinguished which result from utilizing $\rho(\omega)$. First, $\rho(\omega)$ is widely used in the search for the mean values of the energy characteristics. The result of an integration process over a whole range of frequencies is determined by the functional dependence of $\rho(\omega)$ in the region of integration. As an example, we can take the use of $\rho(\omega)$ for calculations of the indirect interaction between adatoms on a tight-binding solid.[1] On the other hand, a number of examples can be presented in which some physical characteristic or other is determined by the value of $\rho(\omega)$ at a certain energy point. For instance the critical temperature of the transition to the superconducting state according to BCS theory is determined by density of states at the Fermi energy ε_F.[2] The second example of the benefit of knowledge of $\rho(\omega)$ is in relation to the Lifshitz transition of order $2\frac{1}{2}$. Such a transition is realized in a layered crystal due to the peculiarities of its structure.[3] The layered crystal can be represented as a set of packed ''sandwiches'' coupled by weak van der Waals forces. Each sandwich is a set of monatomic layers with covalent or ion–covalent bonding. The small but nonzero electron overlap between layers is much better described by a strongly anisotropic three-dimensional dispersion law with different effective masses within the layer plane and normal to it ($m^*_{x,y} \ll m^*_z$).[4] In our paper the layered crystal will be described by a model dispersion law which is distinguished from the isotropic and anisotropic ones by a much smaller electron overlap integral t_c across the layers than within the layer plane α_c. It was first written by Fivaz:[5]

$$\varepsilon(\chi,k)=\alpha_c\chi^2+t_c(1-\cos k), \tag{1}$$

where all the quasi-momenta $\chi=(k_x,k_y)$, $k_z\equiv k$ are written in units of the lattice constant, $\alpha_c=1/2m^*_{\|c}$, $m^*_{\|c}$ is the electron effective mass within the layer plane, $t_c=1/2m^*_{\perp c}$, $m^*_{\perp c}$ is the electron effective mass across the layer plane, and $\hbar=1$. Inasmuch as the parameters α_c, t_c are determined by the effective masses, they will be taken from the experimental data. In terms of the density of states, Eq. (1) corresponds to $\rho_0(\omega)$ as follows:

$$\rho_0(\omega)=\begin{cases}\dfrac{2\pi}{\alpha_c}\arccos\dfrac{2t_c-\omega}{2t_c}, & \text{at } \omega\leqslant 2t_c,\\ \dfrac{\pi^2}{\alpha_c}, & \text{at } \omega\geqslant 2t_c\end{cases}. \tag{2}$$

As follows from (2), at the point $\omega=2t_c$ the derivative $\partial\rho_0/\partial\omega$ is discontinuous, and the value $\omega=2t_c$ corresponds to the topological $2\frac{1}{2}$-order Lifshitz transition, which characterizes the transition from the open to the closed isoenergy surface of a layered crystal.

Discrimination in the chemical bonds causes a number of phenomena specific to layered crystals. One of them is intercalation, which consists in introducing a guest atom into the gaps between sandwiches, the so-called van der Waals gaps. We define the host material as the recipient of the guest species, the intercalate as the guest species resident in the host material, and the intercalant as the guest species substance.[6]

In intercalation of the transition metal dichalcogenides MX_2 (where M is atom of a metal of a transition group, X = S, Se) with various electron-donor species, the changes observed in the electronic properties can be satisfactorily explained by the charge transfer resulting in the gradual filling of the host lattice band without any appreciable change in its shape or its mutual position—a model known as the rigid-band approximation.[7] Firm evidence for the validity of this model is available for the cases where the intercalate is an alkali (or alkaline-earth) metal, a noble metal, or a first-row transition metal. So, by changing the carrier concentration during the intercalation process, the Fermi energy can be raised up to the topological $2\frac{1}{2}$-order Lifshitz transition. The rigid-band model satisfactorily describes effects in which the factors of importance are the integral developments of band structure and population of the band (such as the kinetic properties) rather than the details of the band structure. Naturally, this model can be regarded as a crude approximation.

As is shown in Ref. 8, intercalation of $TlGaS_2$ (space group cc, with lattice constants $a=b=10.31$ Å, $c=15.16$ Å, and thickness of the van der Waals gap 3.64 Å[9]) by Li increases the degree of anisotropy of the electro-, photo-, and x-ray conductivity via the diminution of interlayer mixing. In this case the intercalated crystal has a more pronounced ''two-dimensionality.'' However, this effect is most conveniently achieved by the intercalation of organic molecules, in particular, the long-chain amines and related macromolecules. For example, in a solid such as $2H$-TaS_2 (trigonal structure with lattice constants $a=3.36$ Å, $c=5.89$ Å and a thickness of the van der Waals gap of nearly 3 Å[10]) intercalated with n-octadecylamine, the layers can be separated by a bilayer of octadecylamine molecules with a dimension approaching 60 Å, where the thickness of the single layer is ~ 6 Å. Since the interaction between the layers is now considerably weakened, this also makes the crystal closer to ''two-dimensional.'' [11] All these facts confirm that the rigid-band model is not capable of describing the phenomena concerned with the change of lattice parameters and thus with the energy parameters such as electron overlap.

That is why it seems interesting to study i) the limits of applicability of the rigid-band model, ii) the effect of the host–guest interaction on the shape of the density of states, particularly in the topological $2\frac{1}{2}$-order Lifshitz transition, iii) the change of free energy of the electron subsystem, depending on the intercalant and the carrier concentration, at different microscopic parameters.

The goal of this paper is to analyze $\rho(\omega)$ in the intercalated layer due to the insertion of foreign atoms within the framework of a model with the following features. Intercalants locate only in the van der Waals gap. The guest–guest interaction causes splitting of the intercalant energy level ε_0 into a band with a dispersion law similar to (1). We restrict ourselves to the virtual crystal model, i.e., when N_0 impurities occupy each cell equiprobably with the equal probability $p=N_0/N$, where N is total number of cells.

ELECTRON DENSITY OF STATES IN AN INTERCALATED LAYERED CRYSTAL

The carrier density of states in the intercalated layered crystal will be calculated below as a function of the intercalant concentration in a wide region of energy, and, in particular, in certain energy regions like the band bottom and energy corresponding to the $2\frac{1}{2}$-order Lifshitz transition. Two different descriptions of such a problem exist: i) change of the chemical potential with the dispersion law unaltered, or, in other words, unaltered energy states (the rigid-band model), ii) change of the dispersion law caused by intercalation at an unaltered chemical potential. In fact, the importance of choice (i) or (ii) depends on the concrete problem, namely, chemical bonds and the degree of anisotropy, i.e., the energy characteristics of the host and degree of host–guest interaction.

The case of an interacting host–guest system at unaltered chemical potential will be considered. Let us construct the Hamiltonian of the electron subsystem of the host with N_0 foreign atoms intercalated into it. We will use operational functions

$$\hat{\Psi}(\mathbf{r})=\sum_{\mathbf{n}}\ \hat{c}_{\mathbf{n}}\psi_{\mathbf{n}}(\mathbf{r})+\sum_{\mathbf{n}}\ p(\mathbf{n})\hat{a}_{\mathbf{n}}\varphi_{\mathbf{n}}(\mathbf{r}), \tag{3}$$

where the summation is over all cells; $\psi_{\mathbf{n}}(\mathbf{r})$ is the wave function of an electron at a site of the layered crystal with weighting coefficient $\hat{c}_{\mathbf{n}}$, $\varphi_{\mathbf{n}}(\mathbf{r})$ is the wave function of an electron on the site of the intercalant with weighting coefficient $p(\mathbf{n})\hat{a}_{\mathbf{n}}$: $p(\mathbf{n})$ is the probability

$$p(\mathbf{n})=\begin{cases}1, & \text{if the intercalant is in the } \mathbf{n}\text{-th cell}\\ 0, & \text{otherwise}\end{cases}. \tag{4}$$

In the case of a one-electron description, in the second-quantization representation on the unary Hamiltonian and operational functions (3) Hamiltonian will have the form

$$\begin{aligned}\mathcal{H}=&\sum_{\mathbf{n},\mathbf{n}'}\ t(\mathbf{n},\mathbf{n}')c_{\mathbf{n}}^{+}c_{\mathbf{n}'}+\sum_{\mathbf{n},\mathbf{n}'}\ p(\mathbf{n})p(\mathbf{n}')t_i(\mathbf{n},\mathbf{n}')a_{\mathbf{n}}^{+}a_{\mathbf{n}'}\\&+\sum_{\mathbf{n}}\ p(\mathbf{n})\varepsilon_0 a_{\mathbf{n}}^{+}a_{\mathbf{n}}+\left[\sum_{\mathbf{n}}\ p(\mathbf{n})V_0 a_{\mathbf{n}}^{+}c_{\mathbf{n}}+\text{h.c.}\right]\\&+\left[\sum_{\mathbf{n},\mathbf{n}'}\ p(\mathbf{n})V(\mathbf{n},\mathbf{n}')a_{\mathbf{n}}^{+}c_{\mathbf{n}'}+\text{h.c.}\right].\end{aligned} \tag{5}$$

Here the first term describes electron mixing at the host sites in $\mathbf{n}$, $\mathbf{n}'$ cells ($c_{\mathbf{n}}$, $c_{\mathbf{n}'}^{+}$ are Fermi operators of annihilation and creation, respectively); the second and third terms are an analogous mixing in the guest subsystem (ε_0 is the energy level of the intercalant, $a_{\mathbf{n}}$, $a_{\mathbf{n}'}^{+}$ are Fermi operators of annihilation and creation of the intercalant, respectively). The remaining terms describe an electron host–guest mixing in the same and in the nearest cells, respectively. The electron overlap in the guest subsystem $t_i(\mathbf{n},\mathbf{n}')$ and electron host–guest overlap $V(\mathbf{n},\mathbf{n}')$ satisfy the condition of translational invariance, i.e., $t_i(\mathbf{n},\mathbf{n}')=t_i(\mathbf{n}-\mathbf{n}')$, $V(\mathbf{n},\mathbf{n}')=V(\mathbf{n}-\mathbf{n}')$.

In the virtual crystal approximation in the momentum representation Eq. (5) takes the form

$$\begin{aligned}\mathcal{H}=&\sum_{\mathbf{k}}\ \varepsilon(\mathbf{k})c_{\mathbf{k}}^{+}c_{\mathbf{k}}+p^2\sum_{\mathbf{k}}\ \tilde{\varepsilon}_i(\mathbf{k})a_{\mathbf{k}}^{+}a_{\mathbf{k}}+p\sum_{\mathbf{k}}\ \varepsilon_0 a_{\mathbf{k}}^{+}a_{\mathbf{k}}\\&+p\sum_{\mathbf{k}}\ V(\mathbf{k})c_{\mathbf{k}}^{+}a_{\mathbf{k}}+\text{h.c.},\end{aligned} \tag{6}$$

where $\varepsilon(\mathbf{k})$ k is the dispersion law of the host subsystem (1), $c_{\mathbf{k}}^{+}$ and $c_{\mathbf{k}}$ are Fermi operators of creation and annihilation in the host subsystem, respectively, $a_{\mathbf{k}}^{+}$ and $a_{\mathbf{k}}$ are Fermi operators of creation and annihilation in the guest subsystem,

$$\tilde{\varepsilon}_i(\mathbf{k})=\alpha_i\chi^2+t_i(1-\cos k) \tag{7}$$

is the dispersion law of the guest subsystem, and α_i and t_i are the electron overlap integrals of the nearest guest atoms within and normal to the layer, respectively. The second and third terms in (6) can be combined into one. Then the Hamiltonian (6) will have the form

$$\mathcal{H}=\sum_{\mathbf{k}}\ \varepsilon(\mathbf{k})c_{\mathbf{k}}^{+}c_{\mathbf{k}}+p^2\sum_{\mathbf{k}}\ \varepsilon_i(\mathbf{k})a_{\mathbf{k}}^{+}a_{\mathbf{k}}+p\sum_{\mathbf{k}}\ V(\mathbf{k})c_{\mathbf{k}}^{+}a_{\mathbf{k}}+\text{h.c.} \tag{8}$$

with the dispersion law $\varepsilon_i(\mathbf{k})=\tilde{\varepsilon}_i(\mathbf{k})+\varepsilon_0/p$, measured from ε_0/p, and the Fourier transform of $V_0+V(\mathbf{n},\mathbf{n}')$ is equal to

$V(\mathbf{k})$. The change of intercalant concentration p governs the value of the constants in front of the second and third terms in (8), i.e., $p^2\alpha_i$, $p^2 t_i$, and $pV(\mathbf{k})$.

Let us use method of two-time retarded Green's function and calculate the carrier density of states. For the system described by Eq. (5) the Green's functions for the intercalate and host subsystem are[12]

$$\langle\langle a_k | a_k^+ \rangle\rangle = \frac{\omega - \varepsilon(\mathbf{k})}{[\omega - \varepsilon(\mathbf{k})][\omega - p^2\varepsilon_i(\mathbf{k})] - p^2 V^2(\mathbf{k})} \tag{9}$$

and

$$\langle\langle c_k^+ | c_k^+ \rangle\rangle = \frac{p^2\varepsilon_i(\mathbf{k})}{[\omega - \varepsilon(\mathbf{k})][\omega - p^2\varepsilon_i(\mathbf{k})] - p^2 V^2(\mathbf{k})}, \tag{10}$$

respectively. The density of states $\rho_m(\omega)$ is defined from the corresponding Green's function $\langle\langle a_m | a_m^+ \rangle\rangle$ by[13]

$$\rho_m(\omega) = -\frac{1}{\pi} \operatorname*{Im}_{\varepsilon \to 0} \langle\langle a_m^+ \| a_m^+ \rangle\rangle_{|\omega + i\varepsilon}. \tag{11}$$

Then, we obtain

$$\rho_c(\omega) = \frac{1}{2(2\pi)^2} \int_{k_1}^{k_2} \frac{\omega - p^2\varepsilon_i(q_1)}{|2bK(q_1) + c(cq_1 + d)|} dk - \frac{1}{2(2\pi)^2} \int_{k_3}^{k_4} \frac{\omega - p^2\varepsilon_i(q_2)}{|2bK(q_2) + c(cq_2 + d)|} dk. \tag{12}$$

$$\rho_i(\omega) = \frac{1}{2(2\pi)^2} \int_{k_1}^{k_2} \frac{\omega - \varepsilon(q_1)}{|2bK(q_1) + c(cq_1 + d)|} dk - \frac{1}{2(2\pi)^2} \int_{k_3}^{k_4} \frac{\omega - \varepsilon(q_2)}{|2bK(q_2) + c(cq_2 + d)|} dk, \tag{13}$$

where the notation $b = \frac{1}{2}(\alpha_c + p^2\alpha_i)$, $c = \frac{1}{2}(\alpha_c - p^2\alpha_i)$, $d = \frac{1}{2}[(t - p^2 t_i)(1 - \cos z) - p\varepsilon_0]$ is used, and $K(q_i)$ with $q_i \equiv \chi_i^2$ is

$$K(q_i) = \frac{1}{2}\sqrt{[\varepsilon(\mathbf{k}) - p^2\varepsilon_i(\mathbf{k})]^2 + 4p^2|V(\mathbf{k})|^2}. \tag{14}$$

The regions of integration k_i are determined by the condition $(2\pi)^2 \geqslant q_i \geqslant 0$, and $V(\mathbf{k}) \equiv V$ (the Fourier transform of $V_0 + V(\mathbf{n}, \mathbf{n}')$) will be chosen to be constant.

The total carrier density of states of the intercalated layered crystal is of the form $\rho(\omega) = \rho_c(\omega) + \rho_i(\omega)$. Remember that the goal of this paper is to find out the dependence and the tendency of $\rho(\omega)$ to change in the region of the topological $2\frac{1}{2}$-order Lifshitz transition. To this end it is necessary to know the change of the behavior of the densities of states of the host $\rho_c(\omega)$ and guest $\rho_i(\omega)$ with increasing p and varying microscopic parameters V and t_i. The results of calculations of $\rho_c(\omega)$ and $\rho_i(\omega)$ performed according to (12), (13) for different p, V are given in Figs. 1 and 2, respectively.

As calculations showed, at a small guest concentration p (Ref. 12) its increase leads to the appearance of a "tail" of the states density in the forbidden band and to a certain undershoot in the $\rho_c(\omega)$ dependence. There is also the region of energy where the dependence $\rho_c(\omega)$ is quite similar to $\rho_0(\omega)$ for the pure crystal ($\rho_c(\omega) \to A_0 + \rho_0(\omega)$). This means that the rigid-band model is quite good for the description of $\rho_c(\omega)$ in this case. The higher is p the greater is A_0, and the shape of $\rho_c(\omega)$ is not similar to that of $\rho_0(\omega)$, and the rigid-band model becomes unacceptable. An increase of the guest concentration or of the host–guest interaction V_0 smoothes the behavior of $\rho_c(\omega)$ in the region of the Lifshitz transition and shifts it in the direction of higher energies. The behavior of $\rho_i(\omega)$ as a function of p or V_0 turns out to be opposite. The Lifshitz transition becomes more precise and it shifts in the direction of smaller energies. Only an increase of the guest–guest interaction up to the case when $t_i \to \alpha_i$ leads to the elimination of the Lifshitz transition.

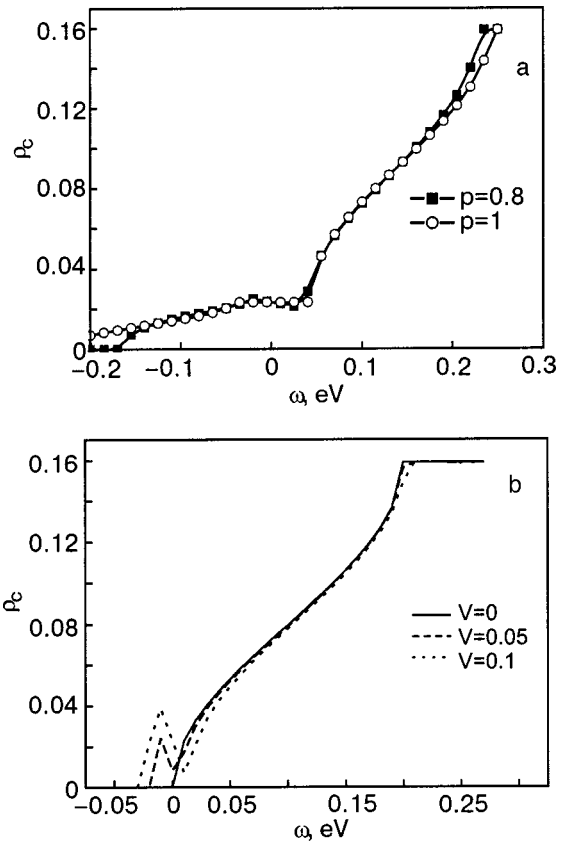

FIG. 1. Spectral dependence of the electron density of states $\rho_c(\omega)$ at $\varepsilon_0 = -0.2$ eV and $\alpha_0 = 0.5$ eV: at $V = 0.1$ eV for different p (a); at $p = 0.2$ for different V (b).

The calculated density of states will be used for analyzing its integral development in the thermodynamic stability of the electron subsystem of the intercalated layered crystal and of the intercalate.

THERMODYNAMIC STABILITY

Let us consider the change of free energy for many-impurity problems at different guest concentrations and ε_0 at various i) Fermi levels, and ii) electron concentrations n. The Fermi level will be the parameter which can be changed in a different way, particularly, by different impurities in the same crystal or by changing the crystal energy parameters.

In our problem the ion–ion interaction was not considered. That is why the change of free energy is studied at low temperatures. Let us consider the limiting case of $T = 0$ (at higher temperatures the Fermi distribution should be taken into account). In the case $T = 0$, the free energy of the electron subsystem coincides with its internal energy $F = E$.[14]

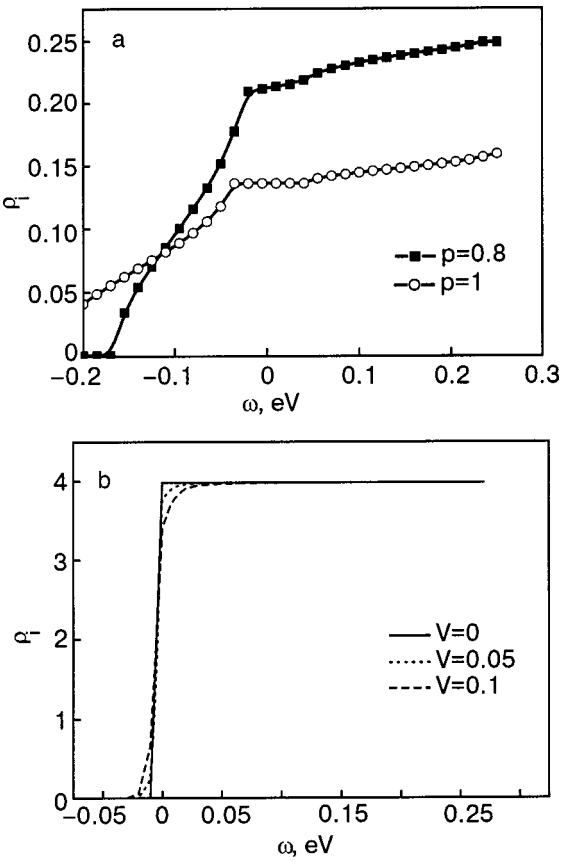

FIG. 2. Spectral dependence of electron density of states $\rho_i(\omega)$ at $\varepsilon_0=-0.2$ eV, $\alpha=0.5$ eV: at $V=0.1$ eV for different p (a); at $p=0.2$ for different V (b).

At a small intercalant concentration the change of free energy (ΔF) of the electron subsystem of the intercalated layered crystal is similar to the interaction between adatoms (or foreign atoms) on a tight-binding solid.[1] According to that paper[1] the chemical potential changes incidentally upon the introduction of adatoms (in our case the intercalant). Then the energy change is determined by the change of the density of states $\Delta\rho(\omega)$ caused by adatomic (or intercalant) states, i.e.,

$$\Delta F=\int_{-\infty}^{\varepsilon_F}[\rho_c(\omega)+\rho_i(\omega)]\omega d\omega-\int_0^{\varepsilon_F}\rho_0(\omega)d\omega-N_0\varepsilon_0, \tag{15}$$

where $\rho_c(\omega)$, $\rho_i(\omega)$, and $\rho_0(\omega)$ are, respectively, the electron densities of states of the host renormalized by interaction with the guest, of the guest renormalized by interaction with the host, and of the pure host; N_0 is the number of the guest species, ε_0 is a guest energy level, and ε_F is the Fermi level.

We calculate ΔF as a function of:

a) ε_F and on ε_0 at various $p(N_0/N)$ (N is the number of crystal sites),

b) the electron concentration n and ε_0, at various $p(N_0/N)$.

The results of the many-impurity problem are obtained in the case of $p\varepsilon_0\leqslant\varepsilon_F\leqslant 2t$ for localized ($\varepsilon_0<0$) and

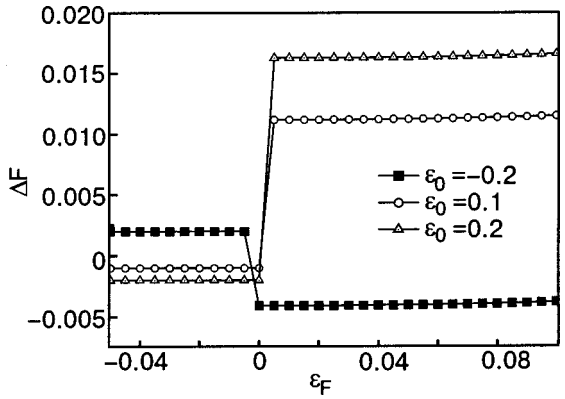

FIG. 3. The free energy difference $\Delta F(\varepsilon_F)$ of an intercalated layered crystal $V=0.01$ eV for different energy levels of the guest and $V=0.01$ eV.

$-p\varepsilon_0\leqslant\varepsilon_F\leqslant 2t$ for resonance ($\varepsilon_0>0$) levels, and $\alpha_c=1$, $t=0.1$, $\alpha_i=0.1$, $t_i=0.01$ (all energy parameters are given in eV).

Numerical calculations show:

i) At $p<p_{\rm cr}$ ($p_{\rm cr}$ is the intercalate concentration defined by $\Delta F(\varepsilon_F)=0$), the dependence $\Delta F(\varepsilon_F)$ is broken into two regions with $\Delta F>0$ and $\Delta F<0$ (Fig. 3), within which ΔF in fact does not change both for localized ($\varepsilon_0<0$) and resonance ($\varepsilon_0>0$) levels. The higher is p, the larger is the interval between such constant values. Here the region of ε_F where the sign of ΔF changes remains the same. For $\varepsilon_0<0$, the thermodynamic equilibrium state ($\Delta F<0$) occurs at $\varepsilon_F>\varepsilon_{\rm cr}^l$, $\varepsilon_{\rm cr}^l<0$, whereas for $\varepsilon_0>0$ it takes place at $\varepsilon_F<\varepsilon_{\rm cr}^r$, $\varepsilon_{\rm cr}^r>0$ ($\varepsilon_{\rm cr}^{l,r}$ are the Fermi energies at which $\Delta F=0$ for localized and resonance levels, respectively). The Fermi level, at which $\Delta F(\varepsilon_F)=0$, is sensitive to the position of the guest energy level, ε_0, namely $\varepsilon_{\rm cr}^r>\varepsilon_{\rm cr}^l$. The higher is $|\varepsilon_0|$, the higher is the value of $p_{\rm cr}$, and the stabler still is the thermodynamic state of the system both for localized and resonance levels.

As the guest concentration increases to $p>p_{\rm cr}$, the dependence of $\Delta F(\varepsilon_F)$ for localized levels is changed (Fig. 4). Namely, in the vicinity of $p_{\rm cr}$ a minimum of $\Delta F(\varepsilon_F)$ takes place. Moreover, at $p>p_{\rm cr}$ one has $\Delta F\geqslant 0$. For resonance levels, the higher is the guest concentration p ($p>p_{\rm cr}$), the smoother is $\Delta F(\varepsilon_F)$ and, what is more, the thermodynamic

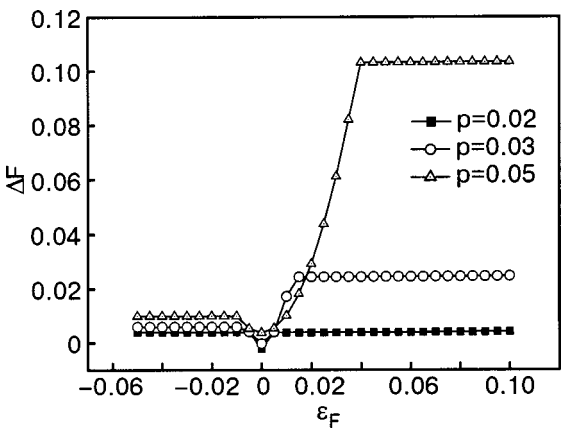

FIG. 4. The free energy difference $\Delta F(\varepsilon_F)$ of an intercalated layered crystal for different guest concentrations.

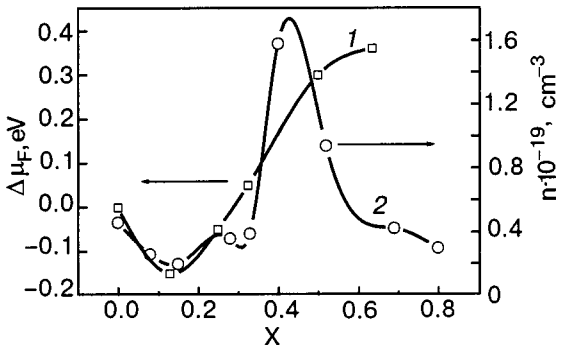

FIG. 5. Difference of the Fermi energy (*1*) and the free carrier concentration (*2*) versus guest loading x in $Li_xBi_2Te_3$ (Ref. 15).

equilibrium region over Fermi level is widened, and the difference between the maximum and minimum values of $\Delta F(\varepsilon_F)$ increases.

ii) In the case of different values of the electron concentrations, the Fermi level may be determined from the following equation

$$n=\int_{-\infty}^{\varepsilon_F}[\rho_c(\omega)+\rho_i(\omega)]d\omega. \tag{16}$$

At small p ($p<p_{cr}$), the $\Delta F(n)$ behavior is similar to $\Delta F(\varepsilon_F)$ both for localized and resonance levels. The higher is p, the narrower is the region of thermodynamic equilibrium and the lower is its stability (ΔF value). The Fermi level corresponding to the minimum of ΔF remains the same. As would be expected, an integral characteristic like the change of free energy does not vary in the region of the Lifshitz transition.

EXPERIMENTAL RESULTS

The measurements of the change of Gibbs energy[15] were carried out by the method of the e.m.f. and its temperature dependence. The position of the Fermi level (Fig. 5, curve *1*) was determined by electrochemical analog of Mott–Schottky method, and free the carrier concentration (Fig. 5, curve *2*) was determined from galvanomagnetic measurements (Hall effect).

The Gibbs thermodynamic potential in the host–guest system is as follows:[16]

$$\Delta G=n_eFE=\Delta S+W+\Delta\mu_F+L\frac{\partial C}{\partial x}+A_0, \tag{17}$$

where F is the Faraday number, n_e is the number of redox electrons, E is the electromotive force, $\Delta S=kT\ln(x/x-1)$ is the configuration entropy component, and x is the number of the introduced guest atoms per formula unit of the host (similar to the theoretical p). The other terms describe the enthalpy component. Among them W describes the interaction between guest component, i.e., the effect of intercalant concentration on the ion–ion interaction in the guest subsystem, $\Delta\mu_F$ is the change of Fermi level position of electrons or holes, L is a coefficient, linear to the potential Lennard-Jones function, $\partial C/\partial x$ is the change of lattice units, and A_0 is a constant and describes the host–guest interaction which is usually taken to be independent of x.[16] As is seen in Fig. 5, the region of the chemical potential minimum corresponds to small intercalant concentrations ($x=p$ is near 0.2). At this value of the concentration the entropy component is already insignificant (the entropy component is much higher than the enthalpy component at small and large x: $x\to 0$, $x\to 1$), and the ion–ion interaction (W) can still be neglected. Thus, the behavior $\Delta\mu(x)$ describes the change of the Gibbs thermodynamic potential $\Delta G(x)$, which at low temperatures coincides with the change of free energy.[14]

Comparing the obtained theoretical results (see Fig. 4) with the experimental ones for intercalated $Li_xBi_2Te_3$ (Ref. 15), one can see (Fig. 5) that at small guest concentrations ($p=x<0.15$) Li intercalation shifts the Fermi level down to the middle of the forbidden band. As a result, the carrier concentration decreases, meaning a decrease of the Gibbs thermodynamic potential, caused by the electron subsystem contribution. As is seen in Fig. 4, the increase of intercalant concentration at a certain Fermi level leads to a decrease of the change of free energy down to a negative value, i.e., stabilization of the system under study.

The fact of the Fermi energy decrease suggests that lithium in the van der Waals gap did not release its electrons, preserving its identity to a certain extent. In terms of the calculation, the degree of guest identity is given by the value of V: the weaker is the host–guest binding, represented by the parameter V, the higher is the guest identity.

CONCLUSIONS

An analysis of the functional dependence of the carrier density of states in an intercalated layered crystal is carried out by two-time retarded Green's functions, considering the host–guest and guest–guest interactions within the framework of virtual crystal model, i.e., intercalants equiprobably occupy each cell ($p\leqslant 1$). It is shown that an increase in concentration p causes the appearence of a certain ''tail'' of the density of states in the forbidden band. Its shape depends on the nature of the guest, i.e., the intercalant energy level ε_0. Either an increase of p or of the host–guest interaction smoothes the Lifshitz transition, shifting it in the direction of higher energies in the $\rho_c(\omega)$ dependence and makes it more distinct, thus shifting the transition point in the direction of smaller energies in the $\rho_i(\omega)$ dependence. The Lifshitz transition in the $\rho_i(\omega)$ dependence disappears only if the anisotropy of the chemical bonds in the intercalate subsystem decreases. Based on the calculated density of states, the change of the free energy of electron subsystem is found. The theoretical results obtained indicate the tendency towards thermodynamic advantages or disadvantages caused by the electron host–guest subsystem, depending on the guest and carrier concentrations in the intercalation process.

The author would like to thank Prof. B. A. Lukiyanets for many stimulating discussions.

*E-mail: tose@polynet.lviv.ua

[1] T. L. Einstein and J. R. Schrieffer, Phys. Rev. B **7**, 3629 (1973).
[2] C. Kittel, *Quantum Theory of Solids*, Wiley, New York–London (1963).
[3] I. M. Lifshitz, Zh. Eksp. Teor. Fiz. **22**, 475 (1952).

[4] H. I. Starnberg, H. E. Brauer, and H. P. Hughes, Phys. Chem. Mater. Low-Dimens. Struct. **24**, 41 (2000).
[5] R. F. Fivaz, J. Phys. Chem. Solids **28**, 839 (1967).
[6] M. S. Dresselhaus, Synthetic Mater. **8**, 351 (1983).
[7] W. Y. Liang, ''Electronic properties of transition metal dichalcogenides and their intercalation complexes,'' in *Proceedings of the 10th Course of the Erice Summer School*, Erice, Italy (1986).
[8] S. N. Mustafayeva, Izv. Ross. Akad. Nauk Neorg. Mater. **30**, 1033 (1994).
[9] Yu. V. Voroshilov and V. Yu. Slyvka, *Quantum Electronics* [in Russian], Republic Interdepartmental Annual, Naukova Dumka, Kiev (1980), Vol. 19, p. 38.
[10] A. Spijkerman, J. L. de-Boer, A. Meetsma, G. A. Wiegers, and S. van Smaalen, Phys. Rev. B **56**, 13757 (1997).
[11] R. F. Gamble, J. H. Osiecki, M. Cais, R. Phisarody, F. J. DiSalvo, and T. H. Geballe, Science **174**, 493 (1971).
[12] N. K. Tovstyuk and B. A. Lukiyanets, Condens. Matter Phys. **5**, 503 (2002).
[13] D. N. Zubarev, Usp. Fiz. Nauk **71**, 71 (1960) [Sov. Phys. Usp. **3**, 320 (1960)].
[14] R. Kubo, *Statistical Mechanics*, North-Holland, Amsterdam (1965).
[15] I. I. Grygorchak, S. V. Gavrylyuk, V. V. Netyagha, and Z. D. Kovalyuk, J. Phys. Stud. **4**, 82 (2000).
[16] A. S. Nagelberg and W. L. Worrell, J. Solid State Chem. **38**, 321 (1981).

This article was published in English in the original Russian journal. Reproduced here with stylistic changes by AIP.

OBITUARY

In memoriam: David Schoenberg (1911–2004)

[DOI: 10.1063/1.1768357]

The famous English experimental physicist David Schoenberg died in Cambridge on March 10 at the age of 93. Schoenberg was one of the creators of the modern low-temperature solid state physics. Schoenberg's name is well known by all who study the physics of metals and superconductivity.

Schoenberg made an enormous contribution to the physics of quantum oscillation phenomena. The oscillatory behavior of the magnetoresistance and magnetic susceptibility of bismuth, discovered in Leiden by Shubnikov and de Haas and by de Haas and van Alphen, respectively, had long been considered as anomalous manifestations of some unusual properties specific to bismuth. Thanks to the efforts of Schoenberg (and also B. G. Lazarev and B. I. Verkin in Kharkov), it became clear that these quantum oscillation effects are of a general and fundamental character. It is now recognized that this is not simply a curious and beautiful effect but also a powerful tool for studying the electronic structure of metals.

Schoenberg lived a long life in continuous connection with Cambridge. From 1947 to 1973 he was the director of the Mond Laboratory, and in 1973–1977 he was a professor and group leader of the low-temperature physics group at Cambridge University.

Schoenberg was a winner of the Fritz London Memorial Prize for outstanding achievements in low-temperature physics and was awarded an honorary doctorate by Lausanne University. He was a member of the Royal Society and a Foreign Honorary Member of the American Academy of Arts and Sciences.

Editorial Board

